Quasi-periodic and periodic photonic crystals:

A simulation study of their self-assemby, stability and photonic properties

Harini Pattabhiraman

Cover: Pictorial representation of self-assembly of a mosaic
Invitation bookmark: Pictorial representation of self-assembly of dodecagons using square and triangle tiles

PhD thesis, Utrecht University, The Netherlands, July 2017.

ISBN: 978-90-393-6796-4

Printed by Gildeprint

A digital version of this thesis is available at http://colloid.nl/publications/theses/

The work described in this thesis was performed in the Soft Condensed Matter group, part of the Debye Institute of Nanomaterials Science at Utrecht University.

Quasi-periodic and periodic photonic crystals:

A simulation study of their
self-assembly, stability and photonic properties

Quasi-periodieke en periodieke fotonische kristallen:

Een simulatie studie van hun
zelforganisatie, stabiliteit en fotonische eigenschappen

(met een samenvatting in het Nederlands)

Proefschrift

ter verkrijging van de graad van doctor aan de Universiteit Utrecht op gezag van de rector magnificus, prof. dr. G. J. van der Zwaan, ingevolge het besluit van het college voor promoties in het openbaar te verdedigen op woensdag 5 juli 2017 des ochtends te 10.30 uur

door

Harini Pattabhiraman

geboren op 13 september 1988 te Chennai, India

Promotor: Prof. dr. ir. M. Dijkstra

This work is part of the Industrial Partnership Programme (IPP) *Computational Sciences for Energy Research* (12CSER004) of the Foundation for Fundamental Research on Matter (FOM), which is part of the Netherlands Organisation for Scientific Research (NWO). This research programme is co-financed by Shell Global Solutions International B.V.

Contents

1

Introduction to quasi-periodic and periodic colloidal photonic crystals

In this introductory chapter, we present the premise for the research presented in this thesis. In this thesis, we study the formation, stability and photonic properties of various quasi-periodic and periodic colloidal crystals. This includes quasicrystals in two-dimensional systems and periodic crystals in three-dimensional systems. This is accomplished by using a system of particles with a core-corona architecture. We begin this chapter by introducing the reader to the term photonic crystals, following which, a differentiation is made between a photonic crystal and a photonic band gap material. We then give an overview of the different types of photonic crystals. Later, we proceed to an explanation of quasicrystals, followed by the relevance of studying these crystals in a system of colloidal particles. Finally, we provide a short overview of the chapters of this thesis.

1.1 Why the interest in photonic crystals?

Before we answer that question, let us first ask what are crystals? According to the present definition of the International Union of Crystallography (IUCr), a crystal is any solid that produces an essentially discrete diffraction diagram [1], i.e. has known positions of constituent entities. Thus, a crystal can be composed of atoms, ions, molecules or other larger particles. Of special interest here are semiconductor crystals in which positive and negative charges are positioned alternatively in a lattice, or positive charges are considered to float in a sea of electrons. In either case, the arrangement of charges leads to an electric potential. Also, in such an arrangement of charges, the energy levels of individual electrons start to overlap forming a continuous band of allowed energy states. This leads to a situation where the highest completely occupied energy state and the subsequent first empty energy state are separated by a region which designates energies that the electrons in the solid cannot possess. This region is termed as an electronic band gap.

How does this relate to a photonic crystal? Photonic crystals are the optical analogue of such crystals; they consist of alternating materials with different dielectric constants. The relative dielectric constant between the constituent materials is the analogue for the electric potential in a semiconductor crystal. In general, photonic crystals can be classified as direct or inverse structures. The former consists of a high-dielectric constant material in a surrounding low-dielectric constant medium, and the latter represents the inverse situation. Additionally, analogous to the formation of energy gaps in the electronic band structures of semiconductors, one finds the formation of photonic band gaps in photonic crystals. This means that for a certain range of frequencies, light cannot propagate through the dielectric structure *irrespective* of its polarisation and direction of propagation. Such materials with a photonic band gap are intuitively termed as photonic band gap (PBG) materials. A one-to-one correlation between certain underlying properties of semiconductors and PBG materials is given in Table 1.1. It is important to note that the theoretical calculation of photonic band structures is more complex than that of electronic band structures. This is because one needs to fully account for the vector nature of the electromagnetic field in the PBG calculations [2].

Table 1.1: Analogy between semiconductors and photonic band gap materials.

Property	Semiconductor	Photonic band gap material
Propagating entity	electronic wave	electro-magnetic wave
Underlying potential	electric potential	relative dielectric constant
Governing equations	Schrödinger's equation	Maxwell's equations

Examples of PBG materials are abundant in nature [3]. For example, they play an important role in generating bright colours in the feathers of birds [4–6], in the scales of beetles [7, 8] and butterflies [9], and in the petals of flowers [10, 11]. Artificial fabrication of photonic crystals aims to mimic the properties of these naturally occurring ones. This brings us to the question of why are artificially fabricated photonic crystals and PBG materials interesting?

The field of photonic crystals boomed with the advent and tremendous growth of fibre-optics in telecommunication systems [12]. These optical devices operate in a range of wavelengths between $1.3 - 1.5 \mu m$, i.e. in the microwave regime. Devices operating in this wavelength regime offer a variety of applications for photonic crystals in the telecommunication sector such as lossless wave guides [13], and non-linear optical switches [14]. In addition, they are also used in areas of (bio-)sensing, bio-medical engineering, energy storage and security [3, 15–17]. However, the holy grail is to make these devices truly ‘optical’, i.e. operate at wavelengths close to the visible or infrared regime of the electromagnetic spectrum. This leads us to ask the question, how far have we actually come with these photonic crystals?

The theoretical possibility of a PBG was proposed in the early nineteen-seventies independently by Bykov [18] and Ohtaka [19]. However, the interest in these structures did not gain momentum until the pioneering works by Yablonovitch [20] and John [21], where they both theoretically showed the realisation of a PBG. Following which, the presence of a PBG has been theoretically predicted in a wide range of structures, [22] ranging from direct and inverse forms of diamond cubic [2, 23] and pyrochlore [24, 25] to inverse forms of face-centered cubic [26, 27] and binary NaCl lattices [28, 29]. However, the experimental realisation of these structures have not been met with considerable success. This is because of the amount of precision required to maintain the alignment and stacking in these structures. This results in time consuming and expensive methods of fabrication, which are often borrowed from the semiconductor industry. One of the earlier fabrication methods that was proposed involved drilling cylindrical holes along specific directions in a block of a dielectric material resulting in a PBG in the microwave regime. The first structure fabricated was the Yablonovite, which contained a connected network of holes with a symmetry that resembled a diamond crystal structure [30, 31]. Later, lithography as a means to create photonic crystals was introduced [32]. This involved a layer-by-layer construction of three-dimensional photonic crystals like the wood-pile structure [13]. However, the two-dimensional nature of lithographic techniques does not ensure perfect alignment of these structures in the third dimension. The more recent methods developed for the fabrication of photonic crystals include anisotropic etching [33] and 3-D nanolithography [34].

The most promising method for fabrication of three-dimensional photonic crystals till now has been the self-assembly of colloidal particles. This is because of two reasons: (1) as the name suggests, this method involves letting nature take its own course, i.e. obtain a close-packed structure as a result of the self-organisation of colloidal particles, for example, silica spheres, and (2) the size of colloidal particles, in the several hundred nanometers to micrometers range, is ideal for formation of a PBG in the required optical frequencies [16]. Experimental fabrication of inverse photonic crystals resulting from the self-assembly of colloids in a face-centered cubic structure [17, 35–40] and a binary mixture in a NaCl structure [41] have been successful. The major contenders for a colloidal PBG material are the diamond and the pyrochlore structures. Even though the existence of a PBG is theoretically determined [2, 24, 25], and the possible routes for self-assembly have been computationally simulated [42, 43], their experimental realisation has not been successful, yet. Primarily, the challenge in these self-assembly methods is to obtain a pure material with sufficient uniformity and without unwanted defects [44]. Notwithstanding, we will discuss the suitability of colloidal systems in more detail in Section 1.4.

Once it was apparent that the fabrication of three-dimensional photonic crystals with a complete band gap is elusive, the direction of research turned to the fabrication of two-dimensional photonic crystals. Not surprisingly, a great deal of success has been achieved in these two-dimensional structures. The major advantage of these structures is that they are comparatively easy to fabricate using the available lithographic techniques. In addition, the lower dimensionality of these structures also accounts for greater ease of manipulation, for example, to include defects. This leads us to our next question.

1.2 How are two-dimensional photonic crystals different?

A photonic crystal is classified to be one-, two- or three-dimensional depending on the number of axis of periodicity. A one-dimensional photonic crystal is periodic along a single axis and homogeneous along the other two. One of the commonly known one-dimensional photonic crystal is a Bragg stack consisting of alternating layers of materials with different dielectric constants. However, these structures possess a band gap for only certain incidence angles [12, 45]. Continuing with the definition, a two-dimensional photonic crystal is periodic along two axes and homogeneous along the third, and a three-dimensional photonic crystal is periodic in all three directions. A schematic of these three classes of photonic crystals is given in Figure 1.1.

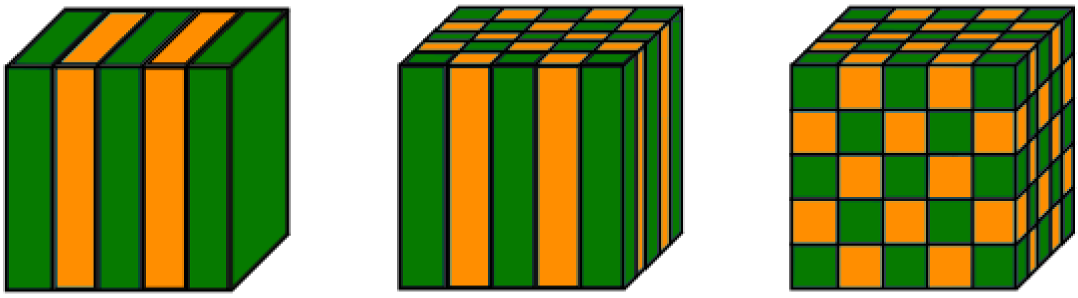

Figure 1.1: Schematic representation of one- **(left)**, two- **(middle)**, and three-dimensional **(right)** photonic crystals. The green and yellow colours respectively represent materials with high and low dielectric constants respectively.

Two-dimensional photonic crystals were first theoretically analysed by Plihal *et al* [46]. This structure consisted of a periodic array of circular dielectric rods with a dielectric constant $\varepsilon = 17$. These rods were arranged in a square lattice, which was embedded in a medium with lower dielectric constant, which in this case was air with $\varepsilon = 1$. Similar to three-dimensional photonic crystals, existence of PBG in two-dimensional photonic crystals was initially confirmed in the microwave regime [47, 48]. Commonly studied two-dimensional photonic crystals conform primarily to either of the following two types, (1) disconnected dielectric rods in air, or (2) air rods drilled in a dielectric matrix resulting in a connected dielectric structure. Examples of structures studied in both configurations include cylindrical rods in square [49], triangular [50], and honeycomb [51] lattices. Alternatively, different rod shapes like square [49], diamond, hexagonal, and triangular [52] have also been theoretically analysed. However, rods with non-cylindrical shapes are less popular for fabrication as the nature of the lithographic and etching techniques used to fabricate these photonic crystals tend to result in rounded features. In stark contrast to the three-dimensional photonic crystals, fabrication of two-dimensional photonic crystals has accomplished considerable progress. Two-dimensional photonic crystals have been fabricated on micron and sub-micron length scales [53–55]. Also, two-dimensional photonic crystals designed to operate at visible or near infra-red frequencies have been fabricated [54, 56–59]. This makes one wonder, what is the current driving force for investigating two-dimensional photonic crystals? Evidently, two-dimensional photonic crystals have their own set of problems as we explain below.

Given the planar structure of the two-dimensional photonic crystals, the electro-magnetic field of light can be decoupled into its two constituent polarisations, i.e. the electric and magnetic fields. Conditions where the magnetic field is considered to be in-plane is termed as transverse magnetic (TM) polarisation, and where the electric field is in-plane is termed transverse electric (TE) polarisation. The interesting feature of this is that the electric field is a vector in TE polarisation and a scalar in TM polarisation [60]. This results in a scenario where the structures that promote the formation of a band gap in the TM and TE polarisations are different. It has been found that a connected dielectric structure favours a band gap in TE polarisation, while a structure with disconnected dielectric rods favours a band gap in the TM polarisation. A schematic of these structures is given in Figures 1.2(a) and 1.2(b). Thus, depending on its structure, a two-dimensional photonic crystal can either have a band gap in the TM or TE polarisation, and not a complete band gap.

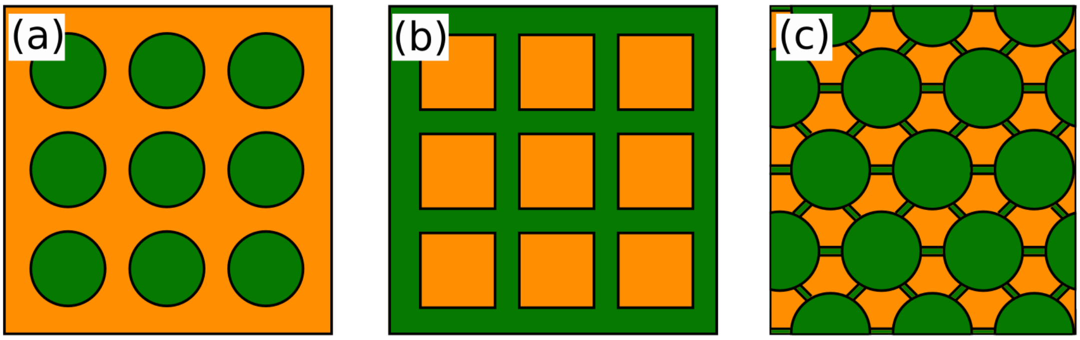

Figure 1.2: Examples of two-dimensional photonic crystals that are favourable for photonic band gap formation in **(a)** TM polarisation, **(b)** TE polarisation, and **(c)** TM+TE polarisations. The green and yellow colours respectively represent materials with high- and low-dielectric constants.

This led to investigations for designing structures having characteristics of both the above configurations that would result in the formation of a complete band gap. This could be a network consisting of dielectric rods connected by dielectric walls such as shown in Figure 1.2(c). Thus, one of the current challenges in the research realm of two-dimensional photonic crystals is construction of such structures to obtain TM and TE band gaps over a common frequency range. This can be seen as the formation of a common TM+TE band gap. A common example of such a photonic structure includes a connected network where dielectric rods are placed in a lattice with symmetry of a honeycomb [61–63]. There are also reports of formation of individual [64] as well as complete (TM+TE) band gaps in two-dimensional amorphous structures, i.e. structures which do not have a periodic arrangement of dielectric structures [65, 66]. More relevant to this thesis are the reports of PBGs reported in quasicrystals [67, 68]. This leads us to the next question.

1.3 What are quasicrystals?

Quasicrystals are materials that exhibit long-range orientational order but no translational periodicity. In other words, they are neither periodically ordered like ordinary crystals nor disordered like amorphous solids. Although they have a well defined, discrete point group symmetry like the ordinary (periodic) crystals, this symmetry is explicitly incompatible with periodic order. To explain, they exhibit the presence of spots in a diffraction pattern showing that they possess long-range order, but this symmetry corresponds to, for example, the presence of five-, eight- or twelve-fold symmetry axes [69]. So how does one create a non-periodic structure with long-range order?

An example for this is the simple one-dimensional Fibonacci chain [70]. To construct the chain, we start with two segments, namely a large segment L and and a short segment S. In order to build successive chains with increasing length, we apply two rules at each iterative step. All S segments undergo an inflation, i.e. $S \rightarrow L$ and the L segments undergo a replacement, $L \rightarrow LS$. If we start with only the S segment, this would lead to the construction of the following chain:

$$\begin{gathered} S \\ L \\ LS \\ LSL \\ LSLLS \\ LSLLSLSL \\ LSLLSLSLLSLLS \\ \ldots \\ \ldots \end{gathered}$$

Of course, there are some rules imposed for creating such a sequence. The most obvious one being that not all starting sequences or iterative rules would lead to a non-periodic chain. If the ratio of the number of L and S segments is $n_L/n_S = \tau$, an irrational number, then the sequence has no repeating distance, i.e. periodicity. And this results in a sequence with long-range order and no translational periodicity [71]. This process of obtaining an aperiodic chain is termed as the method of substitution. This can also be applied to two-dimensional systems where the segments are replaced by tiles. Now, how does this help us to explain two-dimensional quasicrystals?

In general, ordinary (or periodic) crystals can be seen as filling of space with identical unit blocks called the unit cell. In two dimensions, this unit cell is called a tile, and the covering of the plane obtained by means of copying a limited number of tiles, with no overlaps and gaps is termed as a *tiling*. For example, crystals of four- and six-fold symmetry can be created by periodically repeating square and hexagonal tiles, respectively. However, per definition of a quasicrystal, such a tiling method using a single tile to describe a quasicrystal is not possible. This can be thought of as trying to tile a region in space using pentagonal tiles to obtain a quasicrystal with a five-fold symmetry. This, of course, results in the formation of gaps [72]. Nonetheless, there exists an urge to describe quasicrystals as tilings, as this gives a connection with the mathematical notion of tilings for which copious amounts of literature exists. Thus, it has been shown that quasicrystals can be described as a tiling with copies of two or more types of tiles [71]. Such tilings have been extensively used to describe two-dimensional quasicrystals of different symmetries. For example, a decagonal (ten-fold symmetric) quasicrystal can be described using either a Penrose tiling or a or a Tübingen tiling. The former consists of either a combination of a skinny and a fat rhombus [73] or a combination of kite and dart tiles, and the latter consists of a combination of decagon, U-tile, nonagon, hexagon and pentagon tiles [74]. Other examples include a heptagonal tiling exhibiting tetrakaidecagonal (fourteen-fold) symmetry consisting of three kinds of rhombus [73], an octagonal (eight-fold symmetric) tiling consisting of rectangle and triangle tiles [75], or an Ammann-Beenker tiling composed of squares and rhombi [76], and a dodecagonal (twelve-fold symmetric) tiling consisting of a combination of square and triangle tiles, or a combination of square, triangle and shield tiles [77]. As designated here, the nomenclature of these quasicrystals is based on the symmetry of the diffraction pattern that they exhibit [78].

Construction of tilings according to a fixed set of rules as described above is often designated as 'deterministic' [79]. An alternate approach termed as 'random-tiling', was originally suggested by Elser [80, 81]. Here, a network is generated by a randomly distributed configuration of tiles. The only constraint imposed is the preservation of the bond orientational order. Thus, such a non-deterministic tiling exhibits the same symmetry as that of the deterministic tiling because of this orientational order present in the tiles. A comparison between the deterministic and random dodecagonal tiling consisting of squares and triangles is given in Figure 1.3. The deterministic quasicrystal shown in Figure 1.3(a) can either be generated by using the inflation rules with a factor of $(2+\sqrt{3})$ as proposed by Stampfli [82], or by using a projection method with a fractal shaped acceptance region as proposed by Baake [83]. The random-tiling quasicrystal shown in Figure 1.3(b) was adapted from a non-Stampfli square-triangle approximant [84]. As can be noted from Figure 1.3, it is easier to construct an approximation to a random-tiling quasicrystal inside a rectangular/square box, which can then be periodically repeated in space. In addition, as shown in Figure 1.3(c), another method to obtain a periodic structure that is reminiscent of a quasi-periodic lattice is by the construction of an 'approximant'. For example, if we again consider the example of the Fibonacci chain described above and start with a periodic chain of only small segments S, instead of a single S segment as in the previous case [70], and then respectively apply the inflation $S \rightarrow L$ and the replacement $L \rightarrow LS$ rules to each of the S and L segments at each iteration, we get the following chain

$$\begin{gathered} SSSSS.... \\ LLLLL.... \\ LSLSLSLSLS.... \\ LSLLSLLSLLSLLSL.... \\ LSLLSLSLLSLSLLSLSLLSLSLLS.... \\ .... \\ ...... \end{gathered}$$

Once the chain has both L and S segments, we note that the chain is periodic in nature. After each iteration, the period increases as LS, LSL, $LSLLS$, and so on. In other words, the number of L segments to that of S increases with increase in the period of this chain. If we calculate the ratio between the number of L segments to that of S segments, n_L/n_S, we obtain the following series

$$1/1, 2/1, 3/2, 5/3, 8/5, ..., \tau.$$

This is the series of rational approximants to the value of τ, the golden mean. This, also, is the origin of the term 'approximants'. We can intuitively understand that the higher the order of the period, the closer the approximant is to its parent quasicrystal. An example of an approximant is shown in Figure 1.3(c).

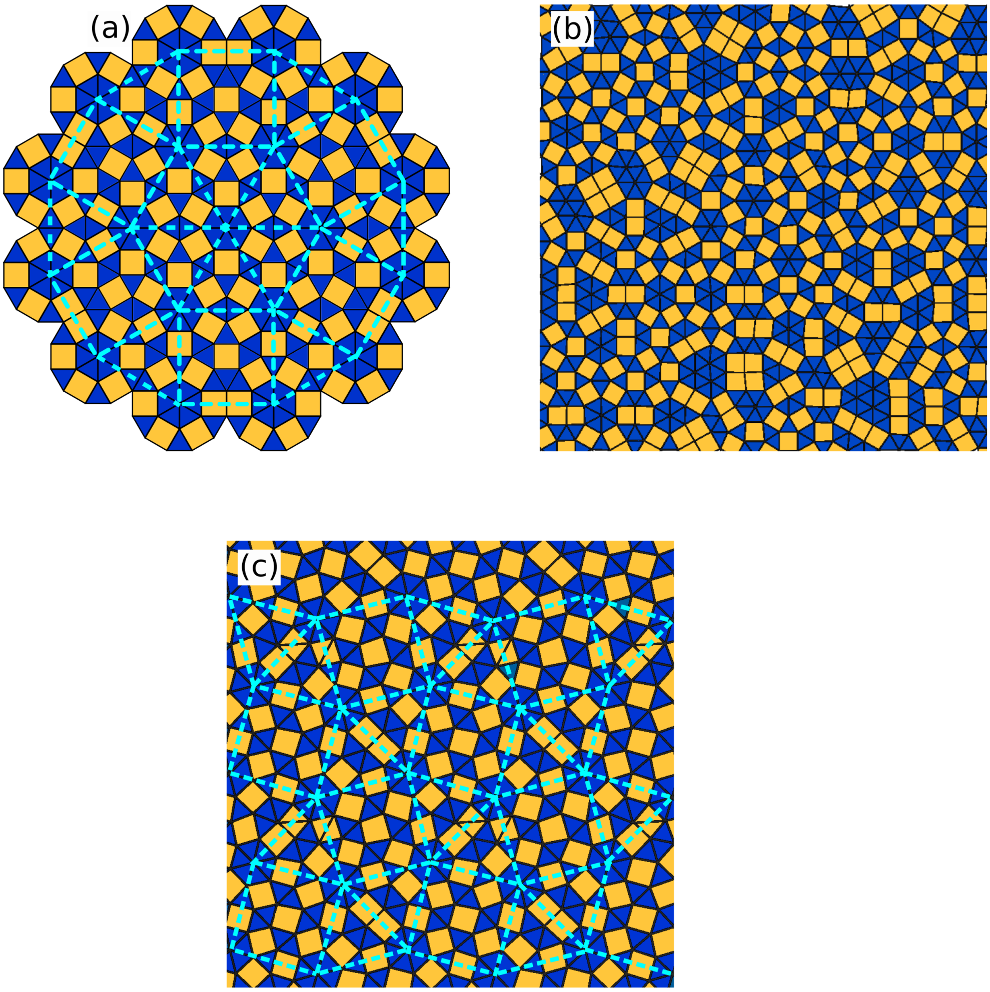

Figure 1.3: Examples of **(a)** a deterministic quasicrystal [83], **(b)** a random-tiling dodecagonal quasicrystal [84], and **(c)** a periodic approximant [85] composed of a tiling with square and triangle tiles. The deterministic quasicrystal and the approximant are constructed using dodecagonal substructures, while the random-tiling quasicrystal is constructed using the squares and triangles that form the dodecagon. The connections between various dodecagons are shown in (a) and (c) using cyan dashed lines. Square and triangle tiles are coloured respectively in yellow and blue.

With this theoretical framework, can we offer some insight to the presence of photonic band gaps (PBGs) in quasicrystals? The origin of the formation of a PBG in a periodic crystal is generally explained by its property to exhibit Bragg-scattering [86], i.e. the structure results in the formation of spots in a diffraction pattern. As explained above, a quasicrystal exhibits the same behaviour as well. Thus, the mechanism of formation of a PBG in a quasicrystal is similar to that in a periodic crystal. In case of quasicrystals, this involves the construction of a (pseudo-) Brillouin zone along which the photonic band structure is evaluated. Interestingly, it has been seen that quasicrystals are, in principle, more favourable for PBG formation than conventional photonic crystals. This is because quasicrystal tackles one of the major challenges in creating photonic crystals, i.e. to design a band gap with the same energy in all directions. This is generally difficult in a periodic crystal because its periodicity is different in different directions. On the other hand, quasicrystals possess a higher symmetry, which results in formation of band gaps at essentially the same energy in all directions of propagations [87]. Correspondingly, PBGs have been theoretically predicted in two-dimensional quasicrystals with five-fold and eight-fold symmetries [67, 88–90], and experimentally realised in a dodecagonal quasicrystal constructed by drilling air holes in a dielectric slab [91, 92]. Additionally, three-dimensional icosahedral photonic quasicrystals were fabricated with band gaps in the microwave [93], infrared [94] and visible ranges [95].

The above reports on fabrications of quasi-periodic photonic crystals leads us to enquire about the experimental realisations of quasicrystals in general. The first observation of a quasicrystal with the forbidden icosahedral symmetry was reported by Shechtman *et al.* in a rapidly cooled Al-Mn alloy [96]. This obviously came as a surprise to crystallographers, metallurgists and material scientists, who had believed for decades that such symmetries cannot exist in crystals [97–99]. Thus, initially, it was thought that the quasicrystals were inherently disordered and unstable [100]. In contrary, thermodynamically stable quasicrystals have been observed in a wide range of intermetallic alloys [101, 102]. In addition to intermetallic alloys, quasicrystals have been found in oxide thin films [103], hydrogen-bonded molecules [104], and metal-organic coordination networks [79]. Surprisingly, in recent times, quasicrystalline order has also been discovered in several soft-matter systems like spherical dendrite micelles [105], block copolymers [106–110], binary mixtures of nanoparticles [111–113], magnetic nanoparticles [114] and mesoporous silica [115]. In addition, quasicrystals can also be fabricated in colloidal systems using external fields such as light or laser beams [116, 117]. To complement these experimental realisations, quasicrystals have been reported in a number of simulation studies of soft-matter systems [77, 118–125]. Additionally, soft-matter quasicrystals have also been identified in systems with non-spherical particles like rhombic platelets [126, 127], patchy platelets [128], binary spherotruncated octahedral particles [113], triangular bipyramids [129], and tetrahedra [130]. In fact, the research in soft-matter quasicrystals has advanced to the extent where an entire series of random-tiling quasicrystals can be described under an unified scheme [123]. These investigations inspire one to look more closely into the intriguing physics and chemistry of soft-matter quasicrystals and try to establish the common elements between different classes of materials, i.e. investigate if the principles of formation and stability in soft-matter systems can be applied to that in traditional alloy systems. For doing this, soft-matter systems have an inherent advantage over the traditional systems of metallic alloys. This paves way the for our next question, why do soft-matter systems, especially colloidal particles, make an ideal model system for our studies?

1.4 Why use colloids as a model system?

Colloidal dispersions refer to a range of systems composed of a dispersion of particles in a continuous medium. These mesoscopic particles, termed as colloids, typically have at least one dimension in the size range of a few nanometers to micrometers. Colloids and its dispersion medium can either be found in gas, liquid or solid phases. Depending on their individual phases, the colloidal system can be classified as a suspension (solid in liquid), an emulsion (liquid in liquid), a foam (gas in liquid) or an aerosol (solid or liquid in gas). The term *colloid*, coined by Thomas Graham in 1861, has its origins from the Greek word ‘$\kappa o \lambda \lambda \alpha$’, which means ‘glue’ [131]. This naming convention resulted from the experiments by Graham where he observed that gluey substances like albumen and caramel did not diffuse through a membrane, while substances like table salt did. Thus, the term colloid came about by attributing the differences in the behaviour of these substances to the gluey nature of the former. However, as mentioned in the beginning of this paragraph, the contemporary definition of colloids is based on its size. So, why is this size range so important?

The lower limit of the size range is dictated by the requirement of treating the dispersion medium as a homogeneous background. In this way, the effect of the background on the particles can then be modelled as an effective interaction. Thus, if the particles are of the size range of the dispersion medium (usually < 1 *nm*), then the background cannot be treated as a homogeneous medium and the colloids will be indistinguishable from it. On the other hand, the upper size limit is determined by the ability of these colloidal particles to exhibit a jittery motion due to their collisions with the molecules of the dispersion medium. This phenomenon of random motion of particles in a medium was first observed by botanist Robert Brown while studying plant pollen in water in 1827 [132]. This random motion of solid particles in a suspension was explained by Albert Einstein [133] by the unbalanced momentum that results from the collisions of the colloids with the molecules of the dispersion medium at any given time. Colloids up to a size of a few micrometers can still experience Brownian motion, which enables them to interact with each other as well as the particles of the dispersion medium. This allows the colloidal particles to physically explore different configurations in phase space. This, in turn, helps the system to reach thermodynamic equilibrium. The fact that thermodynamic equilibrium can be attained in colloidal systems has a galore of advantages. What exactly are these?

The biggest advantage is that the colloidal systems can be used as an analogous system to atoms and molecules, i.e. it can be used as a model system to study physical processes such as phase transformations. Such phase transformations in colloidal systems resulting in the formation of the different states like crystals, liquids or glasses, in accordance to the thermodynamic conditions like pressure and temperature, is termed as colloidal self-assembly. Alternatively, one can say that the colloids self assemble. Why is that of interest? Due to the small size of the real atomic and molecular systems, it is not straightforward either to visualise them individually or to probe their individual trajectories. In contrast, colloidal particles can be visualised in real space using techniques such as confocal microscopy. In addition, owing to the over-damped motion of colloids in the solvent, the time-scale of particle movements is experimentally accessible. Thus, their trajectories can be individually tracked. Secondly, the ability of colloids to probe the available phase space makes them suitable to be studied under a theoretical framework described by the principles of statistical mechanics. Finally, the phase behaviour of colloidal particles can be modified by tuning the interactions between the particles or by using external fields. In summary, colloidal systems offer an unique opportunity in which they can be described theoretically as well as studied experimentally, thereby making them one of the ideal model systems to study phase transformations. This guides us to the ultimate question of this chapter.

1.5 What does this thesis aspire?

In this thesis, we aim to study the phase behaviour and photonic properties of different quasi-periodic and periodic colloidal crystals using computer simulations. This primarily involves identifying the thermodynamic conditions in which these phases are formed and assessing their thermodynamic stability under those conditions. Finally, we evaluate the photonic band diagrams of their corresponding photonic crystals. The layout of the thesis is as follows:

In **Chapter 2**, we give an overview of a system of colloidal particles with a core-corona architecture, the phase behaviour of which is extensively studied in this thesis. We introduce the interaction potential and explain the computational methods used to simulate the phase behaviour, to calculate the free energies of different phases, to map out the equilibrium phase diagram, and to structurally analyse the phases.

The rest of the thesis is divided into three parts: Parts I and II deal with the phase behaviour of various two-dimensional core-corona systems, while Part III deals with the calculations of photonic band diagrams.

Part I is solely devoted to a random-tiling dodecagonal (twelve-fold symmetric) quasicrystal formed in the two-dimensional core-corona system, as this is the most common symmetry associated with quasicrystals in soft matter. In **Chapter 3**, we assess the thermodynamic stability of the dodecagonal quasicrystal with emphasis on comparison with various of its periodic approximants. We, then, evaluate the effect of various parameters such as temperature, corona-size and shape of potential on the formation of this quasicrystal in **Chapter 4**. Finally, **Chapter 5** deals with the formation of this quasicrystal under the influence of a gravitational field, i.e. using sedimentation studies.

Part II deals with random-tiling quasicrystals of various symmetries and other practically interesting phases formed in two-dimensional core-corona systems. In **Chapter 6**, we discuss the formation and stability of an octadecagonal (eighteen-fold symmetric) and a decagonal (ten-fold symmetric) quasicrystal. **Chapter 7** deals with the formation of interesting non-quasicrystalline phases like a mesophase with a stripe texture and an open structure resembling a honeycomb lattice. The former is a two-dimensional equivalent of a nematic phase, while the latter is a known two-dimensional photonic crystal.

Part III addresses the photonic properties of various quasi-periodic and periodic dielectric structures. In **Chapter 8**, we compare the photonic properties of the dodecagonal quasicrystal with some of its periodic approximants. We proceed to study three-dimensional photonic crystals in the last two chapters. **Chapter 9** deals with the formation and stability of a photonic crystal with a pyrochlore lattice in a three-dimensional core-corona system, of which we also evaluate the photonic properties. Finally in **Chapter 10**, we probe the effect of structural defects on the photonic behaviour of a binary NaCl photonic crystal, which can be experimentally fabricated.

2

Description of the core-corona model, simulation, and analysis methods

Core-corona systems are one of the simplest systems which can self-assemble into non-close packed structures. In this chapter, we provide an overview of the core-corona system that is used extensively in this thesis. The interaction potential of this system consists of an impenetrable hard core surrounded by a purely repulsive square shoulder representing the corona. We, then, provide a detailed description of the computational techniques used to simulate the phase behaviour of the system, and the methods used for calculating the free energy of various phases and the equilibrium phase diagram of this core-corona system. We also provide an overview of the various structural analysis routines used in this thesis. We finally provide a description of the methods used for calculating the photonic properties of various structures obtained in this thesis.

2.1 Introduction

Core-corona systems or core-softened systems describe a system of particles consisting of an impenetrable solid core surrounded by a soft-corona that can be inter-penetrated. Core-corona systems were first introduced by Hemmer and Stell in 1970 [134]. In the nascent years of these core-corona systems, the common belief was that their self assembly resulted only in ordered close-packed structures like the hexagonal lattice in a two-dimensional system, due to the radial symmetry of the potential. However, the revelations in the past two decades has been quite contrary. Initial reports of the formation of non-hexagonal lattices in two-dimensional core-corona systems as pioneered by Jagla [118, 135] paved the way for further research. Since then, a zoo of interesting phases such as mesophases like stripes [136–140] and labyrinths [137], Archimedean tiling patterns [106, 141], square lattices [118] and quasicrystals of various symmetries [118, 123, 142] in two dimensions and diamond-cubic lattice [143–147] in three-dimensional systems have been reported. These core-corona systems mimic experimental systems consisting of spherical particles with a rigid core and a squishy corona, e.g., spherical dendrite micelles consisting of a rigid aromatic core with a deformable shell of alkyl chains [105], or block copolymer micelles consisting of a micellar core of hydrophobic polymer surrounded by a large shell of hydrophilic polymer blocks [110].

Theoretically, the soft corona can be modelled by using potentials with a nature that is either purely attractive, or purely repulsive, or a combination of the two. Examples of systems with purely attractive interactions include square-well [121] and flat-well [122] pair potentials, that of purely repulsive interactions are square-shoulder [123, 148, 149] and linear ramp [118] pair potentials, and mixed interactions include Lennard-Jones-Gauss [77] and three-well oscillating [124] pair potentials. In this thesis, we use a completely repulsive square-shoulder potential to describe the corona. A detailed description of the interaction potential, the computational tools used for studying the phase behaviour, and the methods used for calculating the structure and free energy of different phases, and for investigating the photonic properties of these structures are given in the subsequent sections.

2.2 Interaction potential between the core-corona particles

The interaction between the particles of the core-corona system used in this thesis is modelled using a radially symmetric hard-core square shoulder (HCSS) pair potential consisting of a hard core of diameter σ_{HD} and a purely repulsive square shoulder of diameter δ. This HCSS potential can be written as a sum of a hard-disk potential $V_{\mathrm{HD}}(r)$ and a square-shoulder potential $V_{\mathrm{SS}}(r)$, i.e.

$$V_{\mathrm{HCSS}}(r) = V_{\mathrm{HD}}(r) + V_{\mathrm{SS}}(r)$$

where

$$V_{\mathrm{HD}}(r) = \begin{cases} \infty, & r \leq \sigma_{HD} \\ 0, & r > \sigma_{HD} \end{cases}, \tag{2.1}$$

and

$$V_{\mathrm{SS}}(r) = \begin{cases} \varepsilon, & r \leq \delta \\ 0, & r > \delta, \end{cases} \tag{2.2}$$

where r is the interparticle centre-of-mass distance, and $\varepsilon > 0$ is the height of the square shoulder. Figure 2.1 shows a schematic representation of this pair potential, where the hard core and square shoulder are represented respectively by the dark and light red circles. Due to the simple shape of the interaction potential and the ability to explain the arrangements of particles in solid phases on geometric considerations, the HCSS model is also considered as a 'quintessential' test system for solid-solid transitions [150]. The HCSS potential introduces two characteristic length scales in the system; namely the hard-core diameter σ_{HD} and the square shoulder diameter δ. We define ε and σ_{HD}, respectively, as the units of energy and length. In which case, the square shoulder diameter δ is the only tunable parameter for studying the system.

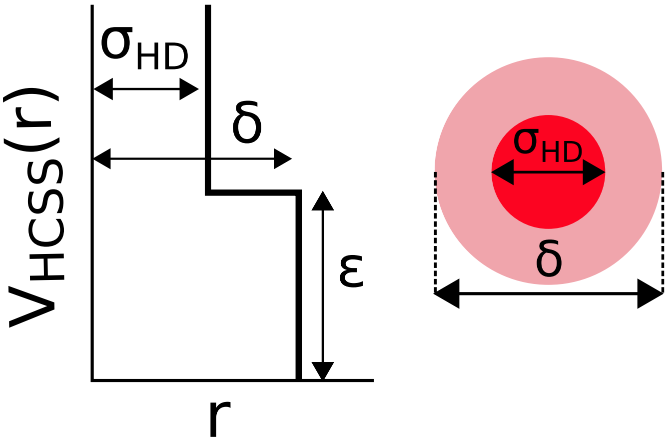

Figure 2.1: Schematic representation of the hard-core square shoulder (HCSS) potential, $V_{\text{HCSS}}(r)$, as a function of the interparticle distance r. The dark and light red circles, respectively, represent the hard core and the soft corona.

The phase behaviour of this core-corona system is influenced as much by the square shoulder diameter as by the density of the system. Both factors influence the relative relevance of the core and the corona. The size of the corona δ determines the range up to which the potential is effective. At $\delta \sim \sigma_{HD}$, the system behaves similar to a system of hard spheres; while at $\delta >> \sigma_{HD}$ and low temperatures, the hard core becomes effectively irrelevant. However, at intermediate shoulder widths, an interplay between the energetic and entropic considerations promotes the formation of phases with exotic and non-trivial structures. On the other hand, the effect of the density of the system on the phase behaviour can be described in terms of three regimes. The first regime occurs at low densities where the coronas do not overlap. The second regime is at high densities, where the coronas entirely overlap and the core repulsion dominates, and finally the third regime is at intermediate densities, where the coronas partially overlap. In this intermediate regime, both the cores and the coronas are partially effective and the competition of these core and corona interactions leads to the formation of phases with unusual symmetries. In other words, the formation of phases with exotic structures in this core-corona system is driven by the minimisation of overlap of the coronas. In this thesis, we probe such a regime of intermediate densities and shoulder widths by studying two- and three-dimensional HCSS systems at different values of δ. Specifically, we study the HCSS system in two dimensions with $\delta = 1.40\sigma_{HD}$ in Chapters 3, 4, and 5, $\delta = 1.27\sigma_{HD}$ and $1.60\sigma_{HD}$ in

Chapter 6, and $\delta = 1.95\sigma_{HD}$ in Chapter 7, and in three dimensions with $\delta = 2.10\sigma_{HD}$ in Chapter 9.

2.3 Simulating the phase behaviour of the system

In this section, we explain the computational techniques used to study the phase behaviour of the system. We analyse the equilibrium phase behaviour by means of Monte Carlo simulations as explained in Section 2.3.1, and probe the dynamics of the system using Event-Driven Brownian Dynamics simulations as explained in Section 2.3.2.

2.3.1 Monte Carlo simulations

Using Monte Carlo simulations, we evaluate various equilibrium characteristics associated with a many-particle system. This is achieved by identifying the relevant states in the phase space associated with the number of different configurations of the system using an effective sampling scheme. A comprehensive description of this method is given in Reference [151] and a short overview is provided here.

Let us first consider a system of N identical particles of mass m interacting with each other by a potential $U(\mathbf{r})$ in a box with fixed volume V at a constant temperature T. This represents the canonical ensemble with constant N, V and T. The Hamiltonian for this system can be written as a function of the positions $\mathbf{r}^N$ and momenta $\mathbf{p}^N$ of the particles as

$$H\left(\mathbf{r}^N,\mathbf{p}^N\right) = \sum_{i=1}^{N} \frac{\mathbf{p}_i^2}{2m} + U\left(\mathbf{r}^N\right). \tag{2.3}$$

The partition function of this system can be derived as

$$Z(N,V,T) = \frac{1}{N!h^{3N}} \int d\mathbf{r}^N d\mathbf{p}^N \exp\left(-\beta H\left(\mathbf{r}^N,\mathbf{p}^N\right)\right), \tag{2.4}$$

where $\beta = 1/k_B T$ is the inverse temperature with k_B the Boltzmann constant, and h is the Planck's constant. In order to calculate any observable property that solely depends on the positions of particles and not on the momenta, we can integrate out the kinetic part of the Hamiltonian associated with the momenta. Thus, the average of any static observable $\mathscr{O}$ can be calculated as

$$\langle \mathscr{O} \rangle = \frac{\int d\mathbf{r}^N \mathscr{O}\left(\mathbf{r}^N\right)\left(-\beta H\left(\mathbf{r}^N,\mathbf{p}^N\right)\right)}{\int d\mathbf{r}^N \left(-\beta H\left(\mathbf{r}^N,\mathbf{p}^N\right)\right)}, \tag{2.5}$$

where the angular brackets denote the average value. However, performing this integration is computationally expensive due to the large number of configurations that need to be sampled. We, thus, utilise the so-called Metropolis algorithm to identify the relevant configurations which follow a Boltzmann distribution and then evaluate $\langle \mathscr{O} \rangle$ using these configurations.

In practice, identification of these relevant configurations is accomplished in the following manner. We first generate a number of random configurations, termed as a Markov chain. For this, we consider a starting configuration in which the particles are at positions $\mathbf{r}^N_{old}$. We, then, perform a trial move to obtain a new configuration. This trial move involves displacing a randomly selected particle i by a small amount $d\mathbf{r}$, i.e. from a position $\mathbf{r}^i_{old}$ to $\mathbf{r}^i_{new} = \mathbf{r}^i_{old} + d\mathbf{r}$. This results in a new configuration with particle positions $\mathbf{r}^N_{new}$. This trial move is either accepted or rejected according to the Metropolis acceptance criteria based on the following probability

$$\mathrm{acc}\left(\mathbf{r}^N_{old} \rightarrow \mathbf{r}^N_{new}\right) = \min\left(1, \exp\left(-\beta \Delta U\right)\right), \tag{2.6}$$

where $\Delta U = U\left(\mathbf{r}^N_{new}\right) - U\left(\mathbf{r}^N_{old}\right)$ is the change in the potential energy of the system accompanying the trial move. If the trial move is rejected, then the old configuration is restored. Alternatively, if the trial move is accepted, then this new configuration becomes the starting configuration for the next trial move. This process is continued for a sufficiently long time in order to facilitate the system to attain equilibrium.

The nature of the trial move and the corresponding acceptance criteria depends on the ensemble under study. For the isothermal-isobaric ensemble, where the pressure P and temperature T for a system of N particles is fixed, in addition to the displacement move, the trial move also includes changing the volume of the box V in order to attain the equilibrium volume at the given conditions. The acceptance criteria for this trial move performed to modify the volume of the system from V_{old} to V_{new} reads as

$$\mathrm{acc}\left(V_{old} \rightarrow V_{new}\right) = \min\left(1, \exp\left(-\beta\left(\Delta U + P\Delta V - k_B T N \log(V_{new}/V_{old})\right)\right)\right), \tag{2.7}$$

where $\Delta V = V_{new} - V_{old}$ is the change in the volume of the system accompanying the trial move.

In this thesis, we largely perform Monte Carlo simulations of core-corona particles in a two-dimensional system described by a rectangular box of area A. We employ both canonical (NVT) and isothermal-isobaric (NPT) ensembles under periodic boundary conditions. We associate the following dimensionless parameters of the system: reduced temperature $T^* = k_B T/\varepsilon$, reduced pressure $P^* = \beta P \sigma^2_{HD}$, and reduced density $\rho^* = N\sigma^2_{HD}/A$, where $\beta = 1/k_B T$ is the inverse temperature with k_B the Boltzmann constant.

2.3.2 Event-Driven Brownian Dynamics simulations

Brownian Dynamics (BD) methods that are used to describe the motion of the particles represent a simplified version of Langevin dynamics [152, 153]. However, BD simulations for systems of hard particles or particles with interaction potentials composed of discontinuous energy levels, like square well or square shoulder, is computationally expensive. Thus, in this work, we use a modified Event-Driven Brownian Dynamics (EDBD) method which resembles the Event-Driven Molecular Dynamics (EDMD) technique. In the following paragraph, we briefly explain the Molecular Dynamics (MD) technique, and then the need for using EDBD technique and finally how our EDBD technique resembles the EDMD method.

In a MD simulation, the movement of particles in a system is calculated by solving Newton's equations of motion. In such situations, the particles exhibit a ballistic motion during the times between the interactions with other particles. In other words, these particles do not exhibit Brownian motion at these times. But, different configurations are sampled according to a Boltzmann distribution. In a time-driven MD simulation, i.e. at conditions of fixed time intervals, the change in velocity of each particle is calculated based on the forces acting on it at each time step. This change in velocity, in turn, results in a change in position of the particle. However, such time-driven simulations are not suitable for systems of particles interacting with discontinuous potentials. This is because, in these cases, the forces acting on particles are instantaneous, i.e. the force between the particles changes only at a specific point in time, and remains constant at other times. For example, in a system of hard spheres, the force between the particles is zero except at the time when the particles touch each other. Thus, such a change can only be detected in the simulation after it has already occurred. To avoid this, event-driven techniques are used. Here, the moment of interaction between particles is explicitly predicted ahead of time, such that it can be detected at the correct moment in the simulation. This is mostly applied in systems where the particles exhibit a simple motion between the interaction times. Fortunately, this holds for particle interacting with a discontinuous potential, where the motion of the particles in between the interaction times correspond to a linear motion of their centres of masses. A detailed description of the implementation and working of the EDMD method is given in Reference [154].

Even though we find that the EDMD method is suitable for simulating a system of particles interacting with the HCSS potential, the particles here do not exhibit a Brownian motion. Thus, we explicitly incorporate the Brownian motion by randomly adjusting the velocities of particles at regular intervals Δt as

$$\mathbf{v}(t+\Delta t) = \alpha_t \mathbf{v}(t) + \beta_t \mathbf{v}_R(t), \tag{2.8}$$

where $\mathbf{v}(t)$ and $\mathbf{v}(t+\Delta t)$ are respectively the velocities of the particles before and after the stochastic velocity adjustment, $\mathbf{v}_R(t)$ is a 3-D Gaussian variable with mean 0 and variance $k_B T/m$, with k_B the Boltzmann constant and T the temperature. Further, α_t has a value $1/\sqrt{2}$ with a probability $\nu\Delta t$ and 1 otherwise. The temperature is kept constant by setting $\beta_t = \sqrt{1-\alpha_t^2}$. In accordance to similar EDBD simulations carried out previously [155, 156], we set ν to $10\tau_{MD}^{-1}$ and Δt to $0.01\tau_{MD}$, where τ_{MD} is the unit of time of an EDMD simulation given as $\tau_{MD} = \sqrt{m/k_B T}\sigma_{HS}$ with σ_{HS} the diameter of the hard core of the spherical particles. A detailed description of this method is given in Reference [155].

2.4 Calculating the free energy of phases

To identify the thermodynamically stable phases in the system and to map out its phase diagram, we first need to calculate the free energy of all the phases involved in the system. For each phase, we calculate the dimensionless Helmholtz free energy per particle $f = \beta F/N$ as a function of density ρ by thermodynamic integration of the equation of state from a reference density ρ_o.

$$f(\rho) = f(\rho_o) + \int_{\rho_o}^{\rho} \frac{\beta P(\rho')}{\rho'^2} d\rho'. \tag{2.9}$$

The Helmholtz free energy at the reference density ρ_o is determined using another thermodynamic integration from a reference system based on the bulk phase of interest as described in the following sub-sections.

2.4.1 Coupling parameter method

For the fluid phases observed in the HCSS system, we calculate the free energy at the reference density by constructing a reversible path from the HCSS system to the hard-disk fluid at the same density [151, 157]. To do so, we introduce an auxiliary potential energy function

$$\beta U_{\mathrm{SS}}(\gamma) = \sum_{i<j}^{N} \beta V_{\mathrm{HD}}(r_{ij}) + \gamma \sum_{i<j}^{N} \beta V_{\mathrm{SS}}(r_{ij}) \tag{2.10}$$

that linearly interpolates between the hard-disk system at $\gamma = 0$ and the HCSS system at $\gamma = 1$, where γ denotes the linear coupling parameter. The free energy of the HCSS system is then determined by

$$f(\rho) = f_{\mathrm{HD}}(\rho) + \frac{1}{N} \int_{\gamma=0}^{\gamma=1} d\gamma \left\langle \frac{\partial \beta U_{\mathrm{SS}}(\gamma)}{\partial \gamma} \right\rangle, \tag{2.11}$$

where the angular brackets refer to the average over different configurations and $f_{\mathrm{HD}}(\rho)$ is the free energy of the hard-disk fluid and is calculated using the following expression by Santos *et al.* [158].

$$f_{\mathrm{HD}}(\rho) = \left[\ln\left(\rho\Lambda^2\right) - 1\right] - \frac{\ln\left(1 - \frac{\eta}{\eta_m}\right)}{2(1-\eta_m)} + \frac{(2\eta_m - 1)\ln\left(1 - \frac{2\eta_m - 1}{\eta_m}\eta\right)}{2(1-\eta_m)}, \tag{2.12}$$

where $\eta = \pi\sigma_{HD}^2 N/4A$ denotes the packing fraction and $\eta_m = \sqrt{3}\pi/6 = 0.907$ corresponds to the packing fraction of the close-packed crystal phase. The first term in Equation 2.12 represents the free energy per particle of an ideal gas in two dimensions.

2.4.2 Frenkel-Ladd method

We employ the Frenkel-Ladd method to calculate the free energy of the various periodic crystal phases, high-density quasicrystals and their approximants reported in this thesis. The reference state used here is the Einstein crystal, an ideal lattice of non-interacting and harmonically oscillating particles [151, 157, 159, 160]. The ideal positions of the particles are taken to be the equilibrium positions in the crystal structure under consideration. We then construct a reversible path from the crystal of interest to the Einstein crystal in two steps. In the first step, the square shoulder potential is switched off. For this, we make use of the auxiliary potential energy function given in Equation 2.10 and change γ from 1 to 0. In the second step, the harmonic springs are switched on, while the hard-core interactions remain unaffected. For this, we use another potential energy function, that reads as

$$\beta U(\lambda) = \sum_{i<j}^{N} \beta V_{\mathrm{HD}}(r_{ij}) + \lambda \sum_{i=1}^{N} \frac{(\mathbf{r}_i - \mathbf{r}_{i,o})^2}{\sigma_{HD}^2}, \tag{2.13}$$

where $\mathbf{r}_{i,o}$ and $\mathbf{r}_i$ are, respectively, the equilibrium and instantaneous positions of particle i. These harmonic springs are switched on by increasing their dimensionless spring constant λ, from 0 to a value λ_{max}. At λ_{max}, the particles are so strongly tied to their ideal lattice positions that they move independently of each other. Therefore, the free energy of the crystal can be approximated to that of the Einstein crystal. Consequently, the free energy of the concerned crystal in a d-dimensional system at the concerned density ρ is calculated as [159]

$$f_{\mathrm{HD}}(\rho) = f_{\mathrm{Ein}} - \Delta f_{\mathrm{CM}} + \frac{\ln\rho}{N} - \frac{d}{2N}\ln N - \frac{d}{2N}\ln\frac{\lambda_{\mathrm{max}}}{\pi}, \tag{2.14}$$

where the first term is the free energy of a non-interacting Einstein crystal given by

$$f_{\mathrm{Ein}} = -\frac{d}{2} \ln \frac{\pi}{\lambda_{\max}}, \tag{2.15}$$

and the second term is the free-energy difference between the solid under consideration and the Einstein crystal

$$\Delta f_{\mathrm{CM}} = \int_{\ln c}^{\ln(\lambda_{\max}+c)} d[\ln(\lambda+c)](\lambda+c) \left\langle \frac{1}{N} \sum_{i=1}^{N} \frac{(\mathbf{r}_i - \mathbf{r}_{i,o})^2}{\sigma_{HD}^2} \right\rangle_{\lambda}, \tag{2.16}$$

with $c = 1 / \left\langle \frac{1}{N} \sum_{i=1}^{N} \frac{(\mathbf{r}_i - \mathbf{r}_{i,o})^2}{\sigma_{HD}^2} \right\rangle_{\lambda \to 0}$. The other terms in Equation 2.14 denote the difference between solids with constrained and unconstrained centers of mass.

In summary, the free energy of a crystal consisting of particles interacting with a HCSS potential is determined as

$$f(\rho) = f_{\mathrm{HD}}(\rho) + \frac{1}{N} \int_{\gamma=0}^{\gamma=1} d\gamma \left\langle \frac{\partial \beta U_{\mathrm{SS}}(\gamma)}{\partial \gamma} \right\rangle. \tag{2.17}$$

2.4.3 Schilling-Schmid method

We calculate the free energy of various low-density phases reported in this thesis using the method proposed by Schilling and Schmid [161, 162]. Calculation of the free energy of the low-density phases calls for a different method because here the particles are not tied to a certain lattice. So, the movement of the particles also needs to be accounted for in the calculations. In this method, we employ a reference state consisting of a system of non-interacting particles that are pinned by a local attractive linear well potential to their respective reference positions. The reference positions correspond to the positions of particles in an arbitrary configuration obtained in the simulations after equilibration. The linear well potential is described by

$$\beta U_{\mathrm{LW}}(\omega) = \omega \sum_{i}^{N} \Phi(|\mathbf{r}_i - \mathbf{r}_i^0|/r_c), \tag{2.18}$$

where $\omega > 0$ is the absolute well depth, $\mathbf{r}_i$ and $\mathbf{r}_i^0$ are the positions of particle i and its corresponding well, respectively, r_c is the radius of the well, and $\Phi(x) = x - 1$ for $x < 1$ or 0 for $x \geq 1$. We use a value of the well radius $r_c = 2\sigma_{HD}$.

The free energy of this reference state can be analytically calculated as

$$f_{ref}(\rho) = \ln(\rho \Lambda^d) - 1 - \ln\left(1 + \frac{V_o}{V} g(\omega)\right), \tag{2.19}$$

where V_o is the volume of a sphere of radius r_c, and V is the box volume and

$$g(\omega) = \frac{d}{\omega^d} \left(e^{\omega} - \sum_{k=0}^{d} \frac{\omega^k}{k!} \right) \tag{2.20}$$

for a d-dimensional system.

We use three separate thermodynamic integration steps to obtain the HCSS system from the reference system composed of non-interacting pinned particles. This consists of (i) switching on the hard-core interactions of the particles, (ii) switching on the square-shoulder interactions of the particles, and (iii) switching off the linear well potentials of the particles. The hard-core interactions are switched on by using the following potential [163]

$$\beta U_{\mathrm{HD}}(r_{ij},\alpha) = \begin{cases} \alpha\left[1-0.9\left(\frac{r_{ij}}{\sigma_{HD}}\right)^2\right], & r_{ij} < \sigma_{HD} \\ 0 & r_{ij} \geq \sigma_{HD}, \end{cases} \tag{2.21}$$

where $r_{ij} = |\mathbf{r}_i - \mathbf{r}_j|$ with $\mathbf{r}_i$ and $\mathbf{r}_j$ the positions of particles i and j, and α is the coupling parameter and increasing α from 0 to $\alpha_{max} = 200$. The square-shoulder interaction is switched on by using the auxiliary potential energy function given in Equation 2.10 and changing γ from 0 to 1. The linear well is switched off by decreasing ω from $\omega_{max} = 10^4$ to 0. The free energy of the HCSS system can ultimately be calculated from

$$\begin{aligned} f(\rho) = f_{ref}(\rho) &+ \int_0^{\alpha_{max}} d\alpha \left\langle \frac{\partial \beta U_{\mathrm{HD}}}{\partial \alpha} \right\rangle_{\alpha,\gamma=0,\omega_{max}} \\ &+ \int_0^1 d\gamma \left\langle \frac{\partial \beta U_{\mathrm{SS}}}{\partial \gamma} \right\rangle_{\gamma,\alpha_{max},\omega_{max}} \\ &- \int_0^{\omega_{max}} d\omega \left\langle \frac{\partial \beta U_{\mathrm{LW}}}{\partial \omega} \right\rangle_{\omega,\alpha_{max},\gamma=1}, \end{aligned} \tag{2.22}$$

where the angular brackets in each integral denote the average over the number of particles in the system. The integrations for switching on the hard-core and square-shoulder potentials are evaluated using a standard 20-points Gauss-Legendre integration scheme. The last integration where the attractive well is switched off, is more challenging and computationally more expensive. This is because one needs to accurately sample the sharp decay of the integrand at moderate values of ω as well as its gradual decay at the higher values. In order to do so, we use a high value of ω_{max} $(= 10^4)$ and perform the integration using the trapezoid rule with varying step size over different intervals as described in Table 2.1. This results in a total of 437 points to perform this integration.

Table 2.1: Sampling scheme used for the third integration in the Schilling-Schmid method to switch off the attractive well by decreasing the well depth ω.

ω_{start}	ω_{end}	Step size
0.001	0.001	-
0.01	0.01	-
0.1	0.1	-
0.2	20	0.2
21	300	1
325	1000	25
1250	5000	250
5500	10000	500

2.5 Constructing the equilibrium phase diagram

We utilise the free energies of the various phases obtained in the previous section to construct an equilibrium phase diagram. To do so, we employ a three-step process as described below:

In the first step, we measure the equation of state (EOS) of the phases of interest at a constant temperature T^*. This isothermal EOS is the variation of the bulk pressure P^* as a function of the equilibrium density ρ^*. We perform compression and expansion runs by either increasing or decreasing the pressure P^* in a step-wise manner in the NPT ensemble to obtain the isothermal EOS. The compression runs are started from an isotropic fluid phase, while the expansion runs are started from the concerned periodic or quasi-periodic crystal phase.

In the second step, we determine the dimensionless Helmholtz free energy per particle $f = \beta F/N$ as a function of density at a fixed temperature T^* for each of the observed phases. This is done by thermodynamic integration of the EOS to a reference density. The free energy at this reference density is calculated as explained in Section 2.4.

In the final step, we determine the thermodynamically stable phases and the corresponding phase boundaries by employing a common tangent construction to the free-energy curves, i.e. the Helmholtz free energy per unit area $\beta F/A$ as a function of the reduced density ρ^*. The points of coexistence between pairs of phases can also be confirmed by plotting the chemical potential $\beta\mu$ of the concerned phases as a function of pressure. For a system at constant temperature, two phases are said to be in coexistence with each other if they have the same chemical potential at the same pressure. The chemical potential at a given density ρ is defined as follows

$$\beta\mu(\rho) = f(\rho) + \rho\frac{\partial f}{\partial\rho}. \tag{2.23}$$

2.6 Analysing the structure of phases

We structurally characterise the different phases formed by calculating the radial distribution function (RDF) of the system $g(r)$, the static structure factor $S(\mathbf{k})$ and the average bond orientational order (BOO) of the system χ_m. Each of these are explained below:

The RDF of a system at density ρ^* gives the probability of finding a pair of particles at a distance $r = |\mathbf{r}-\mathbf{r}'|$, and reads

$$g(r) = \frac{1}{\rho^{*2}}\left\langle \sum_{a=1}^{N}\sum_{b\neq a}^{N} \delta(\mathbf{r}-\mathbf{r}_a)\delta(\mathbf{r}'-\mathbf{r}_b)\right\rangle, \tag{2.24}$$

where $\mathbf{r}_a$ and $\mathbf{r}_b$ are the positions of particles a and b, respectively, and the angular brackets denote the average over the number of particles.

The static structure factor $S(\mathbf{k})$ is obtained by a Fourier transformation of the RDF and is written as

$$S(\mathbf{k}) = \frac{1}{N}\langle\rho_{\mathbf{k}}\rho_{-\mathbf{k}}\rangle = \frac{1}{N}\left\langle \sum_{a=1}^{N}\sum_{b\neq a}^{N} \exp\left(-i\mathbf{k}.(\mathbf{r}_a-\mathbf{r}_b)\right)\right\rangle, \tag{2.25}$$

where ρ_k is the Fourier transform of the microscopic density $\rho(\mathbf{r})$, and the angular brackets denote the average over the number of particles. The structure factor is represented in a two-dimensional space as a diffraction pattern.

The average BOO is defined as [164]

$$\chi_m = \left\langle \left| \frac{1}{N_B(a)} \sum_{b=1}^{N_B(a)} \exp(im\theta_{\mathbf{r}_{ab}}) \right|^2 \right\rangle , \tag{2.26}$$

where m is the integer associated with the symmetry of interest, $\mathbf{r}_{ab} = \mathbf{r}_a - \mathbf{r}_b$ is the vector connecting the center-of-mass of two neighbours, $\theta_{\mathbf{r}_{ab}}$ is the angle between $\mathbf{r}_{ab}$ and an arbitrary axis, and $N_B(a)$ is the number of neighbours of particle a. The angular brackets denote the average over the number of particles.

2.7 Evaluating the photonic band diagram

In this section, we describe the fundamental equations which describe the photonic crystals. We then provide a description of a plane wave method used to calculate the photonic band structure and the super cell method used to describe the presence of a localised defect in photonic crystals.

2.7.1 Plane wave method

The plane wave method for calculating the photonic band structure is given in detail in References [12, 22, 165] and a short overview is given here. We begin the description of the electromagnetic waves using the Maxwell equations. For a homogeneous dielectric medium with no free charges or currents, the Maxwell equations can be written as

$$\begin{aligned} \nabla \cdot \mathbf{D} &= 0 \\ \nabla \cdot \mathbf{B} &= 0 \\ \nabla \times \mathbf{E} + \frac{\partial \mathbf{B}}{\partial t} &= 0 \\ \nabla \times \mathbf{H} - \frac{\partial \mathbf{D}}{\partial t} &= 0, \end{aligned} \tag{2.27}$$

where **E** and **H** are respectively the electric and magnetic fields, **D** is the displacement field and **B** is the magnetic induction field. This set of equations can be solved by writing **D** and **B** in terms of the fields **E** and **H**. In vacuum, these quantities are proportional to each other as

$$\begin{aligned} \mathbf{D} &= \varepsilon_0 \mathbf{E} \\ \mathbf{B} &= \mu_0 \mathbf{H}, \end{aligned} \tag{2.28}$$

where ε_0 and μ_0 are respectively the permittivity and permeability of free space. To apply these relations to a dielectric media, the response of the media to these fields also needs to be considered. This results in the following relations

$$\begin{aligned} \mathbf{D} &= \varepsilon_0 \mathbf{E} + \mathbf{P} \\ \mathbf{B} &= \mu_0 \mathbf{H} + \mathbf{M}, \end{aligned} \tag{2.29}$$

where **P** is the polarization and **M** is the magnetization. These equations can be further simplified using different assumptions. First, we consider a non-magnetic material, i.e. $\mathbf{M} = \mathbf{0}$.

This results in a linear relation between the magnetic field and the magnetic induction. Also, we consider dielectric materials with magnetic permeability close to unity, i.e. $\mu_0\mu(\mathbf{r}) \sim \mu_0$. Then, if we consider small electric field strengths, the relation between **D** and **E** can also be approximated to be linear. Lastly, if the considered dielectric is isotropic, then the dielectric constant $\varepsilon(\mathbf{r})$ is scalar in nature. These considerations result in the following equations

$$\begin{aligned} \mathbf{D} &= \varepsilon_0\varepsilon(\mathbf{r})\mathbf{E} \\ \mathbf{B} &= \mu_0\mathbf{H}. \end{aligned} \tag{2.30}$$

Combining these relations with the Maxwell equations, we obtain

$$\begin{aligned} \nabla\cdot(\varepsilon(\mathbf{r})\mathbf{E}) &= 0 \\ \nabla\cdot\mathbf{H} &= 0 \\ \nabla\times\mathbf{E}+\mu_0\frac{\partial\mathbf{H}}{\partial t} &= 0 \\ \nabla\times\mathbf{H}-\varepsilon_0\varepsilon(\mathbf{r})\frac{\partial\mathbf{E}}{\partial t} &= 0. \end{aligned} \tag{2.31}$$

In the next approximation, we assume a harmonic time-dependence of the electric and magnetic fields of the form

$$\begin{aligned} \mathbf{E}(\mathbf{r},t) &= \mathbf{E}(\mathbf{r})e^{-i\omega t} \\ \mathbf{H}(\mathbf{r},t) &= \mathbf{H}(\mathbf{r})e^{-i\omega t}. \end{aligned} \tag{2.32}$$

Substituting this time dependence into the simplified Maxwell equations, we obtain

$$\begin{aligned} \nabla\cdot(\varepsilon(\mathbf{r})\mathbf{E}(\mathbf{r})) &= 0 \\ \nabla\cdot\mathbf{H}(\mathbf{r}) &= 0 \\ \nabla\times\mathbf{E}(\mathbf{r})-i\omega\mu_0\mathbf{H}(\mathbf{r}) &= 0 \\ \nabla\times\mathbf{H}(\mathbf{r})+i\omega\varepsilon_0\varepsilon(\mathbf{r})\mathbf{E}(\mathbf{r}) &= 0. \end{aligned} \tag{2.33}$$

In the above set of equations, the first two impose the condition that the electromagnetic waves need to be transverse. The other equations can be coupled to obtain a 'master equation'

$$\begin{aligned} \Theta\mathbf{H}(\mathbf{r}) &= \left(\frac{\omega}{c}\right)^2\mathbf{H}(\mathbf{r}) \\ \text{where}\quad \Theta\mathbf{H}(\mathbf{r}) &= \nabla\times\left(\frac{1}{\varepsilon(\mathbf{r})}\nabla\times\mathbf{H}(\mathbf{r})\right), \end{aligned} \tag{2.34}$$

and $c = 1/\sqrt{\varepsilon_0\mu_0}$ is the speed of light in vacuum. The operator Θ in the master equation, written in the current form as a function of **H**, is Hermitian. In other words, Hermiticity establishes that the eigenvalues $\left(\frac{\omega}{c}\right)^2$ are real, and that field distributions with the same eigenfrequency must be orthogonal.

To solve this eigenvalue problem, a plane-wave basis is used to represent the magnetic fields in the dielectric media. This is done by expanding the magnetic field **H** and the dielectric constant $\varepsilon(\mathbf{r})$ in terms of the components of the Fourier series along the reciprocal lattice vector.

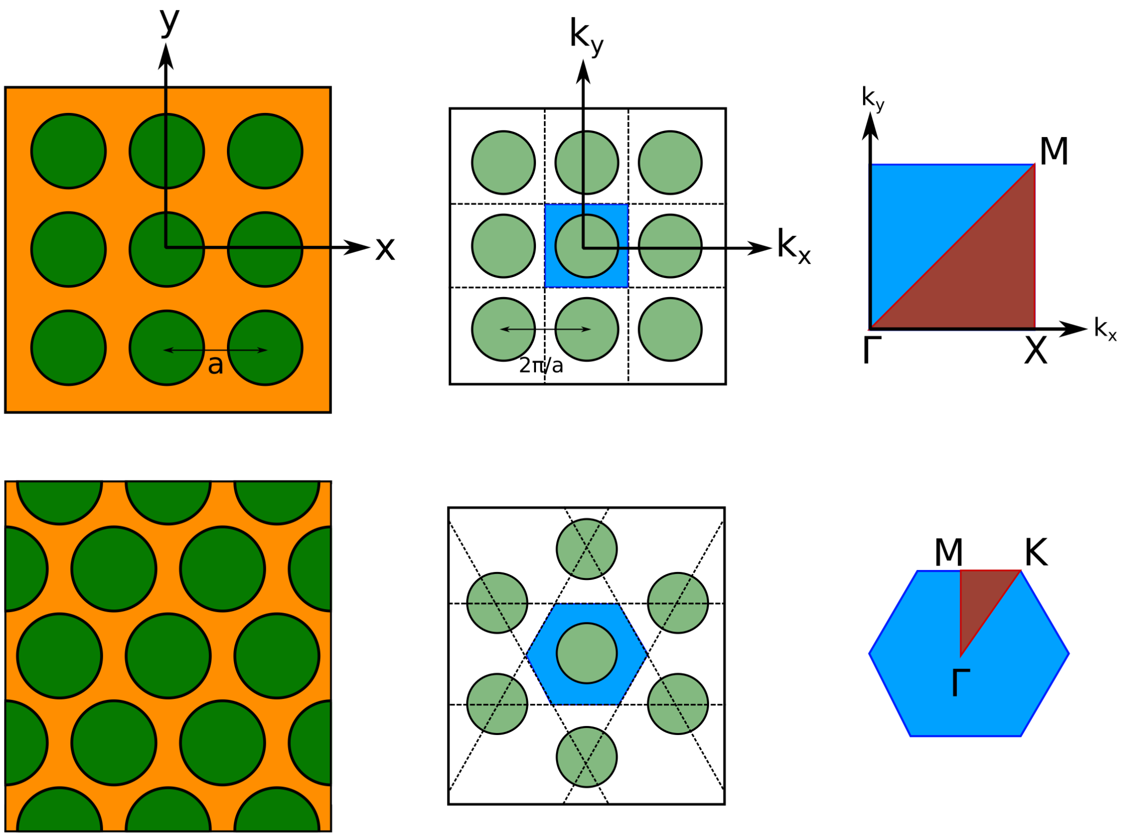

Figure 2.2: Schematic representation of the construction of the irreducible Brillouin zone (IBZ) for **(top)** a square and **(bottom)** a hexagonal lattice. **(left)** The lattice in real space, where the green and yellow colours respectively represent the high- and low-dielectric constant materials. The interparticle distance is a. **(middle)** The reciprocal lattice, where the construction of the first BZ using the perpendicular bisectors to the lattice vectors is shown. The interparticle distance is $2\pi/a$. The perpendicular bisectors are shown as dotted lines and the first BZ is shaded in blue. **(right)** The construction of the IBZ in the first BZ. The IBZ is shaded in brown and the outlining path in terms of the k-points is marked.

Ideally, one needs to consider all possible propagation directions inside a crystal. However, given the symmetry of the crystal, one could restrict the calculations to the wave vectors along the first Brillouin zone (BZ) identified in the reciprocal space. The first BZ is defined as the region of reciprocal space consisting of points which are closer to the origin than any other vertex of the real crystal lattice. For a two-dimensional crystal, the first BZ is constructed by drawing the perpendicular bisectors of each lattice vector that joins the origin to the nearest vertices of the reciprocal lattice. Among the first BZ zone, one can identify the smallest possible set of wave vectors that can still generate the entire reciprocal space of the crystal. This region, along which the dispersion relations are calculated, is termed as the irreducible Brillouin zone (IBZ). An example of the construction of the first BZ and IBZ of two-dimensional lattices with square and hexagonal symmetry is given in Figure 2.2. Finally, the dispersion characteristics resulting from the plane wave calculations is presented in a photonic band diagram, which is a plot of the dispersion relation along the edges of the IBZ. For the calculations performed in this thesis, we use the freely available ‘MIT Photonic Bands (MPB)’ software package [165]. This software package computes fully-vectorial eigenmodes of Maxwell’s equations with periodic boundary conditions by preconditioned conjugate-gradient minimisation of the block Rayleigh quotient in a plane wave basis.

2.7.2 Super cell method

To evaluate the effect of defects in the photonic crystals in the plane wave basis, a super cell is constructed [166]. In these studies, defects are artificially introduced in photonic crystals. This could be done either by changing the size or the dielectric constant of the dielectric particles in the photonic crystal. Introducing such defects disrupts the periodicity of the lattice. Thus, we need to artificially reinstate the disrupted periodicity. This is done by considering a large cell constructed using a number of unit cells and the defect is introduced in the centre of this large cell. This large cell, termed as a super cell, is then periodically repeated in space. This results in an artificial structure consisting of periodic defects separated by regions of perfect photonic crystal. An important consideration while using a super cell for calculations is that the distance between the periodic defects should be sufficiently large so that they do not interact with each other, i.e. the dimensions of the super cell play an important role in these calculations. This is schematically shown using an example of a 5×5 super cell constructed from an unit cell of a square lattice of rods with a vacancy in the centre is given in Figure 2.3. The unit cell along with its periodic images is shown on the left and the super cell and its periodic images are shown on the right. We can note that the super cell consists of alternate regions of regular crystal and defects. Thus, if the region of the intermediate regular crystal is not large enough, the defects can interact with each other.

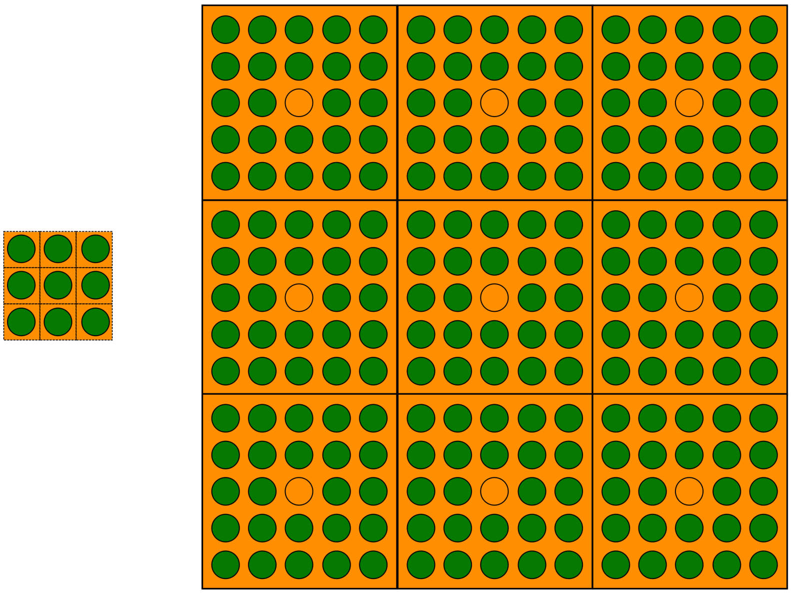

Figure 2.3: Schematic representation of a simulation cell and its periodic images for a a square lattice of dielectric rods. **(left)** An unit cell containing a single particle and **(right)** a 5×5 super cell containing a vacancy defect at the centre. In both, green and yellow colours respectively represent the high- and low-dielectric constant materials.

Acknowledgements

Setting up all these calculations and ensuring they work required a lot of help from a number of people. Firstly, I thank Anjan P. Gantapara and Guido Avvisati for helping me set up the initial codes for performing the Monte-Carlo simulations and also for providing respectively the codes for calculating the static structure factor and the radial distribution function. I thank John R. Edison for providing me with the EDBD code and Tonnishtha Dasgupta for helping me set up the simulations. I thank Guido Avvisati for co-authoring the code for calculating the free energy using the Frenkel-Ladd method and Simone Dussi for answering numerous questions about the Schilling-Schmid method. I, then, thank Guido Avvisati and Nikos Tasios for respectively installing the MPB software on my computer and on the THOR cluster. I would also like to acknowledge the efforts by Job Thijssen (Univeristy of Edinburgh, United Kingdom), Devashish Sharma (University of Twente, The Netherlands) and Luis Froufe-Perez (University of Fribourg, Switzerland) for helping me set up the photonic band structure calculations.

Part I

Dodecagonal quasicrystals in a two-dimensional core-corona system

3

Relative stability of a dodecagonal quasicrystal and its approximants

Using computer simulations we study the phase behaviour of a system of colloidal hard disks with a diameter σ_{HD} and a soft corona of width $1.40\sigma_{HD}$. The particles interact with a hard core and a repulsive square-shoulder potential. We calculate the free energy of the random-tiling quasicrystal and its periodic approximants using the Frenkel-Ladd method. We explicitly account for the configurational entropy arising from the distinct number of configurations that the random-tiling quasicrystal can adapt. From the free-energy calculations, we find that the dodecagonal quasicrystal is stable with respect to the periodic approximants that we considered. At finite temperatures, the quasicrystal is stabilised by its vibrational entropy. We can extrapolate this stability region to extend to zero temperature as the energies of the defect-free quasicrystal and the periodic approximants are equal within our statistical accuracy. Further, we map out the equilibrium phase diagram and find that the system forms hexagonal phases in two distinct ranges of density. This is due to the presence of the two characteristic length scales in the interaction potential.

Based on *On the stability of a quasicrystal and its crystalline approximant in a system of hard disks with a soft corona*, J. Chem. Phys., 143, 164905 (2015) and *Phase behaviour of quasicrystal forming systems of core-corona particles*, J. Chem. Phys., 146, 1114901 (2017)

3.1 Introduction

Quasicrystals are materials that exhibit long-range orientational order but no translational periodicity. The first observation of a metastable quasicrystal was reported by Shechtman *et al.* in a rapidly cooled Al-Mn alloy [96]. Since then, quasicrystals have been observed in a wide range of intermetallic alloys. Surprisingly, quasicrystalline order has also been discovered recently in several soft-matter systems, ranging from spherical dendrite micelles [105], block copolymers [106–110] to binary mixtures of nanoparticles [111, 112]. In addition, soft-matter quasicrystals have also been fabricated in colloidal systems using external fields such as holography [116] or laser beams [117].

Quasicrystalline behaviour arises due to the presence of two competing length scales, either induced by the different sizes of the two particle species in the case of binary mixtures, or due to an effective pair interaction that favours two length scales [141]. This leads to a classification of soft-matter quasicrystals into two categories: 1) binary mixtures of, for example, nanoparticles interacting with simple isotropic pair potentials, and 2) single-component systems, like micelles, with effective pair interactions that favour two length scales. Evidence of spontaneous formation of quasicrystalline order in soft-matter systems belonging to both categories have been observed in computer simulation studies. Examples of *in silico* quasicrystals in binary mixtures include particles interacting with Lennard-Jones [119, 120] and square-well [125] potentials. Single-component quasicrystals have been observed in particles interacting with Lennard-Jones-Gauss [77], square-shoulder [123], square-well [121], linear ramp [118], flat-well [122] and three-well oscillating [124] pair interactions. For completeness, we mention that quasicrystals are also studied in systems of patchy particles and hard non-spherical particles such as tetrahedra [167] and (truncated) triangular bipyramids [129, 168], where the interactions or particle shape generate local arrangements or packings that are compatible with quasicrystals.

From a theoretical point of view, the thermodynamic stability of these soft-matter quasicrystals is widely debated in literature [135, 169]. The presence of two length scales in a single-component system creates a core-corona type structure that is thought to stabilise the quasicrystal [141, 169–172]. Indeed, many experimentally discovered soft-matter quasicrystals in single-component systems frequently consist of spherical particles with a rigid core and a squishy corona, for example, the spherical dendrite micelles consist of a rigid aromatic core with a deformable shell of alkyl chains [105], and the block copolymer micelles consist of a micellar core of hydrophobic polymer surrounded by a large shell of hydrophilic polymer blocks [110]. In addition, it was found by simulations that the mobility of the surface entities and shape polydispersity in the case of single-component micellar systems play an important role in the stabilisation of quasicrystals [173]. It is tempting to speculate that the role of the surface entities with respect to mobility and polydispersity in single-component systems is replaced by the smaller species in the case of quasicrystals of binary systems.

In order to prove the thermodynamic stability of quasicrystals, one has to show that the quasicrystal corresponds to the lowest free-energy state of the system. Quasicrystals can be either energetically or entropically stabilised [174]. An energetically stabilised quasicrystal results when the quasicrystal is the minimum-energy configuration at zero temperature [135]. On the other hand, when the configurational entropy outweighs the energetic contribution, the quasicrystal may be entropically stabilised at finite temperatures [169].

An extension of this debate deals with the relative stability of a random-tiling quasicrystal and its approximant at finite temperatures. An approximant is a periodic quasicrystalline counterpart which is described by a large unit cell with a structure that resembles that of a quasicrystal [129, 175]. While the enthalpic and vibrational contributions to the free energy are assumed to be very similar for the quasicrystal and its approximant, the free energy of a random-tiling quasicrystal involves a configurational entropy contribution due to the number of distinct configurations [176], which is absent for the approximant [177]. From this line of reasoning one could expect that the quasicrystal is more stable than the approximant due to its configurational entropy. On the other hand, one might expect the approximant to be more stable as it is assumed to have a lower energy and is considered to pack more efficiently due to the absence of defects [129, 167, 173]. Hence, we conclude that it is still unresolved whether or not the quasicrystal is more stable than its periodic approximant, and how this relative stability depends on the thermodynamic state of the system.

Determining the stability of these quasicrystals is complex as their free energies cannot be computed in a straightforward manner. This is because, a reference state with known free energy from which thermodynamic integration to a quasicrystal can be performed is unknown. This issue is further complicated by the fact that there is no simple way to sample over the distinct configurations of the quasicrystal and to account for its configurational entropy [176]. Recently, a method was proposed to determine the free energy of a quasicrystal by simulating the direct coexistence of a fluid and quasicrystalline phases of patchy particles [177]. Due to the lack of hysteresis in the fluid to quasicrystal transformation of this system, the free energy could be directly determined from the free energy of the fluid phase.

In this work, we follow a different methodology to determine the free energy of a two-dimensional random-tiling quasicrystal in a system of hard disks interacting with a square-shoulder potential. We determine the free energy of a defect-free random-tiling quasicrystal and some of its approximants using thermodynamic integration to a non-interacting Einstein crystal [151]. We find that the free energy of the random-tiling quasicrystal is slightly lower than that of its periodic approximants. For the random-tiling quasicrystal, we explicitly account for the configurational entropy using an expression from literature [178]. Here, we approximate the configurational entropy by assuming that all possible realizations that are equivalent in the random-tiling model are also equally probable in our system. Finally, we also map out the phase diagram of the system under study and find that the defect-free random-tiling quasicrystal is stable with respect to the periodic approximants that we considered, both with and without the additional configurational entropy term.

3.2 Methods

We first explain the simulation model and computational methods used for this study in Section 3.2.1, and then give describe the free-energy calculations in Section 3.2.2.

3.2.1 Computational methodology

In this chapter, we focus on quasicrystalline order in single-component systems. We consider a 2-D system of spherical particles enclosed by a soft deformable corona mimicking the floppy corona of alkyl chains in the case of micellar particles or the squishy hydrophilic shell of block copolymer micelles. Analogous to previous work [123], we model this system by 2-D hard disks with diameter σ_{HD} interacting with a repulsive square-shoulder potential. This hard-core square shoulder (HCSS) system can be represented by the following pair potential

$$V_{\mathrm{HCSS}}(r) = \begin{cases} \infty, & r \leq \sigma_{HD} \\ \varepsilon, & \sigma_{HD} < r < \delta \\ 0, & r \geq \delta \end{cases} \tag{3.1}$$

where δ and ε are the square shoulder width and height, respectively, and r is the centre-of-mass distance between two particles The characteristics of this potential are described in detail in Chapter 2. Despite the simplicity of the pair interaction, an entire family of quasicrystals with $10-, 12-, 18-$ and $24-$fold symmetry has been observed in a previous simulation study depending on the square shoulder diameter and the packing fraction [123]. Here, we focus on a diameter of the square shoulder $\delta = 1.40\sigma_{HD}$, which gives rise to a dodecagonal (12-fold symmetric) quasicrystal at sufficiently low temperatures and high enough densities [123]. At these conditions of shoulder width, temperatures and densities, the system prefers the formation of square environments with four nearest neighbours to that of six coordinated hexagonal environments, thereby lowering its potential energy.

To address the phase behaviour of this system and the relative stability of various phases, we perform Monte Carlo (MC) simulations in a rectangular box of area A with periodic boundary conditions in the canonical (NVT) and isothermal-isobaric (NPT) ensembles. We choose σ_{HD} and ε, respectively, as the units of length and energy, and define a reduced temperature $T^* = k_BT/\varepsilon$, a reduced pressure $P^* = \beta P\sigma_{HD}^2$, and a reduced density $\rho^* = N\sigma_{HD}^2/A$, where $\beta = 1/k_BT$ is the inverse temperature with k_B the Boltzmann constant. In the simulations, we use a system size between 209 to 256 particles depending on the initial crystal structure, and a system size of 256 particles in case of an initial isotropic liquid phase.

To qualitatively analyse the structures that the system adopts under various conditions, we calculate three parameters, namely, the polygonal tilings corresponding to the particle positions, the local particle environment (LPE) of each particle, and the average bond orientational order (BOO) parameter of the system. The polygonal tiling is obtained by drawing the bonds between the centres of the neighbouring particles. Interpretation of dodecagonal quasicrystals as tilings of squares and triangles is a common practice [178, 179]. The LPE describes the immediate surrounding of each particle. In dodecagonal quasicrystals, the LPE is composed of various possible arrangements of squares and triangles. This includes environments of only triangles (Z) or squares ($A15$), and a combination of the two. Mixed arrangements of squares and triangles primarily result in two five-particle coordinated environments, which are termed as H and σ. All these LPEs are named in analogy to the three-dimensional Frank-Kasper phases [180]. An overview of these LPEs is given in Figure 3.1. Finally, the average BOO parameter χ_m is defined as [164]

$$\chi_m = \left\langle \left| \frac{1}{N_B(x)} \sum_{y=1}^{N_B(x)} \exp(im\theta_{\mathbf{r}_{xy}}) \right|^2 \right\rangle, \tag{3.2}$$

where m is the symmetry of interest, $N_B(x)$ is the number of neighbours of particle x, and $\theta_{\mathbf{r}_{xy}}$ is the angle between the centre-of-mass distance vector $\mathbf{r}_{xy}$ and an arbitrary axis. Any particle y

is defined to be a neighbour of particle x if $r_{xy} = |\mathbf{r}_x - \mathbf{r}_y| \leq \delta$, where $\mathbf{r}_x$ and $\mathbf{r}_y$ are the positions of particles x and y. The angular brackets denote the averaging over different configurations.

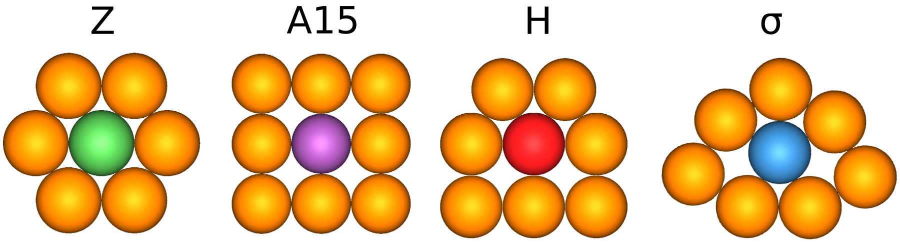

Figure 3.1: Overview of the Z, $A15$, H and σ local particle environments (LPEs) in a dodecagonal quasicrystal. Particles with LPEs other than these are coloured orange.

3.2.2 Free-energy calculations

The method for mapping out the equilibrium phase diagram for the HCSS system is explained in detail in Chapter 2. Here, we give an account of the methods to calculate the free energy of the different phases obtained in this system. We determine the dimensionless Helmholtz free energy per particle $f = \beta F/N$ as a function of density at a fixed temperature T^* for each of the observed phases. This is done by thermodynamic integration of the isothermal equation of state, i.e. the bulk pressure P^* as a function of the equilibrium density ρ^* at constant temperature T^*, to a reference density. The free energy at this reference density is calculated by constructing a reversible thermodynamic path to a reference system for which the free energy is either known or can be analytically calculated. We employ the hard-disk fluid phase at the same density as a reference state for the fluid phase, and the non-interacting Einstein crystal as a reference for the periodic crystals as described in Chapter 2. However, calculating the free energy of the quasicrystal is less trivial. This is because integrating from the fluid or ideal gas would involve crossing an intervening first-order phase transition and on the other hand, using the Einstein crystal as a reference state in the thermodynamic integration would not account for the configurational entropy of the system associated with the number of distinct random-tiling configurations. Also, in our system of particles, we do not observe a clear two-phase coexistence of the quasicrystal with another phase, namely a fluid, square or high-density hexagonal, due to their structural similarities. Thus, we calculate the free energy of the quasicrystal using the Frenkel-Ladd method as for the periodic crystals, and subsequently add an additional configurational entropy contribution associated with the number of distinct random-tiling configurations. This method of configurational entropy correction is explained below.

In order to obtain an estimate of the configurational entropy, we consider the random-tiling model of polygons. Thus, the dodecagonal quasicrystal formed in our system is constructed by a random tiling of equilateral triangles and squares [123]. The configuration resulting in the maximum entropy and thus, the formation of quasicrystals, is obtained at equal area fractions of triangles and squares [83, 123, 178]. For such a configuration of triangles and squares, two different values are reported in the literature for the entropy per unit area $S_{\text{config}}/k_B A$. A value of $S_{\text{config}}/k_B A = 0.12934$ was calculated by Widom [178] by solving the Bethe ansatz for the square-triangle random-tiling model for infinitely large systems [178, 181, 182], and a value of $S_{\text{config}}/k_B A = 0.13137$ was estimated by Oxborrow and Henley [84] using Monte Carlo simulations. In this work, we use the more conservative value obtained by Widom. A negligible effect of system size on this value was reported for system sizes larger than $N = 153$ [178], and a system size of 209 particles is used in our simulations. Further, it is good to note that this analytical description of the configurational entropy considers a perfect random tiling, where all configurations are equally probable. However, this might not be true for the HCSS system, where the probability of finding a certain tiling will also depend on its potential energy and vibrational entropy. The former is determined by the pair interactions and the latter by the number of configurations that the particles can explore while moving around their lattice positions. Thus, the value used here is an upper bound for the configurational entropy of the HCSS system consisting of a square-triangle random tiling.

3.3 Results and discussion

In this section, we first present the construction of the structures of the quasicrystal and the approximants. We then analyse the relative stability between these structures and finally map out the equilibrium phase diagram.

3.3.1 Structure of quasicrystal and its approximants

For a system of HCSS particles with a shoulder width $\delta = 1.40\sigma_{HD}$, a dodecagonal quasicrystal consisting of a random tiling of squares and triangles has been observed in simulations by Dotera *et al.* [123]. The dodecagonal quasicrystal (QC12) was reported to form by cooling a high-density hexagonal (HDH) phase of density $\rho^* = 0.98$ to a lower temperature at a constant density in the NVT ensemble. In addition, we find in our simulations that the dodecagonal quasicrystal also forms when an isotropic fluid (FL) phase is compressed to a higher density at a constant temperature in the NPT ensemble. These transformations can be monitored using the m-fold BOO parameter χ_m. In Figure 3.2, we show the behaviour of three BOO parameters χ_4, χ_6 and χ_{12}, respectively representing square, hexagonal and dodecagonal order. In Figure 3.2(a), we plot the BOO parameter as a function of temperature T^* during the cooling of the HDH phase at a density of $\rho^* = 0.98$. We observe that the value of χ_6 decreases and the values of χ_4 and χ_{12} increase upon decreasing the temperature. This signals the formation of the QC12. This behaviour of χ_m is due to the formation of $A15$, H and σ LPEs at the expense of Z. Similarly, Figure 3.2(b) shows the BOO parameter as a function of pressure P^* during compression of the FL phase at a temperature $T^* = 0.30$. We observe a discontinuity in χ_{12} with pressure, which points to a first-order phase transition from the fluid to the quasicrystal phase.

In Figure 3.3(a), we show a typical configuration of the random-tiling dodecagonal quasicrystal (QC12) on the top, and its accompanying tiling (left) and diffraction pattern (right) at the bottom as obtained from simulations at $\rho^* = 0.98$ and $T^* = 0.278$ in the NVT ensemble. Only the particle cores are shown in the configurations which are coloured according to their LPEs as described in Section 3.2.1. The resulting configuration contains defects of primarily pentagonal shape, which are highlighted in the accompanying tiling. In order to verify the nature of the QC12 tiling, we measure the ratio of number of triangles to squares in the tiling.

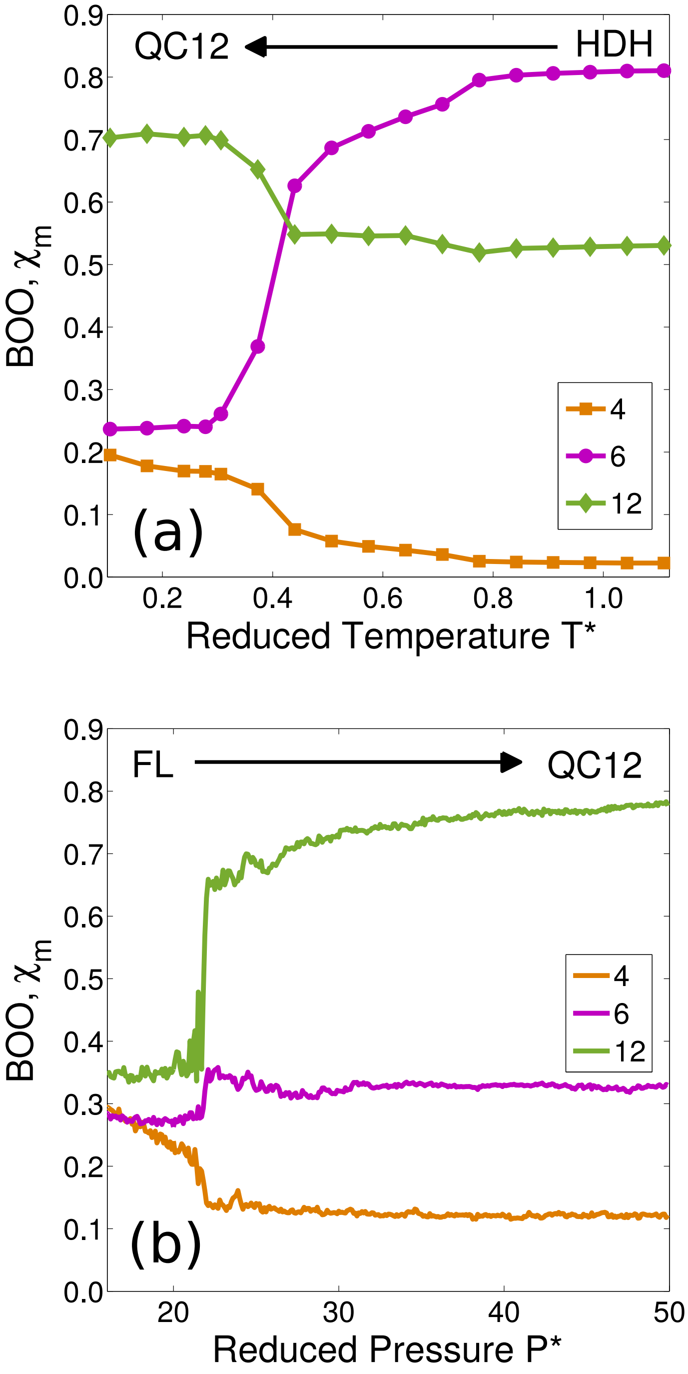

Figure 3.2: Formation of a dodecagonal quasicrystal (QC12) in a simulation of the HCSS system with $\delta = 1.40\sigma_{HD}$. The m-fold bond orientational order (BOO) parameter χ_m is plotted as a function of **(a)** temperature T^* as obtained by cooling a high-density hexagonal (HDH) phase at density $\rho^* = N\sigma_{HD}^2/A = 0.98$ in the NVT ensemble, and **(b)** pressure P^* by compressing a fluid (FL) phase at temperature $T^* = k_BT/\varepsilon = 0.30$ in the NPT ensemble.

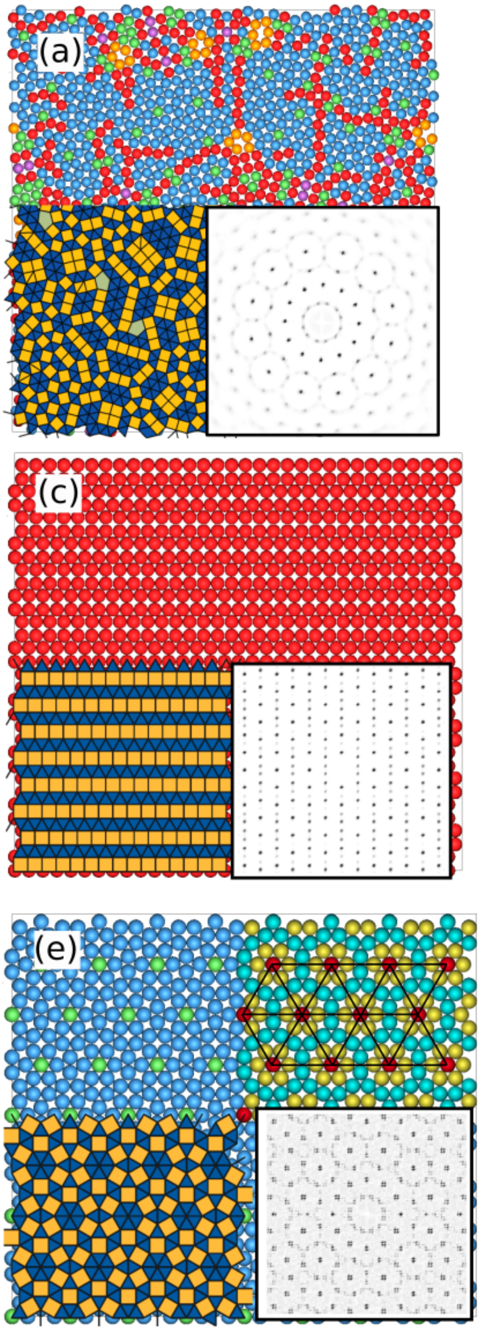

Figure 3.3: Comparison of the quasicrystal and its periodic approximants. Random tiling dodecagonal quasicrystal (QC12) **(a)** as obtained from simulations and **(b)** its defect-free configuration, **(c)** H phase (AC12-H), **(d)** σ phase (AC12-σ), and approximants consisting of dodecagons in a **(e)** triangle (AC12-tr) tiling and **(f)** square-triangle (AC12-st) tiling. Each figure displays a typical configuration **(top)**, where the particles are shown in core-only representation and the colours represent the local particle environments (LPEs) as described in Figure 3.1, along with its corresponding square-triangle tiling **(bottom left)** and diffraction pattern **(bottom right)**. For the AC12-tr and AC12-st approximants in (e, f), the tiling of dodecagons is highlighted **(top right)**.

We obtained a value of 2.30 ± 0.20, which is close to that of a dodecagonal quasicrystalline tiling $4/\sqrt{3} \approx 2.309$ [83, 178, 181–183], providing confidence that the additional configurational entropy contribution can be approximated by that of the random square-triangle tiling. In order to eliminate the effect of these defects on the phase diagram calculations, a defect-free configuration was adapted from a non-Stampfli square-triangle approximant [84]. We used the structure given in Figure 3 of Reference [84] containing 209 particles. This is shown in Figure 3.3(b) along with its tiling and diffraction pattern and was used as the initial configuration for the expansion runs of the equation of state.

A significant fraction of local particle environments in dodecagonal quasicrystals have a coordination number of five. Depending on the local arrangement of squares and triangles around the central particle, these environments can be categorised as H or σ LPEs as given in Figure 3.1. Periodic structures consisting entirely of these LPEs can be considered as a periodic approximants to the dodecagonal quasicrystals. We term these as first-order approximants. Their structures and corresponding diffraction patterns are shown in Figures 3.3(c) and 3.3(d). It can be noted from the diffraction patterns that the AC12-H phase shows more linear order than the required dodecagonal symmetry, while the dodecagonal symmetry obtained in the AC12-σ phase is somewhat distorted. This is attributed to the low number of particles in the approximant unit cell, namely 8 and 32 in the AC12-H and AC12-σ phases respectively.

Thus, we construct second-order approximants with a larger number of particles in their unit cells. These consist of dodecagonal motifs of particles arranged either in a triangle (AC-tr) [177, 180] or a square-triangle (AC-st) [84] tiling, constituting 52 and 56 particles respectively in their unit cells. The latter was adapted from a repeated vertex substitution of the $(3^2.4.3.4)$ Archimedean tiling consisting of squares and triangles [85]. These structures are shown in Figures 3.3(e) and 3.3(f). In the top-left panel of these figures, the particles are coloured according to their LPEs. On the top-right, the individual dodecagons and the tiling formed by connecting the centres of these dodecagons is shown. From the colouring of the particles in these structures according to their LPEs, we can identify the structural differences between the QC12 and the approximants. On basis of the two five-particle coordinated LPEs, H and σ, we observe that the AC12-tr consists solely of σ environments, while the AC12-st consists of both H and σ environments. In addition, the ratio of σ to H LPEs is much higher in AC12-st in comparison to that in QC12. In other words, the AC12-st consists predominantly of σ LPEs, while the QC12 consists of similar fractions of σ and H LPEs. Also, the $A15$ LPE, resulting from the presence of neighbouring square tiles, is found only in QC12 and is absent in all approximants.

3.3.2 Relative stability of quasicrystal and its approximants

To study the relative stability of the quasicrystal and the approximants, we first compare their equations of state (EOS), i.e. the pressure P^* as a function of the density ρ^*. We measure the EOS by varying the pressure in a step-wise manner in the NPT ensemble. We perform expansion runs starting with a defect-free random-tiling quasicrystal (QC12) or either of its four periodic approximants (AC12-H, AC12- σ, AC12-tr or AC12-st). We also calculate the EOS of crystal phases with a square (SQ) or a hexagonal (HDH) symmetry, which flank the quasicrystal and approximant phases on either side in terms of density. We plot the results for $T^* = 0.10$ in Figure 3.4. Two essential observations can be made from these plots, namely (1) the first-order approximants are less dense than the QC12 and the second-order approximants;

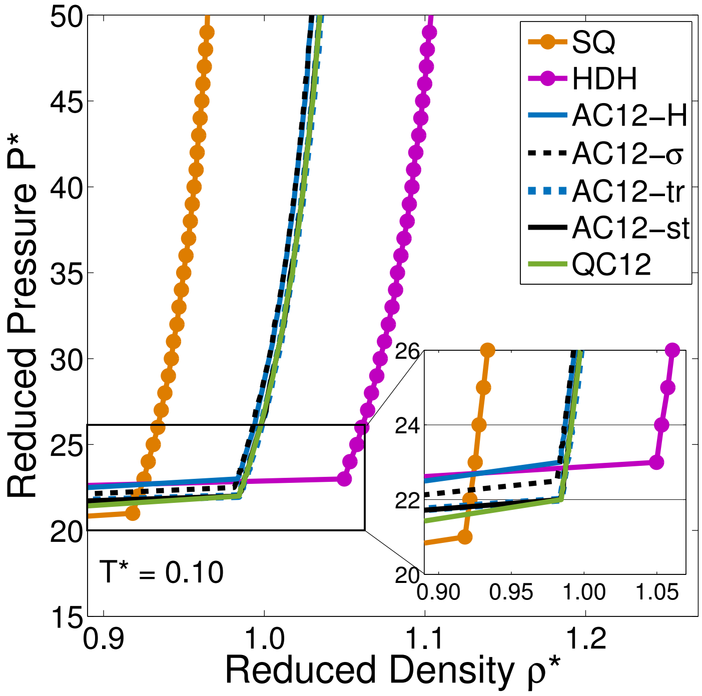

Figure 3.4: Equations of state, reduced pressure $P^* = \beta P\sigma_{HD}^2$ versus reduced density $\rho^* = N\sigma_{HD}^2/A$ calculated at reduced temperature $T^* = k_BT/\varepsilon = 0.10$ for a HCSS system with $\delta = 1.40\sigma_{HD}$ for the following phases: square (SQ), high-density hexagonal (HDH), quasicrystal (QC12), the first-order approximants, H phase (AC12-H) and σ phase (AC12-σ), and the second-order approximants consisting of dodecagons in a triangle (AC12-tr) and square-triangle (AC12-st) tiling. **Inset** gives a closer look at the pressures at which the solid phases melt.

which are all equally dense for all pressures higher than the melting point, and (2) the first-order approximants melt before the second-order approximants and the quasicrystal. This hints towards lower thermodynamic stability of the first-order approximants, namely the AC12-H and AC12-σ phases, in comparison to the others.

In the next step, we construct common tangents between different pairs of phases to evaluate the relative stability between these phases. The common-tangent construction between SQ and HDH at a temperature $T^* = 0.10$ is presented in Figure 3.5. Here, we plot the Helmholtz free energy per unit area $\beta F/A$ as a function of reduced density ρ^* for the following phases: SQ, HDH, AC12-H, AC12- σ, AC12-tr, AC12-st and QC12 without (QC12-woS), and with (QC12-wS) the configurational entropy contribution $S_{\text{config}}/k_BA = 0.12934$ as taken from literature [178]. For convenience, we subtract a linear fit $(\rho\mu_c - P_c)$ from the free-energy curves, where μ_c denotes the bulk chemical potential at the (metastable) SQ-HDH phase coexistence and P_c the corresponding bulk pressure. This ensures that the 'resultant' free energy of the two-phases between which the common-tangent is drawn is zero. In other words, the phases with a negative 'resultant' free energy in this plot are more stable with respect to the concerned two-phase coexistence. From Figure 3.5, we first note that the minima of the free-energy curves of QC12 and all approximants lie below the zero-level showing that all these phases with dodecagonal symmetry are more stable than the SQ-HDH phase coexistence. The magnitude of this difference of

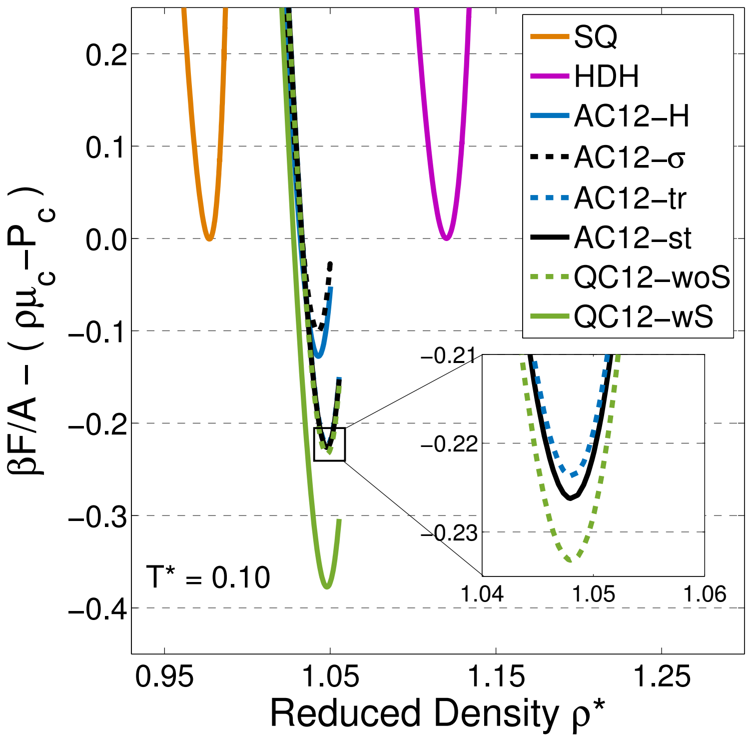

Figure 3.5: Common tangent construction at the (metastable) square-high-density hexagonal (SQ-HDH) phase coexistence obtained for the HCSS system with $\delta = 1.40\sigma_{HD}$ at reduced temperature $T^* = k_B T/\varepsilon = 0.10$. The plot shows the Helmholtz free energy per unit area $\beta F/A$ as a function of reduced density $\rho^* = N\sigma_{HD}^2/A$. A linear fit $(\rho\mu_c - P_c)$ is subtracted from the free energy, where μ_c and P_c are respectively the bulk chemical potential and bulk pressure at the (metastable) SQ-HDH phase coexistence. The phases shown are square (SQ), high-density hexagonal (HDH), the first-order approximants, H phase (AC12-H) and σ phase (AC12-σ), and the second-order approximants consisting of dodecagons in a triangle (AC12-tr) and square-triangle (AC12-st) tiling, and the dodecagonal quasicrystal without the entropy correction (QC12-woS) and the dodecagonal quasicrystal with the entropy correction (QC12-wS). **Inset** shows a closer look of the free energy curves of QC12-woS, AC12-tr and AC12-st phases.

these curves below the zero level gives the bias for the squares and triangles to mix and to form a square-triangle tiling, rather than phase separate into SQ and HDH regions. Also, as seen in the equations of state, the first-order approximants, AC12-H and AC12-σ are metastable with respect to the second-order approximants, AC12-tr and AC12-st, and the quasicrystal.

To identify the relative stability between the QC12-woS, AC12-tr and AC12-st phases, we take a closer look at their free energy curves in the inset. From the inset, we see that the QC12 is more stable than the other approximants even *without* the additional configurational entropy correction. This leads us to infer that the QC12 phase is stabilised by its vibrational entropy, i.e. the entropy associated with the number of configurations that the QC12 can probe by the vibrational motion of the particles around their lattice positions. This stems from the fact that the free energy calculated by the Frenkel-Ladd method has only two contributions, namely the potential energy of the particles and their vibrational entropy. Given that the QC12, AC12-tr and AC12-st have the same potential energy (for example, $U^* = U/\varepsilon N = 2.536 \pm 0.002$ at

$\rho^* = 1.07$), the difference in the free energy is attributed to the vibrational entropy. This entropy pertaining to the vibrational motion of the particles is inherently calculated in the Frenkel-Ladd method by integrating the mean square displacements of the particles around their lattice sites as a function of the spring constant of the harmonic springs that tie the particles to their respective lattice positions. The higher vibrational entropy of the QC12 could be due to long-wavelength phonon contributions. However, we do not systemically study this aspect here.

For all temperatures considered in this study ($T^* \geq 0.05$), we find that the QC12, even without the configurational entropy correction, is thermodynamically more stable than its approximants. Previous studies have reported a quasicrystal-approximant transition for a random-tiling quasicrystal at lower temperatures [176]. On the other hand, the conjecture by Dotera *et al.* [123], suggests the formation of a stable random-tiling dodecagonal quasicrystal at 0 K with a density $\rho^* \approx 1.07$ and ground state energy $U/\varepsilon N = 2.536$. We find that the closed packed density of the quasicrystal and the second-order approximants is indeed $\rho^* = 1.07$ with a potential energy $U^* = U/\varepsilon N$ equal to 2.536 ± 0.002. Extrapolating to lower temperatures, at $0.00 < T^* < 0.05$, we speculate that the quasicrystal remains more stable than its approximants. At zero temperature, the quasicrystal and the second-order approximants may be equally probable, considering their equal potential energy within our error bars.

The subsequent chain of thought leads to a question regarding the formation of the first-order approximants, AC12-H and AC12-σ, in the HCSS system. This arises because, in comparison to the triangle-to-square ratio of $4/\sqrt{3} \simeq 2.309$ resulting in the formation of the dodecagonal quasicrystal, we find that this ratio for the second-order approximants is 2.3, whereas that for the first-order approximants is 2.0. This means that the first-order approximants can be formed in between the SQ and QC12 phases. This can be explained by considering the transformation from the square to the hexagonal phase as an increase in the triangle-to-square ratio upon increasing the density of the system. In other words, we find that the triangle-to-square ratio increases with density until it matches with the maximum entropy random tiling consisting of equal area fractions of squares and triangles. Thus, the first-order approximants with a lower triangle-to-square ratio can be formed at a density in between that of the square phase and the random-tiling quasicrystal phase as can be seen in Figure 3.4. However, as seen in Figure 3.5, they have a higher free energy than the QC12 and thus, are not thermodynamically stable.

3.3.3 General phase behaviour

In order to map out the equilibrium phase diagram, we determine the equations of state (EOS) at a range of temperatures. The EOS calculated at three temperatures $T^* = 0.50$, 0.30, and 0.15 are shown in Figure 3.6. At the highest temperature of $T^* = 0.50$, the system exhibits hard-disk-like behaviour with a fluid phase at low densities, a hexagonal phase at sufficiently high densities and a two-phase coexistence region in between. At the intermediate temperature of $T^* = 0.30$, various high-density solid phases, namely SQ and QC12, start to appear, whereas at the lowest temperature, $T^* = 0.15$, the formation of a low-density hexagonal (LDH) phase bounded by the FL phase is observed. We show sample configurations of the four solid phases in Figure 3.7. Here, both the particle cores and coronas are shown, which are respectively coloured in blue and red.

Subsequently, we map out the phase diagram by performing the common tangent construction at various temperatures. The phase diagram in the reduced pressure-temperature ($P^* - T^*$)

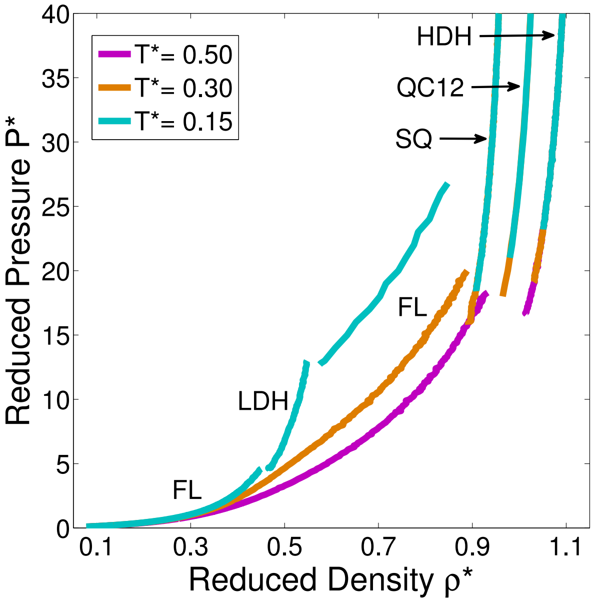

Figure 3.6: Equations of state ($P^* = \beta P \sigma_{HD}^2$ versus $\rho^* = N\sigma_{HD}^2/A$) obtained for the HCSS system with $\delta = 1.40\sigma_{HD}$ and temperatures $T^* = k_B T/\varepsilon = 0.50$, 0.30 and 0.15. The phases shown are fluid (FL), square (SQ), low-density hexagonal (LDH), high-density hexagonal (HDH), and the dodecagonal quasicrystal (QC12).

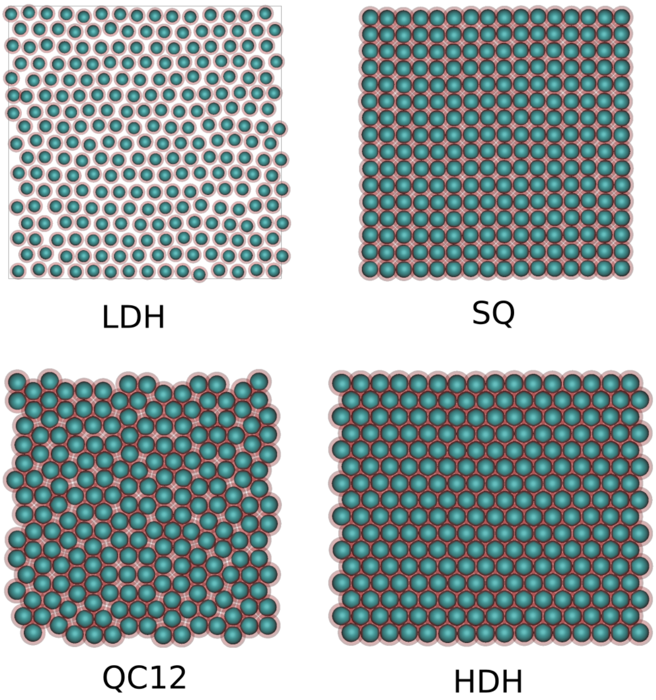

Figure 3.7: Sample configurations of the solid phases formed in the system, namely low-density hexagonal (LDH), square (SQ), dodecagonal quasicrystal (QC12) and high-density hexagonal (HDH). The particle cores are coloured in blue and the coronas is red.

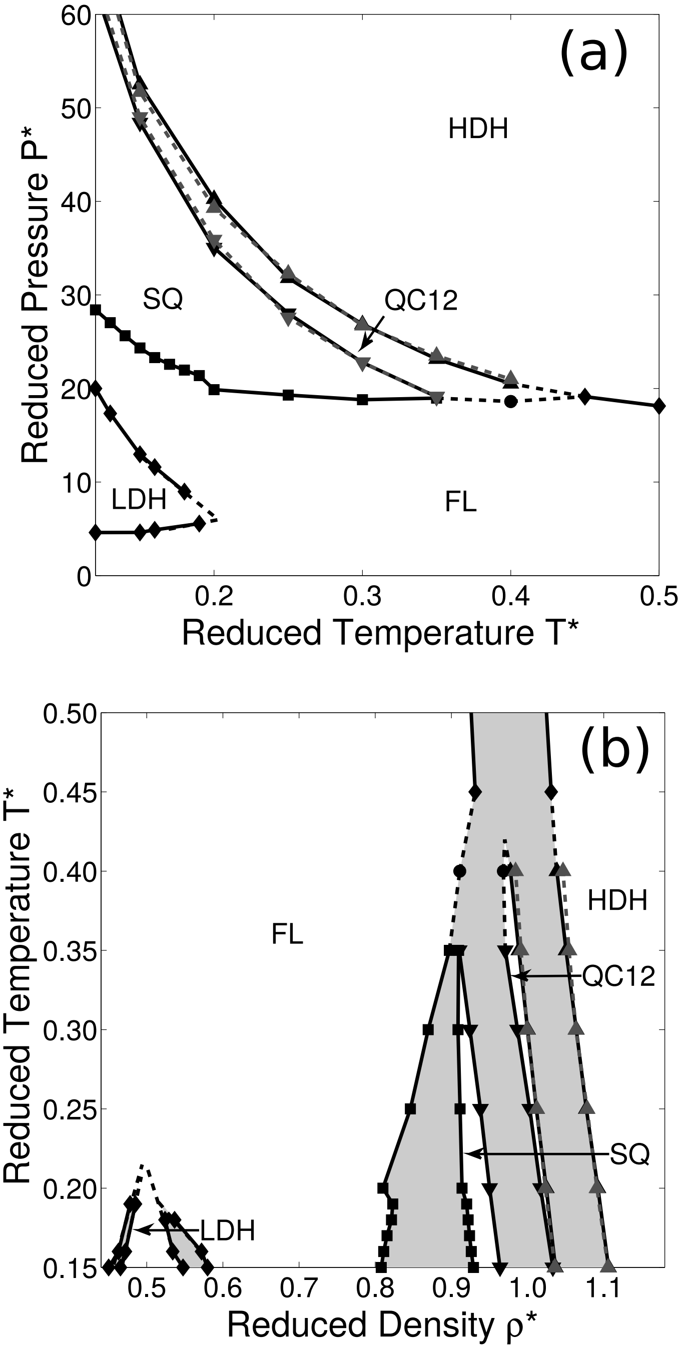

Figure 3.8: Phase diagram of a two-dimensional hard-core square-shoulder (HCSS) system with a shoulder width $\delta = 1.40\sigma_{HD}$ in the **(a)** pressure-temperature and **(b)** temperature-density planes. All quantities are represented in reduced units as $P^* = \beta P \sigma_{HD}^2$, $T^* = k_B T/\varepsilon$ and $\rho^* = N\sigma_{HD}^2/A$. The phases represented are fluid (FL), square (SQ), low-density hexagonal (LDH), high-density hexagonal (HDH), and random-tiling dodecagonal quasicrystal (QC12). The phase boundaries of the QC12 without the entropy correction, that accounts for the number of distinct configurations, are shown with dashed grey lines.

and temperature-density ($T^* - \rho^*$) planes are given in Figure 3.8. We make the following four observations from the phase diagram. Firstly, the stable phases identified in the system are the fluid (FL), square (SQ), low-density hexagonal (LDH), high-density hexagonal (HDH), and the dodecagonal quasicrystal (QC12). Further, we note that the quasicrystal is the thermodynamically stable dodecagonal symmetric phase in the system and is stable over a range of temperatures ($0.10 \leq T^* < 0.45$) even without the configurational entropy term associated with the number of distinct configurations. The phase boundaries of the QC12 calculated without the additional configurational entropy correction are also shown with dashed grey lines. Secondly, as noted from the EOS, a re-entrant fluid (FL) phase encompassing the low-density hexagonal (LDH) phase is found to be stable at low temperatures and densities. The LDH phase is a consequence of the repulsive square shoulder, which stabilises a hexagonal phase with a lattice spacing on the order of the square shoulder width. Thirdly, the stable close-packed phase is the high-density hexagonal (HDH) phase. At higher temperatures, $T^* \geq 0.45$, the phase behaviour of the system is similar to that of hard disks, with a fluid phase at low densities and a hexagonal phase at higher densities and a fluid-solid coexistence region in between. Given the system sizes used in this study, the presence of the hexatic phase is not considered [184, 185]. Finally, at moderate densities, the square phase is stabilised due to a lower energy, and the quasicrystal with dodecagonal symmetry is sandwiched between the SQ and HDH phases at low temperatures and between the FL and HDH phases at high temperatures.

3.4 Conclusions

In conclusion, we investigated the phase behaviour of a model system of colloidal particles with a core-corona architecture. The particles are modelled by a hard-core square-shoulder pair potential with a shoulder width $\delta = 1.40\sigma_{HD}$. We investigated the thermodynamic stability of a random-tiling dodecagonal quasicrystal formed at this shoulder width with respect to a disordered fluid phase, periodic crystal phases, and periodic approximants. We calculate the free energy of this random-tiling dodecagonal quasicrystal by explicitly accounting for its configurational entropy. For this system, we find a stable quasicrystal region sandwiched between the high-density hexagonal phase and a square phase at sufficiently low temperatures, and between the high-density hexagonal phase and a fluid phase at sufficiently high temperatures. We confirm that the quasicrystal is stabilised over the approximants by its vibrational entropy. We also stress that the phase boundaries are insensitive to whether or not the configurational entropy term is included in the free-energy calculations. We also study the overall phase behaviour of the system. At low densities, the fluid exhibits a re-entrant phase behaviour circumscribing a low-density hexagonal phase due to the presence of two length scales in the interaction potential. At high and intermediate densities, a high-density hexagonal phase and a square phase are respectively found to be stable.

Acknowledgements

I thank Guido Avvisati and John R. Edison for helpful discussions and Jan-Willem Buurlage and Anjan P. Gantapara for performing initial work on this project.

4

The effect of interaction range and pair potential on the formation of the dodecagonal quasicrystal

In this chapter, we first examine the formation of the dodecagonal quasicrystal reported in the hard-core square-shoulder system in Chapter 3 using bond orientational order parameters, correlation functions and tiling distributions. We find that this dodecagonal quasicrystal forms from a fluid phase. We then study the effect of the shoulder width of the repulsive shoulder and the effect of the shape of the interaction potential on the formation of this quasicrystal. For the former, we simulate the system over a range of values of the shoulder width δ. For the range of densities and temperatures considered, we observe the formation of the dodecagonal quasicrystal for $1.30\sigma_{HD} \leq \delta \leq 1.44\sigma_{HD}$. For the latter, we simulate the system using three other interaction potentials with two length scales, namely hard-core plus a linear ramp, a modified exponential, and Buckingham (exp-6) potential. We observe the presence of the quasicrystal in all three systems. However, depending on the shape of the potential, the formation of the quasicrystal takes place at lower temperatures (or higher interaction strengths). In addition, using free-energy calculations, we demonstrate that the quasicrystal is thermodynamically stable in the square-shoulder and linear-ramp system.

Based on *The effect of temperature, interaction range, and pair potential on the formation of dodecagonal quasicrystals in core-corona systems*, J. Phys. Cond. Matt., 29, 094003 (2017)

4.1 Introduction

Quasicrystals are materials that exhibit long-range orientational order but no translational periodicity. They were first reported by Shechtman *et al.* in a rapidly cooled Al-Mn alloy [96]. Since then, the world of quasicrystals has been blooming. Although, quasicrystals were initially found mostly in intermetallic systems, they have now also been reported in several soft-matter systems ranging from spherical dendrite micelles [105, 110], block copolymers [106–109] to binary mixtures of nanoparticles [111, 112]. Furthermore, there have been reports of colloidal quasicrystals obtained using external fields such as holography [116] or laser beams [117].

One of the most fascinating properties of quasicrystals is the formation of photonic band gaps, which is relevant for applications in optical devices. Photonic quasicrystals were first described for a one-dimensional quasicrystal by Kohmoto *et al.* [186] and have been extensively studied since then in two- and three-dimensional systems [68, 78, 187]. In general, soft-matter photonic quasicrystals have potential interesting applications in the telecommunications sector which require materials with a photonic band gap in the visible region of light [188]. This is due to the larger size of the constituent particles than their atomic counterparts and the relative ease of formation by self-assembly [44, 189]. Correspondingly, a complete photonic band gap was observed in a 12-fold symmetric quasicrystal obtained by etching air holes through a planar wave guide [91]. However, to the best of our knowledge, a quasicrystal self-assembled from colloidal particles with a full photonic band gap has not yet been realised experimentally. Thus, in order to facilitate the synthesis and self-assembly of these two-dimensional soft-matter quasicrystals, we investigate here extensively their formation and stability by computer simulations.

It is now widely accepted that the formation of quasicrystals in soft-matter systems is aided by the presence of two competing length scales [141, 169, 190–193]. This could either be the particle sizes of the two species in binary systems or an effective pair interaction that favours two length scales in a single-component system. Evidences have been found for both these classes using computer simulations. The former has been observed in particles interacting with Lennard-Jones [119, 120] and square-well [125] potentials, and the latter in systems with Lennard-Jones-Gauss [77], square-shoulder [123], square-well [121], linear ramp [118], flat-well [122] and three-well oscillating [124] pair interactions.

Computational studies of soft-matter quasicrystals using systems with core-corona architecture gained attention after the work of Dotera *et al.*, in which they studied the formation of quasicrystals of various symmetries using Monte Carlo simulations [123]. They reported six quasicrystals at different sizes of the corona with respect to the hard core. More recently, Schoberth *et al.* studied the formation of quasicrystals using a more realistic model for core-shell micelles [142]. They used a repulsive-shoulder potential to account for the entropic interactions of the overlapping polymer brushes. They provide a comparison with the system used by Dotera *et al.* [123]. The focus of these two works has been to identify the regions of quasicrystal formation in a density-corona diameter parameter space. One of the more appealing quasicrystals reported in both these studies is the high-density dodecagonal quasicrystal, which is more commonly observed in experimental soft-matter systems. Though there have been studies reported on the formation of a low-density dodecagonal quasicrystal [192, 193], we did not find any reports regarding the nature of formation of a high-density dodecagonal quasicrystal. Our present work is a step in this direction.

In this chapter, we study various aspects of the formation of a dodecagonal quasicrystal reported by Dotera *et al.* in a system of particles interacting with a hard core and a square-shoulder potential with a shoulder range equal to 1.4 times the hard-core diameter [123]. We divide this study into three parts. In the first part, we qualitatively and quantitatively follow the formation of a dodecagonal quasicrystal in a core-corona system using bond orientational order parameters, correlation functions and tiling distributions. In the second and third parts, we analyse the robustness of the formation of the quasicrystal by respectively studying the effect of shoulder width and the shape of the interaction potential.

4.2 Methods

We first explain the simulation model and computational methods used for this study in Section 4.2.1, and then give an account of the analysis methods in Section 4.2.2.

4.2.1 Computational methodology

In the first two parts of this study, we use a hard-core square shoulder (HCSS) model to represent the core-corona architecture. This model consists of a two-dimensional system of particles interacting with a pair potential consisting of a hard core of diameter σ_{HD} and a repulsive square shoulder of diameter δ, and was earlier used to model interparticle interactions in Cesium and Cerium [194]. A detailed description of the model is given in Chapter 2. This step potential, with a shoulder height ε, introduces two characteristic length scales in the system, respectively, at the hard core diameter σ_{HD} and the square shoulder diameter δ. We consider the shoulder width in units of the hard core diameter. This ultimately results in a single tunable parameter in the system, i.e. the shoulder width δ.

The basis of this study is a dodecagonal quasicrystal at $\delta = 1.40\sigma_{HD}$ initially reported in a simulation study by Dotera *et al.* [123] and recently re-established by Schoberth *et al.* [142]. In both works, bond orientational order parameters and bond orientational correlation functions were used to identify and characterise the resultant phase. However, the characterisation during the formation of this quasicrystal and details on its thermodynamic stability are absent. In Chapter 3, we studied the thermodynamic stability of this dodecagonal quasicrystal with emphasis on its relative stability over approximants with various periodic square-triangle tilings. We found that the quasicrystal is thermodynamically stable with respect to the considered tilings over the range of temperatures and densities that were studied. Therefore, we only consider the formation of this quasicrystal in this chapter. Here, we critically evaluate the formation of this quasicrystal in terms of a number of order parameters. This also acts as a summary of various methods that can be utilised to identify the quasicrystal. Further, we analyse the scope for formation of this quasicrystal in a three-dimensional parameter space consisting of the shoulder width, temperature and density.

In the last part of this study, we make use of the following three interaction potentials, which exhibit two characteristic length scales:

- Hard-core linear ramp (HCLR) potential, which is written as

$$V_{\mathrm{HCLR}}(r) = \begin{cases} \infty, & r \leq \sigma_{HD} \\ \varepsilon \frac{\delta - r}{\delta - \sigma_{HD}}, & \sigma_{HD} < r \leq \delta \\ 0, & r > \delta \end{cases} . \tag{4.1}$$

  This model has previously been shown to demonstrate a density anomaly during cooling and also formed a decagonal quasicrystal [118]. In this study, we take the width of the ramp to be equal to that of the square shoulder in the HCSS model, i.e. $\delta = 1.40\sigma_{HD}$.

- Hard-core modified exponential (HCME) potential represents a modified form of an exponential potential to fit inside the square shoulder. The pair potential $V_{\mathrm{HCME}}(r)$ reads

$$V_{\mathrm{HCME}}(r) = \begin{cases} \infty, & r \leq \sigma_{HD} \\ \varepsilon \exp\left[-\left(\frac{r-\sigma_{HD}}{\lambda}\right)^{m}\right], & r > \sigma_{HD} \end{cases} . \tag{4.2}$$

  The values of $m = 5$ and $\lambda = 0.31\sigma_{HD}$ are used in this study.

- Hard-core Buckingham or exp-6 (HCE6) potential is a classical potential used to model the soft-interactions that describe the anomalous behaviour of atomic substances at high pressures resulting from core-softening [195, 196], and reads

$$V_{\mathrm{HCE6}}(r) = \begin{cases} \infty, & r \leq \sigma_{HD} \\ \frac{-6\varepsilon}{\alpha - 6}\left[\exp\left(-\alpha\left(\frac{r}{\sigma_{HD}} - 1\right)\right) - \alpha\left(\frac{\sigma_{HD}}{r}\right)^{6}\right], & r > \sigma_{HD} \end{cases} , \tag{4.3}$$

  where the parameter α controls the steepness of the potential and is taken to be 15 in the present simulations.

In Figure 4.1, we show a comparison between all four interaction potentials. The HCLR is a linear ramp along the diagonal between the core and the corona diameters. The HCME is a short-ranged exponential potential that fits within the square shoulder. It initially follows the shape of the square shoulder and then decreases exponentially. On the other hand, the HCE6 is a long-ranged exponential potential which initially follows the shape of the linear ramp and then extends beyond the square shoulder. The parameters of each potential are chosen such that the shape of the potential largely fits inside the square shoulder at $\delta = 1.40\sigma_{HD}$.

We perform Monte Carlo (MC) simulations in the canonical (NVT) and isothermal-isobaric (NPT) ensembles. We use a rectangular box of area A with periodic boundary conditions. The hard-core diameter σ_{HD} and the shoulder height ε are, respectively, taken to be the units of length and energy. We define the following dimensionless (reduced) quantities: temperature $T^* = k_B T/\varepsilon$, pressure $P^* = \beta P \sigma_{HD}^2$, and density $\rho^* = N\sigma_{HD}^2/A$, where $\beta = 1/k_B T$ is the inverse temperature with k_B the Boltzmann constant. A system size N of 4900 particles was used in the first part of this study and that of 256 was used in the second and third parts.

4.2.2 Structural analysis

We perform an array of analyses to study the local structure of the system and to differentiate between the phases. This comprises of constructing the polygonal tiling of the structure, calculating the m-fold bond orientational order parameter (BOO) of a particle j, χ_m^j, the average

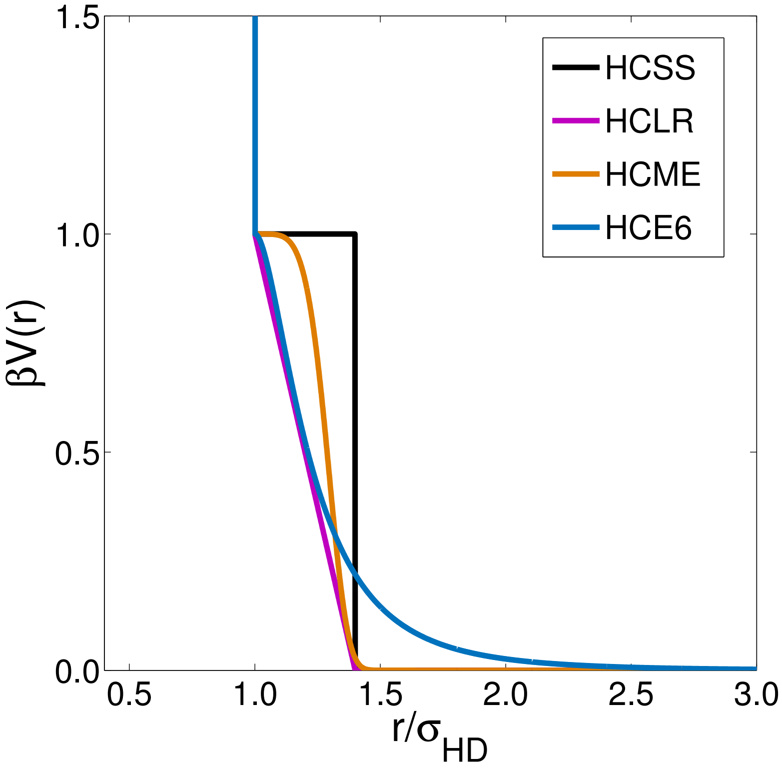

Figure 4.1: Comparison of the various two length scale interaction potentials used in this study shown as a function of the interparticle distance r. The pair potentials are the hard-core square shoulder (HCSS) potential, the hard-core linear ramp (HCLR) potential, the hard-core modified exponential (HCME) potential and the hard-core Buckingham or exp-6 (HCE6) potential.

BOO of the system, χ_m, the m-fold bond orientational correlation function, $g_m(r)$, the radial distribution function, $g(r)$, and the static structure factor, $S(k)$. We provide a description regarding the calculation of the tiling and bond orientational order parameters and the consequent correlation functions below.

We obtain the polygonal tiling of a structure by drawing bonds between the neighbouring particles of each particle j. The neighbouring particles are identified as particles that are at a centre-of-mass distance smaller than the square shoulder diameter δ from particle j. This is done to correlate the structures formed in our system with dodecagonal quasicrystals which are described in terms of tilings consisting of squares and equilateral triangles [83, 178, 181–183]. Analysis of the tiling allows us to distinguish between the various phases formed in the system and thus, the phase behaviour of the system. It is good to mention that such tilings have previously been used to study other phenomena in condensed matter systems like melting and condensation [197] and entropic demixing [198]. In our analysis of the tilings, we exclusively identify the triangle and the square tiles. We note that most of the defects in a hexagonal lattice result in a rhombic tile. Given the resemblance between the rhombus and square tiles, we also mark the rhombus tiles separately in order to prevent any effect of these tiles on the relative square-triangle tile calculations. Finally, the remainder of the tiles are grouped together and termed as 'defect' tiles. In this study, we colour the triangles in green, squares in yellow, rhombi in orange and defects in grey.

To calculate the BOO of the system, we first define the m-fold BOO of a particle j as

$$\chi_m^j = \left| \frac{1}{N_B(j)} \sum_{k=1}^{N_B(j)} \exp(im\theta_{\mathbf{r}_{jk}}) \right|^2 , \tag{4.4}$$

where m is the symmetry of interest, $\mathbf{r}_{jk}$ is the centre-of-mass distance vector between two neighbours j and k, $\theta_{\mathbf{r}_{jk}}$ is the angle between $\mathbf{r}_{jk}$ and an arbitrary axis, and $N_B(j)$ is the number of neighbours of particle j, which are defined as particles for which $|\mathbf{r}_{jk}| \leq \delta$. For each particle j, we calculate χ_4^j representing square symmetry, χ_6^j representing hexagonal symmetry and χ_{12}^j representing dodecagonal symmetry. We use the method described in Table 4.1 to classify the particles based on their BOO. We consider a particle to be fluid-like if each of the three χ_m^j is less than 0.5. On the other hand, if each of χ_m^j is greater than 0.5, then a particle is said to have symmetry $m1$ if χ_{m1}^j is greater than the other two, namely χ_{m2}^j and χ_{m3}^j. Further, we identify and colour the particles according to the following scheme: particles of square symmetry in purple, those of hexagonal in green, dodecagonal in red and fluid-like in orange as shown in Figure 4.2. Analogous to the three dimensional Frank-Kasper phases, the four LPEs shown in this figure can also be addressed as $A15$, Z, H and σ, respectively [180].

Table 4.1: Method of classification of particle j according to its bond orientational order (BOO) χ_m^j.

Symmetry	BOO conditions	Colour scheme
Fluid/Other (OT)	$\chi_4^j, \chi_6^j, \chi_{12}^j < 0.5$	orange
Crystal	$\chi_4^j, \chi_6^j, \chi_{12}^j > 0.5$	
- Square (SQ)	$\chi_4^j > \chi_6^j, \chi_{12}^j$	purple
- Hexagonal (HX)	$\chi_6^j > \chi_4^j, \chi_{12}^j$	green
- Dodecagonal (QC)	$\chi_{12}^j > \chi_4^j, \chi_6^j$	red

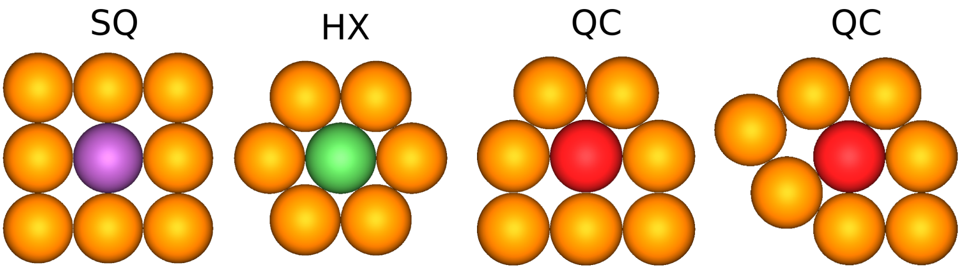

Figure 4.2: Colour scheme for classes of particles based on the BOO classification as described in Table 4.1.

After calculating the BOO of each particle, the average BOO of the system is then evaluated as [164]

$$\chi_m = \frac{1}{N}\sum_{j=1}^{N} \chi_m^j. \tag{4.5}$$

Ultimately, the $m-$fold bond orientational correlation function $g_m(r)$ with $r = |\mathbf{r} - \mathbf{r}'|$ is calculated as

$$g_m(r) = \left\langle \chi_m^j(\mathbf{r}).\chi_m^{k*}(\mathbf{r}') \right\rangle. \tag{4.6}$$

There are previous accounts of identifying quasicrystals using BOO, BOO correlation functions and radial distribution functions [123, 142]. In this work, we apprehend all these methods along with tiling calculations to provide a comprehensive overview of the various methods that can be used. We aim to verify the consistency achieved by using these methods in addition to studying the nature of quasicrystal formation.

4.3 Results and discussion

As indicated in the previous sections, this section will be presented in three parts. In the first part (Section 4.3.1), we take a meticulous look at the process of formation of the dodecagonal quasicrystal in the HCSS system. In the second part (Section 4.3.2), we study the influence of the shoulder width of the HCSS potential on the quasicrystal formation. And finally in the third part (Section 4.3.3), we study the response of the system when the shape of the interaction potential is modified.

4.3.1 Formation of dodecagonal quasicrystal

By now, the presence of a random-tiling high-density dodecagonal quasicrystal in the HCSS system is well reported [123, 142]. However, the process of its formation is seldom studied. It is formed either by cooling a hexagonal structure from a high to a low temperature at a constant density or by compressing an isotropic fluid phase to a higher density at a constant temperature. In this work, we delve into the former method where we cool a hexagonal lattice of (reduced) density $\rho^* = 0.98$ from (reduced) temperature $T^* = 1.0$ to 0.1. This cooling simulation is marked using a red dashed line in the phase diagram shown in Figure 4.3(a).

To start, we inspect the change in the potential energy per particle as a function of temperature as presented in Figure 4.3(b). We note six different branches in the plot indicating distinct phase behaviours. We have marked these individual regions after studying various structural properties of the obtained configurations, for example, its tiling, BOO and corresponding diffraction patterns. In order to obtain a better understanding of these phase transformations, we study the energy plot in Figure 4.3(b) in conjunction with typical configurations at a fixed temperature at each of these branches as shown in Figure 4.4. These configurations as presented in Figure 4.4 are composed of four features: (1) the positions of the hard cores of the particles are displayed at the top, (2) the polygonal tiling is presented at the bottom, (3) the calculated diffraction pattern is shown in the inset at the centre, and (4) the labels indicate the different phases. The colouring schemes used for the hard core of the particles in the top region and the tiles in the bottom region are explained in Section 4.2.2.

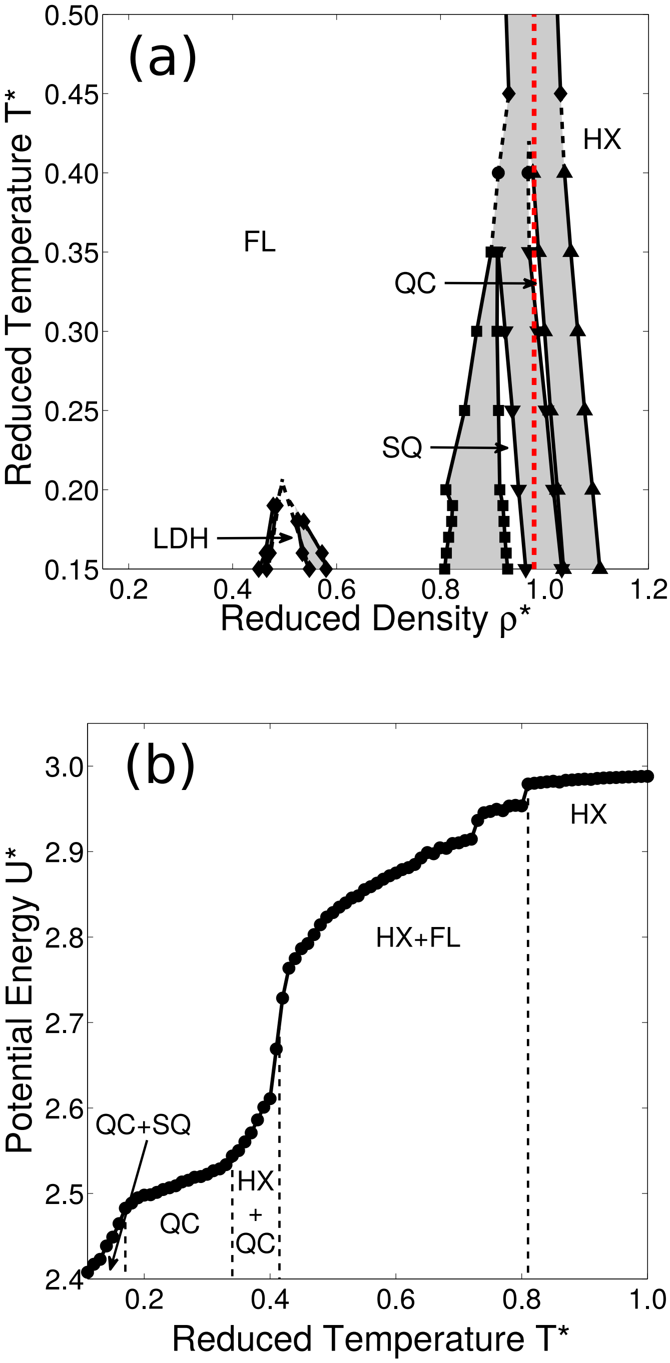

Figure 4.3: **(a)** Phase diagram in the (reduced) temperature-density plane in which the path followed during the cooling of the system at a constant (reduced) density $\rho^* = 0.98$ is marked using the dashed line in red. **(b)** Potential energy per particle U^* as a function of temperature T^* during this cooling simulation. The calculations were performed for the HCSS system with shoulder width $\delta = 1.40\sigma_{HD}$. The reduced quantities are defined as $T^* = k_B T/\varepsilon$, $\rho^* = N\sigma_{HD}^2/A$ and $U^* = U/\varepsilon N$. The phases marked are fluid (FL), high-density hexagonal (HX), dodecagonal quasicrystal (QC), square (SQ) and low-density hexagonal (LDH).

Let us first take a qualitative look at the phase behaviour shown in Figure 4.3(b) and Figure 4.4 starting from high temperatures. At high temperatures ($T^* > 0.80$), the potential energy ($U^* = U/\varepsilon N$) decreases very slowly with decreasing temperature and is close to 3.0. The potential energy per particle of an ideal hexagonal lattice in the HCSS system with $\delta = 1.40\sigma_{HD}$ is 3.0. Thus, the structure at these temperatures should be hexagonal in nature. However, the potential energy at these temperatures is not exactly equal to that of the perfect hexagonal lat-

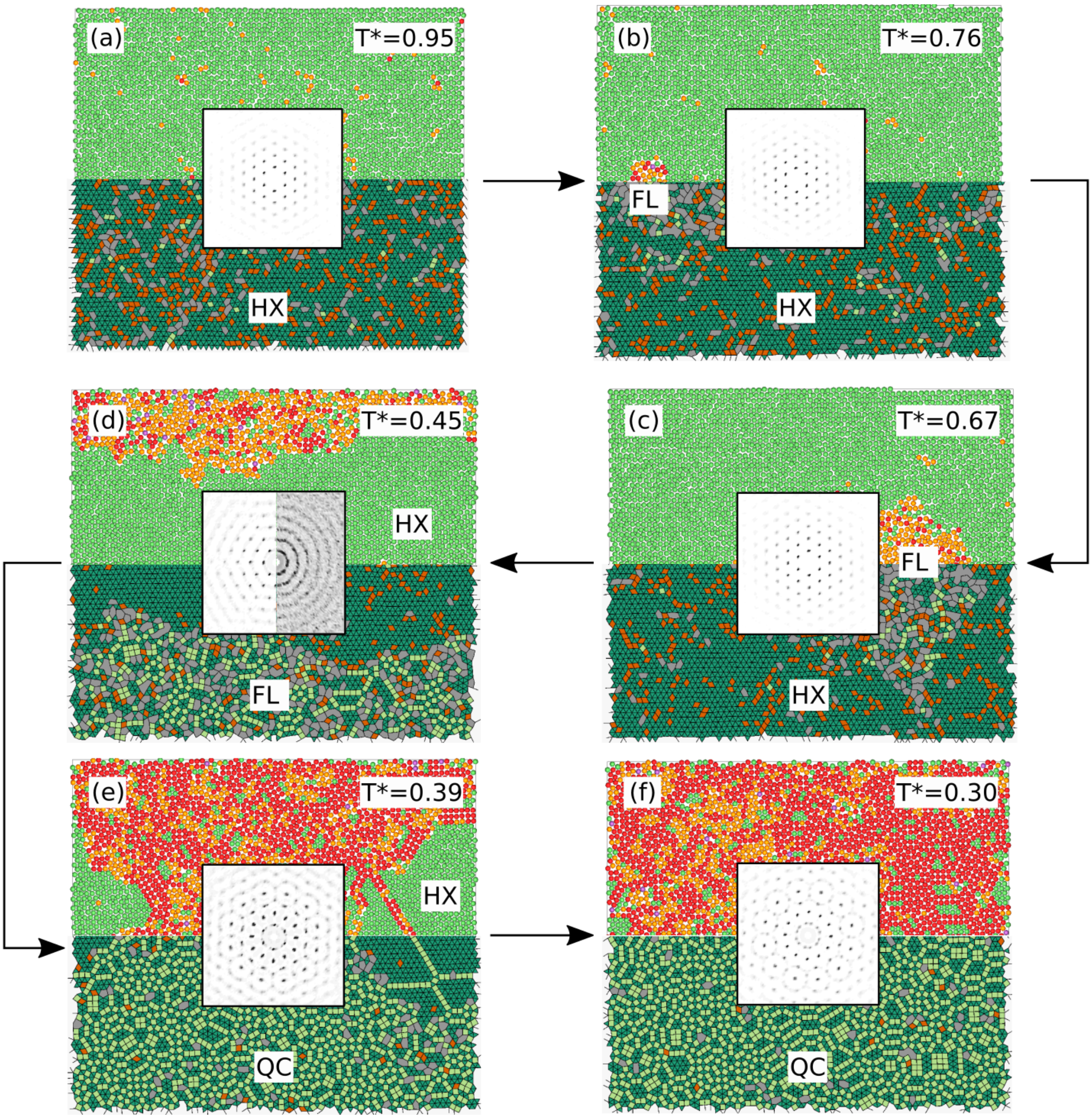

Figure 4.4: Phases formed at various temperatures ($T^* = k_B T/\varepsilon$) during cooling of a hexagonal phase at a (reduced) density $\rho^* = N\sigma_{HD}^2/A = 0.98$ interacting with a HCSS pair potential with a shoulder width $\delta = 1.40\sigma_{HD}$. The phases marked are hexagonal (HX), fluid (FL) and dodecagonal quasicrystal (QC). Each panel consists of (top) positions of the hard cores of the particles, (bottom) polygonal tiling, (inset) calculated diffraction pattern of the structure. The particles and the tiles are, respectively, coloured according to the schemes explained in Section 4.2.2. The arrows denote the path followed in temperature during the cooling simulation.

tice. This indicates the presence of defects, which are seen as the orange rhombi and other grey shapes in Figure 4.4(a). Upon decreasing the temperature further, these individual defects accumulate and form a nucleus of the fluid phase as noticed in Figure 4.4(b). A further decrease in temperature from $T^* = 0.72$ to 0.43 is characterised by a continuous decrease in potential energy. This refers to the growth of the fluid nucleus (Figure 4.4(c)). Towards the end of this growth regime, we observe a hexagonal-fluid phase coexistence (Figure 4.4(d)). At $T^* = 0.45$ shown in Figure 4.4(d), each of these phases occupy almost half of the simulation box and this allows us to calculate the diffraction pattern of the fluid and the hexagonal phase, separately. This is displayed in the inset of Figure 4.4(d). When the temperature is decreased even further, we notice a sudden drop in the potential energy at $T^* \sim 0.41$. This drop coincides with the formation of a dodecagonal quasicrystal from the fluid, which results in the formation of a two-phase coexistence region between hexagonal and quasicrystal phases (Figure 4.4(e)). It is affirmative to note that the diffraction pattern calculated at $T^* = 0.39$, shown in the inset of Figure 4.4(e), clearly displays characteristics of both the quasicrystal and hexagonal structures. Comparing this transformation with the previous formation of the fluid phase from hexagonal, we note the absence of a single nucleus of the quasicrystal. However, the sudden change in the potential energy hints towards a first-order phase transition. With further lowering the temperature (and further decrease in energy), we observe a concurrent growth of the quasicrystal region and decline of the hexagonal region; the outcome of which is a dodecagonal quasicrystal spanning the entire simulation box (Figure 4.4(f)). We remark that the energy in the quasicrystal regime is not constant, but decreases with decreasing temperature. This implies the formation of more squares at lower temperatures. Thus, the following energy drop is associated with the formation of a two-phase coexistence region between the square and quasicrystal phase.

Let us now quantitatively analyse the phase transformation with the help of order parameters as explained in Section 4.2.2. In Figure 4.5(a) and Figure 4.5(b), we investigate the behaviour of the bond orientational order parameters. In Figure 4.5(a), we plot the fraction of different types of particles (f_X^p) as obtained from the BOO classification in Table 4.1 as a function of temperature. The particle types X that we distinguish are square (SQ), hexagonal (HX), dodecagonal quasicrystal (QC), and others (OT). We notice that the fraction of hexagonal (f_{HX}^p) particles decrease and that of the quasicrystal (f_{QC}^p) particles increase with decreasing temperature indicating the formation of the quasicrystal from the hexagonal phase. However, the fraction of square particles (f_{SQ}^p) remains almost constant throughout the entire temperature range except at very low temperatures. This indicates that no square phase is formed during the initial quasicrystal formation, but there is a small indication of its formation at very low temperatures. Another interesting feature is the fraction of 'fluid-like' particles (f_{OT}^p). We observe a very low, but non-zero, value at high temperatures indicating defects in the hexagonal lattice. With decreasing temperature, we observe a significant increase in f_{OT}^p through the two-phase coexistence region of the hexagonal and fluid phase. This complies with the formation of larger amounts of fluid phase. This increase, however, ceases with the formation of the quasicrystal and the f_{OT}^p remains at a constant value. We further confirm the first-order nature of the fluid to the quasicrystal transformation from the sudden drop in f_{HX}^p and the simultaneous increase in f_{QC}^p.

We then focus our attention on Figure 4.5(b), where we plot the average m-fold bond orientational order as a function of temperature. On the one hand, we notice that the behaviour of χ_6 and χ_{12}, respectively, follow that of the fraction of hexagonal (f_{HX}^p) and quasicrystal

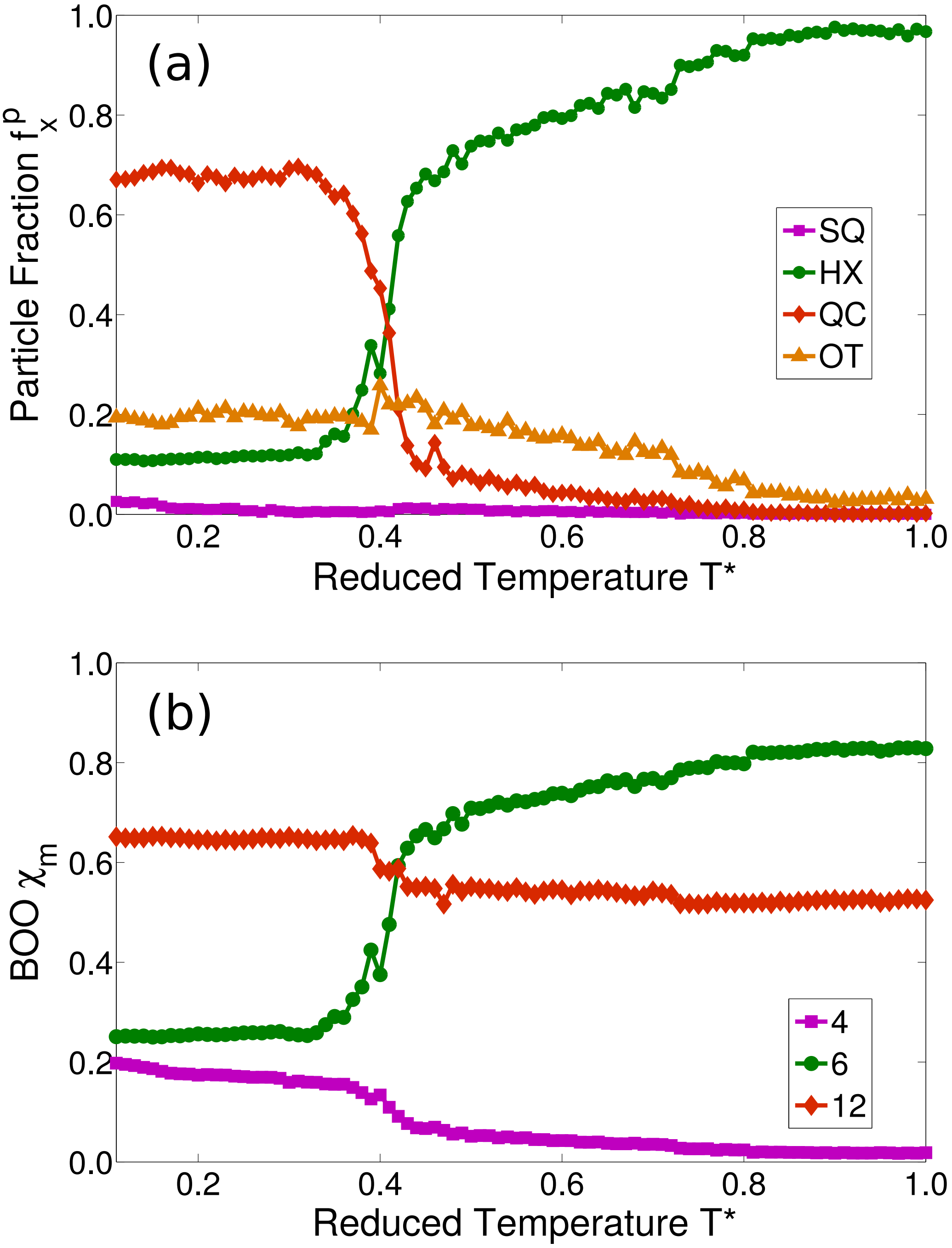

Figure 4.5: Various order parameters as a function of temperature ($T^* = k_B T/\varepsilon$) describing the quasicrystal formation for the HCSS system with shoulder width $\delta = 1.40\sigma_{HD}$ at a constant (reduced) density $\rho^* = N\sigma_{HD}^2/A = 0.98$: **(a)** Fraction of different types of particles based on its BOO classification, f_X^p. The particle types X that we distinguish are square (SQ), hexagonal (HX), dodecagonal quasicrystal (QC), and others (OT). **(b)** m-fold bond orientational order (BOO) of the system, χ_m, with $m = 4, 6$, and 12. For convenience, the curves are coloured according to the same schemes as in Figure 4.4.

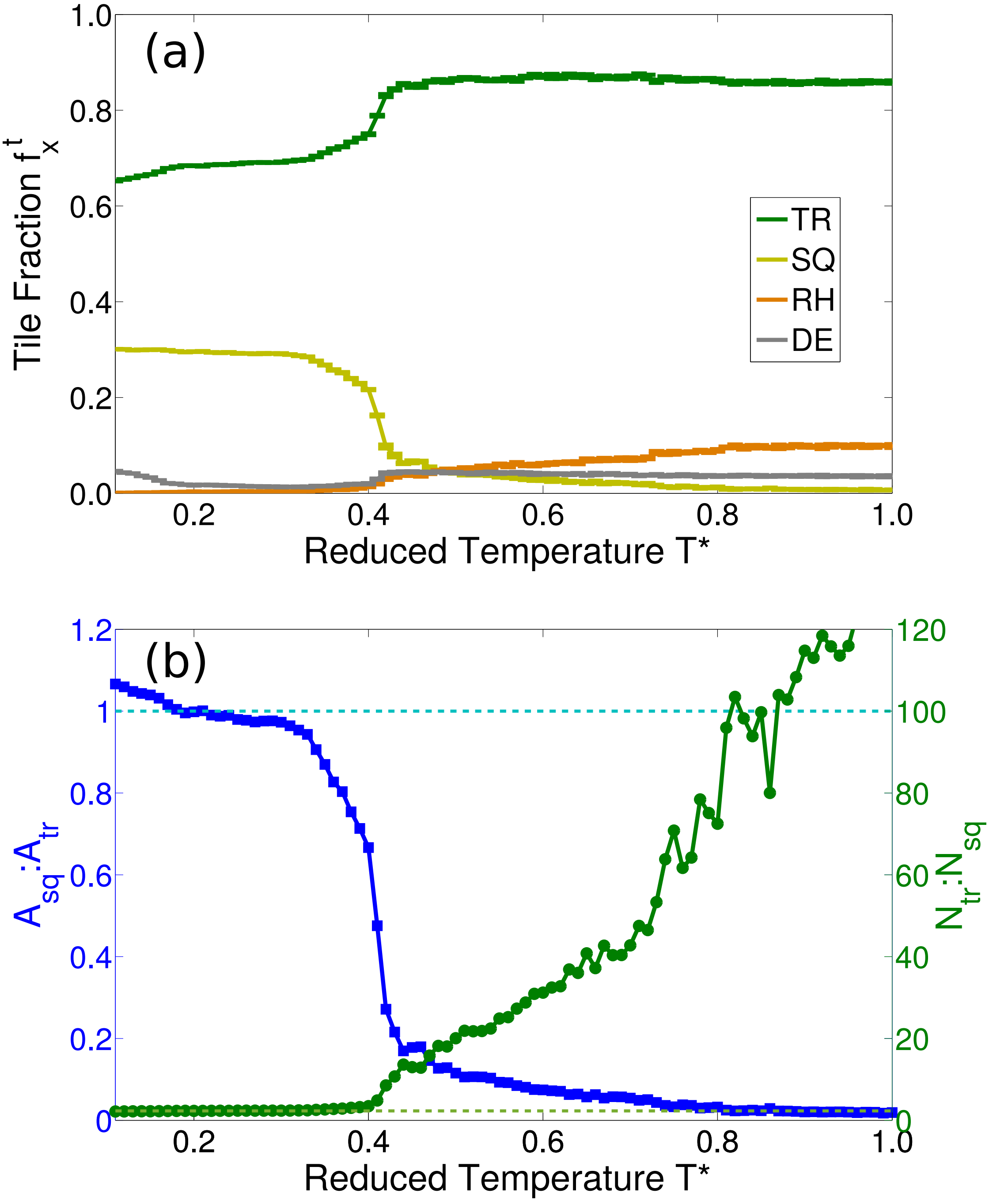

Figure 4.6: Various order parameters as a function of temperature ($T^* = k_B T/\varepsilon$) describing the quasicrystal formation for the HCSS system with shoulder width $\delta = 1.40\sigma_{HD}$ at a constant (reduced) density $\rho^* = N\sigma^2_{HD}/A = 0.98$: **(a)** Fraction of different tile types, f^t_X. The tile types X that are considered are triangle (TR), square (SQ), rhombus (RH) and defects (DE). **(b)** Number and area ratio of square and triangle tiles. The ideal number and area ratios of squares and triangles are marked with dashed lines. For convenience, the curves in (a) are coloured according to the same schemes as in Figure 4.4.

(f^p_{QC}) particles in Figure 4.5(a), i.e. χ_6 decreases and χ_{12} increases with decreasing temperature. However, on the other hand, unlike the constant behaviour of f^p_{SQ}, we find an increase in the values of χ_4 at temperatures close to the quasicrystal formation. This further reinforces the fact that the formation of the quasicrystal is aided by the replacement of particles of hexagonal symmetry by ones with square symmetry. The increase in χ_4 values at even lower temperatures $T^* \sim 0.18$ indicates the formation of the square phase.

Next, we correlate the behaviour of the particles with that of the tilings obtained from connecting the nearest neighbours of particles. To do so, we plot the behaviour of the fraction of tiles during cooling of the system in Figure 4.6(a) and Figure 4.6(b). Figure 4.6(a) shows the fraction of triangle tiles f^t_{TR}, square tiles f^t_{SQ}, rhombus tiles f^t_{RH}, and defect tiles f^t_{DE} as a function of temperature. The fraction of triangle tiles f^t_{TR} is almost constant in the temperature range where the hexagonal phase and fluid-hexagonal phase coexistence is observed. The difference between these two regions is brought about by the relative fractions of the rhombus tiles f^t_{RH} and defect tiles f^t_{DE}. In the temperature range where the hexagonal phase is found, we observe a larger fraction of rhombus tiles f^t_{RH} representing the defects in the hexagonal lattice. Upon lowering the temperature, we find an increase in the fraction of defect tiles f^t_{DE} signalling the formation of the fluid phase. At lower temperatures, closer to the quasicrystal formation, we observe a simultaneous decrease in the fraction of rhombus tiles f^t_{RH} and defect tiles f^t_{DE} and an increase in the fraction of square tiles f^t_{SQ}. We note the almost constant values of f^t_{TR} and f^t_{SQ} in the quasicrystal region. In the low temperature regime of the quasicrystal region, we note a further increase in f^t_{SQ} denoting the formation of the square phase. These observations are concurrent with those of the particle fractions in Figure 4.5(a).

Now, we turn our attention to Figure 4.6(b), where we study the composition of the tiling in terms of the constituent square and triangle tiles. This is done because the dodecagonal quasicrystals described by a square-triangle tiling have a triangle-to-square number ratio of $4/\sqrt{3} \simeq 2.309$ [183]. At this ratio, both the squares and triangles occupy equal areas, thereby giving a square-to-triangle area ratio of 1. Thus, in Figure 4.6(b), we show the behaviour of two ratios, i.e. (1) the ratio of the areas of square and triangle tiles, and (2) the ratio of the number of triangles and squares as a function of temperature. We have also marked the ideal triangle-to-square area and number ratios using dashed lines. The prominent observation that results from this plot is that both the area and the number ratios are close to their ideal values in the range of temperatures pertaining to the quasicrystal region. Furthermore, the increase in the area ratio towards the end of the temperature spectrum coincides with the formation of the SQ phase.

Finally, we examine the long-range order of the system by means of the radial distribution function $g(r)$ and the 6- and 12-fold bond orientational correlation functions $g_6(r)$ and $g_{12}(r)$. These quantities are shown in Figure 4.7 and Figure 4.8 as a function of temperature. The curves corresponding to different phases are separately marked. In Figure 4.7, we see the evolution of the $g(r)$ from the hexagonal (HX) to the quasicrystal (QC) phase upon decreasing the temperature. The initial peaks of the $g(r)$ of the HX phase lies at $1.0\sigma_{HD}$ and $\sqrt{3} \sim 1.732\sigma_{HD}$ denoting the hard-core diameter and a sequence of consecutive equilateral triangles, respectively. The formation of quasicrystals is indicated by the appearance of a peak at $1.40\sigma_{HD}$ (marked by an arrow in Figure 4.7) corresponding to a sequence of squares. In Figure 4.8(a) and Figure 4.8(b), we present the 6-fold and 12-fold bond orientational correlation functions $g_6(r)$ and $g_{12}(r)$, respectively. Both the $g_6(r)$ and $g_{12}(r)$ reach a constant value for both the hexagonal and quasicrystal phases and do not decline to zero at larger r. This confirms the presence of long-range orientational order in the system. As can be expected, the $g_6(r)$ of the HX phase is higher than that of the QC phase; while the inverse holds for $g_{12}(r)$. This confirms the dominant orientational order in these phases. Also, the decaying nature of both the $g_6(r)$ and $g_{12}(r)$ curves at temperatures $T^* = 0.40$ and 0.50 indicates the absence of long-range orientational order in the system, i.e. the presence of a fluid (FL) phase. The value of $g_{12}(r)$ decreases from $T^* = 0.30$

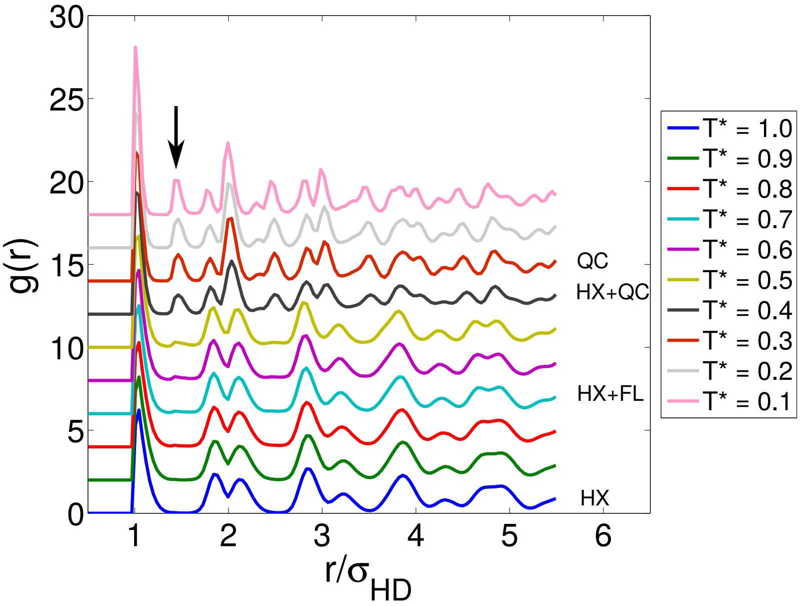

Figure 4.7: Radial distribution function $g(r)$ as a function of temperature during quasicrystal formation. The phases indicated are hexagonal (HX), fluid (FL), and dodecagonal quasicrystal (QC). For clarity, we shifted the $g(r)$ at each temperature in the vertical direction by an additional $\Delta y = 2$. The peak at $1.40\sigma_{HD}$ denoting the formation of quasicrystals is marked with an arrow.

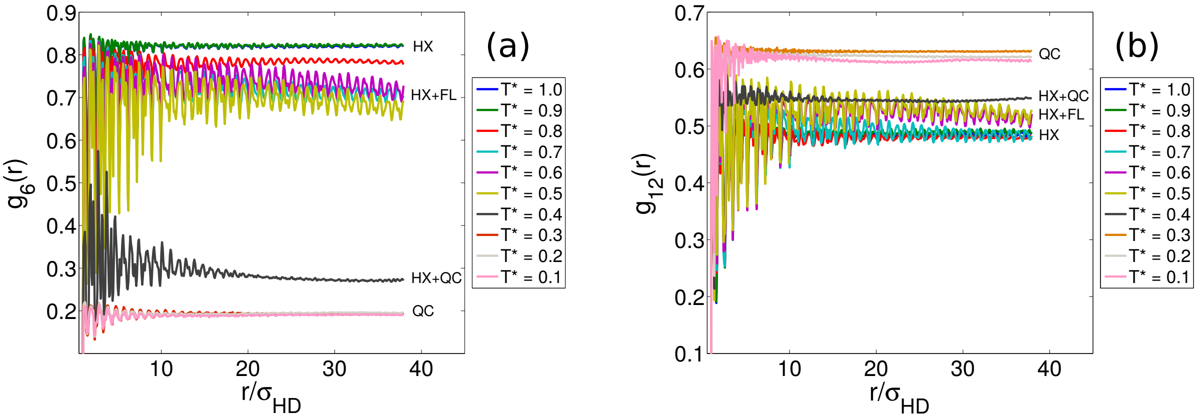

Figure 4.8: Structural properties at various temperatures during quasicrystal formation: **(a)** 6-fold bond orientational correlation function $g_6(r)$, and **(b)** 12-fold bond orientational correlation function $g_{12}(r)$. The phases indicated are hexagonal (HX), fluid (FL), and dodecagonal quasicrystal (QC).

to 0.10 indicating the ‘loss’ of fraction of QC phase, i.e the formation of another phase in the system. From our previous discussions, we know this to be the square (SQ) phase.

To summarise this section, we have investigated the formation of the QC phase by cooling a hexagonal phase at a constant density. Upon lowering the temperature, we first find the formation of a fluid phase via a nucleation and growth mechanism, resulting into a phase coexistence of the fluid and hexagonal phase. By further cooling the system, we find that a QC phase forms within the fluid phase, and continues to grow until the whole system is quasicrystalline. Further, these phase transformations encountered during the cooling process is consistent with the phase diagram as presented in Figure 4.3(a).

4.3.2 Effect of shoulder width

The calculations discussed in Section 4.3.1 were performed at a single value of the width of the square shoulder. Here, we assess the effect of the shoulder width on the formation of the dodecagonal quasicrystal by performing simulations in the NVT ensemble at shoulder widths δ from $1.26\sigma_{HD}$ to $1.50\sigma_{HD}$, densities ρ^* between 0.96 and 0.99, and temperatures T^* between

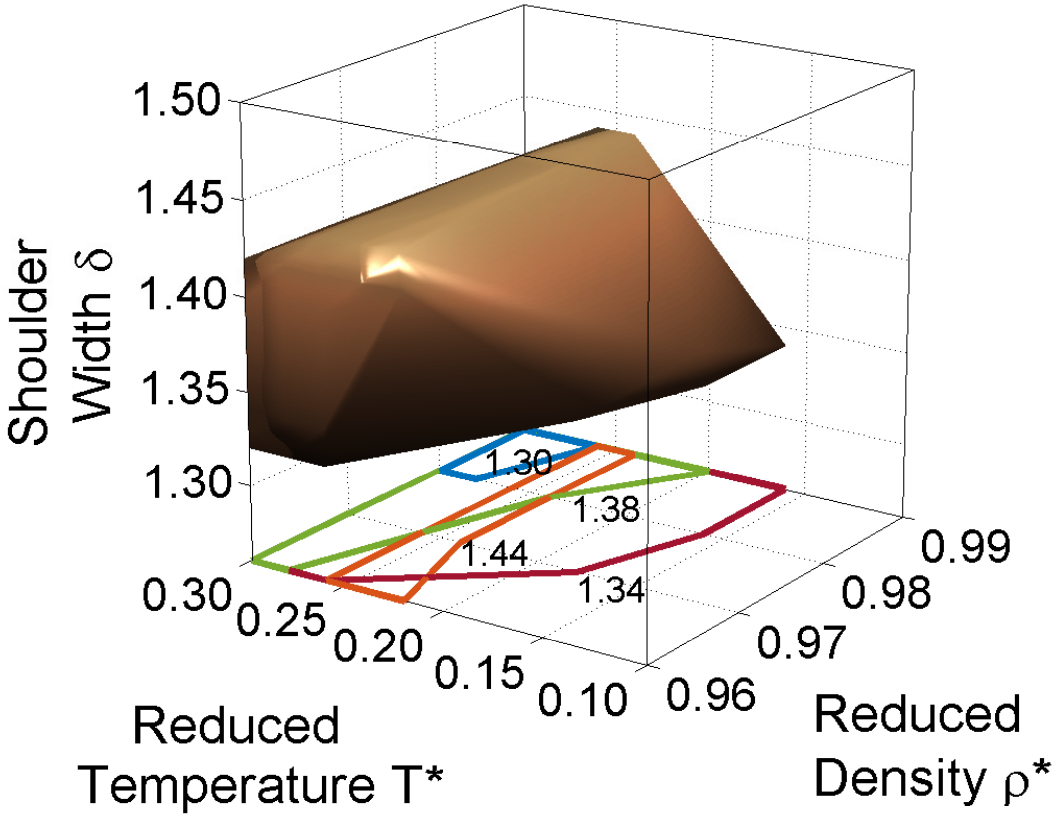

Figure 4.9: Three-dimensional phase space of (reduced) density ρ^*, temperature T^* and shoulder width δ where the dodecagonal quasicrystal (QC) is observed as denoted by the coloured volume for the HCSS system. The reduced quantities are defined as $T^* = k_B T/\varepsilon$ and $\rho^* = N\sigma_{HD}^2/A$. The box represents the range of data points that were considered. The shoulder width is plotted in units of σ_{HD}. The contours in the $\rho^* - T^*$ plane for a few shoulder widths, namely 1.30, 1.34, 1.38, and 1.44, are also given.

0.10 and 0.30. We analyse the resulting configurations with the help of their polygonal tiling, diffraction pattern and average bond orientational order (BOO) of the system, χ_m.

We observe the formation of the dodecagonal quasicrystal (QC) in a range of densities, temperatures and shoulder widths. This three-dimensional phase space is given in Figure 4.9. The coloured volume shown represents the limits of the quasicrystal formation and the box displays the range of data points simulated. We also plot the contours in the density-temperature plane for a few shoulder widths. It is evident from these plots that the quasicrystal forms over a range of all three parameters. For clarity, we perform further analysis at constant temperature $T^* = 0.28$.

We plot the state diagram in the shoulder width-density ($\delta - \rho^*$) plane at $T^* = 0.28$ in Figure 4.10. At shoulder widths $\delta > 1.45\sigma_{HD}$, we find that the system behaves similar to the hard-disk model. Even though we only observe a FL+HX phase coexistence at the densities shown here, it is apparent that this region will be bordered by FL at lower densities and HX at

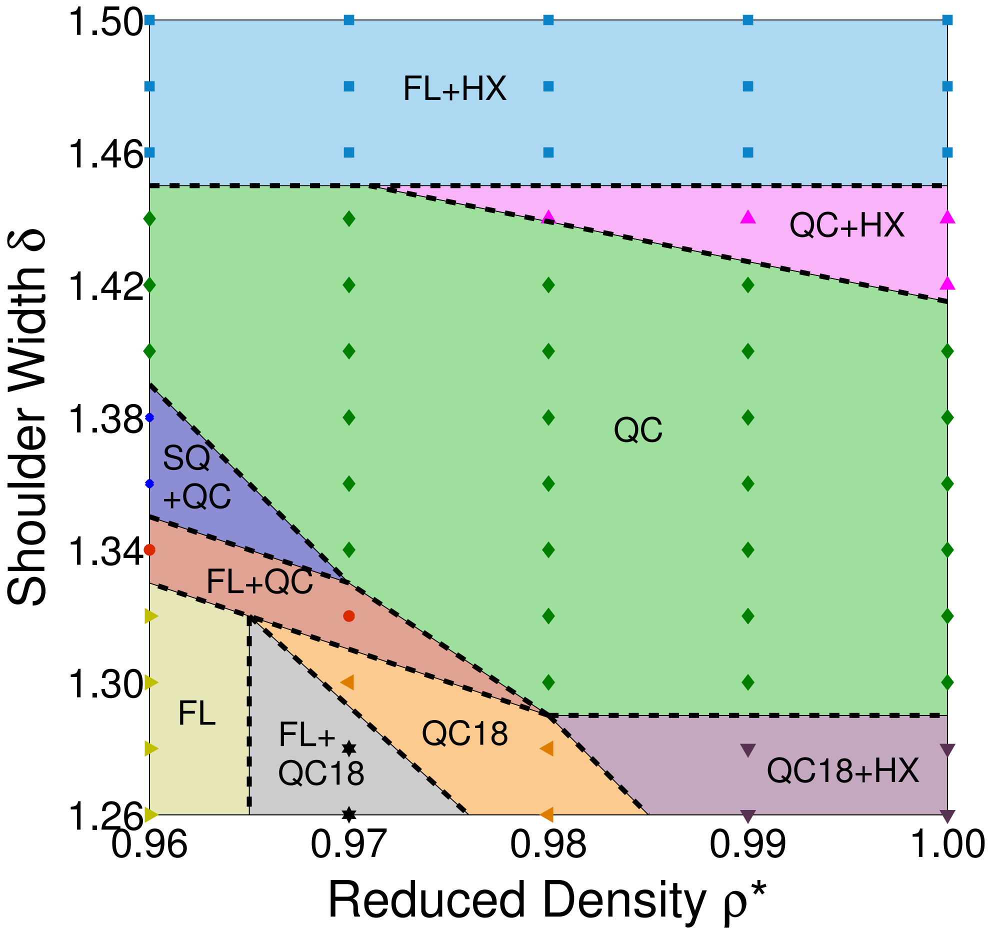

Figure 4.10: State diagram in the shoulder width δ-(reduced) density ρ^* plane for the two-dimensional HCSS system at (reduced) temperature $T^* = 0.28$. All quantities are represented in reduced units as $T^* = k_B T/\varepsilon$ and $\rho^* = N\sigma_{HD}^2/A$. The phases represented are fluid (FL), hexagon (HX), square (SQ), dodecagonal quasicrystal (QC) and octadecagonal quasicrystal (QC18). The symbols denote the state points that were considered in the simulations.

higher densities. Further, we recognise the formation of the dodecagonal quasicrystal QC over a range of shoulder widths $1.30\sigma_{HD} \leq \delta < 1.45\sigma_{HD}$. Lastly, we note that at even lower shoulder widths $\delta \leq 1.30\sigma_{HD}$, we find a 18-fold symmetric quasicrystal (QC18), which was previously reported by Dotera *et al.* at $\delta = 1.27\sigma_{HD}$ [123].

This state diagram is substantiated by the calculation of 4-, 6-, 12-, and 18-fold BOO at each density and shoulder width. This is plotted as four separate surface plots in Figure 4.11. In the χ_4 plot given in Figure 4.11(a), we notice higher values of the order parameter at lower densities and moderate shoulder widths indicating the presence of the SQ phase. Looking at Figure 4.11(b), we confirm higher χ_6 values at higher densities and shoulder widths showing the presence of the HX phase. It is interesting to note that at these conditions of densities and

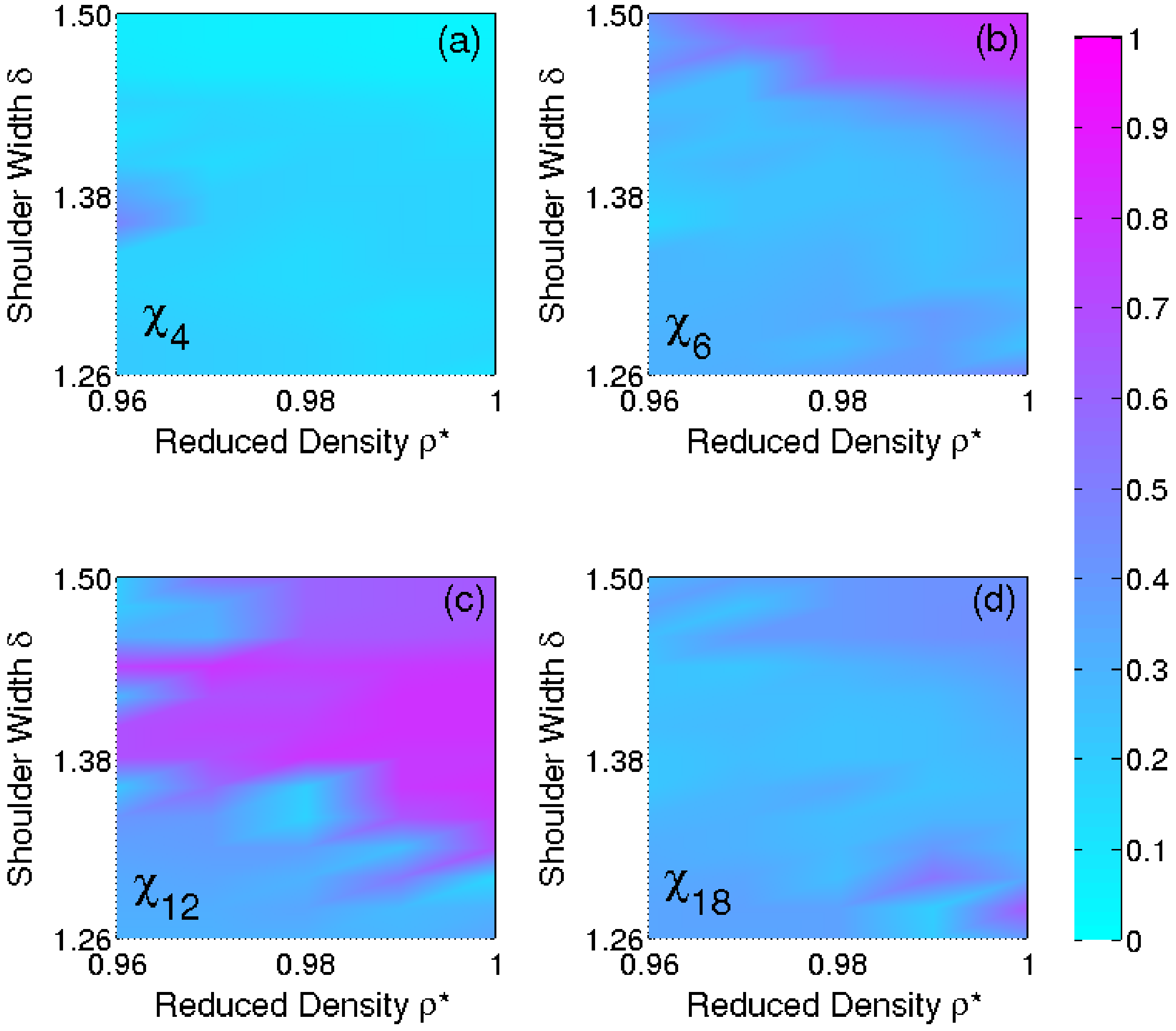

Figure 4.11: Average bond orientational order parameters representing **(a)** square χ_4, **(b)** hexagonal χ_6, **(c)** dodecagonal χ_{12} and **(d)** octadecagonal χ_{18} symmetries as a function of density $\rho^* = N\sigma_{HD}^2/A$ and shoulder width δ at (reduced) temperature $T^* = k_BT/\varepsilon = 0.28$.

shoulder widths where the HX phase is found, the values of χ_6, along with χ_{12} and χ_{18} shown respectively in Figure 4.11(c) and Figure 4.11(d) are in the order $\chi_6 > \chi_{12} > \chi_{18}$. This is because the χ_{12} and χ_{18} are respectively the 2nd and 3rd order terms of χ_6. Thus, when χ_6 is non-zero, the χ_{12} and χ_{18} parameters will also have a non-zero value which decreases with increasing order of symmetry. Lastly, the dominant phase in the lower right quadrant is recognised to be the QC18; while the dodecagonal quasicrystal QC is formed at all densities in the middle range of the shoulder widths considered. In summary, we recognise that the calculations shown here validates the state diagram in Figure 4.10 and shows that the QC is formed over a range of shoulder widths, temperatures and densities.

4.3.3 Effect of the shape of interaction potential

The HCSS system is a minimalistic approach to model the core-corona architecture of colloidal particles. However, the assumption of a constant repulsion through the entire width of the shoulder is not experimentally realisable owing to the non-uniformity of the shape and size of the polymer brushes that surround the solid core. Thus, to account for this non-uniformity, we examine the effect of the shape of the interaction potential without effectively altering the characteristic length scales in this work. In other words, we modify the shape of the interaction potential while keeping the core size, the corona size, and the repulsive strength at the core intact.

We wish to point out here that a similar study was recently reported by Schoberth *et al.* [142] wherein they accounted for an increasing repulsive force in the corona mimicking the entropic interactions of spherical polymer brushes in core-shell micelles. Their assumption, in turn, results in (1) smoothening of both characteristic length scales, viz. the core and corona diameter, and (2) increased repulsive forces near the core. In our present study, we maintain the bounds of the two length scales and the maximum interaction strength near the core at the same values as the HCSS system; i.e. we only modify the shape of the curve in the corona region.

For this study, we make use of three other potentials in addition to the hard-core square-shoulder (HCSS) potential; namely the hard-core linear-ramp (HCLR) potential, the hard-core modified-exponential (HCME) potential, and the hard-core Buckingham or exp-6 (HCE6) potential. The details regarding these potentials are given in Section 4.2. We compare the phases formed in systems with each of these potentials at a range of densities and temperatures. For the HCSS and HCLR potentials, we calculate the respective equilibrium phase diagrams using free-energy calculations; while for the other two potentials namely HCME and HCE6, we plot the state diagrams resulting from simulations in the NVT ensemble at a range of densities and temperatures. The process of mapping out the phase diagram for the HCSS system is explained in Chapter 2 and we follow a similar procedure for the HCLR system.

The calculated phase diagrams and state diagrams are given in Figure 4.12. The potential corresponding to each of these plots along with the outlining square shoulder is shown in the respective insets. In general, we report that the same phases are formed in all these systems. The phases comprise of fluid (FL), square (SQ), low- and high-density hexagonal (LDH, HDH) and dodecagonal quasicrystal (QC). The formation of the hexagonal phase in two density ranges is driven by the presence of two length scales in the interaction potentials such that the interparticle distances in LDH and HDH are at the core and corona diameters, respectively. We make the following observations regarding the QC phase. First, we find that the QC phase is found in all four cases; and second, the temperature of the formation of the QC depends on the interaction potential. The first observation regarding the QC phase in all these systems shows that the shape of the interaction potential inside the corona does not matter for the QC formation as long as the two length scales are uniquely defined. The second observation is related to the temperature range where the QC is formed. We find that the temperature range shifts to lower temperatures

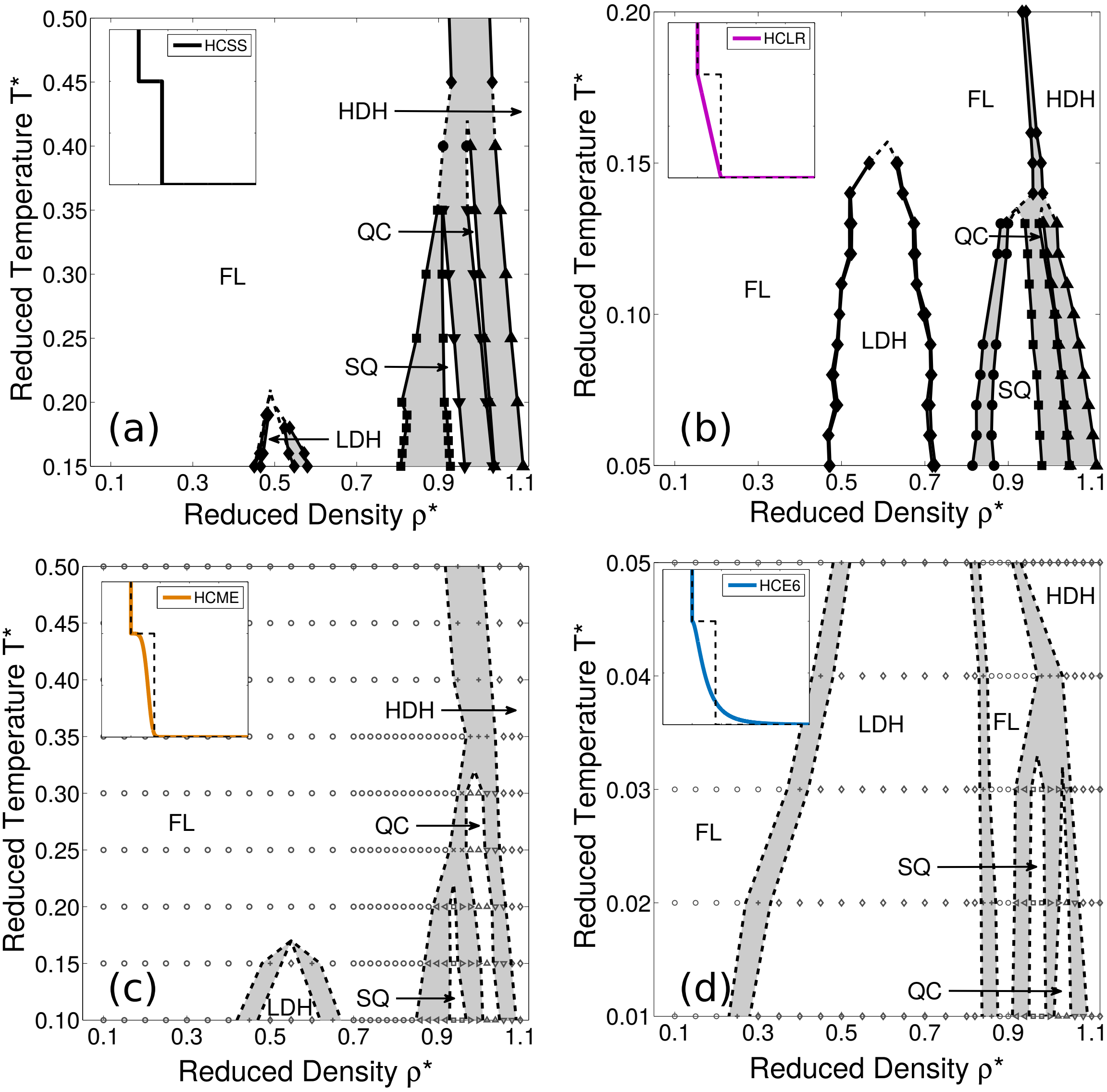

Figure 4.12: Effect of the interaction potential on quasicrystal formation: phase diagram **(a, b)** and state diagram **(c, d)** in the (reduced) temperature-density plane obtained for systems interacting with **(a)** hard-core square shoulder potential (HCSS), **(b)** hard-core linear ramp potential (HCLR), **(c)** hard-core modified exponential potential (HCME), and **(d)** hard-core exp-6 potential (HCE6). Please note that the temperature axis in the figures are different. The reduced units are $T^* = k_B T/\varepsilon$ and $\rho^* = N\sigma_{HD}^2/A$. The phases shown are fluid (FL), low-density hexagonal (LDH), square (SQ), dodecagonal quasicrystal (QC) and high-density hexagonal (HDH). The dotted lines act as guides to the eye, and the open symbols in (c) and (d) denote the state points that were considered in the simulations.

when the interparticle potential becomes less repulsive going from the HCSS to the HCME and the HCLR potential, i.e. the energy penalty for the particles to be in the middle of the corona decreases. Thus, a higher interaction strength (or lower temperature) is required to compensate for this penalty loss. This interaction strength can be tuned by varying the density of polymer brushes in experimental core-corona systems. Supplementary to this energy penalty loss, one also needs to account for the much larger corona size ($\sim 2.50\sigma_{HD}$) in the HCE6 system. This large corona size is a result of the long exponential tail in the potential. This results in a much lower temperature for the formation of the QC in the HCE6 system in comparison to the other three interaction potentials.

In summary, we find that the dodecagonal quasicrystal is formed irrespective of the shape of the interaction potential, as long as the two length scales are maintained. The shape of the potential does affect the temperature range in which the dodecagonal quasicrystal is stable.

4.4 Conclusions

We investigated the formation of a colloidal dodecagonal quasicrystal in a simple model of particles interacting with a potential consisting of a hard core of diameter σ_{HD} and a repulsive square shoulder of diameter $\delta = 1.40\sigma_{HD}$. We scrutinised the formation process using bond order parameters, correlation functions and tiling fractions in the first part of this work. Upon cooling the hexagonal phase at a constant density, we find the nucleation and growth of a fluid phase, resulting in a two-phase coexistence of the fluid and hexagonal phase. Lowering the temperature further, we find that the quasicrystal forms from the fluid phase. Finally, it is worth noting that the different phase transformations encountered during the cooling process, shown in Figures 4.4 - 4.8 , is consistent with the phase diagram presented in Figure 4.3(a).

In the second part of this work, we studied the formation of the dodecagonal quasicrystal for a range of shoulder widths, temperatures and densities. We found that the quasicrystal formation is robust with respect to all three parameters. For example, at a temperature $T^* = 0.28$, we find that the quasicrystal is formed at densities ρ^* between 0.96 and 1.00 and shoulder widths δ between $1.30\sigma_{HD}$ and $1.44\sigma_{HD}$.

In the last part we studied the effect of the shape of the interaction potential on the formation of the quasicrystal. We used four interaction potentials, each of which have two inherent length scales, namely a hard-core potential supplemented with a square shoulder, a linear ramp, a modified exponential, and a Buckingham (exp-6) potential. We observed the formation of a dodecagonal quasicrystal in all these systems. However, the shape of the potential influences the temperature range of the stability regime of the quasicrystal formation.

Our studies provide a comprehensive summary of parameters that can be used to identify quasicrystals in soft-matter systems including bond order parameters, bond correlation functions and tiling calculations. Furthermore, our investigations provide insight into the robustness of the formation of the quasicrystal, which is of considerable importance for performing experimental studies on these systems. This could enable tailoring of experiments to synthesise more quasicrystal-forming systems.

Acknowledgements

A huge thanks to Wessel S. Vlug for performing the calculations for identifying the polygonal tiles. If not for that, I would have spent all my train rides in the past year counting the tiles. I would like to thank Simone Dussi for reading this chapter under a strict time constraint and Guido Avvisati for helping with identifying various interaction potentials. I also thank Weikai Qi for helping with the code for calculating the correlation functions.

5

The curious case of periodic layers of dodecagonal quasicrystal and floating crystals

---

We investigate the behaviour of a system of particles interacting with a hard-core and a repulsive square shoulder potential under the influence of a gravitational field using Event-Driven Brownian Dynamics simulations. We use a fixed square shoulder diameter equal to 1.4 times the hard-core diameter. The parameters in the simulations are chosen such that the pressure at the bottom of the sediment facilitates the formation of phases in accordance with the phase diagram presented in Chapter 3. We indeed observe the formation of layers with dodecagonal, square and hexagonal symmetries at the relevant pressures. In addition, we also observe a re-entrant behaviour exhibited by the fluid phase, engulfing a hexagonal phase, in the sedimentation column. In other words, a floating crystal is formed between the fluid regions.

5.1 Introduction

In case of colloidal suspensions consisting of particles of sizes in the order of micro-meters, the effect of the gravitational force is not negligible. Under these conditions, the gravitational energy and the thermal energy of the colloids are comparable. This leads to the formation of a spatially inhomogeneous suspension in which the density of the particles varies along the height of the suspension. The inhomogeneous distribution of the colloidal particles along the height under the influence of gravity is termed as sedimentation.

As a result of this inhomogeneous density distribution in colloidal suspensions, the particles at the bottom of the sediment can crystallise when they reach a certain critical density. In other words, sedimentation is one of the common manifestations of self-assembly of colloidal particles. Thus, experimentally, sedimentation is regarded as a prevalent tool to extract information regarding the equilibrium phase behaviour of the system. For example, the measured concentration profiles can be inverted to obtain the osmotic equation of state. But, sedimentation processes can also be used the other way around, i.e. they can be used to validate the theoretically calculated equilibrium phase behaviour of a system and thereby, its bulk phase behaviour. For example, a system of hard spheres has been a model system for sedimentation studies. This system exhibits a phase behaviour characterised by a fluid phase at lower densities and a face-centered cubic phase at higher densities. This behaviour, which was earlier theoretically predicted [199], has later been corroborated by sedimentation studies [200].

Sedimentation behaviour of various charged particles [201], mixtures of hard particles [202] and particles of different shapes [203] which result in the formation of periodic crystals has been extensively studied. However, similar studies involving the formation of quasicrystals has not been that extensive. Quasicrystals are solids with long-range orientational order and no periodicity. Their experimental realisations are important in order to extract the advantages of its exceptional properties including the formation of photonic band gaps, as will be shown in Chapter 8. As mentioned above, simulation studies of the sedimentation behaviour of quasicrystals can be a guiding star to their experimental self-assembly. In fact, experimental [204–207] and simulation [208, 209] studies have been carried out to study the ordering of atoms on metallic quasicrystalline surfaces. However, the soft-matter counterpart of metallic quasicrystals have not come far. Although, recently, a simulation study involving the growth of colloidal particles interacting with a screened potential has been shown to form multiple quasicrystalline layers [210]. However, no such experimental realisations have been reported till now.

We wish to combine the above two propositions, i.e. sedimentation as a tool to study the phase behaviour and the formation of layers of quasicrystal by sedimentation. In the previous chapters, i.e. Chapters 3 and 4, we have theoretically calculated the phase diagram of a two-dimensional system of particles interacting with a hard-core and repulsive square shoulder potential. At a shoulder width of 1.4 times the hard core diameter, we find a stable random-tiling dodecagonal quasicrystal. We intend to explore the formation of this quasicrystal by sedimentation, which could pave the way for its experimental realisation.

This chapter is organised as follows. In Section 5.2, we present the simulation and analysis methods used. In Section 5.3, we individually discuss the formation of layers with various symmetries and finally we present the conclusions and the direction of future studies in Section 5.4.

5.2 Methods

We first explain the simulation model and computational methods used for this study in Section 5.2.1, and then give an account of the analysis methods in Section 5.2.2.

5.2.1 Computational methodology

We perform Event-Driven Brownian Dynamics (EDBD) simulations of N spherical particles of diameter σ_{HS} and buoyant mass m interacting with the HCSS potential in the NVT ensemble. The HCSS potential can be written as a sum of a hard-sphere potential $V_{\mathrm{HS}}(r)$ and a square-shoulder potential $V_{\mathrm{SS}}(r)$, i.e.

$$V_{\mathrm{HCSS}}(r) = V_{\mathrm{HS}}(r) + V_{\mathrm{SS}}(r), \tag{5.1}$$

where

$$V_{\mathrm{HS}}(r) = \left\{ \begin{array}{ll} \infty, & r \leq \sigma_{HS} \\ 0, & r > \sigma_{HS} \end{array} \right. , \tag{5.2}$$

and

$$V_{\mathrm{SS}}(r) = \left\{ \begin{array}{ll} \varepsilon, & r \leq \delta \\ 0, & r > \delta \end{array} \right. , \tag{5.3}$$

where r is the interparticle centre-of-mass distance, and $\varepsilon > 0$ is the height of the square shoulder.

In the EDBD method, a sequence of collision events involving only two particles at any given instant is computed. During the simulation, the velocities of the particles are randomly adjusted at regular intervals Δt as

$$\mathbf{v}(t+\Delta t) = \alpha_t \mathbf{v}(t) + \beta_t \mathbf{v}_R(t), \tag{5.4}$$

where $\mathbf{v}(t)$ and $\mathbf{v}(t+\Delta t)$ are respectively the velocities of the particles before and after the stochastic velocity adjustment, $\mathbf{v}_R(t)$ is a 3-D Gaussian variable with mean of 0 and variance of $k_B T/m$, with k_B the Boltzmann constant and T the temperature. Further, α_t has a value $1/\sqrt{2}$ with a probability $\nu\Delta t$ and 1 otherwise. The temperature is kept constant by setting $\beta_t = \sqrt{1-\alpha_t^2}$. In accordance to previous EDBD simulations [155, 156], we set ν to $10\tau_{MD}^{-1}$ and Δt to $0.01\tau_{MD}$, where τ_{MD} is the unit of time of an event-driven Molecular Dynamics simulation given as $\tau_{MD} = \sqrt{m/k_B T}\,\sigma_{HS}$.

The simulation box of volume V has a square cross-section of area A and is elongated in the z-direction. Periodic boundary conditions are applied along the cross section; while in the elongated direction, the particles are confined between two smooth walls at $z = 0$ and $z = H$, where H is the height of the sedimentation column. The height H is chosen such that the density at $z = (H - \sigma_{HS}/2)$ is sufficiently small, which allows us to consider the system to be infinitely long in the z-direction. We perform simulations starting with a non-overlapping isotropic fluid state filling the entire sedimentation column with packing fraction $\eta = 0.01$. To mimic sedimentation experiments, these particles are further subjected to a gravitational field, which is expressed as an external potential $\phi(z)$ written as

$$\phi(z) = \left\{ \begin{array}{ll} mgz, & \sigma_{HS}/2 \leq z \leq H - \sigma_{HS}/2 \\ \infty, & \text{otherwise} \end{array} \right. , \tag{5.5}$$

where g is the acceleration due to gravity and z is the vertical coordinate of the particle. The effect of the gravitational field on the particles is quantified in terms of the gravitational Peclet number defined as $g^* = mg\sigma_{HS}/k_BT$.

In this work, we scrutinise the kinetic formation of the thermodynamic stable phases described for the two-dimensional HCSS system with $\delta = 1.40\sigma_{HD}$, where σ_{HD} is the hard-disk diameter, given in Chapters 3 and 4. To do so, we perform simulations such that the pressure measured at the bottom of the sedimentation column, i.e. at $z = 0$, corresponds to the region of stability of a particular phase. This pressure is calculated as $\beta P(z=0)\sigma^3 = g^*.\rho_A^*$, where ρ_A^* is the mean area defined as the number of particles at the bottom of the sample $\rho_A^* = N\sigma_{HS}^2/A$.

The phases considered in this study are a dodecagonal quasicrystal, square, low-density hexagonal and fluid phases. We especially focus on the possibility of the formation of the quasicrystal, and thus, consider the cross-section to be squares with sides of length $58\sigma_{HS}$, which can accommodate a random-tiling dodecagonal quasicrystal of density $\rho^* = 1.07$. The list of parameters used to simulate the different phases is given in Table 5.1. The corresponding values of pressures at the bottom $\beta P(z=0)$ are marked in the phase diagram given in Figure 5.1. As a supplementary study, we use two parameter sets having different Peclet numbers to simulate the quasicrystal. A higher value of Peclet number results in a condition of high settling rate of the particles, i.e. the particles do not have enough time to rearrange and equilibrate, and vice versa. Using systems with different Peclet numbers, we can study the effect of the settling rate on the formation of the quasicrystal.

Table 5.1: System parameters used in the EDBD simulations of a HCSS system with $\delta = 1.40\sigma_{HS}$ under gravity.

N	k_BT	mg	g^*	$\beta P(z=0)\sigma^3$	Stable phase
5×10^4	0.25	0.50	2.00	30.0	Quasicrystal
2×10^4	0.25	1.26	5.00	30.0	Quasicrystal
2×10^4	0.25	1.00	4.00	23.8	Square
5×10^4	0.15	0.10	0.67	10.0	Low-density hexagonal
1×10^5	0.15	0.10	0.67	20.0	Fluid

5.2.2 Structural analysis

In order to characterise the different phases, we employ an analysis method that is two-dimensional in nature since this study is based on the phase behaviour of the two-dimensional HCSS system, and correspondingly, we find that the phases observed in the sedimentation column have a layered structure. Specifically, we first identify different layers of the sediment and then carry out the following analysis procedure in these layers. We construct the polygonal tiling of the layer and calculate the two-dimensional m-fold bond orientational order parameter (BOO) of each particle j in layer l, $\chi_m^l(j)$, and the average BOO of each layer χ_m^l.

The polygonal tiling of each layer is constructed by drawing bonds between the neighbouring particles of each particle j, which are at a centre-of-mass distance smaller than the square shoulder diameter δ from particle j.

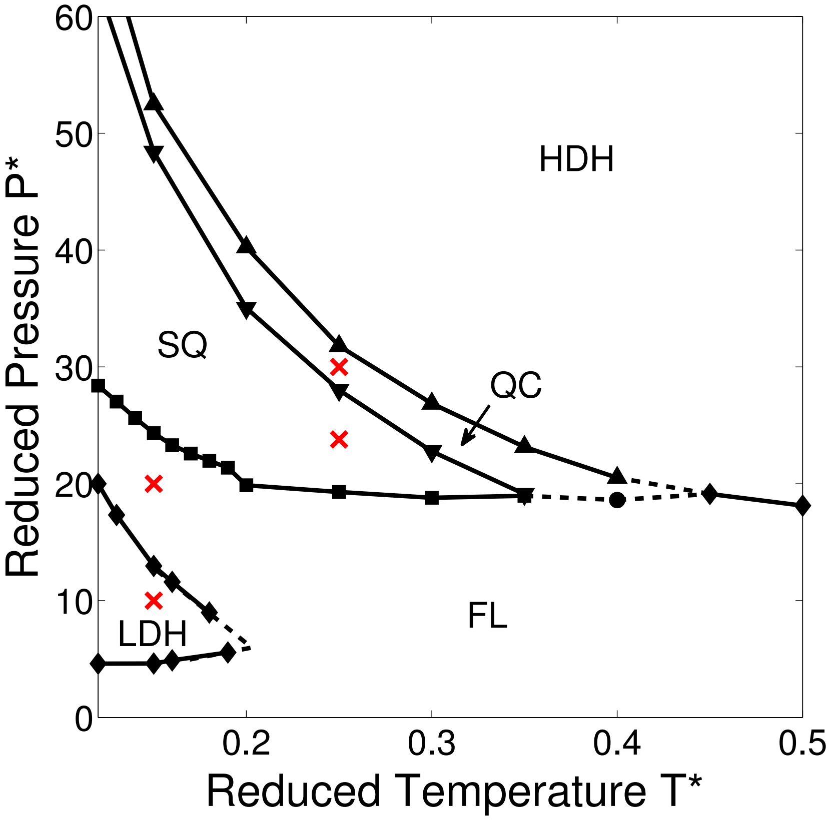

Figure 5.1: Phase diagram in the (reduced) pressure-temperature plane for a two-dimensional HCSS system with shoulder width $\delta = 1.40\sigma_{HD}$. The reduced quantities are defined as $P^* = \beta P \sigma_{HD}^2/A$ and $T^* = k_B T/\varepsilon$. The phases marked are fluid (FL), low-density hexagonal (LDH), square (SQ), dodecagonal quasicrystal (QC) and high-density hexagonal (HDH). The crosses denote the state points corresponding to the pressures at the bottom of the sediment.

We, then, calculate the m-fold BOO of each particle j in layer l as

$$\chi_m^l(j) = \left| \frac{1}{N_B(j)} \sum_{k=1}^{N_B(j)} \exp(im\theta_{\mathbf{r}_{jk}}) \right|^2 , \tag{5.6}$$

where m is the symmetry of interest, $\mathbf{r}_{jk}$ is the centre-of-mass distance vector between two neighbours j and k, $\theta_{\mathbf{r}_{jk}}$ is the angle between $\mathbf{r}_{jk}$ and an arbitrary axis, and $N_B(j)$ is the number of neighbours of particle j in the same layer. For each particle j, we calculate $\chi_4^l(j)$, $\chi_6^l(j)$, and $\chi_{12}^l(j)$ respectively representing square, hexagonal and dodecagonal symmetries.

The particles are classified based on their BOO according to the method given in Table 5.2. We consider a particle to be fluid-like if each of the three $\chi_m^l(j)$ is less than 0.5. On the other hand, if each of $\chi_m^l(j)$ is greater than 0.5, then a particle is said to have symmetry $m1$ if $\chi_{m1}^l(j)$ is greater than the other two, namely $\chi_{m2}^l(j)$ and $\chi_{m3}^l(j)$. Further, we identify and colour the particles according to the following scheme: particles of square symmetry in purple, those of hexagonal in green, dodecagonal in red and fluid-like in orange as shown in Figure 5.2.

Table 5.2: Method of classification of particle j belonging to layer l according to its bond orientational order (BOO) $\chi_m^l(j)$.

Symmetry	BOO conditions	Colour scheme
Fluid/Other (OT)	$\chi_4^l(j), \chi_6^l(j), \chi_{12}^l(j) < 0.5$	orange
Crystal	$\chi_4^l(j), \chi_6^l(j), \chi_{12}^l(j) > 0.5$	
- Square (SQ)	$\chi_4^l(j) > \chi_6^l(j), \chi_{12}^l(j)$	purple
- Hexagonal (HX)	$\chi_6^l(j) > \chi_4^l(j), \chi_{12}^l(j)$	green
- Dodecagonal (QC)	$\chi_{12}^l(j) > \chi_4^l(j), \chi_6^l(j)$	red

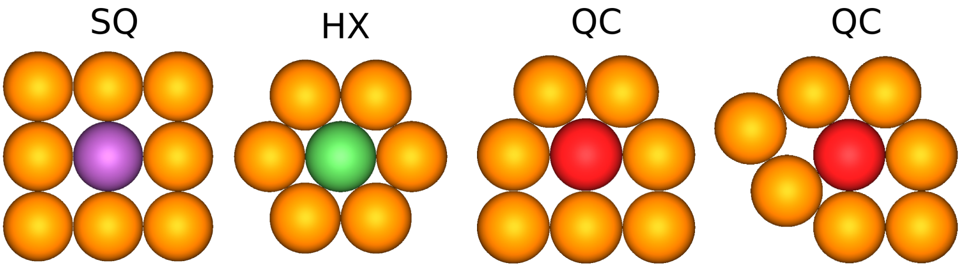

Figure 5.2: Colour scheme for classes of particles based on the BOO classification described in Table 5.2.

After calculating the BOO of each particle, the average BOO of each layer is then evaluated as [164]

$$\chi_m^l = \frac{1}{N_l} \sum_{j=1}^{N_l} \chi_m^l(j), \tag{5.7}$$

where N_l is the number of particles in each layer.

5.3 Results and discussion

In this section, we consider individually the different sedimentation simulations carried out to obtain the various stable phases calculated for the two-dimensional HCSS system. Due to the computationally expensive nature of these calculations, not all the simulations have attained equilibrium. Here, we present the results obtained so far.

5.3.1 Formation of layers with dodecagonal symmetry

We start with the formation of layers with dodecagonal symmetry. In this section, we present the sedimentation simulations using two different Peclet numbers in order to assess the effect of the settling rate on the formation of the quasicrystal. We first compare the formation of the quasicrystal formed in these simulations. We then analyse the driving force behind the formation of these layers. Finally, we review the validity of the phase diagram given in Figure 5.1 by comparing the phases formed in the sedimentation column. Of special interest is the dodecagonal quasicrystal (QC) which, as seen in the phase diagram, is sandwiched between two periodic crystal phases with square and hexagonal symmetries. Thus, it is interesting to note if and how the interfaces between the quasicrystal and the periodic crystals are formed in the sedimentation column.

We first present a typical configuration of the sediment forming quasicrystalline layers in Figure 5.3. The panels on the left correspond to simulations with a Peclet number $g^* = 5.0$ and those on the right are obtained for $g^* = 2.0$. The particles here are coloured according to the convention explained in Figure 5.2. We notice the formation of about two quasicrystalline layers for $g^* = 5.0$ and about four for $g^* = 2.0$. This difference in the number of layers is due to a difference in height range that corresponds to the pressure range of the stable quasicrystal phase. This height range decreases with increasing g^*. Additionally, we observe that most of the particles seen in these layers are coloured either in purple or red which, respectively, represent square or dodecagonal symmetries. Therefore, we follow the dynamics of the formation of these layers by calculating the BOO χ_4^l and χ_{12}^l of each layer as a function of time. The time evolution of χ_4^l is given in the middle panel in Figure 5.3 and that of χ_{12}^l is given at the bottom. In these time evolution heat maps, the time scale t/τ_{MD} is plotted on the horizontal axis and the layer number is plotted along the vertical axis.

We make the following observations from these plots: (1) In both cases, the value of χ_{12}^l is higher than that of χ_4^l, which confirms the dodecagonal symmetry of these layers. (2) With increasing time, we find that the fraction of fluid in the sedimentation column decreases, as seen by the receding blue region in these plots. Alternatively, this means that more crystalline layers are formed with time. (3) The value of χ_{12}^l at a given time decreases as we go up in the sediment indicating that the layers on the top are more fluid-like than the bottom layer. (4) Finally, we see that the χ_{12}^l obtained for the sediment at higher Peclet number is larger than that at lower Peclet number. This is counter-intuitive as this suggests that faster settling of the particles result in the formation of a better quasicrystal.

We investigate this further by plotting the polygonal tiling constructed for the bottom two layers as a function of time for both the sediments. The top view of these tilings is given in Figure 5.4 for $g^* = 5.0$ and in Figure 5.5 for $g^* = 2.0$. Two striking features are conspicuous from these polygonal tilings. Firstly, there are large portions of connected square tilings in the sediment obtained for the lower Peclet number, while the square tilings are more uniformly distributed in the case of the high Peclet number sediment. Secondly, the position of the tiles in the first and second layers seem to be on top of each other. Let us now evaluate each of these observations separately.

Firstly, we analyse the tilings and quantify the square tiles by calculating the ratio of areas occupied by the square tiles to that of the triangle tiles. This also relates to the square-triangle tiling description of a dodecagonal quasicrystal, where the maximum entropy of the tiling corresponds to equal areas of squares and triangles. In the current sediments, we find that the ratio of the areas of squares to triangles for $g^* = 2.0$ is 1.40 ± 0.05 and for $g^* = 5.0$ is 1.15 ± 0.03. In other words, in both cases, there are more squares formed than in an ideal dodecagonal tiling. This excess of squares is larger for the low Peclet number sediment. This can be explained as follows. A lower Peclet number refers to a lower rate of sedimentation, which allows for the particles to rearrange. The pressure at the bottom of the sample increases slowly since the beginning of the sedimentation simulation, as more and more particles descend through the column. This means that the pressure at the bottom layer first reaches the value where a square phase is found to be stable. Thus, nuclei consisting of particles with square symmetry start to form. This can be observed in the snapshot of the second layer at $t/\tau_{MD} = 60$ at both Peclet numbers. However, in case of the sediment with lower Peclet numbers, these nuclei have enough time to aggregate and thus, start forming larger square structures. On the other hand, the square nuclei of the fast settling sediment does not have enough time to rearrange and thus, are spread all over

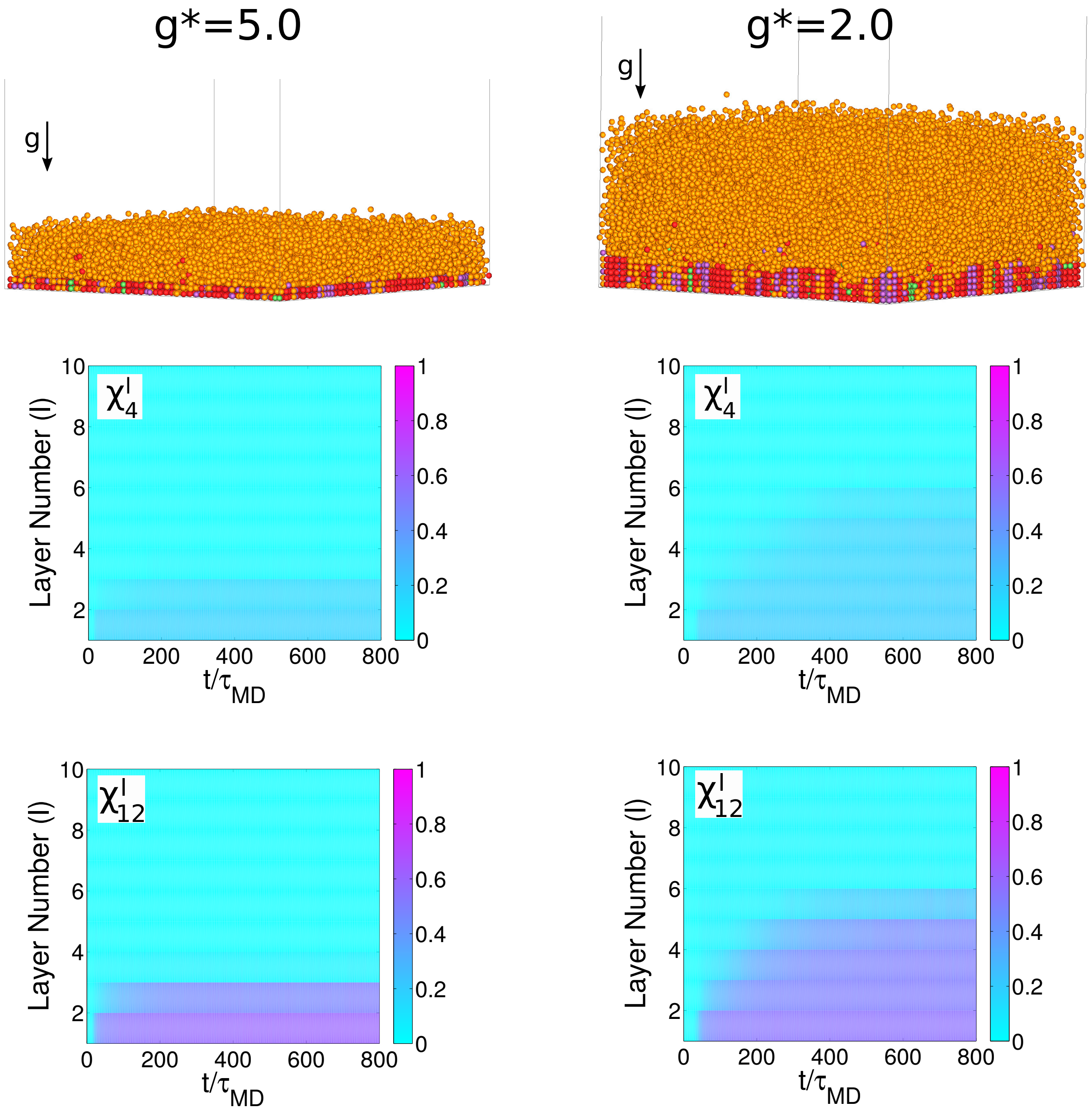

Figure 5.3: Comparison of the quasicrystal (QC) sediment formed for Peclet numbers $g^* = 5.0$ **(left)** and 2.0 **(right)** using side view of a configuration of the sedimentation column obtained at $t/\tau_{MD} = 800$ **(top)**. The particles are coloured according to their individual BOO: quasicrystal (red), square (purple), hexagonal (green), and fluid (orange). The m-fold BOO of each layer with time calculated for symmetries $m = 4$ **(middle)** and 12 **(bottom)** showing, respectively, the formation of layers with square and dodecagonal symmetries.

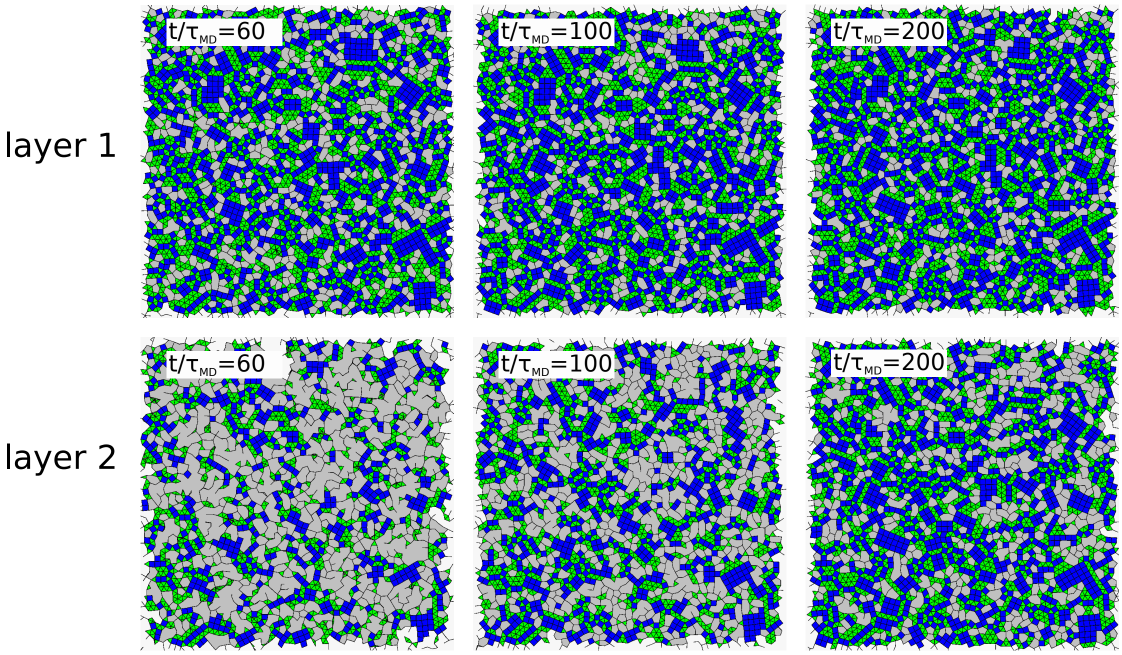

Figure 5.4: Polygonal tilings as obtained from particle configurations of the first **(top)** and second **(bottom)** layers of the QC sediment for Peclet number $g^* = 5.0$ showing the formation of the quasicrystal for varying times t/τ_{MD} as labelled. The triangle, square and defect tiles are respectively coloured in blue, green and grey.

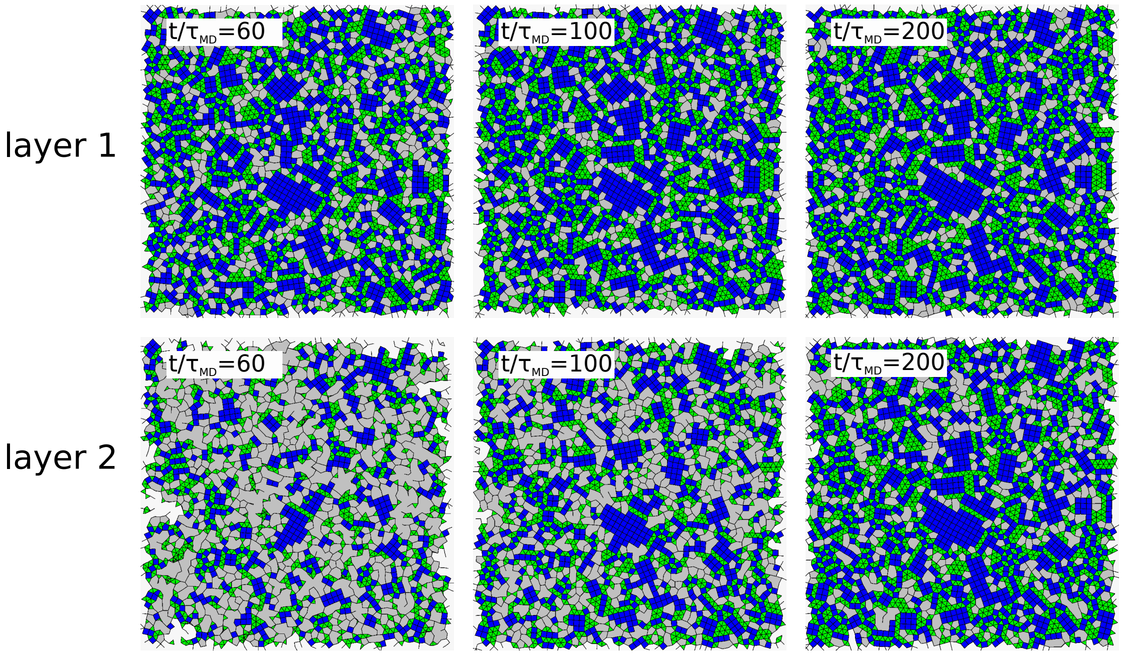

Figure 5.5: Polygonal tilings as obtained from particle configurations of the first **(top)** and second **(bottom)** layers of the QC sediment for Peclet number $g^* = 2.0$ showing the formation of the quasicrystal for varying times t/τ_{MD} as labelled. The triangle, square and defect tiles are respectively coloured in blue, green and grey.

the area. Also, a larger settling rate means that the pressure corresponding to the formation of the quasicrystal is reached faster at the bottom of the sediment. This again means that lesser amount of square tiles are formed in the sediment with higher Peclet number. Because of these reasons, the sediment with a high Peclet number results in the formation of lesser number of square tiles and also lower aggregation of these tiles than the slow settling sediment.

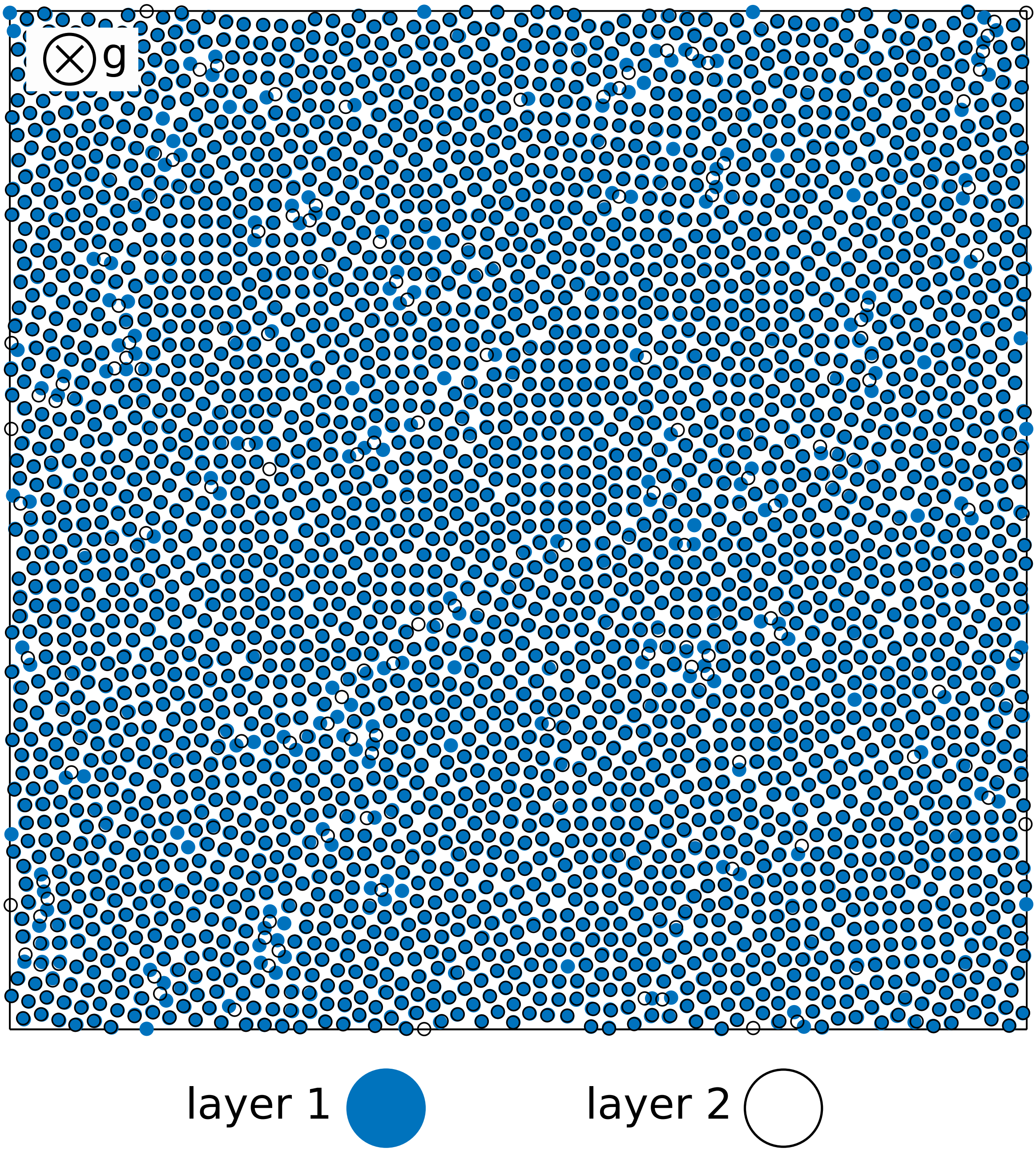

Figure 5.6: Top view of the center-of-mass of particle configurations of the first and second layers obtained for the QC sediment with Peclet number $g^* = 5.0$ at $t/\tau_{MD} = 800$. The particles in the bottom layer are plotted as filled circles in blue and the particles in the top layer are represented as open black circles. The gravitational field points into the plane of the paper as marked in the top-left corner.

Now, let us examine the observation regarding the position of the tiles of the second layer directly on top of the first layer. This, in essence, refers to the formation of quasicrystal layers which are periodic in the third direction. To assess this, we show the top view of the particles of the first and second layers obtained for the fast settling sediment in Figure 5.6. Here, the particles in the first layer are represented as filled blue circles, while those of the second layer are represented as open black circles. In the figure, we observe that a majority of the blue particles are enclosed in a black circle. In other words, the position of the particles of the second layer are on top of the first layer, which confirms that these structures are periodic in the third dimension. This leads us to the question of why do the particles of the second layer not position themselves in the voids of the particles of the bottom layer, as is expected from simulations involving gravitational fields?

The answer to this question lies in the fact that the interaction potential between the particles is purely repulsive. We explain this further by using a schematic description in Figure 5.7. The colour coding of the particles is the same as described above; the particles in the first layer are represented as filled blue circles, while those of the second layer are represented as open black circles. On the top we represent the situation where the particles of the second layer fall in the voids of the particles of the first layer. The front view of the sediment is shown on the left and the top view on the right. The present case of the periodic layers is shown at the bottom. First, let us look at the scenario with alternating layers. In this case, we see that each particle in the second layer, in addition to its nearest neighbour in the second layer, has three neighbours in

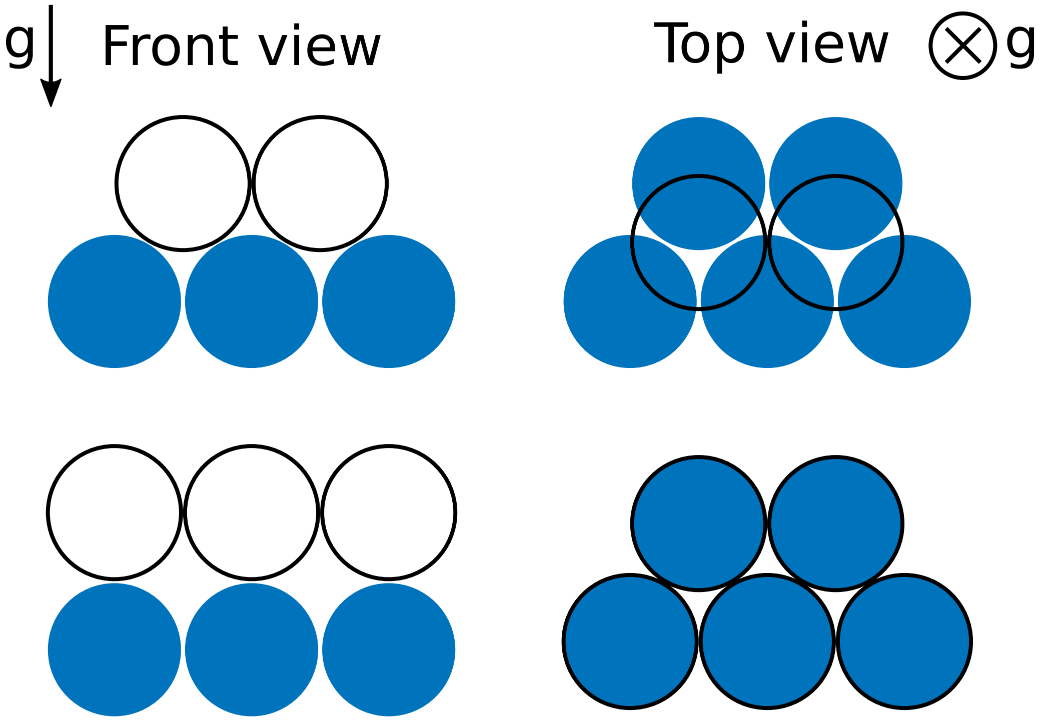

Figure 5.7: Schematic representation of the energetic driving force behind the formation of layers with particles on top of each other. The particles in the bottom layer are plotted as filled circles in blue and the particles in the top layer are represented as open black circles. The direction of the gravitational field in each case in also marked on the top.

the first layer. In contrast, in case of the present situation of periodic layers, each particle of the second layer has only a single neighbouring particle in the bottom layer. The same also applies for the third layer on top of the second, thereby doubling the number of neighbours of each particle. This reduction in the number of neighbours is translated as a reduction in the energy of the particle and thus, of the entire system. This configuration is favoured, if this reduction in energy is more than the increase in potential energy of the particle for being at a higher position in the sedimentation column, i.e. at a higher position on top of a particle instead of a lower position in the void. This happens to be the case in our simulations, which leads to the formation of these periodic layers.

Finally, we proceed to the validation of the phase diagram in terms of the phases formed along the height of the sedimentation column, which corresponds to a decrease in pressure. To analyse this, we plot the pressure and density profiles along the height of the sedimentation column calculated for both Peclet numbers in Figure 5.8. The pressure and density profiles corresponding to the high Peclet number is on the left and that of the low Peclet number on the right. In these plots, we explicitly mark the pressure boundaries denoting the stability of each phase as obtained from the phase diagram. From the density profiles, we observe that the formation of two crystalline layers at high Peclet number and five at low Peclet number. Beyond this pressure, we find the presence of an isotropic fluid, which agrees well with the phase diagram prediction. However, the puzzling part is the absence of the square phase.

From the density plots, we see that the crystalline layers are formed in the sediment for pressures corresponding to the stable QC or SQ regime in the phase diagram. However, all the layers formed in the sediment exhibit dodecagonal symmetry, which leads to the question, why are layers of square symmetry not formed? This could be because of either one of the following reasons: (1) The formation of an interface between the quasicrystal and the periodic

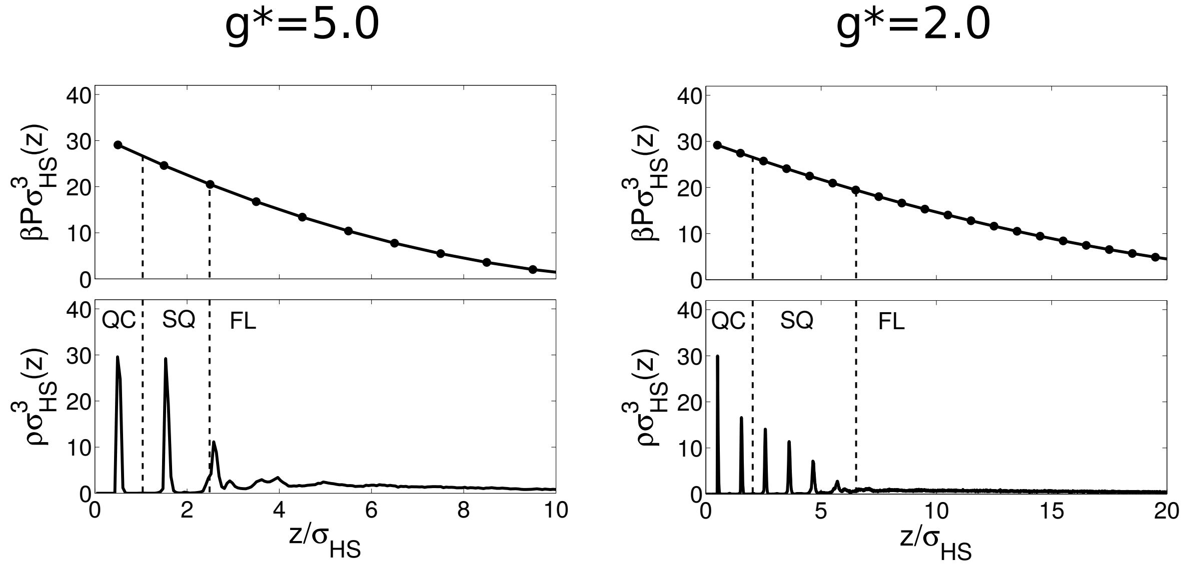

Figure 5.8: Pressure **(top)** and density **(bottom)** profiles calculated for the QC sedimentation column for Peclet numbers $g^* = 5.0$ **(left)** and 2.0 **(right)** at $t/\tau_{MD} = 800$. The stability regions of the dodecagonal quasicrystal (QC), square (SQ) and fluid (FL) phases in terms of the reduced pressure $P^* = \beta P \sigma_{HD}^2$ as taken from Figure 5.1 are marked.

crystal might not be energetically favourable, or (2) during sedimentation, it might be easier for the particles to settle on top of the particles below because of energetic reasons as explained previously. In addition, a higher settling rate could also contribute to it, i.e. the particles belonging to the top layers do not have sufficient time to rearrange into a square lattice. Also, for the particles to arrange into a square lattice on top of a quasicrystal would mean that the particles of the square layer would fall in the voids of the underlying quasicrystal layer. This again causes an increase in potential energy. Thus, it is possible that these energetic constraints outweigh those for the formation of a square lattice thereby leading to the formation of only layers with quasicrystal symmetry in the sedimentation column. Additionally, it is good to mention here that in the free-energy calculations performed to map out the phase diagram, a defect-free quasicrystal structure was used. However, it might be possible that the kinetic formation of the quasicrystal with defects precedes that of the defect-free structure. This could also contribute to the formation of the quasicrystal at lower pressures.

5.3.2 Formation of layers with square symmetry

At the end of the previous section, we found that it is not feasible for a layer with square symmetry to form on top of a layer with dodecagonal symmetry. Does that mean that the formation of layers with square symmetry is never possible in this system? We address the formation of layers with square symmetry in this section. For this, we first perform sedimentation simulations using the parameters promoting the formation of a square phase as given in Table 5.1, and

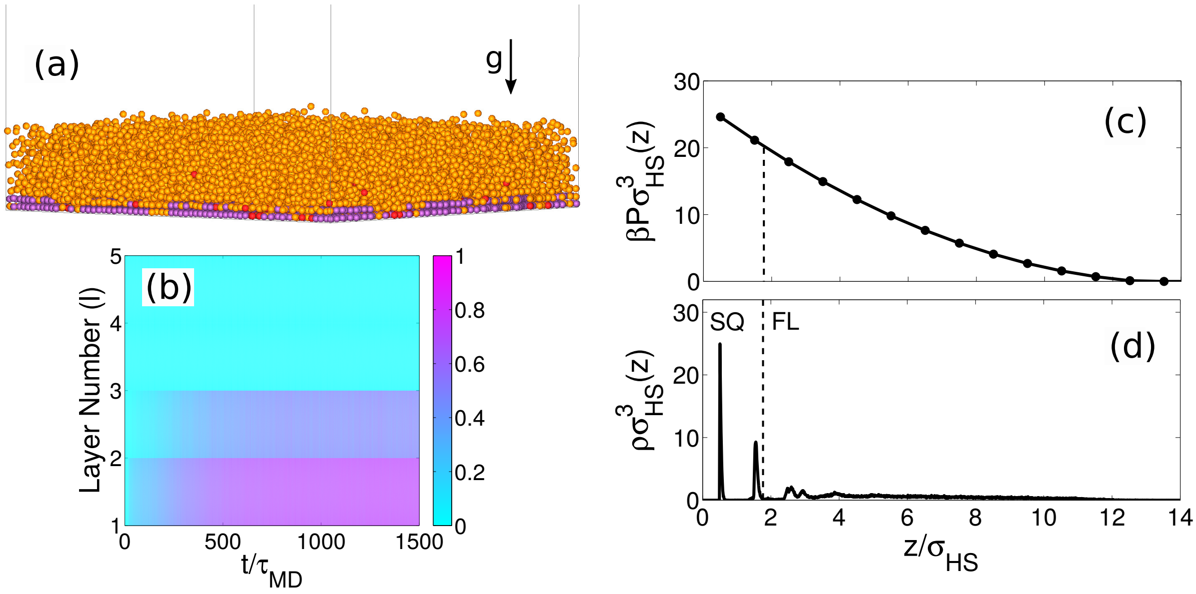

Figure 5.9: **(a)** Side view of a configuration of the SQ sedimentation column obtained at $t/\tau_{MD} = 1500$. The particles are coloured according to their individual BOO: quasicrystal (red), square (purple), hexagon (green), and fluid (orange). **(b)** The BOO χ_4^l of each layer as a function of time showing the formation of layers with square symmetry. **(c)** Pressure and **(d)** density profiles calculated for the sedimentation column at $t/\tau_{MD} = 1500$. The stability regions of square (SQ) and fluid (FL) phases in terms of reduced pressure $P^* = \beta P\sigma_{HD}^2$ as taken from Figure 5.1 are marked.

then employ the same analysis methods as those used for studying the quasicrystal formation in the sediment.

First, we show a typical configuration of the sedimentation column obtained at $t/\tau_{MD} = 1500$ in Figure 5.9(a). The particles are coloured according to the convention in Figure 5.2 with particles possessing square symmetry in purple. As can be noticed in the figure, two layers at the bottom of the column have a large concentration of purple coloured particles, denoting the formation of layers with square symmetry. This is further confirmed by the evolution of the BOO χ_4^l of the bottom two layers to values close to one, as given in Figure 5.9(b). Further, we plot the pressure and density profiles along the sedimentation column respectively in Figure 5.9(c) and Figure 5.9(d). From these, we see that the formation of two layers with square symmetry agrees well with the respective phase diagram.

We then follow the dynamics of the formation of these layers by analysing the snapshots of the bottom two layers as a function of time. The top views of these layers is given in Figure 5.10. Similar to the behaviour during the nascent time scales in the QC sediment seen previously in Figures 5.4 and 5.5, the crystal formation in the bottom layer begins by the formation of small crystalline domains of particles with square symmetry ($t/\tau_{MD} = 100$). These crystalline domains coalesce with time and form larger grains separated by grain boundaries consisting of fluid-like particles or particles with dodecagonal symmetry ($t/\tau_{MD} = 1000$). Finally, these grain boundaries anneal out with time ($t/\tau_{MD} = 1500$). Obviously, the settling rate plays an important role in the annealing process. In the present scenario, we find that most of the second layer is formed before the grain boundaries in the bottom layer are annealed out. Thus, these grain

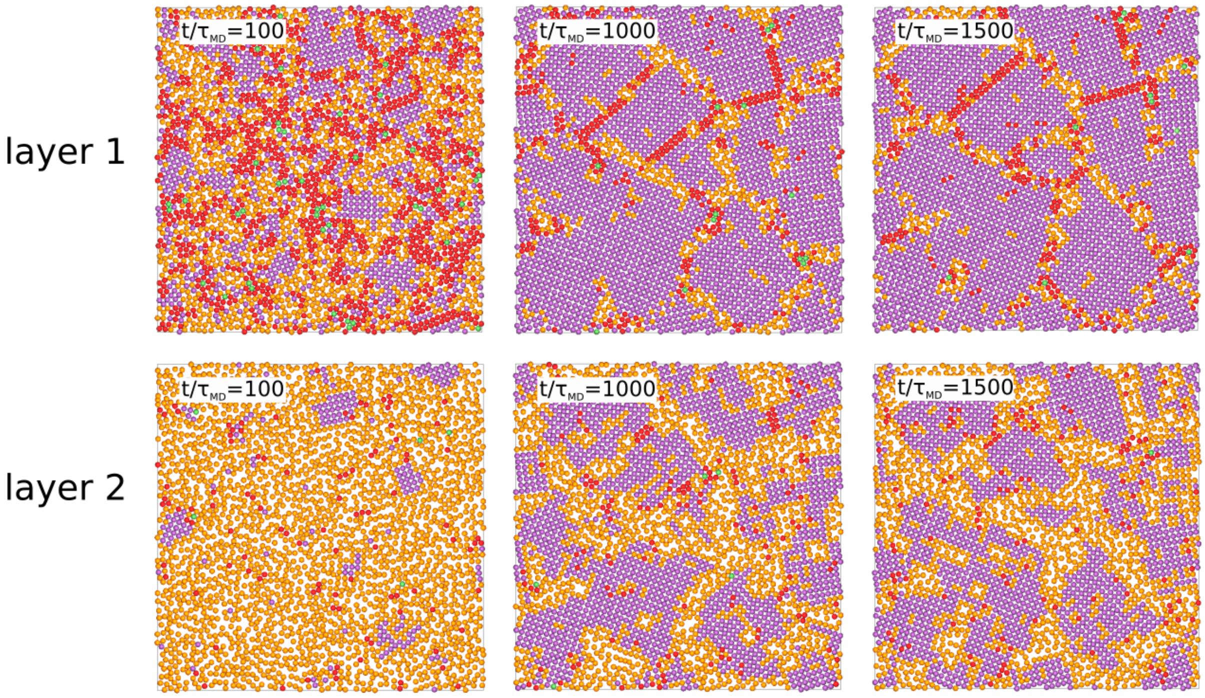

Figure 5.10: Typical configurations showing the top view of the first **(top)** and second **(bottom)** layers of the SQ sediment for varying times t/τ_{MD} as labelled. The particles are coloured according to their individual BOO, namely quasicrystal (red), square (purple), hexagonal (green), and fluid (orange).

boundaries remain till the end of our simulation. Additionally, we observe that this structure also consists of periodic layers, with the particles of the second layer lying on top of each other.

5.3.3 Formation of (suspended) layers with hexagonal symmetry

One of the peculiar features exhibited by the HCSS system is the formation of a low-density hexagonal phase, where the particles are separated by a distance equal to the square shoulder diameter δ. The formation of this phase induces a re-entrant behaviour of the fluid phase. Our objective in this section is two-fold. We attempt to (1) demonstrate the formation of layers

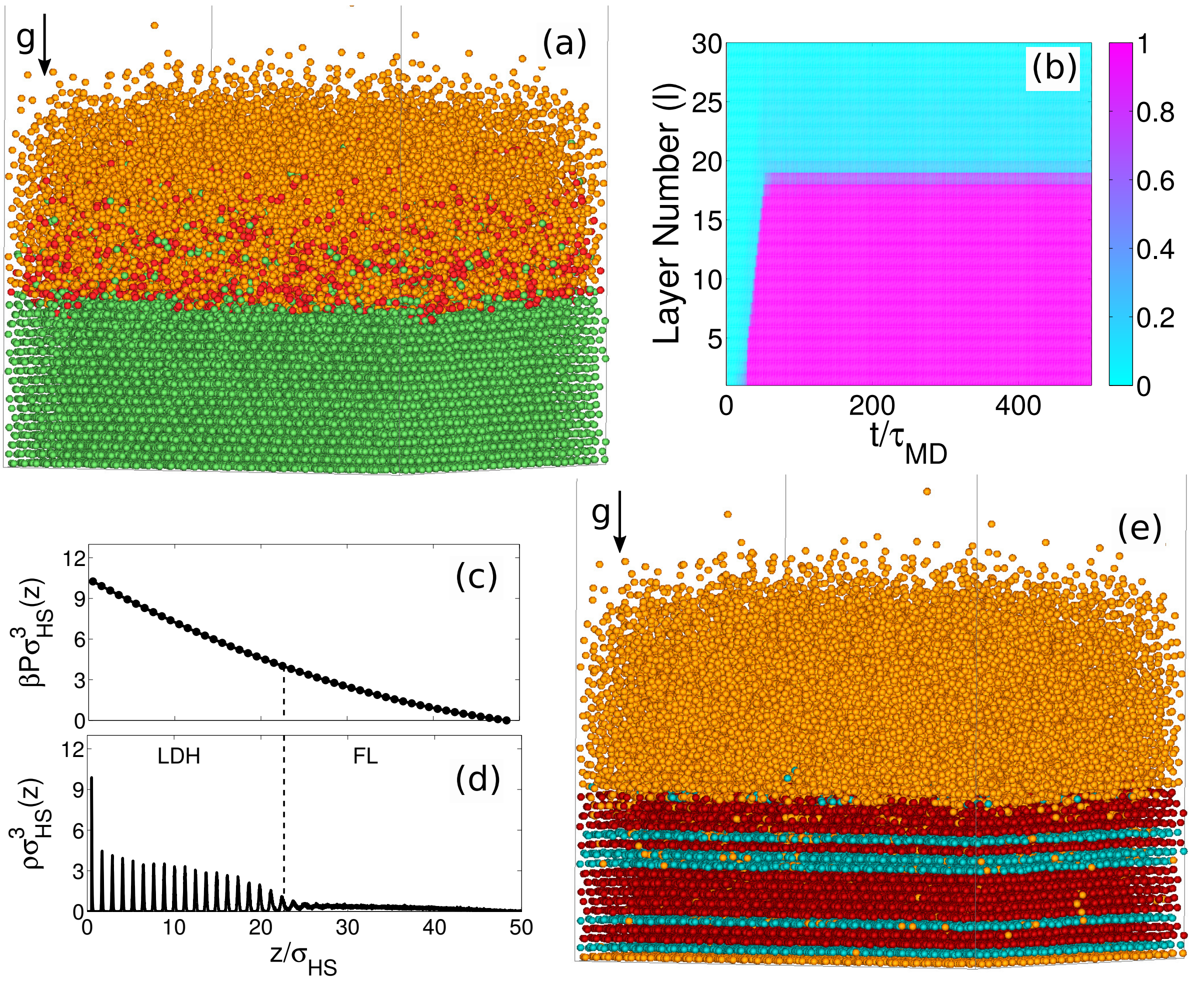

Figure 5.11: **(a)** Side view of a configuration of the low-density hexagonal (LDH) sedimentation column obtained at $t/\tau_{MD} = 500$. The particles are coloured according to their individual BOO: quasicrystal (red), square (purple), hexagon (green), and fluid (orange). **(b)** The BOO χ_6^l of each layer as a function of time showing the formation of layers with hexagonal symmetry. **(c)** Pressure and **(d)** density profiles calculated along the height of the sedimentation column. The stability regions of low-density hexagonal (LDH) and fluid (FL) phases in terms of reduced pressure $P^* = \beta P \sigma_{HD}^2$ as taken from Figure 5.1 are marked. **(e)** Identification of layers as FCC or HCP stacking in the sediment. The particles are coloured as FCC (red) and HCP (blue).

of the low-density hexagonal phase and analyse if it conforms to either a face-centered cubic (FCC) or hexagonal close-packed (HCP) stacking and (2) determine if the fluid displays a re-entrant behaviour along the height of the sedimentation column, i.e. with decreasing pressure. This would result in a configuration where hexagonal layers are suspended in between two fluid phases.

Accordingly, we first simulate the sedimentation of particles with parameters that promote the formation of the low-density hexagonal phase as given in Table 5.1. A typical configuration of the sedimentation column at $t/\tau_{MD} = 500$ is given in Figure 5.11(a). The particles here are coloured according to the convention given in Figure 5.2. Correspondingly, the layers at the

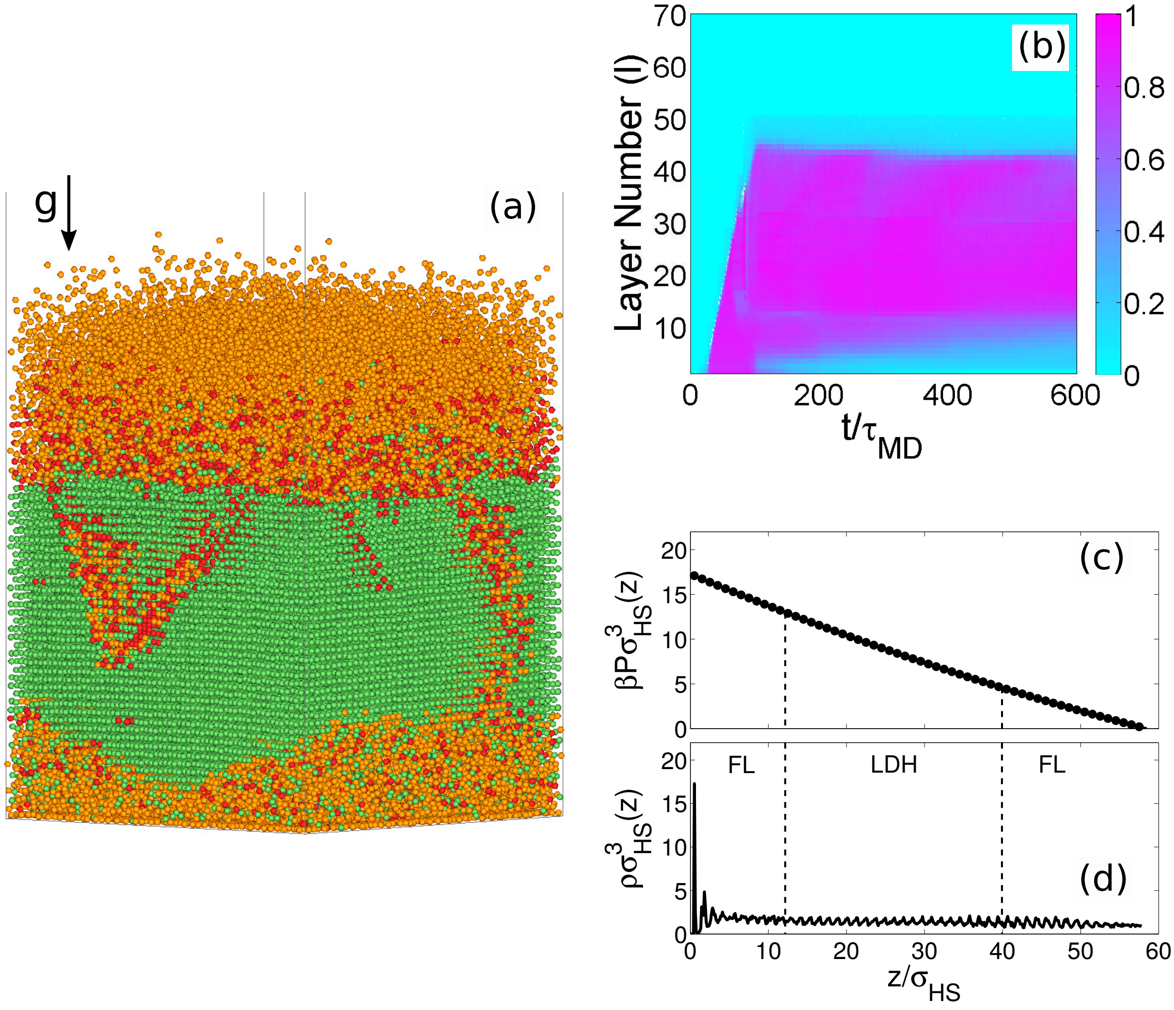

Figure 5.12: **(a)** Side view of a configuration of the FL sedimentation column obtained at $t/\tau_{MD} = 500$. The particles are coloured according to their individual BOO: quasicrystal (red), square (purple), hexagon (green), and fluid (orange). **(b)** The BOO χ_6^l of each layer as a function of time showing the formation of layers with hexagonal symmetry. **(c)** Pressure and **(d)** density profiles calculated along the height of the sedimentation column. The stability regions of low-density hexagonal (LDH) and fluid (FL) phases in terms of reduced pressure $P^* = \beta P \sigma_{HD}^2$, as taken from Figure 5.1, are marked.

bottom composed of particles coloured in green exhibit hexagonal symmetry. The presence of hexagonal symmetry of these layers is confirmed by the high values of the χ_6^l values calculated as a function of time for these layers and plotted in Figure 5.11(b). Combining this time evolution of BOO and the pressure (Figure 5.11(c)) and density (Figure 5.11(d)) profiles along the sedimentation column, we find the formation of about twenty layers of hexagonal symmetry. This also agrees well with the pressure boundaries obtained from the phase diagram. Further, we try to analyse the composition of these hexagonal layers to identify the nature of stacking. It is common to find the formation of randomly stacked hexagonal layers in experimental and simulation sedimentation studies conducted at low Peclet numbers [155, 156]. This is because the free-energy difference between the face-centered cubic (FCC) and hexagonal close-packed (HCP) phases is very small. We calculate the nature of stacking by using the method described by Marechal *et al.* [155]. We represent this by colour coding layers stacked as FCC in red and HCP in blue in Figure 5.11(e). We observe a behaviour analogous to that of a system of hard spheres, i.e. the formation of randomly stacked hexagonal layers. However, we did not find any slanted stacking faults as observed in previous EDBD simulations on sedimenting hard spheres [155, 156].

We then proceed to explore the formation of suspended crystalline layers of hexagonal symmetry bordered by a fluid phase in the sediment. For this, we use a set of parameters conforming to the formation of a fluid phase at the bottom of the sedimentation column as given in Table

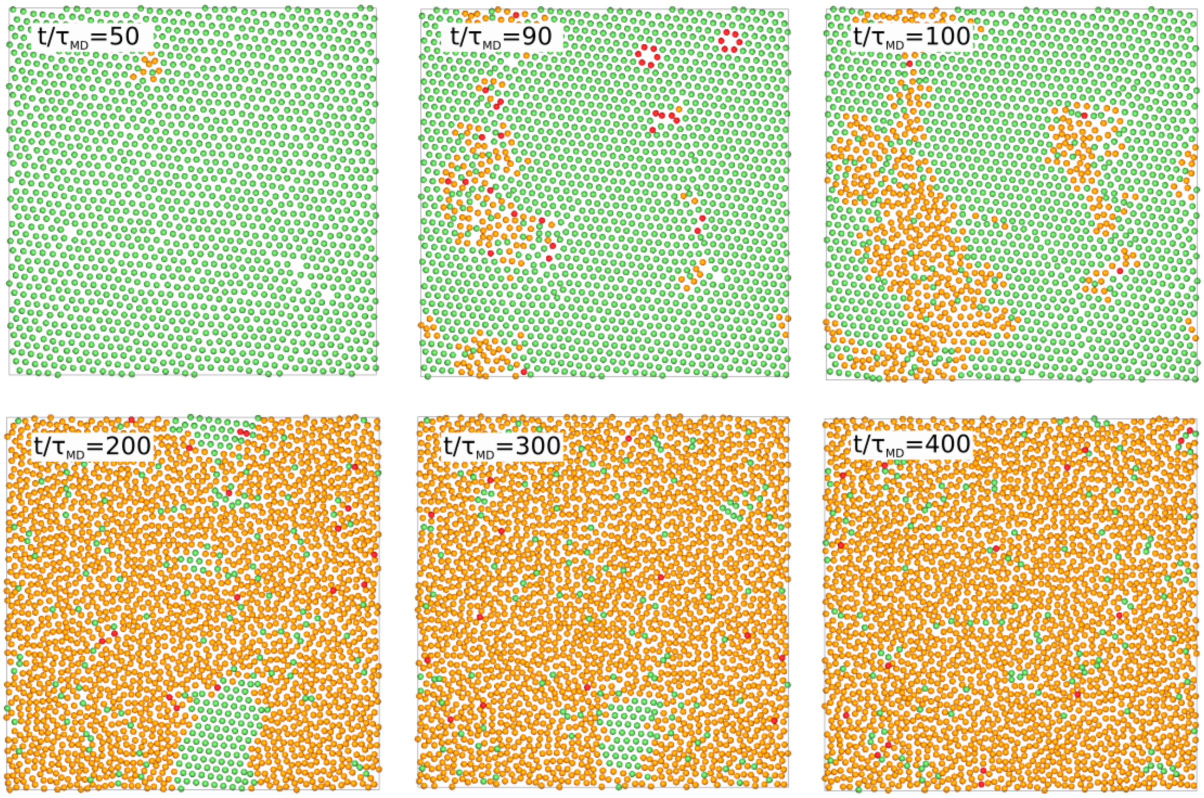

Figure 5.13: Top view of the first layer of the sediment showing the melting of the hexagonal phase to a fluid for varying t/τ_{MD} as labelled. The particles are coloured according to their individual BOO, namely quasicrystal (red), square (purple), hexagon (green), and fluid (orange).

5.1. The system size used here is larger than the previous simulations to accommodate the formation of three phases along the height of the sediment. This is computationally expensive. Thus, the particles have not yet completely sedimented in this simulation. Here, we present the results obtained till date.

Following the convention, we first show a typical configuration of the sedimentation column in Figure 5.12(a) and colour the particles according to the BOO explained in Figure 5.2. We indeed find the formation of crystalline layers with hexagonal symmetry in between two fluid phases. From the snapshot, we notice that the hexagonal layers have not completely melted to a fluid phase at the bottom, and the hexagonal layers at the top are not completely formed. As mentioned before, this simulation is yet to equilibrate and these layers should even out with time. The non-equilibrated nature of this simulation is also evident in the time evolution of the χ_6^l BOO given in Figure 5.12(b) and the corresponding pressure (Figure 5.12(d)) and density (Figure 5.12(c)) profiles. Nevertheless, it is safe to say that the re-entrant behaviour of the fluid phase is observed.

The interesting feature of this sedimentation process is the formation of alternate regions of hexagonal symmetry and fluid with time. This is expressed in terms of the time evolution of the hexagonal BOO χ_6^l in Figure 5.12(b). At the start of the sedimentation process, the sedimentation column is filled with an isotropic fluid, as seen by the low value of χ_6^l in blue. With time, the pressure at the bottom increases. Once it reaches the pressure where the hexagonal phase is found to be stable, structures with hexagonal symmetry start to form at the bottom layers. This is seen as an increase in the values of χ_6^l represented by pink colour. With time, we observe that more hexagonal layers start to form. In contrast, we also see that the pink colour at the bottom gives way to the blue colour again denoting the melting of the hexagonal layers into a fluid. We also observe more layers melting as time proceeds. This melting process of the first layer of the sediment can also be seen from the particle configurations taken at different times, which is shown in Figure 5.13. We observe the formation of larger fractions of fluid with time in these snapshots.

5.4 Conclusions and outlook

To summarise, we studied the sedimentation behaviour of a system of particles interacting with a hard-core and a repulsive square shoulder potential with a fixed shoulder width equal to 1.4 times the hard-core diameter. We find that the system forms a two-dimensional layered structure because of the energetic constraints. This enables us to validate the formation of the thermodynamically stable phases as predicted by the two-dimensional phase diagram. Accordingly, we confirm that layers with symmetries of a dodecagonal quasicrystal, square and low-density hexagonal are formed in the pressure range corresponding to the respective stability regions in the phase diagram. Further ascertaining the validity of the calculated phase diagram, we find that the fluid phase exhibits a re-entrant phase behaviour along the height of the sedimentation column. In addition, we evaluated the effect of settling rates on the formation of the quasicrystal and find that faster settling rates lead to the formation of a quasicrystal with a tiling composition closer to that of the maximum entropy tiling.

For future work, it is interesting to study the formation of the dodecagonal quasicrystal in detail, and to determine the optimal pressure and settling rates for its formation. It is also interesting to see how the quasicrystal formation is affected in case of colloidal epitaxy.

Acknowledgements

I thank John R. Edison for providing me with the EDBD code used in this chapter. This work would not have been possible otherwise. Secondly, I thank Tonnishtha Dasgupta for answering numerous questions regarding carrying out the sedimentation simulations, for calculating the FCC and HCP stacking of the hexagonal layers, and for reading this chapter. Lastly, I thank Wessel S. Vlug for performing the tiling calculations.

Part II

Phase behaviour of other two-dimensional quasicrystal forming core-corona systems

6

Phase behaviour of systems forming octadecagonal and decagonal quasicrystals

Using Monte Carlo simulations and free-energy calculations, we study the phase behaviour of a two-dimensional system of particles interacting with a hard core of diameter σ_{HD} and a repulsive square shoulder potential. The interest in this system lies in the formation of quasicrystals of different symmetries at specific square-shoulder widths δ as previously reported by Dotera *et al.* [123]. However, an insight into other possible periodic phases formed in these systems and the thermodynamic stability of both the periodic and quasicrystal phases is yet to be addressed. Here, we study the phase behaviour and map out the phase diagrams for two different shoulder widths $\delta = 1.27\sigma_{HD}$ and $1.60\sigma_{HD}$, where octadecagonal and decagonal quasicrystals were, respectively, reported. In addition, we verify the thermodynamic stability of these quasicrystals with respect to their periodic approximants. In general, we find that the system at these shoulder widths forms hexagonal phases in two distinct density ranges due to the two characteristic length scales in the interaction potential. Further, we find that the octadecagonal quasicrystal is stable in between two periodic crystal phase regimes. In contrast, the decagonal quasicrystal is not bounded by a low-density periodic crystal phase regime due to the lower density of this quasicrystal. From the free-energy calculations, we find indications that the decagonal quasicrystal is thermodynamically stable with respect to its approximant, and the octadecagonal quasicrystal is stabilised by a configurational entropy contribution.

Based on *Phase behaviour of quasicrystal forming systems of core-corona particles*, J. Chem. Phys., 146, 1114901 (2017)

6.1 Introduction

Despite a huge interest in recent years in the synthesis of novel colloidal building blocks with different shapes and inter-particle interactions for obtaining new structures, it is intriguing to note that very simple particle systems can still exhibit surprisingly rich phase behaviour with unexpected novel phases. For instance, a simple architecture consisting of spherical particles with a rigid core and a squishy corona has been used as a simple model system to explain quasicrystals in soft matter [141]. Quasicrystals are materials that exhibit long-range orientational order without translational periodicity [96]. This architecture emulates either spherical dendrite micelles consisting of a rigid aromatic core with a deformable shell of alkyl chains [105], or block copolymer micelles consisting of a micellar core of hydrophobic polymer surrounded by a large shell of hydrophilic polymer blocks [106–110]. Computational studies of soft-matter quasicrystals essentially involve mimicking this core-corona architecture using a suitable inter-particle interaction potential. In two-dimensional systems, this includes attractive potentials like Lennard-Jones-Gauss [77, 211, 212], square-well [121, 125], flat-well [122] and three-well oscillating [124] interactions, and purely repulsive interactions like the linear ramp [118], square-shoulder [123, 142], repulsive shoulder [142] and various forms of exponential [192, 213, 214] interactions.

A comprehensive exploration of quasicrystals in a two-dimensional system with an inter-particle potential consisting of a hard core and a repulsive square shoulder was performed by Dotera *et al.* [123]. They identified six quasicrystals of various symmetries in the density and shoulder width parameter space. These quasicrystals were identified as low temperature phases formed by cooling a hexagonal phase from a high temperature. A similar analysis was more recently carried out by Schoberth *et al.* [142] wherein they also analysed, in addition to the above mentioned square-shoulder system, a system where the repulsive interaction within the corona was not constant. Similar to the procedure adopted by Dotera *et al.*, Schoberth *et al.* identified the low temperature phases formed at each point in the density-shoulder width parameter space. This also included periodic crystals of square and hexagonal symmetries. These fundamental studies pave the way for a number of questions regarding the overall phase behaviour of these systems, which includes the presence of other periodic crystals as well as the thermodynamic stability of all of these phases.

By studying the overall phase behaviour of these systems, we direct our attention to the formation and stability of various periodic crystals and quasicrystals in core-corona systems. The formation of soft-matter quasicrystals is aided by the presence of two characteristic length scales in the system [141, 169–172]. Also, the formation of periodic crystals in core-corona systems is interesting due to the formation of lattices exclusively in core-corona systems, such as the A15 lattice in three-dimensional system [150, 215] and the square or rhombus lattices in two-dimensional systems [77, 118, 148]. We wish to explore the formation of such uniquely formed periodic crystals in two-dimensional core-corona systems. Further, to determine the stable phases in the system, we calculate the free energy of all identified phases and map out the phase diagram. The presence of quasicrystals in the system complicates the free-energy calculation in a number of ways: Firstly, a suitable reference state with known free energy from which we can construct a thermodynamic integration path to the quasicrystal in the system of our interest is not known. Secondly, the configurational entropy of the quasicrystal needs to be incorporated, but sampling over all of its possible distinct configurations is non-trivial.

Thirdly, assessing the stability of quasicrystal would involve the inclusion of their approximants [129, 130, 167, 176]. Approximants are periodic crystals that approximate the structure of a quasicrystal on a local level, i.e. have identical local tiling structure as the quasicrystal [129, 130, 167, 175]. The higher stability of the quasicrystal is favoured by its configurational entropy accounting for the number of distinct configurations [176], while the approximant is stabilised by its lower energy and more efficient packing [129, 167, 173]. And finally, the relative stability of quasicrystals and their approximants is dependent on the system under study and needs to be exclusively addressed for each system.

In this work, we address the above points of interest by studying the phase behaviour and mapping out the phase diagram for a two-dimensional system of hard disks interacting with a repulsive square-shoulder potential at two shoulder widths $\delta = 1.27\sigma_{HD}$ and $1.60\sigma_{HD}$ for which octadecagonal and decagonal quasicrystals were, respectively, reported previously [123]. We identify the various phases formed in the system by using Monte Carlo simulations. We calculate the free energy of the periodic crystal phases using the Frenkel-Ladd method, and we employ different methods for calculating the free energy of the high-density octadecagonal quasicrystal and the low-density decagonal quasicrystal. For the high-density quasicrystal, where the movement of particles is restricted, we perform a thermodynamic integration to a non-interacting Einstein crystal, i.e. the Frenkel-Ladd method [151, 157], and account for the configurational entropy by using an expression from literature [178]. For the low-density quasicrystal, where particle movements need to be accounted, the reference state is a system of non-interacting particles pinned to their respective positions by an attractive linear well (Schilling-Schmid method [161, 162]). Eventually, we map out the phase diagrams in the temperature-density plane at both shoulder widths.

This chapter is organised as follows. In Section 6.2, we present our simulation model and the computational methods that we employ to calculate the phase diagram. The results are presented in Section 6.3, and we end with some conclusions in Section 6.4.

6.2 Methods

We first explain the simulation model and computational methods used for this study in Section 6.2.1, and then give an account of the analysis methods in Section 6.2.2. Following which, we discuss the procedure to construct the phase diagram in Section 6.2.3 and then pay special attention to the free-energy calculation of quasicrystals in Section 6.2.4.

6.2.1 Computational methodology

Here, we study a two-dimensional system of hard disks with a soft corona, which is represented by a repulsive square-shoulder potential. The inter-particle potential of this hard-core square shoulder (HCSS) system reads

$$V_{\mathrm{HCSS}}(r) = \begin{cases} \infty, & r \leq \sigma_{HD} \\ \varepsilon, & \sigma_{HD} < r < \delta \\ 0, & r \geq \delta \end{cases}, \tag{6.1}$$

where r is the centre-of-mass distance between two particles, and δ and ε are the square shoulder width and height, respectively. The characteristics of this potential are described in detail in Chapter 2.

We study the phase behaviour of the HCSS system at two different shoulder widths. Phases with 18- and 10-fold symmetry, namely octadecagonal and decagonal quasicrystals, were reported previously for shoulder width values of $\delta = 1.27\sigma_{HD}$ and $1.60\sigma_{HD}$, respectively [123, 142]. These shoulder widths are close to the optimal irrational ratios that promote the formation of quasicrystals, viz. $2\cos 50^\circ \approx 1.286$ and $2\cos 36^\circ \approx 1.618$ as explained in reference [123]. In order to facilitate comparisons with earlier studies, we use the values as employed by Dotera *et al.* instead of employing the optimal ones given above. In addition, we also refer to the dodecagonal (12-fold symmetric) quasicrystal studied in Chapters 3 and 4 formed at a shoulder width $\delta = 1.40\sigma_{HD}$.

We perform Monte Carlo (MC) simulations in the canonical (NVT) and isothermal-isobaric (NPT) ensemble, where the number of particles N, the temperature T, and the volume V or pressure P, respectively, are fixed. The particles are simulated in a rectangular box of area A under periodic boundary conditions. We introduce the following reduced (dimensionless) quantities: temperature $T^* = k_B T/\varepsilon$, pressure $P^* = \beta P \sigma_{HD}^2$, and density $\rho^* = N\sigma_{HD}^2/A$, where $\beta = 1/k_B T$ is the inverse temperature with k_B the Boltzmann constant.

6.2.2 Structural analysis

To qualitatively analyse the structures that the system adopts under various conditions, we calculate their corresponding polygonal tilings by drawing the bonds between the neighbouring particles. Decoding quasicrystals as random tilings of polygons is a common practice. Commonly known examples of such tilings include the square-triangle tiling of a dodecagonal quasicrystal [178, 179] and the polygon tiling of a decagonal quasicrystal consisting of regular and nonconvex decagons, nonagons, hexagons, and pentagons [74, 77, 176]. Dotera *et al.* [123] proposed an alternative overview of these tilings by deconstructing each polygon as combinations of two of the four possible Robinson triangles that can be constructed by three particles. In this work, we use the formerly stated more widely used multi-polygonal tiling descriptions. This helps in correlating the quasicrystals and their approximants to previous literatures as explained separately for each quasicrystal in Section 6.3. To summarise, the dodecagonal quasicrystal consists of a square-triangle tiling, the octadecagonal quasicrystal consists of a rhombus-triangle tiling and the decagonal quasicrystal consists of a tiling composed of regular and nonconvex polygons.

For further quantitative analysis, we calculate the average bond orientational order parameter (BOO) of the system and the local environment of each particle. The average BOO parameter χ_m is defined as [164]

$$\chi_m = \left\langle \left| \frac{1}{N_B(i)} \sum_{j=1}^{N_B(i)} \exp(im\theta_{\mathbf{r}_{ij}}) \right|^2 \right\rangle, \tag{6.2}$$

where m is the symmetry of interest, $N_B(i)$ is the number of neighbours of particle i, with particle j defined to be a neighbour if $r_{ij} = |\mathbf{r}_i - \mathbf{r}_j| \le \delta$, $\mathbf{r}_i$ and $\mathbf{r}_j$ are the positions of particles i and j, and $\theta_{\mathbf{r}_{ij}}$ is the angle between the centre-of-mass distance vector $\mathbf{r}_{ij}$ and an arbitrary axis.

Given the similarity in the tiling between an octadecagonal and dodecagonal quasicrystal, we identify the same local particle environments (LPE) in both. The LPE in dodecagonal quasicrystals is composed of the various possible arrangements of squares and triangles. This includes environments of only triangles (Z) or squares ($A15$), and a combination of the two. Mixed arrangements of squares and triangles primarily result in two five-particle coordinated environments, which are termed as H and σ. These LPEs are named in analogy to the Frank-Kasper phases [180]. An overview of these LPEs is given in Figure 6.1.

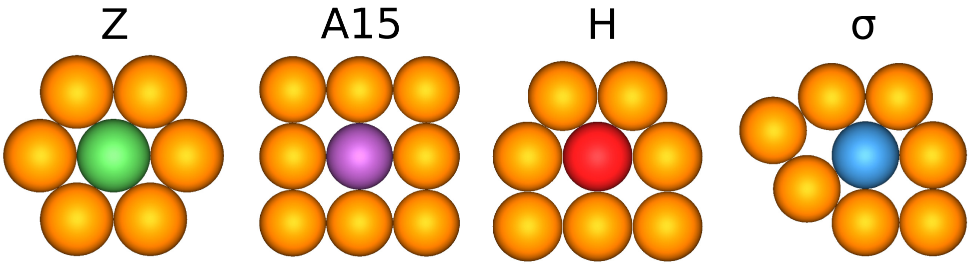

Figure 6.1: Overview of the Z, $A15$, H and σ local particle environments (LPEs) in dodecagonal and octadecagonal quasicrystals. Particles with LPEs other than these are coloured orange.

6.2.3 Phase diagram construction

Obtaining the phase diagram is essentially a three step process. Firstly, the equation of state (EOS), i.e. the bulk pressure P^* as a function of density ρ^*, is constructed. This is done by measuring the equilibrium density at a fixed pressure in a NPT-MC simulation, and by subsequently changing the pressure in a step-wise manner. Compression runs are always started from a disordered isotropic fluid (FL) phase and expansion runs from a periodic crystal or a quasicrystal phase with symmetries according to the system under study. We then determine the free energy as a function of density by integrating the respective EOS from a reference density where the free energy is known. The free energy at the reference density for the periodic crystals is calculated using the Frenkel-Ladd method and that for the fluid phase using the coupling parameter method. Both these are explained in Chapter 2. The free-energy calculation for the quasicrystals is explained in Section 6.2.4. Finally, a common tangent construction is employed to the free-energy curves of all phases to determine the thermodynamically stable phases.

6.2.4 Free-energy calculation of quasicrystals

The methods we use to calculate the free energy of the octadecagonal and decagonal quasicrystals are different. In case of the octadecagonal quasicrystal that forms at a high density, the movements of the particles are restricted, and we can therefore use a representative ‘ideal lattice’ for calculating the free energy as in case of the Frenkel-Ladd method [151]. In contrast, the particles in the decagonal quasicrystal that forms at lower densities are highly mobile and can thus not be represented by an ‘ideal lattice’. Therefore, we employ the method proposed by Schilling and Schmid for arbitrary fluids and disordered solids [161, 162]. The Schilling-Schmid method can also be used to calculate the free energies of the high-density octadecagonal quasicrystal. We find that the difference between the free energies obtained using the

Frenkel-Ladd and the Schilling-Schmid methods was in the order of the statistical error of the free-energy calculations in these methods. We, eventually, employ Frenkel-Ladd method as it is computationally less intensive than the Schilling-Schmid method.

For both the octadecagonal and decagonal quasicrystals, we need to account for the configurational entropy contribution associated with the number of distinct random-tiling configurations. In case of the octadecagonal quasicrystal, the entropy correction is necessary because the Einstein crystal, which is employed as the reference state, does not account for the configurational entropy of the system. In order to obtain an estimate of the configurational entropy, we consider the random-tiling model of polygons. There have been reports of calculation of the configurational entropy for dodecagonal quasicrystals consisting of a random-tiling of squares and triangles [84, 178, 181, 182]. However, we did not find any similar reports for the octadecagonal tiling of rhombus and triangle. We postulate that since the configurational entropy of a dodecagonal square-triangle [178] and an octagonal rectangle-right-angled triangle [75] random tiling is very similar, a similar value will also apply to the octadecagonal rhombus-triangle tiling. We, thus, employ the same value of configurational entropy for both the dodecagonal and the octadecagonal quasicrystal, i.e. a value of entropy per unit area of $S_{\text{config}}/k_B A = 0.12934$ reported by Widom [178]. We, however, note here that we expect a higher configurational entropy for the octadecagonal rhombus-triangle tiling and an even higher one for the octagonal rectangle-right-angled triangle tiling than the dodecagonal square-triangle tiling because of the lower symmetry of the rhombus, rectangle and right-angled triangle. On the other hand, for the low-density decagonal quasicrystal, the free energy is calculated using the method proposed by Schilling and Schmid [161, 162]. As this method allows the sampling of distinct configurations, we do not add an additional configurational entropy term. However, it is good to note that this method does not effectively sample the discrete phason flips in the structure, and thus, underestimates the configurational entropy.

6.3 Results and discussion

In this section, we discuss the phase behaviour of the HCSS system at each shoulder width separately.

6.3.1 Shoulder width $\delta = 1.27\sigma_{HD}$

We first describe the HCSS system with shoulder width $\delta = 1.27\sigma_{HD}$, which exhibits the formation of an octadecagonal (18-fold symmetric) random-tiling quasicrystal (QC18) composed of rhombi and triangles as shown in Reference [123]. The structure is analogous to the dodecagonal quasicrystal (QC12) described in Chapters 3, 4 and 5. Both tilings are constructed from three- and four-sided polygons. The four-sided polygon is a square in QC12 and a rhombus in QC18, the three-sided polygon is an equilateral triangle in both types of quasicrystals. All these polygons have sides of length σ_{HD}, whereas the rhombus in the QC18 is constructed such that the diagonals are equal to the shoulder width $\delta = 1.27\sigma_{HD}$. Figure 6.2(a) shows a configuration of the QC18 obtained at $\rho^* = 0.98$ and $T^* = 0.20$ in the NVT ensemble. The particle configuration in the core-only representation is shown on the top which are coloured according to their LPEs described in Section 4.2.2. The bottom contains the rhombic-triangle tiling (left) and calculated diffraction pattern (right). Defects of predominately pentagonal shapes are observed.

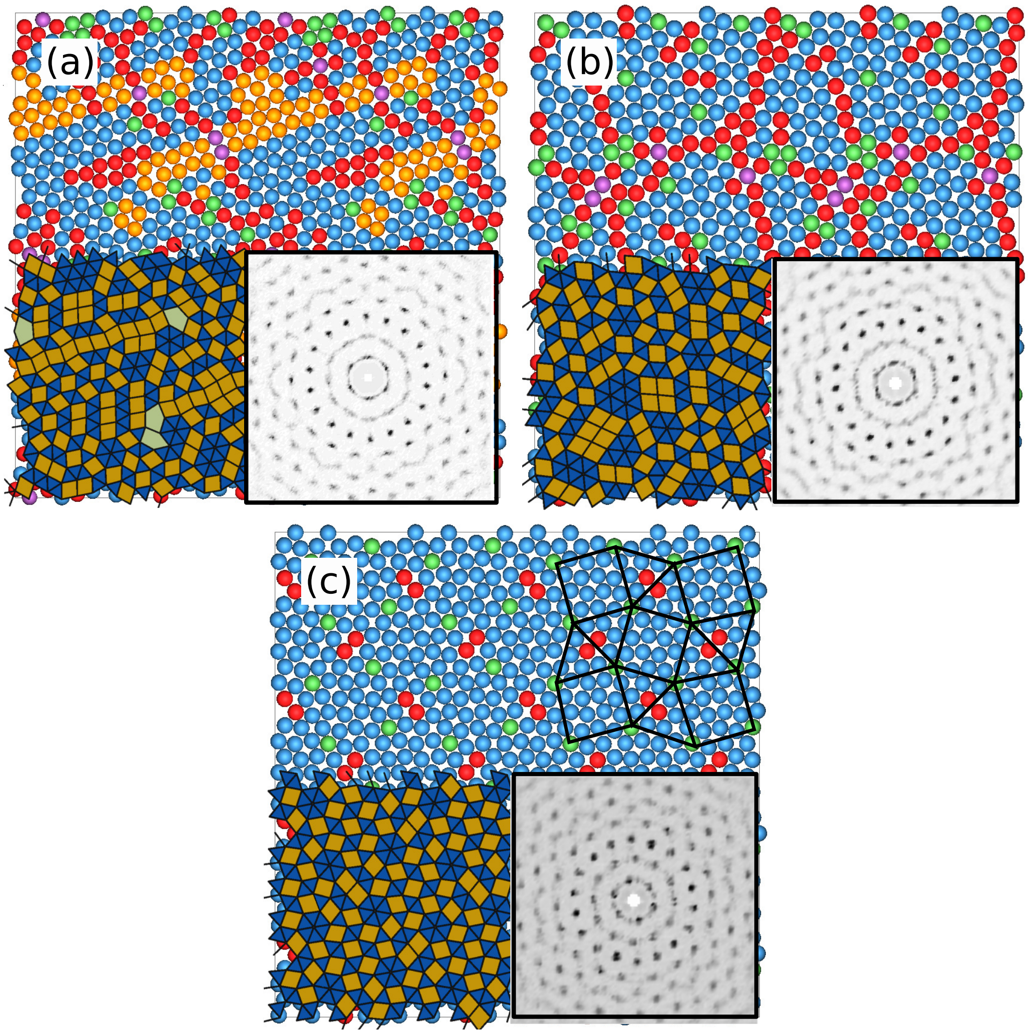

Figure 6.2: The random-tiling octadecagonal quasicrystal (QC18) **(a)** as obtained from simulations, **(b)** a defect-free construction of a random-tiling QC18, and **(c)** a periodic approximant (AC18). Each figure displays a typical configuration **(top)**, where the particles are shown in core-only representation and the colours represent the local particle environments (LPEs) as described in Figure 6.1, along with its corresponding rhombus-triangle tiling **(bottom left)** and diffraction pattern **(bottom right)**. The rhombus-triangle tiling formed by the centres of the distorted dodecagons in the approximant in (c) is highlighted.

Constructing the defect-free configuration and a periodic approximant for this octadecagonal quasicrystal is not straightforward as random rhombus-triangle tilings are not as widely studied as the square-triangle tilings. However, it has previously been observed that the QC18 can be formed from the QC12 by decreasing the temperature followed by gradually decreasing the shoulder width [123]. Here, we use a similar method to obtain the defect-free quasicrystal (QC18) and the approximant (AC18) by exclusively decreasing the shoulder width from $1.40\sigma_{HD}$ to $1.27\sigma_{HD}$ at a constant temperature $T^* = 0.20$ starting with a defect-free dodecagonal quasicrystal (QC12) and an approximant (AC12). The QC12 was adapted from a non-Stampfli square-triangle approximant and contains 209 particles. The AC12 was adapted from a repeated vertex substitution of the (3^2.4.3.4) Archimedean tiling consisting of squares and triangles [85] and contains 224 particles. This particular approximant was chosen as it was the most stable among the different approximants studied in Chapter 3.

In Figures 6.2(b) and 6.2(c), we present the resulting configurations of the defect-free QC18 and the AC18. The accompanying diffraction patterns affirm the 18-fold symmetry. In addition, we plot the 4-, 6-, 12-, and 18-fold BOO parameters as a function of the shoulder width in Figure 6.3 to monitor the transformation from AC12 to AC18 at temperature $T^* = 0.20$. A decrease in χ_{12} accompanied with an increase in χ_{18} is observed upon decreasing the shoulder width δ from $1.40\sigma_{HD}$ to $1.27\sigma_{HD}$. Upon decreasing the shoulder width further, we find that both χ_{12} and χ_{18} decrease and χ_6 increases. From this behaviour, we establish the presence of an 18-fold symmetric phase in a range of shoulder widths between $1.23\sigma_{HD}$ and $1.32\sigma_{HD}$, bordered by a 12- and a 6-fold symmetric phase. We further call attention to the high value of χ_6 at these intermediate shoulder widths. This can also be noticed in the diffraction patterns in Figures 6.2(b) and 6.2(c). This is due to the small system sizes used in this study.

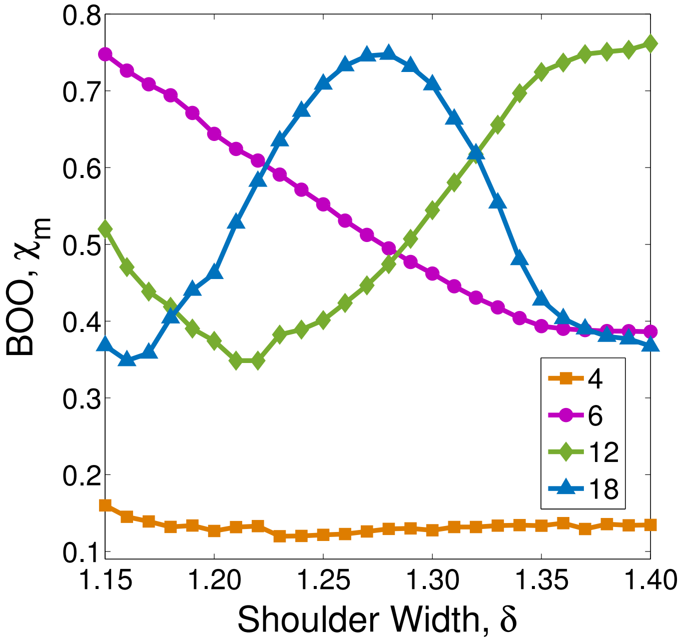

Figure 6.3: The m-fold bond orientational order (BOO) parameter χ_m showing the formation of an octadecagonal quasicrystal (QC18) from a dodecagonal quasicrystal (QC12) in the HCSS system at temperature $T^* = k_B T/\varepsilon = 0.20$ by reducing the shoulder width δ in a Monte Carlo simulation in the NVT ensemble.

To characterise the QC18, we first follow the formation of the QC18 by studying the behaviour of the BOO parameters as a function of temperature and pressure in Figure 6.4 and the equations of state (EOS) in Figure 6.5. The QC18 is formed either by cooling of the high-density hexagonal (HDH) phase to a lower temperature at constant density or by compressing

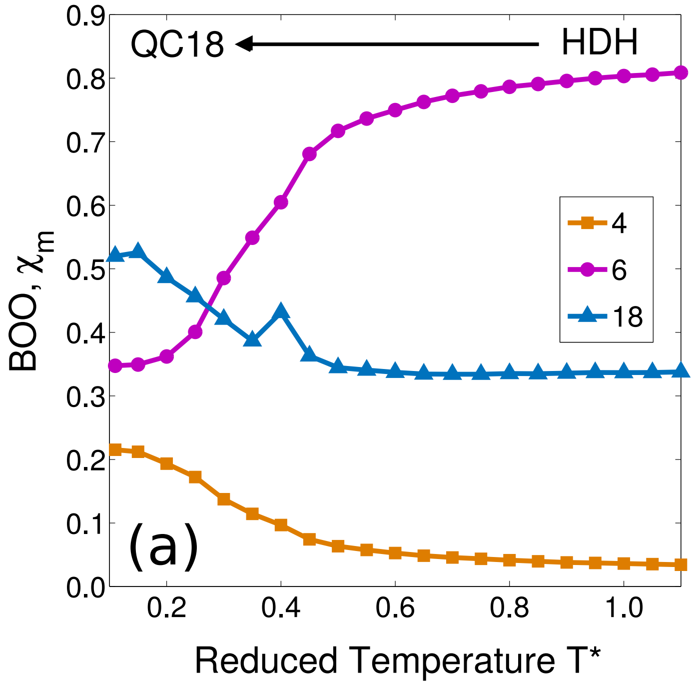

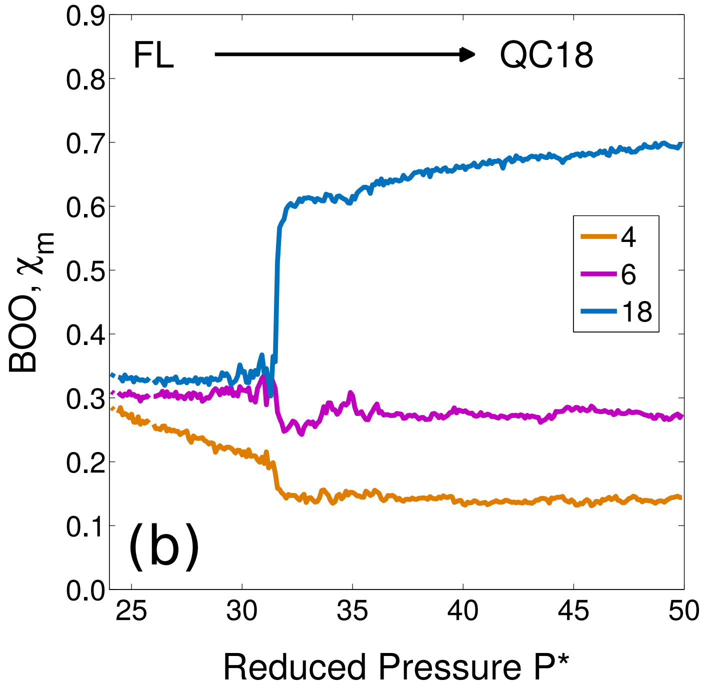

Figure 6.4: The m-fold bond orientational order (BOO) parameter χ_m in a simulation of the HCSS system with $\delta = 1.27\sigma_{HD}$ as a function of **(a)** temperature T^* as obtained by cooling a high-density hexagonal (HDH) phase at density $\rho^* = N\sigma_{HD}^2/A = 0.98$ in the NVT ensemble, and **(b)** as a function of pressure P^* by compressing a fluid (FL) phase at temperature $T^* = k_B T/\varepsilon = 0.30$ in the NPT ensemble.

the fluid (FL) phase to higher density at constant temperature. The behaviour of the BOO parameters χ_4, χ_6 and χ_{18}, respectively representing rhombic, hexagonal and octadecagonal symmetries, during these transformations are shown in Figure 6.4. An increase in χ_{18} upon decreasing the temperature (Figure 6.4(a)) or increasing the pressure (Figure 6.4(b)) establishes the formation of the QC18 phase. The EOS is the bulk pressure P^* as a function of the equilibrium density ρ^* at constant temperature T^*. To construct the EOS, we use the rhombus (RH), the high-density hexagonal (HDH) phase, the approximant (AC18) and the defect-free octadecagonal quasicrystal (QC18) as starting configurations for the expansion runs. We plot the EOS obtained at temperatures $T^* = 0.40$ and 0.15 in Figure 6.5. We find that the system displays hard-disk like phase behaviour at the high temperature and a re-entrant fluid followed by the formation of a quasicrystal at the low temperature. The re-entrant behaviour of the fluid is mediated by the formation of a low-density hexagonal phase, where the interparticle distance is equal to the width of the square shoulder.

We, then, evaluate the relative stability of the QC18 and AC18 phases by constructing a common tangent between the RH and HDH phases. Figure 6.6 shows this common tangent construction at $T^* = 0.20$. Here, we plot the Helmholtz free energy per unit area $\beta F/A$ as a function

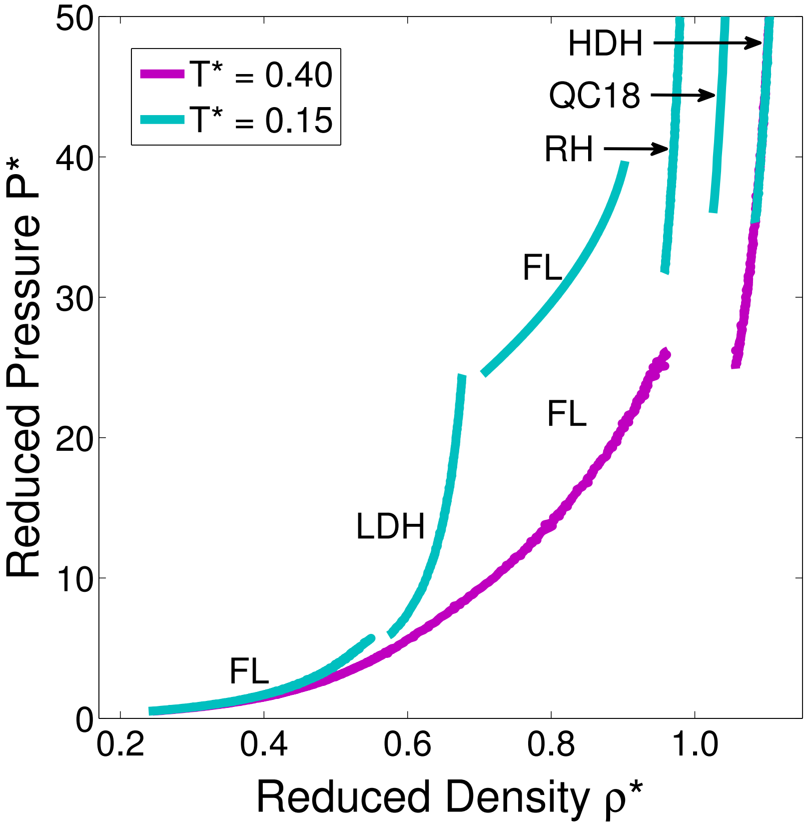

Figure 6.5: Equations of state ($P^* = \beta P \sigma_{HD}^2$ versus $\rho^* = N\sigma_{HD}^2/A$) obtained for the HCSS system with $\delta = 1.27\sigma_{HD}$ and temperatures $T^* = k_B T/\varepsilon = 0.40$ and 0.15. The phases shown are fluid (FL), rhombus (RH), low-density (LDH) and high-density hexagonal (HDH) phases and the random-tiling octadecagonal quasicrystal (QC18).

of reduced density ρ^* for the following phases: RH, HDH, AC18, and QC18 without (QC18-woS), and with (QC18-wS) the configurational entropy contribution $S_{\text{config}}/k_B A = 0.12934$ as taken from literature [178]. For convenience, we subtract a linear fit $\rho\mu_c - P_c$ from the free-energy curves, where μ_c denotes the bulk chemical potential at the (metastable) RH-HDH phase coexistence and P_c the corresponding bulk pressure. This nullifies the free energy of the two-phases, between which the common-tangent is drawn, at the coexistence densities. Thus, the phases with a negative free energy minima in this plot are more stable with respect to the concerned two-phase coexistence. From Figure 6.6, we first note that the minima of the free-energy curves of both QC18 and AC18 lie below the zero-level showing that all these phases are more stable than the RH-HDH phase coexistence. Now, to evaluate the relative stability between the QC18 and AC18, we take a closer look at the minima of these curves, as shown in the inset. We

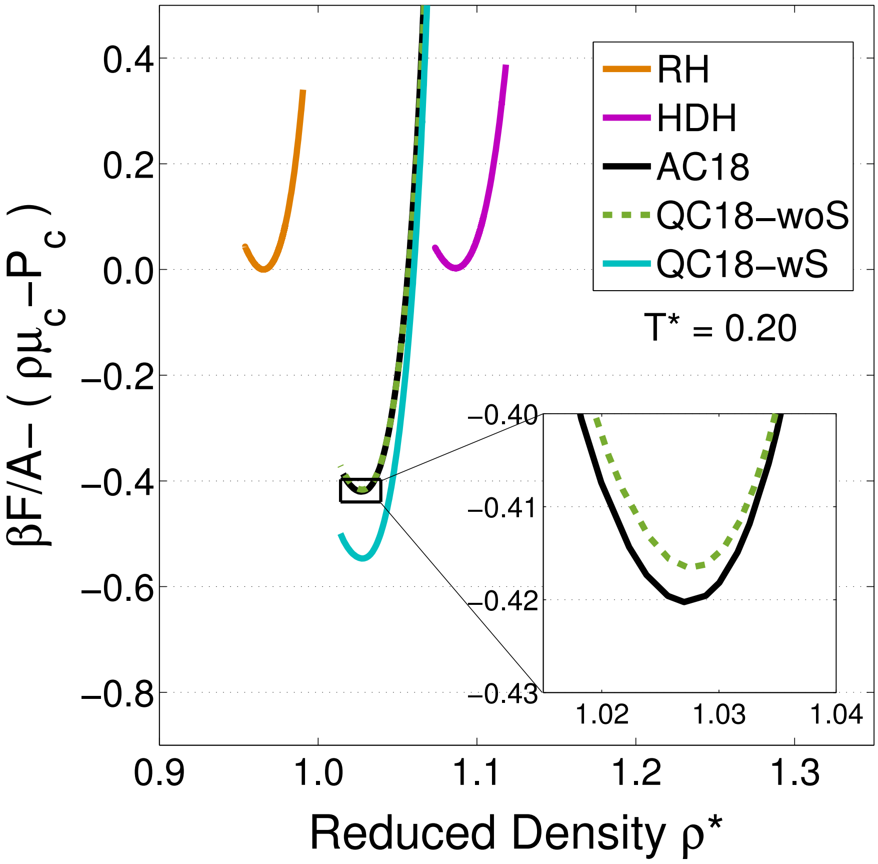

Figure 6.6: Common tangent construction at the rhombus-high-density hexagonal (RH-HDH) phase coexistence obtained for the HCSS system with $\delta = 1.27\sigma_{HD}$ at reduced temperature $T^* = k_B T/\varepsilon = 0.20$. The plot shows the Helmholtz free energy per unit area $\beta F/A$ as a function of reduced density $\rho^* = N\sigma_{HD}^2/A$. A linear fit $\rho\mu_c - p_c$ is subtracted from the free energy, where μ_c and P_c are the bulk chemical potential and bulk pressure at the (metastable) RH-HDH phase coexistence. The phases shown are rhombus (RH), high-density hexagonal (HDH) phase, periodic approximant (AC18) and octadecagonal quasicrystal without (QC18-woS) and with the entropy correction (QC18-wS). **Inset** shows a closer look of the free energy curves of QC18-woS and AC18 phases.

find that the difference between them is very small and is of the order of the statistical error of the free-energy calculation. Thus, the relative stability of one over the other cannot be accurately established. Further, we find that at the close-packed density of $\rho^* = 1.07$, both AC18 and QC18 have a potential energy per particle $U/\varepsilon N$ equal to 2.536 ± 0.002. Thus, the QC18 and the AC18 are approximately equally stable without the entropy correction, whereas any extra configurational entropy contribution arising from the number of distinct configurations of the QC18, stabilises the QC18 over the AC18. We thus assume that the QC18 is more stable than the AC18.

The phase diagram was subsequently mapped out using the free energy of the QC18 phase with the configurational entropy contribution. We stress here that the shift in the phase boundaries is insignificant whether or not the configurational entropy contribution is taken into account, as seen in Figure 3.8. Figure 6.7 displays the phase diagram in the (reduced) temperature-density ($T^* - \rho^*$) plane. The low density-low temperature region ($T^* < 0.25$ and $\rho^* < 0.3$) of the phase diagram is represented by a re-entrant fluid (FL) engulfing the low-density hexagonal

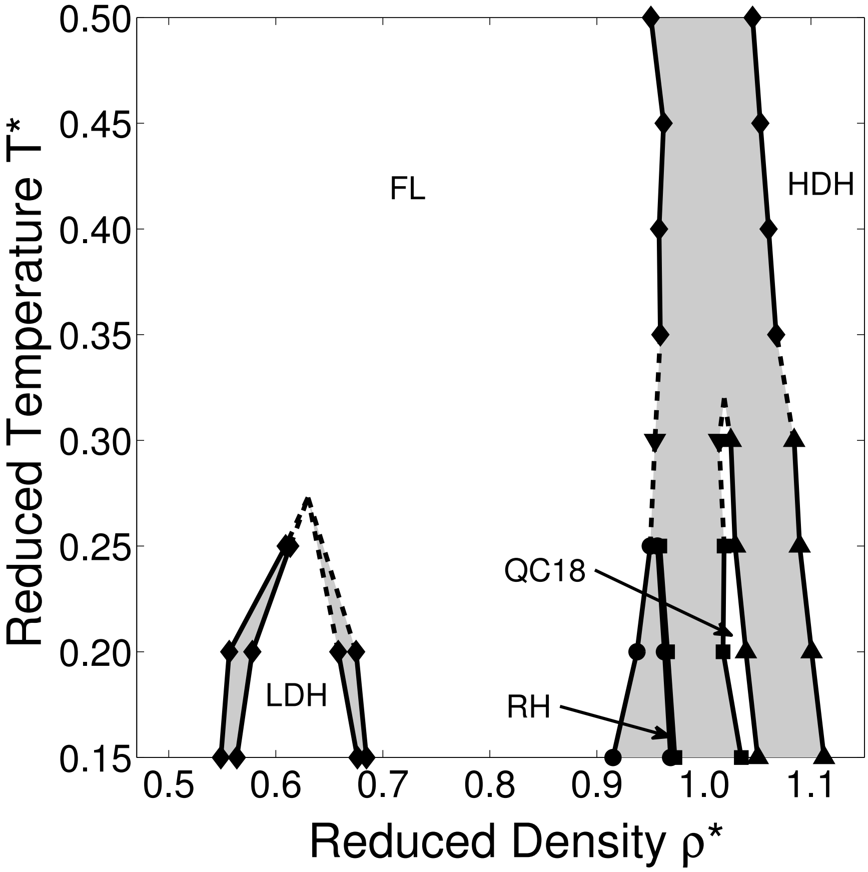

Figure 6.7: Phase diagram in the (reduced) temperature-density representation obtained for the HCSS system with shoulder width $\delta = 1.27\sigma_{HD}$. The reduced quantities are defined as $T^* = k_B T/\varepsilon$ and $\rho^* = N\sigma_{HD}^2/A$. The phases shown are fluid (FL), rhombus (RH), low-density (LDH) and high-density hexagonal (HDH) phases and the random-tiling octadecagonal quasicrystal (QC18). The grey regions denote the two-phase coexistence regions.

(LDH) phase. The LDH phase is formed with the particles separated from each other at a distance equal to the shoulder width $\delta = 1.27\sigma_{HD}$. The high temperature regime ($T^* \geq 0.35$) is characterised by a fluid at low densities and a high-density hexagonal (HDH) phase at high densities with the FL-HDH two-phase coexistence region in between. At low temperatures, a stable QC18 region adjoined by a stable rhombus (RH) and the HDH phase is observed. At intermediate temperatures, the QC18 region is bordered by a FL and the HDH phases. The narrowness of the density regime of the stable rhombus phase is attributed to the geometric constraints enforced by the structure of the phase on the side lengths of the rhombi. This constraint does not allow the sides of the rhombi to change independently and thus, does not accommodate large changes in densities.

6.3.2 Shoulder width $\delta = 1.60\sigma_{HD}$

Next, we investigate a system consisting of HCSS particles with shoulder width $\delta = 1.60\sigma_{HD}$, where a random-tiling decagonal (10-fold symmetric) quasicrystalline (QC10r) phase was previously reported by Dotera *et al.* [123]. The decagonal quasicrystal differs from the octadecagonal quasicrystal on the basis of two factors, namely density and tiling. Firstly, the close-packed density ρ^* of QC18 was 1.07, whereas the QC10r obtained in simulations had a density $\rho^* \approx 0.70$ [123]. Secondly, in stark contrast to the two-member polygonal tiling of QC18, the tiling of QC10r consists of a series of polygons with at least five sides. We show in Figure 6.8(a) a typical configuration of a QC10r at $T^* = 0.20$ as obtained by cooling the HDH phase to a lower temperature at constant density $\rho^* = 0.70$. In the left panel, we show the particle configuration with both the hard core and soft corona. The inset shows the calculated diffraction pattern exhibiting decagonal symmetry. The accompanying tiling is drawn on the right. We see that the tiling is constituted by the following polygonal tiles: Pentagon (Pe), hexagon (He), heptagon (Hp), octagon (Oc), nonagon (No), decagon (De), collapsed decagon (Ud) and question-mark (Qm). The polygonal tiles with more sides than the ones listed above are shaded in grey in Figure 6.8(a). These tiles are identified keeping in mind the constituent tiles of commonly studied decagonal quasicrystals and approximants as described below [74, 77, 176, 212].

As in the previous case of QC18, we construct a perfect decagonal quasicrystal (QC10) and a decagonal approximant (AC10) to study their relative stabilities. The QC10 is adapted from a Mikulla-Roth binary tiling as a decoration of the Tübingen triangle tiling [74] and is shown in Figure 6.8(b). It has a close-packed density of 0.7608. It is composed of 330 particles arranged into five constituent polygons; namely Pe, He, No, De, and Ud tiles. The AC10, on the other hand, consists of decagons arranged in a rhombic super tiling [77] as shown in Figure 6.8(c). We use a large system of 2028 particles such that a rectangular super cell can be carved out of the rhombic super tiling. It has a closed-packed density of 0.7617 and consists of Pe, He and De tiles. Comparing the tilings of the QC10r, QC10 and the AC10 in Figure 6.8, it is obvious that the QC10r tiling is described by additional polygonal tiles than those in the QC10 and AC10. This polygonal tiling of the QC10r has previously been interpreted by constructing the five constituent polygons using two types of Robinson's triangles [123]. In that interpretation, these additional polygonal tiles are considered to be derived from combinations of the constituent polygonal tiles. Among these derived polygonal tiles, we explicitly mark the Hp, Oc and Qm tiles, which appear frequently in the simulations. We do not categorise the other derived tiles

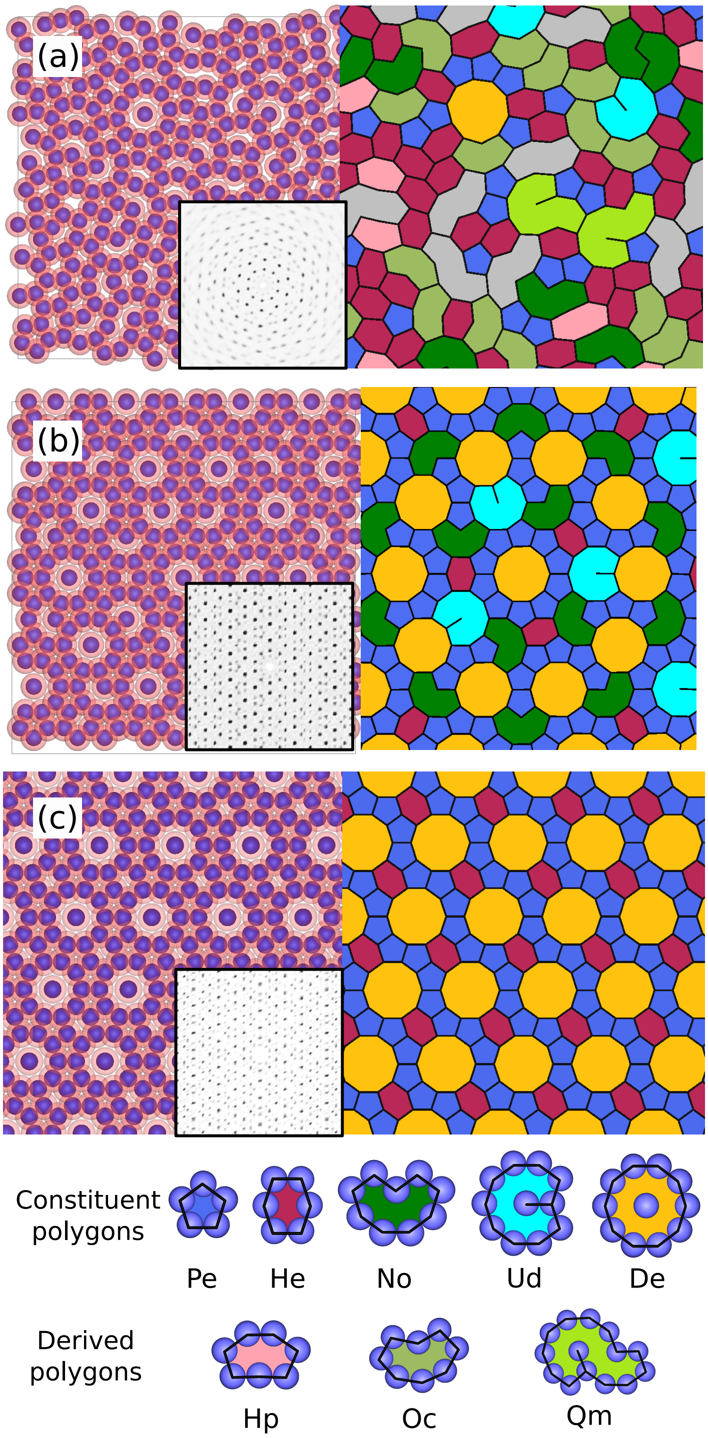

Figure 6.8: Difference between **(a)** the random-tiling decagonal quasicrystal as obtained in simulations (QC10r) **(b)** the constructed decagonal quasicrystal (QC10) and **(c)** the decagonal approximant (AC10). The particle configurations containing both the hard core and the soft shoulder of the particles are shown on the left. Their respective tilings are drawn on the right. **Inset** shows the calculated diffraction pattern. The legend of the constituent and derived polygonal tiles is given at the bottom.

which can be construed as tube-like polygons of various lengths. These are shaded in grey in Figure 6.8(a).

We study the phase behaviour of this system by first constructing the EOS of the various phases present at different temperatures. The expansion runs were started with the decagonal quasicrystal (QC10), the decagonal approximant (AC10) and the high-density hexagonal (HDH) phase. We do not start the expansion runs with the random-tiling quasicrystal (QC10r). Instead, we observe the formation of the QC10r phase from both the QC10 and the AC10 phases at lower pressures. In Figure 6.9, we show the EOS obtained at temperatures $T^* = 0.30$, 0.16 and 0.13. Firstly, we notice that the fundamental behaviour of the system at this shoulder width is similar to that at $\delta = 1.27\sigma_{HD}$. Notably, we observe hard-disk-like behaviour at high temperature ($T^* = 0.30$) and the formation of a low-density hexagonal (LDH) phase at low temperature

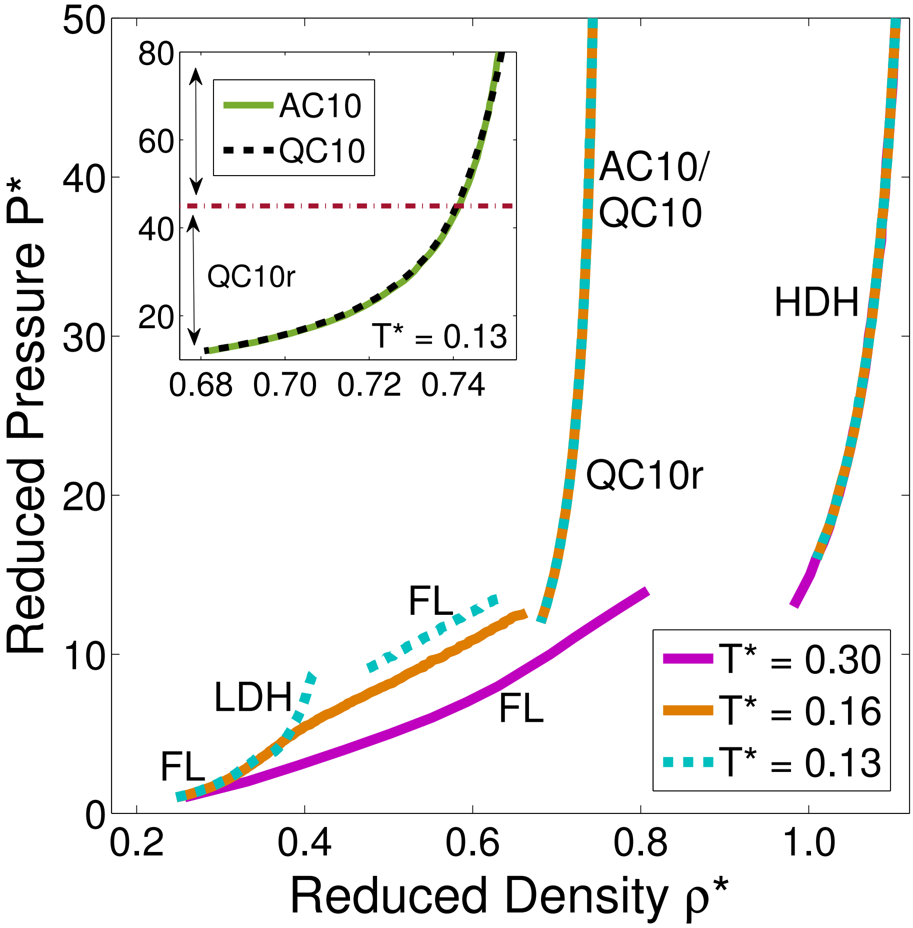

Figure 6.9: Equations of state obtained for the HCSS system with $\delta = 1.60\sigma_{HD}$ and temperatures $T^* = k_BT/\varepsilon = 0.30$, 0.16 and 0.13. The phases shown are fluid (FL), low-density (LDH) and high-density hexagonal (HDH), a decagonal approximant (AC10) and a perfect (QC10) and a random-tiling decagonal quasicrystal (QC10r). **Inset** shows a zoomed in view of the equations of state of the AC10, QC10 and QC10r phases at $T^* = 0.13$. The red-dash-dot line here indicates the pressure below which the derived polygonal tiles start to form in these structures, corresponding to the QC10 (or AC10) to QC10r transition.

($T^* = 0.13$). The difference appears at intermediate density ranges, especially in the EOS of the quasicrystal.

We find that the EOS of the QC10 and AC10 lie very close to each other. To analyse them in detail, we plot a closer view of their EOS at $T^* = 0.13$ in the inset of Figure 6.9. We find that, at these conditions, the difference between the two EOS is of the order of the statistical error in our calculations. During the expansion of both QC10 and AC10, we find that derived polygonal tiles start to form in order to accommodate the extra space available in the structure due to a lower density. The pressure at which the derived polygonal tiles start to form from QC10 or AC10 is marked by the dash-dot line in the inset of Figure 6.9. Given that both these structures, QC10 and AC10, exhibit similar behaviour, we explain only that of the QC10 here. We find that the local rearrangements of particles which result in the formation of derived polygonal tiles are accommodated by phason flips. For example, in Figure 6.10, we present the tilings of a typical particle configuration at pressures $P^* = 46$ and 45 for a temperature $T^* = 0.13$. We clearly find that a tiling consisting of a Pe, a Ud, and a De tile rearranges into a tiling consisting

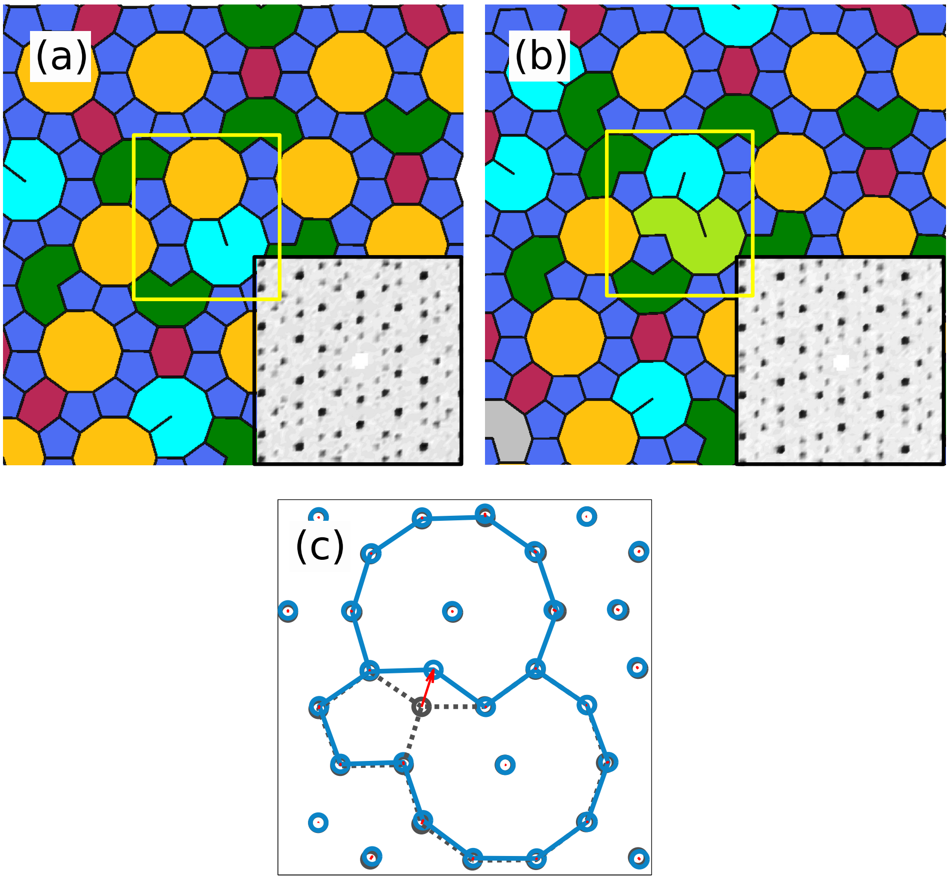

Figure 6.10: Tilings of particle configurations obtained at pressures $P^* = \beta P \sigma_{HD}^2 =$ **(a)** 46 **(b)** 45 at temperature $T^* = k_B T/\varepsilon = 0.13$ showing the formation of derived polygonal tiles in the constructed decagonal quasicrystal (QC10) structure. The tiles are coloured according to the convention given in Figure 6.8. Inset shows the calculated diffraction pattern. **(c)** A closer look at the tile rearrangement, marked by the yellow squares in (a) and (b). The particles positions at $P^* = 46$ are in grey and that at $P^* = 45$ are in blue. The displacement vectors are in red.

of a Ud and a Qm tile. A closer look at this rearrangement is given in Figure 6.10(c). Here the centre-of-mass of the particles is depicted along with their nearest-neighbour bonds. The particle positions at $P^* = 46$ are in grey and those at $P^* = 45$ are in blue. We also draw in red the vectors denoting the displacement of each particle between these two states. The formation of the derived polygonal tiles essentially denotes a transition from the QC10 to the QC10r structure. However, we do not see any clear signature of this transition in the EOS as shown in Figure 6.9. This indicates that the rearrangements in the tilings are required to accommodate the change in density, i.e. more open derived polygons form at lower densities.

The free energies of the FL, QC10 and AC10 phases were calculated according to the Schilling-Schmid method and that of the HDH phase using the Frenkel-Ladd method as explained in Chapter 2. The stable phases at each temperature were then calculated using common tangent constructions between each pair of phases. For example, Figure 6.11 displays the relative stability of the phases at $T^* = 0.11$. Here, the chemical potential $\beta\mu$ of the phases as a function of pressure P^* is plotted. Two phases coexist when their respective chemical potentials are equal at a given pressure. This can be seen as a point of intersection between two curves in the $\beta\mu - P^*$ plot in Figure 6.11. The stability region of each phase is marked by arrows at

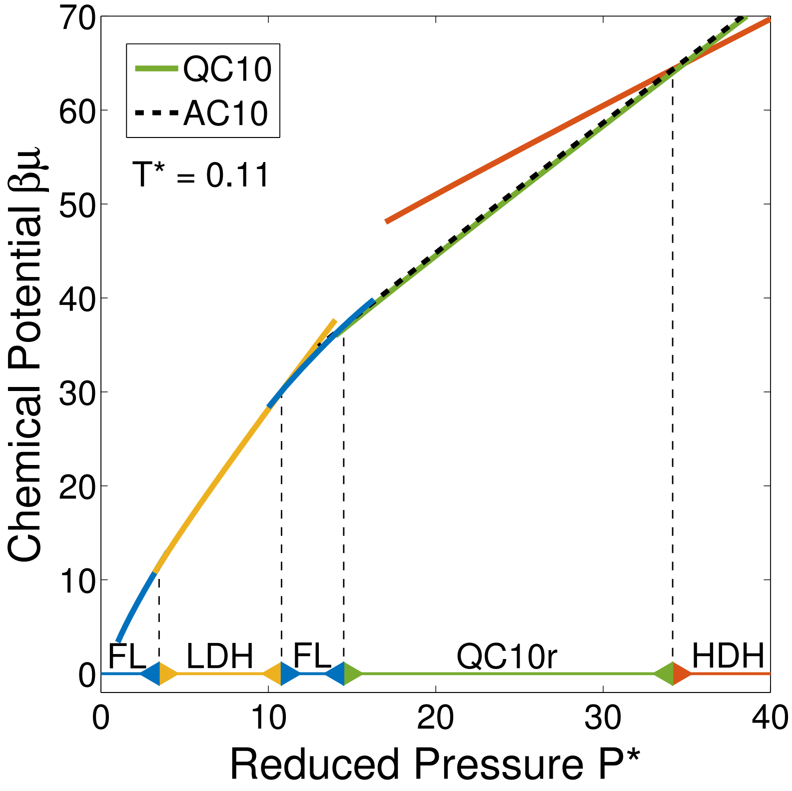

Figure 6.11: The chemical potential $\beta\mu$ as a function of reduced pressure $P^* = \beta P \sigma_{HD}^2$ at temperature $T^* = k_B T/\varepsilon = 0.11$ for the HCSS system with $\delta = 1.60\sigma_{HD}$. The stable phases are fluid (FL), low-density (LDH) and high-density hexagonal (HDH), and random-tiling decagonal quasicrystal (QC10r). The stability region of QC10r is obtained from the curves pertaining to the perfect decagonal quasicrystal (QC10) and its approximant (AC10). The arrows denote the phase stability regions.

the bottom of the figure. We individually mark the curves pertaining to the QC10 and AC10 phases, which lie on top of each other. Comparing the pressure range of formation of the QC10 (or AC10) phases with the EOS given in Figure 6.9, we find that it corresponds to the region where the structure comprises of derived polygonal tiles, i.e. the QC10r structure. Thus, we conclude that the stable phase with decagonal order in the system is QC10r. Ultimately, the order of stability of the phases at this temperature is found to be FL-LDH-FL-QC10r-HDH upon increasing the pressure P^*.

In Figure 6.12, we plot the phase diagram in the (reduced) temperature-density ($T^* - \rho^*$) plane. Similar to the behaviour at $\delta = 1.27\sigma_{HD}$, the low-temperature low-density behaviour is characterised by a re-entrant phase behaviour of the fluid (FL) phase encompassing the low-density hexagonal (LDH) phase. The stable phase at high densities is the high-density hexagonal (HDH). The quasicrystal (QC10r) is formed at intermediate densities at low temperatures ($T^* \leq 0.20$). We find that the maximum density of the stable QC10r phase is ≈ 0.73, whereby the structure always contains derived polygonal tiles. This essentially means that the QC10 and AC10, which solely consist of the constituent polygons, is not a stable phase in this system. It is, however, interesting to note that stable QC10 and AC10 phases have previously

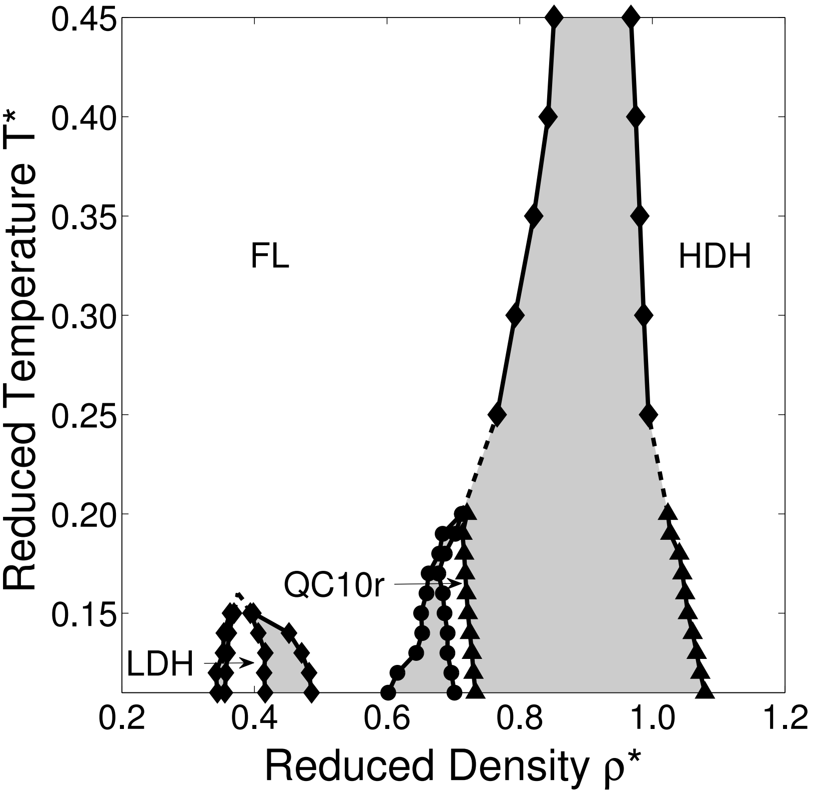

Figure 6.12: Phase diagram in the (reduced) temperature-density representation obtained for the HCSS system with shoulder width $\delta = 1.60\sigma_{HD}$. The reduced quantities are defined as $T^* = k_B T/\varepsilon$ and $\rho^* = N\sigma_{HD}^2/A$. The stable phases shown are fluid (FL), low-density (LDH) and high-density hexagonal (HDH), and the random-tiling decagonal quasicrystal (QC10r). The grey regions denote the two-phase coexistence regions.

been reported in a system of particles interacting with Lennard-Jones-Gauss potential [176]. The absence of QC10 (or AC10) in the HCSS system emphasises the strong dependence of the formation of a quasicrystal (or approximant) on the interaction potential.

6.4 Conclusions

To summarise, we investigated the bulk phase behaviour of a system of colloidal particles interacting through a hard core and a purely repulsive square-shoulder pair potential for two different shoulder widths $\delta = 1.27\sigma_{HD}$ and $1.60\sigma_{HD}$. The system shows similar phase behaviour at low and high densities for both shoulder widths. At low densities, the fluid exhibits a re-entrant phase behaviour circumscribing a low-density hexagonal (LDH) phase due to the presence of two length scales in the interaction potential. At high densities, a high-density hexagonal (HDH) phase is found to be stable. At intermediate densities, for $\delta = 1.27\sigma_{HD}$, a rhombus phase is observed. No periodic crystal phase is observed at intermediate density for $\delta = 1.60\sigma_{HD}$.

The most distinguished feature of the HCSS system is the formation of quasicrystals as reported by Dotera *et al.* [123]. They demonstrated the formation of quasicrystals with different symmetries at different shoulder widths. An octadecagonal (18-fold symmetric) quasicrystal is formed at $\delta = 1.27\sigma_{HD}$ and a decagonal (10-fold symmetric) quasicrystal at $\delta = 1.60\sigma_{HD}$. Here, we investigated the thermodynamic stability of these quasicrystals with respect to a disordered fluid phase, periodic crystal phases, and periodic approximants. To this end, we calculate the free energy of the octadecagonal quasicrystal using the Frenkel-Ladd method and add an extra contribution pertaining to the configurational entropy. For the decagonal quasicrystal, we employ the Schilling-Schmid method to calculate the free energy. We find that the octadecagonal quasicrystal without the entropy correction and its approximant were equally stable for a HCSS system at shoulder width $\delta = 1.27\sigma_{HD}$. However, any configurational entropy contribution associated with the number of distinct configurations of the octadecagonal quasicrystal phase will stabilise it over its approximant. We thus assume that the octadecagonal quasicrystal phase will be more stable than the approximant. In the case of the decagonal quasicrystal, we find that the approximant is not stable at the densities where the quasicrystal is formed for a HCSS system at shoulder width $\delta = 1.60\sigma_{HD}$. In conclusion, we have mapped out the phase diagrams of HCSS systems for two different shoulder widths. We show that the phase diagrams display stable regions of the decagonal and octadecagonal quasicrystal phases. We also stress that the phase boundaries are insensitive to the configurational entropy term corresponding to the number of distinct QC configurations.

Finally, we mention that we do not consider the other 18-fold ($\delta = 1.43\sigma_{HD}$) and 24-fold ($\delta = 1.29\sigma_{HD}$) quasicrystalline phases reported at densities just above that of the LDH by Dotera *et al.* [123] as their reported temperatures of formation ($T^* \sim 0.09$) are outside the temperature range of this study ($0.15 \leq T^* \leq 0.50$).

Acknowledgements

I thank Wessel S. Vlug for helping with the tiling calculations, and Simone Dussi and Guido Avvisati for critical reading of this chapter. Guido Avvisati is also acknowledged for providing *inspiration* for the chemical potential versus pressure plot.

7

On the formation of stripe, sigma, and honeycomb phases in a core-corona system

Using Monte Carlo simulations and free-energy calculations, we investigate the phase behaviour of a two-dimensional core-corona system. We model this system as particles consisting of an impenetrable hard core of diameter σ_{HD} surrounded by a purely repulsive soft corona of diameter $\delta = 1.95\sigma_{HD}$. At low densities, we observe the spontaneous formation of a phase with a stripe texture as well as a honeycomb-like phase driven by both energy and entropy considerations. At high densities, we find that a two-dimensional analogue of the periodic sigma phase, considered as a periodic approximant of dodecagonal quasicrystals, is energetically stabilised with respect to two distinct dodecagonal quasicrystals, namely, a square-triangle tiling and a square-triangle-shield tiling. We also find the formation of stable hexagonal phases at three distinct density ranges, which are energetically driven, i.e. by minimising the overlap of the coronas. Furthermore, our calculations show that the low-density dodecagonal quasicrystal that was previously reported by Dotera *et al.* [123] is kinetically formed in the coexistence region between the honeycomb and the medium-density hexagonal phases.

Based on *On the formation of stripe, sigma, and honeycomb phases in a core-corona system*, Soft Matter (2017)

7.1 Introduction

Self-assembly, the process of spontaneous organisation of simple components into complex structures, is often controlled by a competition between different interactions in soft matter systems. Anisotropic interactions due to external fields [216–224], particle shapes [113, 129, 167, 225], particle sizes [111, 112], or surface modifications [226, 227] induce the formation of mesophases like stripes [216, 217, 220, 221, 228, 229], open structures like honeycomb [218, 220, 227, 230] and Kagome lattices [223, 225, 226] and even quasicrystals [105–112, 231]. These open structures and quasicrystals are interesting for their applications as photonic crystals [25, 63, 91, 232]. Alternatively, monodisperse colloidal particles interacting with potentials comprising of two length scales can also self-assemble into such phases with non-trivial symmetries. Such systems, which are driven by two competing length scales, are termed as core-softened systems, systems with a core-corona architecture, or simply core-corona systems. Evidences of formation of mesoscale patterns like stripes [136–140] and labyrinths [137], Archimedean tiling patterns [106, 141], square lattices [118] and quasicrystals of various symmetries [118, 123, 142] have been reported in core-corona systems.

These core-corona systems can be represented in simulations by a variety of models with different interparticle interactions. In simple terms, three kinds of core-corona interactions can be identified, namely purely attractive, purely repulsive, or a combination of the two. Examples of systems with purely attractive interactions include square-well [121] and flat-well [122] pair potentials, that of purely repulsive interactions are square-shoulder [123, 148, 149] and linear ramp [118] pair potentials, and mixed interactions include Lennard-Jones-Gauss [77] and three-well oscillating [124] pair potentials. Experimentally, these systems consist of spherical particles with a rigid core and a squishy corona, for example, spherical dendrite micelles consisting of a rigid aromatic core with a deformable shell of alkyl chains [105], or block copolymer micelles consisting of a micellar core of hydrophobic polymer surrounded by a large shell of hydrophilic polymer blocks [110].

The interactions observed between these experimental core-corona particles are primarily steric in nature, which results in a strongly repulsive core interaction supplemented with a soft repulsive corona interaction. This form of interaction can be described in terms of three regimes. The first regime occurs at low densities where the coronas do not overlap. The second regime is at high densities, where the coronas entirely overlap and the core repulsion dominates, and finally the third regime is at intermediate densities, where the coronas partially overlap. In this intermediate regime, both the cores and coronas are partially effective and the competition of these core and corona interactions leads to the formation of phases with unusual symmetries. In other words, the minimisation of overlap of the coronas drives the formation of the phases described above.

Although the formation of these mesophases and open structures has been investigated in core-corona systems, the thermodynamic stability of these phases has received less attention. Given that (1) the presence of two-length scales aids the formation of quasicrystals in soft-matter systems [141, 169, 190–193] and that (2) such two-length scale systems are capable of forming mesophases [136–140], a question that naturally arises is how the thermodynamic stability of these mesophases and quasicrystals is related to each other in a system that forms both. To the best of our knowledge, we have not come across any such study.

We address these issues in this chapter by combining Monte Carlo simulations and free-energy calculations. We evaluate the thermodynamic stability of a mesophase, an open structure and quasicrystals formed in a core-corona system. We model this system by using two-dimensional disks with diameter σ_{HD} interacting with a hard core and a purely repulsive square-shoulder potential at a fixed shoulder width of $1.95\sigma_{HD}$. We find the formation of a stripe, a honeycomb and a two-dimensional sigma phase along with hexagonal and fluid phases in this system. This chapter is organised as follows. In Section 7.2, we introduce the model and describe the simulation methods that we employ to study the phase behaviour of this system. We present the results regarding the formation and stability of a striped mesophase, quasi-periodic and periodic phases in Section 7.3 and we end with an overview of the phase behaviour in our conclusions in Section 7.4.

7.2 Methods

We first explain the simulation model and computational methods used for this study in Section 7.2.1, and then the procedure to construct the phase diagram in Section 7.2.2, and we subsequently give an account of the analysis methods in Section 7.2.3.

7.2.1 Model and simulations

The core-corona model used in this study consists of a two-dimensional system of spherical particles interacting with a hard-core square shoulder (HCSS) pair potential $V_{\text{HCSS}}(r)$. This radially symmetric pair potential consists of a hard core of diameter σ_{HD} and a purely repulsive square shoulder of diameter δ and reads

$$V_{\text{HCSS}}(r) = \begin{cases} \infty, & r \leq \sigma_{HD} \\ \varepsilon, & \sigma_{HD} < r \leq \delta \\ 0, & r > \delta \end{cases}, \tag{7.1}$$

where r is the interparticle centre-of-mass distance, and $\varepsilon > 0$ is the height of the square shoulder. The general behaviour of this interaction potential is explained in Chapter 2. The HCSS potential introduces two characteristic length scales in the system; one at the diameter of the hard core σ_{HD} and the other one at the soft shoulder δ. The latter is the only tunable parameter for studying the system. It has been previously shown by Dotera *et al.* [123] and Schoberth *et al.* [142] that quasicrystals of various symmetries form at specific values of δ. In this chapter, we use a value of $\delta = 1.95\sigma_{HD}$. This chosen shoulder width is close to (1) the shoulder width of $\delta = 2.00\sigma_{HD}$ [233, 234] and $\delta = 2.50\sigma_{HD}$ [136, 138, 140] where stripe phases have previously been reported in certain computational studies as well as (2) the irrational ratio of $2\cos 15^\circ \approx \sqrt{2+\sqrt{3}} \approx 1.932$ where quasicrystals of dodecagonal symmetry at a high density have been reported to form in various theoretical and/or computational studies [77, 123, 169, 190, 235]. Thus, this shoulder width is an ideal starting point to locate both the stripe phase and the dodecagonal quasicrystal. Furthermore, a dodecagonal quasicrystal at a lower density has also been reported by Dotera *et al.* at this shoulder width $\delta = 1.95\sigma_{HD}$ [123].

To address the phase behaviour of this system and the relative stability of various phases, we perform Monte Carlo (MC) simulations in a rectangular box of area A with periodic boundary conditions in the canonical (NVT) and isothermal-isobaric (NPT) ensembles. We choose σ_{HD} and ε, respectively, as the units of length and energy, and define a reduced temperature $T^* = k_BT/\varepsilon$, reduced pressure $P^* = \beta P\sigma_{HD}^2$, and a reduced density $\rho^* = N\sigma_{HD}^2/A$, where $\beta = 1/k_BT$ is the inverse temperature with k_B the Boltzmann constant. In the simulations, we use a system size between 209 to 256 particles depending on the initial crystal structure, while a system size of 1600 particles was used in case of an isotropic fluid phase as initial configuration.

7.2.2 Phase diagram construction

We determine the phase diagram of the system in a three-step process. In the first step, we measure the isotherms of the equation of state (EOS) of the phases of interest at a fixed temperature T^*. These isothermal EOS, i.e. the bulk pressure P^* as a function of the equilibrium density ρ^*, are obtained by performing compression and expansion runs by either increasing or decreasing the pressure P^* in a step-wise manner in the NPT ensemble. We start the compression runs from a disordered isotropic fluid phase, while the expansion runs are started using a periodic crystal or a quasicrystal phase. In the second step, we determine the dimensionless Helmholtz free energy per particle $f = \beta F/N$ as a function of density at a fixed temperature T^* for each of the observed phases. This is done by thermodynamic integration of the EOS to a reference density. The free energy at this reference density is calculated by constructing a reversible thermodynamic path to a reference system for which the free energy can be calculated analytically. We employ the hard-disk fluid phase at the same density as a reference state for the fluid phase [151, 157], and the non-interacting Einstein crystal [151, 159, 160] as a reference for the periodic crystals. For all other phases in the system, namely the quasicrystal, its approximants, and the stripe phase, we use a non-interacting system of particles pinned by an attractive linear well [161, 162] to their reference positions as a reference system. All these three methods for calculating the free energy are explained in Chapter 2. In the final step, we employ a common tangent construction to the free-energy curves, i.e. the Helmholtz free energy per unit area $\beta F/A$ as a function of reduced density ρ^*, to determine the thermodynamically stable phases and the corresponding phase boundaries.

Additionally, we also monitor the nature of phase transitions in the NVT ensemble by calculating the specific heat C_v at constant volume defined by

$$C_v = \frac{\langle U^2 \rangle - \langle U \rangle^2}{k_BT^2}, \tag{7.2}$$

where U is the potential energy of the system.

7.2.3 Structural analysis

We calculate various order parameters to study the local structure and to differentiate between the phases. This includes the radial distribution function (RDF) of the system $g(r)$, the static structure factor $S(k)$, and the average m-fold bond orientational order parameter (BOO) of the system χ_m and the bond orientational correlation function $g_m(r)$. In addition, we calculate the polygonal tiling corresponding to each structure. We define the m-fold bond orientational correlation function $g_m(r)$ with $r = |\mathbf{r} - \mathbf{r}'|$ as

$$g_m(r) = \left\langle \chi_m^j(\mathbf{r}).\chi_m^{k*}(\mathbf{r}') \right\rangle. \tag{7.3}$$

Further, in the case of the dodecagonal quasicrystal phase and its approximants, we calculate the local particle environment (LPE) to differentiate between the σ and H environments [180] as shown in Figure 7.1. The H and σ LPEs respectively correspond to the periodic Archimedean tilings $\left(3^3 4^2\right)$ and $\left(3^2 434\right)$ [180]. Each Archimedean tiling is characterised by an unique vertex obtained by the arrangement of the constituent tiles around it. Thus, the naming of an Archimedean tiling refers to cyclic order of the number of sides of the polygonal tiles around the vertex.

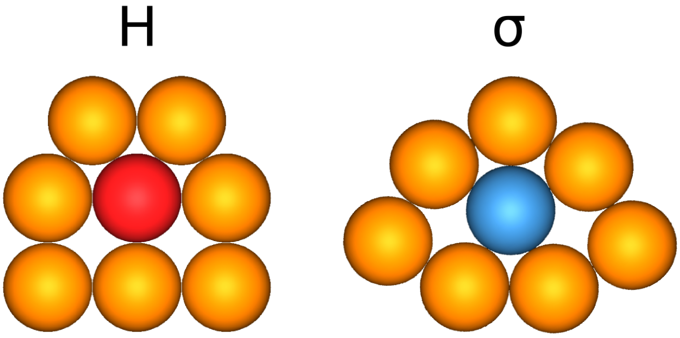

Figure 7.1: Schematic overview of the H and σ local particle environments (LPE).

Furthermore, we utilise an anisotropic scaling index method to distinguish between the fluid and stripe phases [236, 237]. Here, a weighted scaling index α of the system is calculated as

$$\alpha = \frac{\left\langle \sum_{i=1}^{N} \sum_{j\neq i}^{N} \delta(\mathbf{r}-\mathbf{r}_i)\delta(\mathbf{r}'-\mathbf{r}_j) q (r_c/r_{ij})^q e^{-(r_c/r_{ij})^q} \right\rangle}{\left\langle \sum_{i=1}^{N} \sum_{j\neq i}^{N} \delta(\mathbf{r}-\mathbf{r}_i)\delta(\mathbf{r}'-\mathbf{r}_j) e^{-(r_c/r_{ij})^q} \right\rangle}, \tag{7.4}$$

where $r_{ij} = |\mathbf{r}_i - \mathbf{r}_j|$ is the distance between particles i and j at positions $\mathbf{r}_i$ and $\mathbf{r}_j$, r_c is a cut-off distance, and q is a control parameter. In this study, the cut-off distance r_c is taken to be $2.50\sigma_{HD}$ and the control parameter q is set to 2. The index α is a local non-linear measure used to characterise the symmetry of the structure along a certain direction. The change in symmetry of the system due to the formation of stripes can then be quantified by the probability distribution functions of α in the directions parallel and perpendicular to the stripes. Hence, a scalar order parameter to quantify the transition between fluid and stripe phases is defined as the difference between the average parallel and perpendicular scaling indices [236, 237],

$$\Delta\alpha = \int \alpha P_{\|}(\alpha)\mathrm{d}\alpha - \int \alpha P_{\perp}(\alpha)\mathrm{d}\alpha. \tag{7.5}$$

7.3 Results and discussion

In this section, we first present the phase diagram of the HCSS system with a shoulder width $\delta = 1.95\sigma_{HD}$ and then separately examine the formation and stability of the different phases.

The phase behaviour at the chosen shoulder width is particularly interesting due to the comparative sizes of the shell of the soft corona ($0.95\sigma_{HD}$) and the diameter σ_{HD} of the hard core.

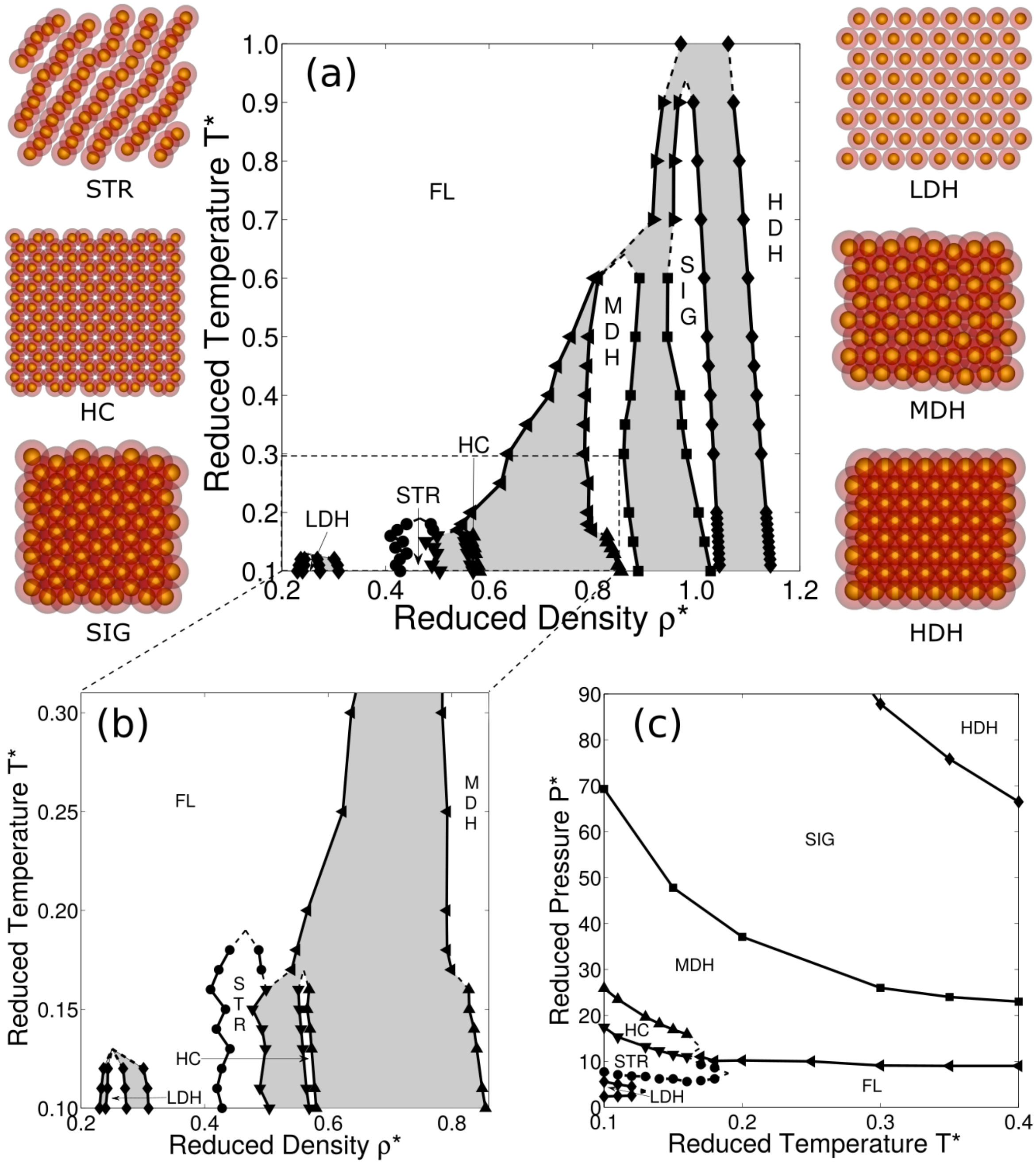

Figure 7.2: **(a)** Phase diagram of the HCSS system with a shoulder width $\delta = 1.95\sigma_{HD}$ in the (reduced) temperature T^* - density ρ^* plane. A zoomed in version of the phase diagram in the low-temperature regime is given in **(b)** in the (reduced) temperature T^* - density ρ^* plane and in **(c)** in the (reduced) pressure P^* - temperature T^* plane. The reduced quantities are defined as $T^* = k_B T/\varepsilon$, $\rho^* = N\sigma_{HD}^2/A$ and $P^* = \beta P \sigma_{HD}^2$. The stable phases include fluid (FL), stripe (STR), honeycomb (HC), low-density hexagonal (LDH), medium-density hexagonal (MDH), and high-density hexagonal (HDH) and sigma (SIG). The grey areas denote the coexistence regions between two phases. Typical configurations of the phases obtained from Monte Carlo simulations are shown on either side of (a). The hard cores are coloured in yellow and the soft coronas in red.

Consequently, the interplay between energy and entropy determines the peculiar phases formed at low and intermediate densities. We show the calculated phase diagram in the (reduced) temperature T^* - density ρ^* representation in Figures 7.2(a) and 7.2(b), along with typical configurations of the various phases in the core-shoulder representation. We also take a closer look at the low-temperature regime of this phase diagram in the (reduced) pressure P^* - temperature T^* representation in Figure 7.2(c). From these figures, it is clear that the system shows a rich phase behaviour with a fluid (FL), a stripe (STR), a honeycomb (HC), and a sigma (SIG) phase, and hexagonal phases at three distinct ranges of density, namely a low-density (LDH), a medium-density (MDH), and a high-density (HDH) hexagonal phase. The SIG phase is a periodic approximant of a dodecagonal quasicrystal and is named after its three-dimensional analogue of the Frank-Kasper phase [180, 238].

At low temperatures and densities, we recognise a re-entrant behaviour of the FL phase encompassing the LDH phase. At moderate densities, we find the STR and HC phases at low temperatures $T^* < 0.2$ and a broad two-phase coexistence region between the HC and MDH phases. On the other hand, at $T^* > 0.2$, the STR and HC phases are unstable and we find a broad coexistence between the FL and MDH phases. With increasing densities, three periodic crystal phases are observed in this system, namely the MDH, SIG and HDH phases. At much higher temperatures, $T^* > 0.6$ and $T^* > 0.9$, the MDH and STR phases respectively are unstable and the system displays hard-disk like behaviour described by the FL at low densities and HDH at high densities with a two-phase coexistence region in between. We individually examine the formation and stability of each of these phases in the following sections.

7.3.1 Formation of the hexagonal phases

We begin with the formation of the three different hexagonal phases observed in this system. With the inherent presence of two length scales in the system, the presence of two hexagonal phases in the system is self-evident. The inter-particle distance in these two hexagonal phases is expected to correspond to the diameter of the core σ_{HD} and the diameter of the corona δ. However, at this shoulder width $\delta = 1.95\sigma_{HD}$, we observe three distinct hexagonal phases instead of the expected two! In order to investigate the formation of these three phases, we calculate their radial distribution function (RDF), $g(r)$ and plot them in Figure 7.3.

Consistent with the above expectation of the two hexagonal phases, we indeed notice that the first peak of the RDF of the HDH and LDH phases lies at a distance r that, respectively, equals σ_{HD} and δ. This confirms their inter-particle distances at the diameters of the core and corona, respectively. The puzzling question is the formation of the MDH phase. From the RDF, we note that the first peak corresponds to an inter-particle distance that lies in between the core and corona diameters, and the second peak corresponds to a distance that equals the corona diameter δ. This means that the corona limits the position of the second nearest neighbours and thus, results in the formation of the MDH. This difference in the inter-particle distance between the three structures can also be seen in terms of the overlaps of the coronas as observed in the configurations given in Figure 7.2. For the LDH phase, the corona of a particle is in contact with the coronas of its neighbouring particles. On the other hand, for the HDH phase the cores are in contact, i.e. the corona of the particle entirely overlaps with the core of its neighbouring particles. For the MDH structure, the corona of a particle just touches the corona of its second nearest neighbours.

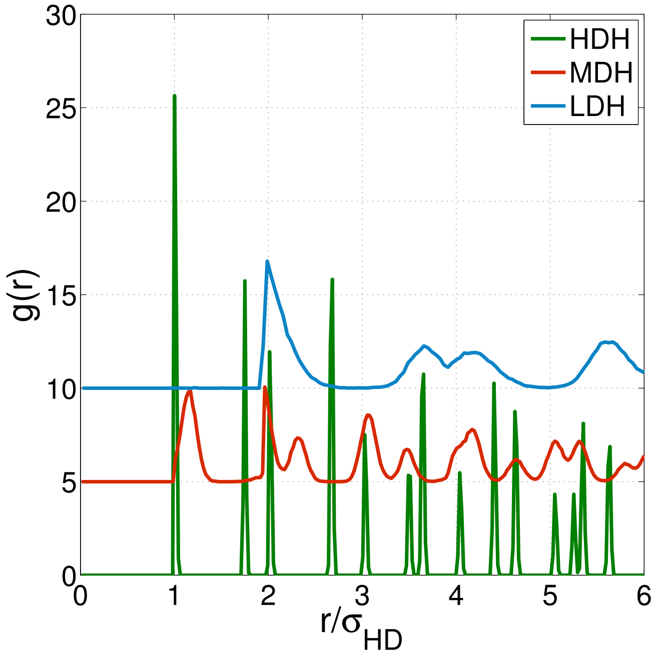

Figure 7.3: Radial distribution functions $g(r)$ calculated for the high-density (HDH), medium-density (MDH) and low-density (LDH) hexagonal phases. For clarity, we shifted the $g(r)$ of MDH in the vertical direction by $\Delta y = 5$ and that of LDH by $\Delta y = 10$.

7.3.2 Formation and stability of dodecagonal quasicrystals and its approximants

As previously mentioned, the chosen shoulder width $\delta = 1.95\sigma_{HD}$ is close to the value of $2\cos 15^\circ \approx \sqrt{2+\sqrt{3}} \approx 1.932$ at which random-tiling dodecagonal (12-fold symmetric) quasicrystals have been reported either theoretically and/or computationally in various systems [77, 123, 169, 190, 235]. Hence, we also expect the formation of a similar quasicrystal phase in the system under investigation.

In order to address this possibility, we obtain the equation of state (EOS) by expanding the system starting from a high-density hexagonal (HDH), a defect-free random tiling dodecagonal quasicrystal (HQC), or either of the two dodecagonal approximant crystals considered in this study, namely the sigma (SIG) phase and a square-triangle tiling of dodecagons (HAC). The high-density quasicrystal (HQC) structure is adapted from a non-Stampfli square-triangle approximant [84]. The HQC is similar in structure to the dodecagonal quasicrystal previously reported by Dotera *et al.* in a HCSS system at $\delta = 1.40\sigma_{HD}$ [123], but without the presence of any tiling defects as previously described in Chapter 3. The SIG structure is a periodic representation of the σ particle environment with a unit cell consisting of 32 particles. The high-density approximant crystal (HAC) is an adaptation of a repeated vertex substitution of the $(3^2.4.3.4)$ Archimedean tiling consisting of squares and triangles [85]. It has a unit cell of 56 particles and contains both σ and H particle environments. Figure 7.4 shows a comparison between the quasicrystal (HQC) and the two approximants, i.e. the SIG and HAC phase, where a representative configuration is given on the left and its accompanying tiling on the right. The

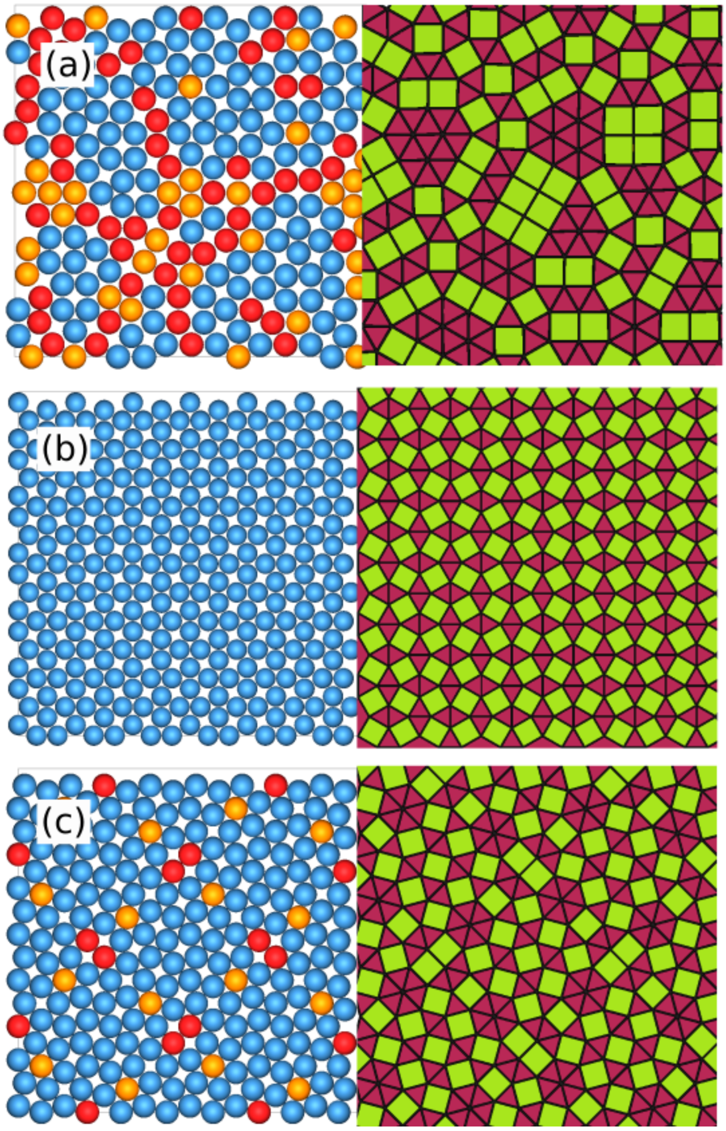

Figure 7.4: Structural difference between the dodecagonal quasicrystal and its approximants **(a)** defect-free random-tiling quasicrystal (HQC), **(b)** sigma (SIG), **(c)** square-triangle tiling of dodecagons (HAC). **(left)** A typical configuration is shown with the particles coloured according to their local particle environment (LPE) described in Section 7.2.3: H in red and σ in blue and particles not belonging to either in orange. **(right)** The tiling obtained by drawing bonds between the neighbouring particles.

particles in the configurations are coloured according to the LPEs described in Section 7.2.3. From this colouring, we can see that the HQC has a higher H/σ LPE ratio than the HAC. In the EOS calculations, we use a system size of 209 particles for the HQC, 288 particles for SIG, 224 particles for the HAC, and 256 particles for the HDH phase.

In Figure 7.5(a), we plot the EOS articulating the various expansion runs, i.e. decreasing pressure P^*, starting from the HDH, SIG and HQC phases. We exclude the EOS of the HAC phase for clarity as it is qualitatively similar to that of the HQC phase. From the EOS shown in Figure 7.5(a), we observe a single phase transition around $P^* = 30$ during the expansion of the SIG phase, i.e. upon decreasing pressure. However, in the case of the expansion of the HDH and HQC phases, we find an additional transition at pressures higher than $P^* = 30$ resulting into a structure with a density lower than that of the SIG phase. To investigate the nature of the resulting structure, we calculate the BOO parameter and determine the different LPEs in the system as explained in Section 7.2.3.

Let us first consider the behaviour of the BOO parameter of this system. We calculate the χ_6 and χ_{12} order parameters, which quantify the hexagonal and dodecagonal order in the system. In Figures 7.5(b), 7.5(c), and 7.5(d), we plot χ_6 and χ_{12} during the expansion of the HDH, SIG and HQC structures, respectively. During the expansion of the HDH phase in Figure 7.5(b), we find that χ_6 has a higher value than χ_{12} at higher ($48 \leq P^* \leq 70$) and lower ($15 \leq P^* \leq 33$) pressures, while χ_{12} is only slightly higher than χ_6 at intermediate ($33 < P^* < 48$) pressures. This implies the presence of three distinct regions of hexagonal, dodecagonal, and hexagonal order with increasing pressure. The decrease in χ_{12} during the expansion of the SIG phase in Figure 7.5(c) at $P^* = 30$ denotes a transition from dodecagonal to hexagonal order. The behaviour of χ_{12} during the expansion of the HQC phase in Figure 7.5(d) is peculiar. Upon decreasing the pressure, we find a drop in the value of χ_{12} at $P^* = 44$ coinciding with the discontinuity in the EOS; while that of χ_6 remains unchanged. This indicates the presence of two different structures of dodecagonal symmetry in between the two with a hexagonal order.

To differentiate between the two structures with dodecagonal symmetry, we calculate the fraction of H and σ particle environments. The fraction of H (f_H) and σ (f_σ) particle environments as a function of pressure obtained by expanding the HDH, SIG and HQC structures are respectively plotted in Figures 7.5(e), 7.5(f), and 7.5(g). In Figure 7.5(e) we notice a sizeable fraction of σ environments at intermediate pressures which conforms with the previously observed increase in χ_{12} at these pressures ($33 \leq P^* \leq 48$). The lower fraction of H environments in comparison to σ is also interesting to note. In Figure 7.5(f), we observe that the fraction of σ environments drops from one to zero at $P^* = 32$ during the expansion of the SIG phase and we do not observe any significant fraction of H environments. In Figure 7.5(g), the change in both the fraction of H and σ environments coincides with the decrease in χ_{12} at $P^* = 44$ during the expansion of HQC phase in Figure 7.5(d). However, we note that the fraction of H environments drops close to zero whereas the fraction of σ environments remains close to the previous non-zero value. Thus, considering the presence of a sizeable fraction of H-phase and a lower density than that of the SIG phase as shown by the EOS, we suggest that the HQC transforms to a σ-rich phase and not the SIG phase.

We further analyse the σ-rich phase by comparing the configurations obtained just before ($P^* = 44$) and after ($P^* = 43$) the transition during the expansion of HQC phase in Figure 7.6. The particle configuration is shown on the left and its accompanying tiling obtained by drawing bonds between the neighbouring particles is shown on the right. The inset shows the calculated diffraction pattern. It can be noted from the inset that both structures possess dodecagonal symmetry. Furthermore, we also note the difference between the tilings of the two structures: The HQC phase shown in Figure 7.6(a) consists of a square-triangle tiling while the σ-rich phase shown in Figure 7.6(b) consists of a square-triangle-shield tiling. Though the square-triangle tiling is the most common description of a dodecagonal quasicrystal tiling, tilings involving shields and/or rhombi are not uncommon [173, 179, 211, 230, 239]. Therefore, we term this σ-rich phase as a quasicrystal with shields (QCS). It is surmised that upon decreasing the pressure, the simultaneous decrease in density and preservation of the dodecagonal symmetry is made possible by the formation of shields which have a larger area than the combination of

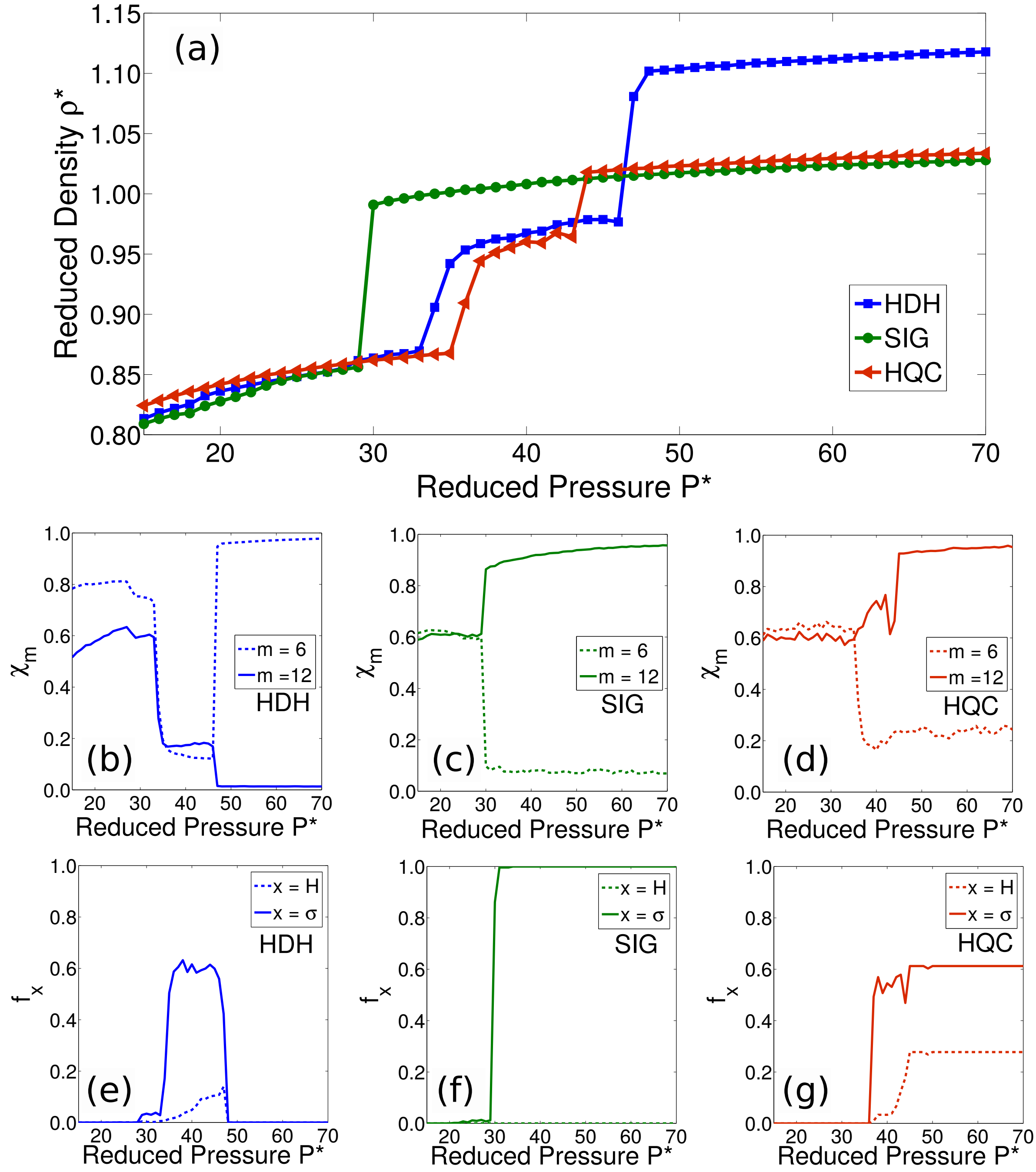

Figure 7.5: Formation of a 12-fold symmetric phase at $T^* = 0.20$ as obtained by expanding the high-density hexagonal (HDH), sigma (SIG) and random-tiling dodecagonal quasicrystal (HQC) phase in a HCSS system with shoulder width $\delta = 1.95\sigma_{HD}$. **(a)** Density $\rho^* = N\sigma_{HD}^2/A$ (equation of state), **(b, c, d)** bond orientational order (BOO) parameter χ_6 and χ_{12}, and **(e, f, g)** fraction of H and σ environments, f_H and f_σ, as a function of the reduced pressure $P^* = \beta P\sigma_{HD}^2$.

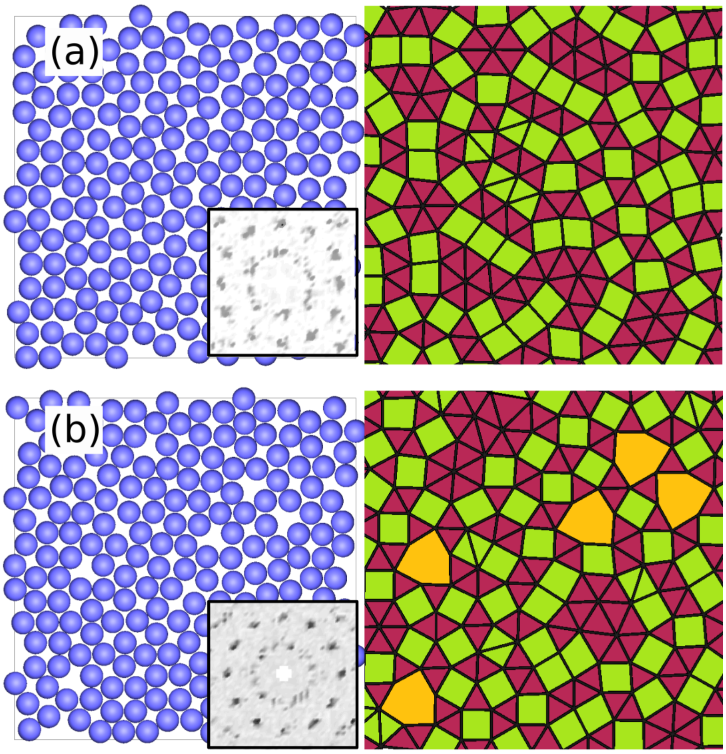

Figure 7.6: Structural difference between the two random-tiling dodecagonal quasicrystals with **(a)** square-triangle tiling (HQC) at $P^* = 44$ **(b)** square-triangle-shield tiling (QCS) at $P^* = 43$ for a HCSS system with shoulder width $\delta = 1.95\sigma_{HD}$ at temperature $T^* = k_B T/\varepsilon = 0.20$. A typical configuration is shown on the left with the calculated diffraction pattern in the inset. The tiling obtained by drawing bonds between the neighbouring particles is given on the right.

squares and triangles. In summary, we find four structures with dodecagonal symmetry, i.e. the two approximant crystals, which are the sigma (SIG) phase and the square-triangle tiling of dodecagons (HAC), and the high-density random-tiling dodecagonal quasicrystal (HQC) with a square-triangle tiling and the quasicrystal with shields (QCS).

Subsequently, we deduce the stable phases by calculating the free energies and employing common tangent constructions as explained in Section 7.2.2. In Figure 7.7(a), we show the common tangent construction between the SIG and the MDH phase at temperature $T^* = 0.20$ and in Figure 7.7(b), between the SIG and HDH phases at $T^* = 0.70$. In both these figures, we plot the Helmholtz free energy per unit area $\beta F/A$ as a function of reduced density ρ^*. We then subtract a linear fit $\rho\mu_c - P_c$ from the free energy, where μ_c is the bulk chemical potential of the coexisting phases at pressure P_c. This ensures that the ‘resulting’ free energy of the two-phases between which the common-tangent is drawn is zero at the coexistence densities. In other words, the phases with a positive free energy in this plot are meta-stable with respect to the concerned two-phase coexistence. Based on this, it is conspicuous from both Figure 7.7(a) and Figure 7.7(b) that the SIG is more stable than all other phases exhibiting dodecagonal symmetry, namely the HAC, HQC and QCS phases. Also, as (not) shown in Figure 7.7(b), we do not find the formation of the QCS phase at higher temperatures.

It is intriguing to note that the free energy of the phases under the present conditions (SIG $<$ HAC $<$ HQC) contrasts to that reported at $\delta = 1.40\sigma_{HD}$ in Chapter 3, where the free en-

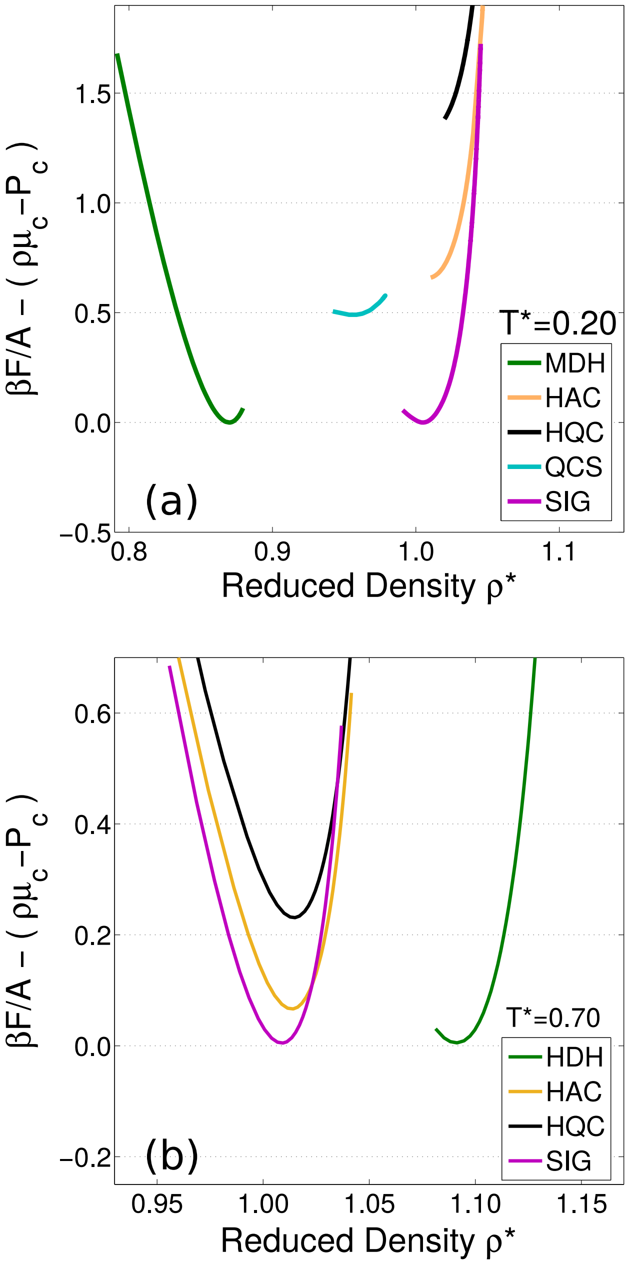

Figure 7.7: Common tangent construction to determine the stable phases in the HCSS system with shoulder width $\delta = 1.95\sigma_{HD}$. The common tangent is constructed between **(a)** MDH and SIG phases at $T^* = 0.20$, and **(b)** the SIG and HDH at $T^* = 0.70$. The plot shows the Helmholtz free energy per unit area $\beta F/A$ as a function of reduced density $\rho^* = N\sigma_{HD}^2/A$. A linear fit $\rho\mu_c - P_c$ is subtracted from the free energy, where μ_c and P_c are the bulk chemical potential and bulk pressure at the (a) MDH-SIG and (b) HDH-SIG phase coexistence. The involved phases are the medium- (MDH) and high-density hexagonal (HDH) and the sigma (SIG). Other phases exhibiting 12-fold symmetry that are plotted are the approximant crystal (HAC) and the random-tiling quasicrystal with a square-triangle (HQC) and a square-triangle-shield (QCS) tiling. The reduced temperature is expressed as $T^* = k_B T/\varepsilon$.

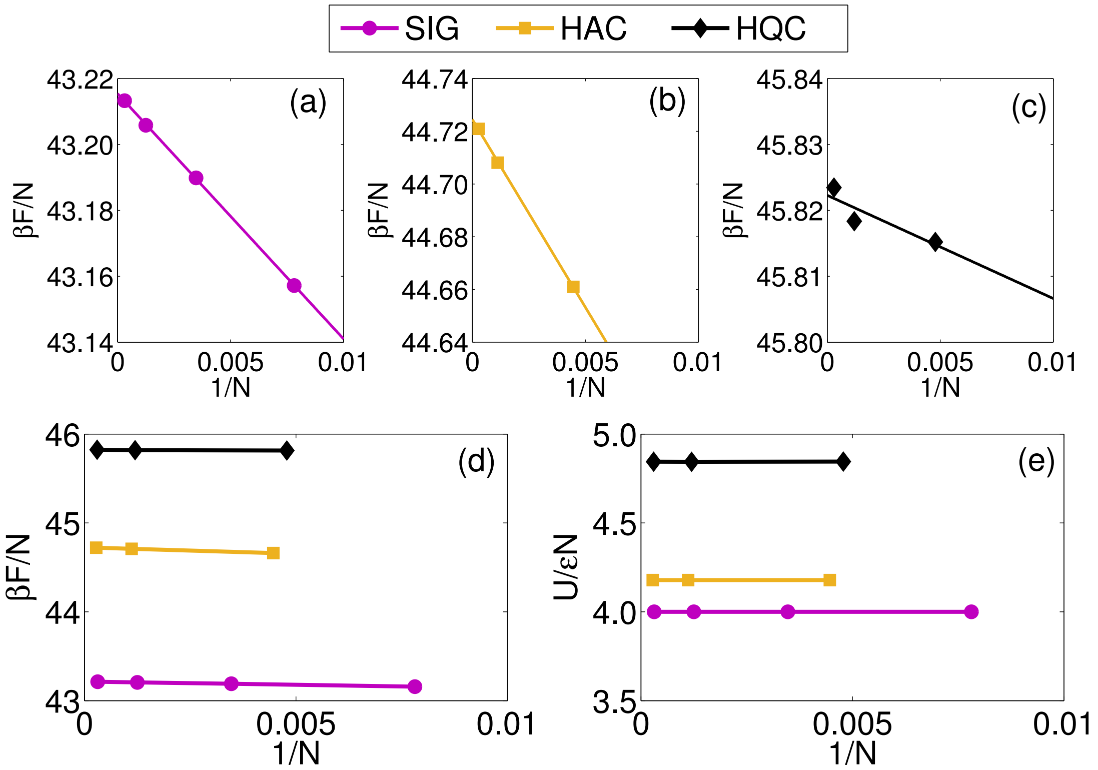

Figure 7.8: Variation of Helmholtz free energy per particle $\beta F/N$ as a function of inverse of the system size N for **(a)** sigma (SIG), **(b)** approximant (HAC), **(c)** quasicrystal (HQC) phases, and **(d)** combined view of all three phases. **(e)** Variation of potential energy per particle $U/\varepsilon N$ as a function of system size. The values were calculated for the phases with a density $\rho^* = N\sigma_{HD}^2/A = 1.03$ at a temperature $T^* = 0.11$ for the HCSS system with shoulder width $\delta = 1.95\sigma_{HD}$. The lines in (a, b, c) are linear fits of the data points.

ergy increased in the order of HQC $<$ HAC $<$ SIG. To further investigate this, we first eliminate the effect of finite system size on the free energy. To do so, we evaluate the variation in potential energy and Helmholtz free energy as a function of system size for these three phases. Figure 7.8 shows the calculations performed at $\rho^* = 1.03$ and $T^* = 0.11$ at different system sizes. In Figures 7.8(a)-(c), we individually show the variation in free energy per particle as a function of inverse system size for the SIG, HAC and HQC phases. Figure 7.8(d) is a combination of these three plots. We can extrapolate the free energy to the thermodynamic limit $1/N \to 0$ by calculating the intercept of these curves. We obtain the following values of bulk free energies, $\beta F/N \sim 43.22$ (SIG), 44.73 (HAC) and 45.82 (HQC). This shows that the SIG phase has the lowest free energy among the three phases. We also find that the difference between the free energies of the three phases is much larger than the variation in the free energy of individual phases as a function of system size. The surprising part is the difference in potential energy per particle in these phases as shown in Figure 7.8(e). As previously studied in Chapter 3, the potential energy per particle for these phases at $\delta = 1.40\sigma_{HD}$ is similar. However, here, we find the potential energy increases in the order SIG $<$ HAC $<$ HQC. This is, obviously, caused by the difference in the shoulder width of these two systems. For the system at $\delta = 1.40\sigma_{HD}$, only the nearest neighbours contribute to the potential energy of the particles. However, in the present system with $\delta = 1.95\sigma_{HD}$, the second nearest neighbours of particles at a distance $1.40\sigma_{HD} < r < 1.95\sigma_{HD}$ also contribute to the potential energy. In other words, not only does the composition of a structure in terms of its LPE matters, but also the arrangement of neighbouring LPEs affects the potential energy. We find that the SIG phase, with the least random LPE arrangement, has the lowest potential energy, thereby making it the thermodynamically stable structure among these three, followed by the HAC and HQC phases.

Even though we have seen than the SIG phase has a lower free energy than the HQC and QCS phases, it is important to point out here that the presence of phasonic movements in these tilings contribute to the configurational entropy of these quasicrystals [171, 179, 240]. In case of the HQC, the configurational entropy that accounts for the distinct number of configurations has a maximum value of $S_{\text{config}}/k_BA = 0.12934$ [178], which is much smaller than the difference between the free energies of the SIG and HQC phases. Considering this value, we do not expect the configurational entropy of the square-triangle-shield tiling to exceed the difference between the free energies of the SIG and QCS phase, i.e. $S_{\text{config}}/k_BA > 0.5$. We thus conclude that the SIG phase is thermodynamically more stable than all the other phases with dodecagonal symmetry considered in this study, namely HAC, HQC and QCS phases.

7.3.3 Formation of the stripe phase

The most striking feature of the phase diagram presented in Figure 7.2 is the phase behaviour observed at low densities and temperatures, especially the formation of the stripe (STR) phase. Such spontaneous pattern formations are observed in core-corona systems when the size of the corona is similar or much larger than that of the core [136–140].

Stripe formation in purely repulsive systems is driven by the minimisation of the system's potential energy. The configuration of the STR phase as given in Figure 7.2 shows that each particle has overlapping coronas with two other neighbouring particles along the stripe. However, the stripes are spaced such that the distance between them is larger than the size of the corona and thus, there is no overlap between the coronas between adjacent stripes. In other words, the effective repulsive length scales are the diameter of the hard core σ_{HD} along the stripes and the soft-shoulder diameter δ orthogonal to the stripes. As a consequence, each particle essentially has only two neighbours. This is energetically more favourable than a structure with equally spaced particles in which the shoulder of each particle partially or completely overlaps with all of its neighbours.

In order to study the formation of the STR phase in the system, we first obtain the EOS of the different phases by compressing the system starting from an isotropic fluid phase and by expanding the system starting with the HC and MDH phases. In Figure 7.9, we plot the EOS obtained at temperatures $T^* = 0.18$, 0.15 and 0.12. First, we recognise the formation of two hexagonal phases: (1) The LDH phase sandwiched in between two FL phases by two first-order phase transitions at temperature $T^* = 0.12$ and (2) the MDH at higher densities, for which at all three temperatures the EOSs lie on top of each other (and thus are not individually identifiable in the figure). The EOS of the HC phase at $T^* = 0.12$ and 0.15 lie on top of each other, whereas the HC is not stable at $T^* = 0.18$. We also notice first-order phase transitions between the HC and the STR at $T^* = 0.12$, 0.15 and between MDH and FL at $T^* = 0.18$. The confounding feature of the EOS at all these temperatures is the continuous transition from the FL phase to the STR phase. This also applies to the further re-entrant transition from the STR phase to the FL phase with increasing density at the highest temperature $T^* = 0.18$. The only observed development in the EOS is the change in slope during these transitions. However, this cannot be used to determine the transition from the FL to the STR phase and we therefore resort to order parameters. The parameters used for this include the number of clusters in the system, the number of neighbours of the particles in the system and the anisotropic scaling index method as described in Section 7.2.3. The method of calculation and behaviour of these three parameters during this phase transition are explained below.

The first parameter we use is the normalised cluster size N_c/N as a function of pressure P^*, where N_c is the average cluster size in number of particles and N is the total number of particles in the system. In other words, the normalised cluster size N_c/N is the inverse of the number of clusters in the system and varies from approximately zero in case of the FL phase to unity in case of the STR phase. The second parameter consists of studying the probability distribution of the average number of neighbours per particle $P(N_n)$ at different pressures P^*. The basis of using this as an order parameter emerges from the fact that the particles in the STR phase have on an average two neighbours, which is not a requisite in the FL phase. Finally, the scalar order parameter $\Delta\alpha$ is the difference between the distributions of $P_\perp(\alpha)$ and $P_{||}(\alpha)$. The distributions coincide with each other for an isotropic structure like the fluid phase, but not for an anisotropic structure like the stripe phase. Thus, $\Delta\alpha$ is non-zero for anisotropic structures and it vanishes for isotropic structures. We believe that as each of these three parameters address a different

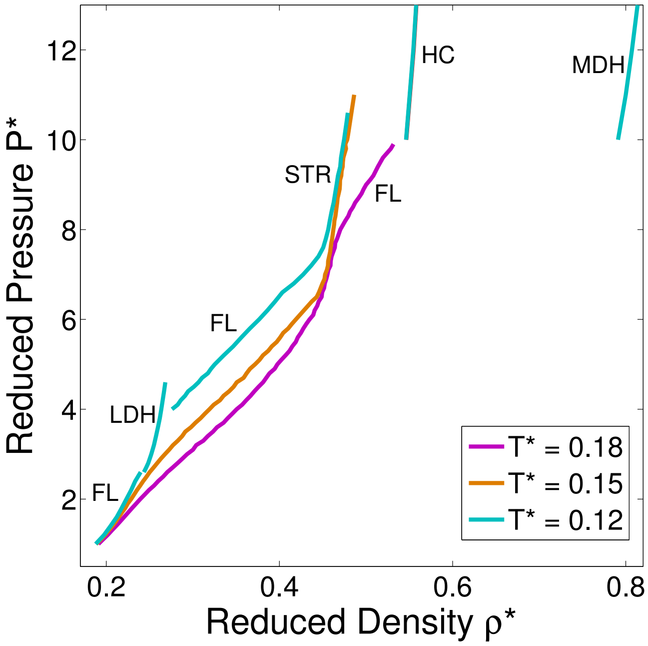

Figure 7.9: Equation of state (pressure $P^* = \beta P \sigma_{HD}^2$ as a function of density $\rho^* = N\sigma_{HD}^2/A$) of a HCSS system with shoulder width $\delta = 1.95\sigma_{HD}$ at temperatures $T^* = k_B T/\varepsilon = 0.18$, 0.15, and 0.12. The phases observed are fluid (FL), low-density hexagonal (LDH), stripe (STR), honeycomb (HC) and medium-density hexagonal (MDH). The equations of state of the MDH phase at all three temperatures lie on top of each other. The equations of state of the HC phase at $T^* = 0.12$ and 0.15 also lie on top of each other, while this phase is absent at $T^* = 0.18$.

property of the system and especially of the STR phase; we obtain complementary insights about the STR phase by investigating all of them.

Let us begin with addressing the formation of the STR phase from the FL phase. As shown in the EOS in Figure 7.9, this fluid-to-stripe (FL-STR) phase transition was observed at all three temperatures studied. Here, we will explore this transition at $T^* = 0.15$. The various aspects of monitoring this phase transition is shown in Figure 7.10. Let us first take a qualitative look at this transition by observing the typical configurations obtained using Monte Carlo simulations at different pressures. This is shown in Figures 7.10(a)-(d). Each cluster is represented in a different colour. As shown in Figures 7.10(b)-(c), a cluster can also consist of multiple strings. From Figures 7.10(a)-(d), we see that the number of clusters decreases with increasing pressure and that the stripes essentially form a percolating cluster. We can differentiate between the FL and the STR phase using the calculated diffraction pattern shown as insets; the ones corresponding to the FL phase show the presence of isotropic rings, while that of the STR phase shows spots which are arranged in layers. We, therefore, can use the number of clusters in the system as a parameter to determine the FL to STR transition. In Figure 7.10(e), we present the resulting cluster size distribution as a function of pressure P^*. We notice that the distribution exhibits a rapid change to unity at $P^* \sim 6.2$ indicating the formation of a single cluster in the system. However, the formation of a percolating cluster does not entirely refer to the formation of a STR phase. Thus, in this same plot, we also show the variation of the scalar order parameter $\Delta\alpha$ as a function of pressure P^*. As previously discussed, a non-zero value of $\Delta\alpha$ relates to an anisotropic layered structure. We indeed do notice that $\Delta\alpha$ becomes non-zero close to the transition pressure of the cluster size distribution confirming the phase formed to be STR and then vanishes at $P^* \sim 10.9$ with the formation of the MDH phase. Furthermore, we verify the string nature of these layers by studying the probability distribution of the average number of neighbours per particle $P(N_n)$ as a function of the number of neighbours N_n at different pressures P^*. This is shown in Figure 7.10(f), where the pressures correspond to the ones in Figures 7.10(a)-(d). As expected, the average number of neighbours per particle increases with increasing pressure. The average number of neighbours per particle N_n goes from zero in the FL phase at $P^* = 1.0$ to unity at $P^* = 3.8$ and to a value of two at $P^* = 7.3$, where the STR phase is observed. This verifies the energetic driving force of the formation of the STR by having only two nearest neighbours per particle.

Now, let us study the inverse transition, i.e. formation of the FL phase from the STR phase at higher densities. As shown in the EOS in Figure 7.9, of the three temperatures studies, we observe this stripe-to-fluid (STR-FL) phase transition only at $T^* = 0.18$. Similar to the previous case, we show the various aspects of this phase transition in Figure 7.11. In Figure 7.11(a), we show the behaviour of N_c/N and $\Delta\alpha$ as a function of pressure P^*. As expected, we notice the discontinuous change of N_c/N to unity with the formation of a single cluster and the non-zero value of $\Delta\alpha$ signalling a stripe phase at pressures $5.9 < P^* < 8.3$. Then, we analyse the probability distributions of neighbours $P(N_n)$ at different pressures P^* given in Figure 7.11(b). For convenience and comparison, typical configurations corresponding to these pressures are given in Figures 7.11(c)-(f). Here, the particles are coloured according to the number of neighbours in contrast to Figure 7.10, where the colours denote distinct clusters. The colour legend is at the bottom of the figure. From the $P(N_n)$ distributions and the particle configurations, we observe that the STR phase with $N_n = 2$ is obtained at reduced pressure $P^* = 7.0$ and at the highest pressure of $P^* = 10.1$, the system forms a hexagonal structure with

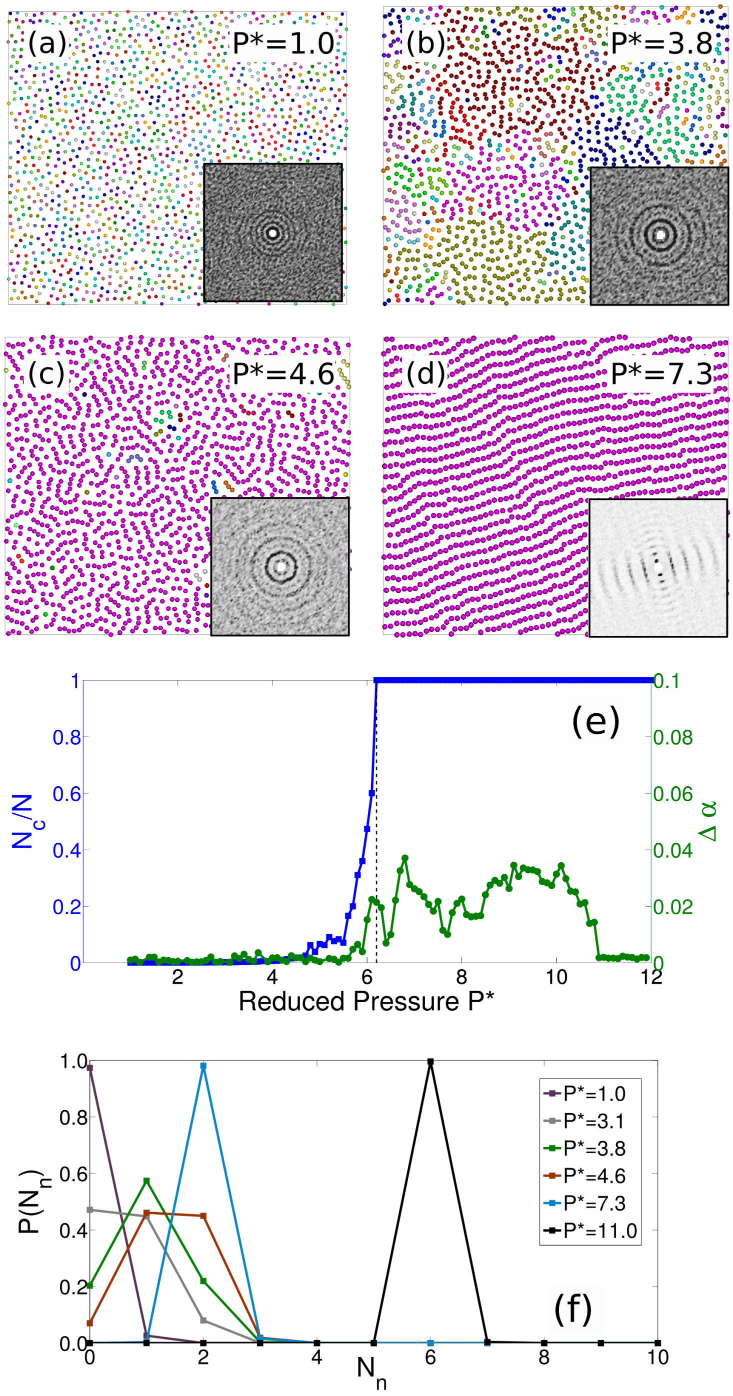

Figure 7.10: Monitoring the fluid-to-stripe (FL-STR) phase transition in a HCSS system with shoulder width $\delta = 1.95\sigma_{HD}$ at temperature $T^* = k_B T/\varepsilon = 0.15$. **(a-d)** Typical configurations as obtained from Monte Carlo simulations at different reduced pressures $P^* = \beta P \sigma_{HD}^2$ as labelled. Colours represent different clusters. **Insets** show the corresponding diffraction patterns. **(e)** The normalised cluster size N_c/N and the scalar order parameter $\Delta\alpha$ as a function of the reduced pressure P^*. N_c is the average cluster size and N is the total number of particles in the system. **(f)** Probability distributions of the number of nearest neighbours per particle $P(N_n)$ at varying pressures P^* as labelled.

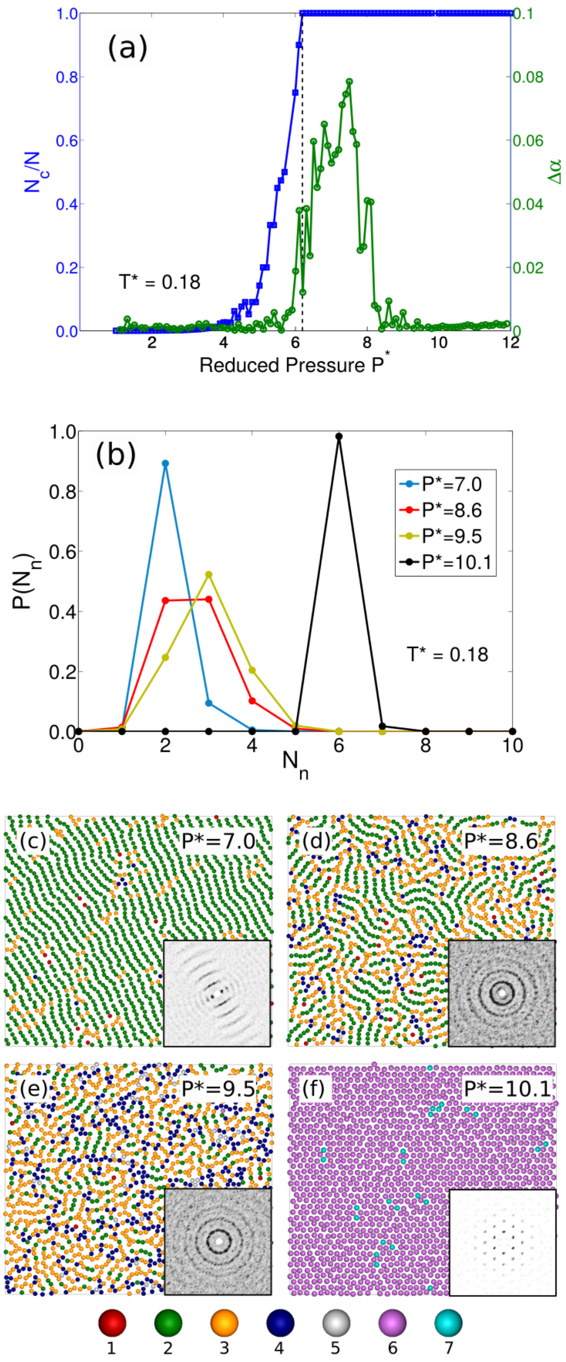

Figure 7.11: Monitoring the stripe-to-fluid (STR-FL) phase transition in a HCSS system with shoulder width $\delta = 1.95\sigma_{HD}$ at temperature $T^* = k_B T/\varepsilon = 0.18$. **(a)** The normalised cluster size N_c/N and the scalar order parameter $\Delta\alpha$ as a function of the reduced pressure $P^* = \beta P \sigma_{HD}^2$. N_c is the average cluster size and N is the total number of particles in the system. **(b)** Probability distributions of the number of nearest neighbours per particle $P(N_n)$ at varying pressures P^* as labelled. **(c-f)** Typical configurations as obtained from Monte Carlo simulations corresponding to the pressures P^* in (b). The particles are coloured according to the number of neighbours as shown in the legend at the bottom of the panel. **Insets** show the corresponding diffraction patterns.

$N_n = 6$. As evident from the diffraction pattern given in the insets of Figures 7.11(d) and 7.11(e), a FL phase is formed at pressures intermediate to these. From the $P(N_n)$ distribution given in Figure 7.11(b), we note that the FL phase has an average of three neighbours per particle and starts to form at $P^* = 8.6$. The ‘coexisting’ nature of this structure with FL and STR is evident from Figure 7.11(d), where short stripe segments in green are connected by yellow and blue particles. This implies that the stripes become shorter as the system becomes more fluid-like with increasing pressure.

The above observations of discontinuity in the N_c/N and $\Delta\alpha$ distributions and the coexisting nature of the $P(N_n)$ at certain pressures hint at a first-order transition between the FL and STR phases. However, to ascertain this speculation further, we assess the FL-STR transition by using the specific heat at constant volume C_v as described in Section 7.2.2 and the fraction of defects. Defects in the structure are defined as particles which have other than two neighbouring particles. We study the system at constant density $\rho^* = 0.46$, where we find that the system undergoes a sharp transition from a STR phase to a FL phase upon increasing the temperature. The C_v as a function of temperature T^* is plotted in Figure 7.12(a). In Figure 7.12(b), we plot the variation of the fraction of defects along the same transition. The C_v shows a λ-shaped cusp around the transition temperature $T^*_{\text{STR-FL}} = 0.187$, from which one may conclude that the transition is likely first-order in nature. However, even though we find a substantial difference between the fractions of defects in the STR and FL phases, the change from STR to FL is not as abrupt as in case of C_v. This change in the fraction of defects extends over a range of temperatures between $T^*_{\text{STR-FL}} \pm 0.01$. This difference between the two phases in terms of the defects is shown in Figure 7.12(c) and 7.12(d). Here, we show the configurations obtained at temperatures $T^* = 0.18$ and 0.19, where the particles are coloured according to the number of neighbours as given in the legend at the bottom of the figure. At temperatures lower than $T^*_{\text{STR-FL}}$, a single percolating network of parallel stripes mostly containing two neighbouring particles is observed and at temperature $T^* > T^*_{\text{STR-FL}}$, the particles form winding structures consisting of small segments of stripes. This continuous melting of the STR phase to an isotropic FL fluid phase mediated by defects (dislocations or disclinations) bears resemblances to the scenario studied in detail by Toner and Nelson [241, 242], also known as the Kosterlitz-Thouless (K-T) transition. In general, the K-T transition can be described to occur between a phase with order in the orientation of the bond angles and a phase which is devoid of such an order.

Thus, we evaluate if the STR phase possess a two-fold bond orientational symmetry and subsequently analyse the STR to FL phase transition by calculating the positional correlation function $g(r)$ and bond orientational correlation function $g_2(r)$. These correlation functions as a function of temperature are given in Figures 7.13(a) and 7.13(b). Firstly, we observe that the positional correlation function shown in Figure 7.13(a) decays exponentially through the entire range of temperatures. This indicates that both the STR and the FL phases do not possess long-range positional order. Further, the bond orientational correlation function plotted in Figure 7.13(b) reaches a constant value at lower temperatures indicating that the STR phase formed at these temperatures possess quasi long-range bond orientational order, i.e. two-fold rotational symmetry. With increasing temperature, the bond orientational correlation function starts to decay rapidly. This represents the loss of the bond orientational order in the system. Consequently, the transition from the STR to the FL phase can be described as a elimination of the bond orientational order of the system, i.e. a K-T transition. Additionally, we also verify if the same

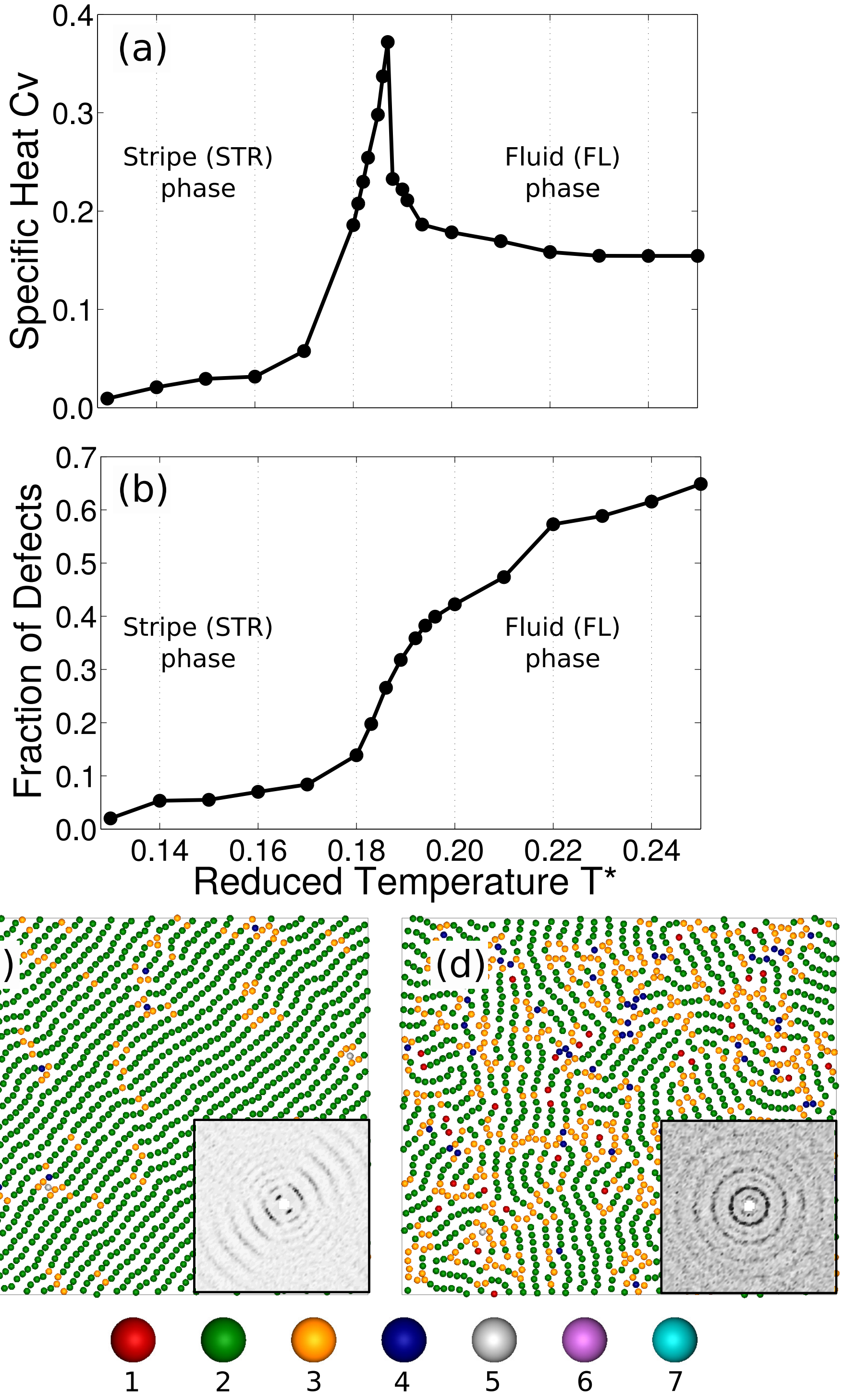

Figure 7.12: Phase transition from the stripe (STR) phase to the fluid (FL) phase for a HCSS system with a shoulder width $\delta = 1.95\sigma_{HD}$ and density $\rho^* = N\sigma_{HD}^2/A = 0.46$: **(a)** Specific heat C_v at constant volume and **(b)** fraction of defects as a function of reduced temperature T^*. Typical configurations obtained at temperature $T^* = k_B T/\varepsilon =$ **(c)** 0.18, and **(d)** 0.19, where the particles are coloured according to the number of neighbours as shown in the legend at the bottom of the figure.

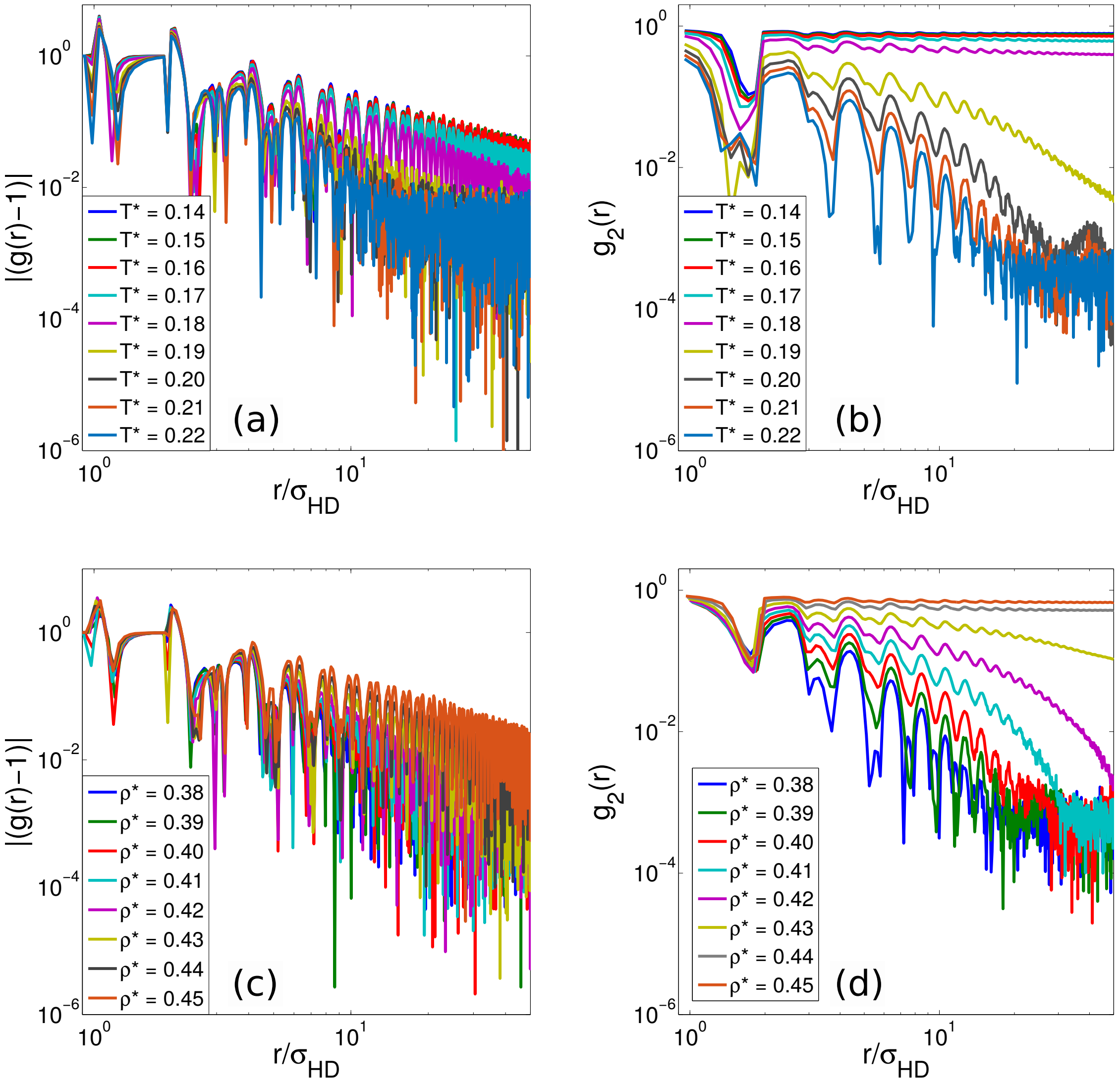

Figure 7.13: **(a,c)** Positional correlation function $|g(r)-1|$ and **(b,d)** bond orientational correlation function $g_2(r)$ describing the phase transition from the stripe (STR) phase to an isotropic fluid (FL) phase for a HCSS system with a shoulder width $\delta = 1.95\sigma_{HD}$ calculated at: (a,b) different temperatures at constant density $\rho^* = N\sigma_{HD}^2/A = 0.46$ and (c,d) different densities at temperature $T^* = k_BT/\varepsilon = 0.15$. All plots are in log-log scale.

holds for the FL to STR transition described in Figure 7.10. For this, we plot the positional and bond orientational functions at varying densities for a constant temperature $T^* = 0.15$. This is given in Figures 7.13(c) and 7.13(d). We, again, observe the presence of quasi-long range bond orientational order correlations in the STR phase and the absence of long-range positional order in both the STR and FL phases, thereby providing support for a K-T phase transition. Also, the density at which the transition from the FL to the STR phase takes place, i.e. $\rho^* \sim 0.43$, agrees well with the phase diagram given in Figure 7.2.

In conclusion, we find that the STR phase displays quasi-long range bond orientational order and short-range positional order which melts to an isotropic FL phase with neither bond-orientational nor positional order upon increasing the temperature or decreasing the density. Although we observe a sharp cusp in the specific heat C_v, the continuous change in the defect concentration as well as the loss of bond orientational order provide evidence for a K-T transition.

7.3.4 Stability of the honeycomb phase

Another interesting feature of this system is the formation of a honeycomb (HC) phase wedged between the stripe (STR) and medium-density hexagonal (MDH) phases. HC phases have previously been reported to form in patchy colloids [227], DNA nanostructures [243, 244] and binary mixtures of particles under external electric [218, 219] and magnetic fields [223]. Thus, it is fascinating that our mono-disperse core-corona system with no external forces forms a stable honeycomb lattice. In this core-corona system, formation of the HC phase from the STR phase with increasing density is a logical step forward. This can be seen as an increase in the number of neighbours per particle from two in the STR to three in the HC phase. In order to evaluate the thermodynamic stability of the HC phase, we plot the chemical potential $\beta\mu$ of the STR, HC and MDH phases, as obtained from the free-energy calculations, as a function of pressure $P^* = \beta P \sigma_{HD}^2$. In Figure 7.14, we show this plot at $T^* = 0.15$. As expected, we find that the HC phase is more stable than the STR-MDH two-phase coexistence.

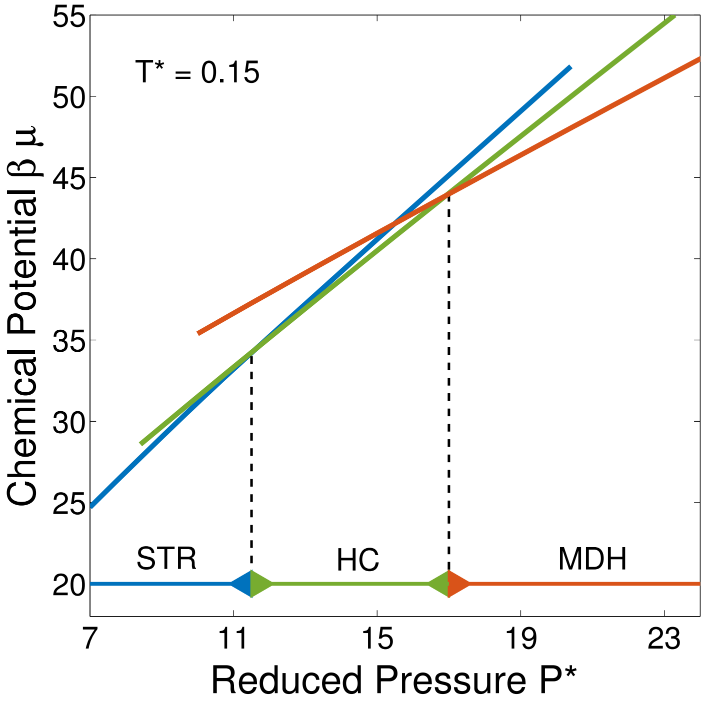

Figure 7.14: The chemical potential $\beta\mu$ as a function of reduced pressure $P^* = \beta P \sigma_{HD}^2$ at temperature $T^* = k_B T/\varepsilon = 0.15$ for the HCSS system with $\delta = 1.95\sigma_{HD}$. The stable phases are stripe (STR), honeycomb (HC) and medium-density hexagonal (HDH). The arrows at the bottom denote the phase stability regions.

The enigma in the stability of the HC phase is introduced by the previous report of formation of a low-density dodecagonal quasicrystal (LQC) by Dotera *et al.* [123]. This quasicrystal was reported to form when cooling a hexagonal phase with density $\rho^* = 0.55$ to a lower temperature $T^* \leq 0.154$ [123]. However, these conditions of density and temperature correspond to the stability region of the HC phase calculated above. In order to determine which of these two phases, LQC and HC, is indeed stable, we perform direct coexistence simulations. We started the simulations by juxtaposing LQC structure with $\rho^* = 0.55$ and MDH structure with $\rho^* = 0.79$ in a simulation box which results in a overall density of $\rho^* = 0.65$. This initial configuration is shown in Figure 7.15(a). The particles here are coloured according to the number of neighbours given in the legend at the bottom. The diffraction pattern given in the inset confirms the dodecagonal symmetry of the LQC. The final configuration obtained from the simulation is given in Figure 7.15(b). We observe that the LQC has transformed to the HC phase as corroborated by the particle neighbours and the corresponding diffraction pattern. This confirms that the HC phase is thermodynamically stable and that the LQC is, in fact, kinetically formed in the two-phase coexistence region between the HC and MDH phases.

7.4 Conclusions

To summarise, we study the phase behaviour of a system consisting of particles with a core-corona molecular architecture using Monte Carlo simulations and free-energy calculations. The model is described by an inter-particle pair potential consisting of a hard core of diameter σ_{HD} and a purely repulsive soft shoulder of diameter $\delta = 1.95\sigma_{HD}$. We observe a rich phase behaviour consisting of a fluid phase, a striped mesophase, honeycomb, sigma and three distinct hexagonal phases. We find the different phases are energetically stabilised.

At higher densities, we find that the sigma phase is energetically stabilised with respect to the random-tiling dodecagonal quasicrystals with square-triangle and square-triangle-shield tilings and the square-triangle approximant. This is in contrast to the entropic stabilisation of the random-tiling dodecagonal quasicrystal consisting of squares and triangles previously reported at $\delta = 1.40\sigma_{HD}$ in Chapter 3. Due to the larger shoulder width, the position of particles beyond the second nearest neighbours play an important role in the potential energy of the concerned structure. Thus, in contrast to the system at $\delta = 1.40\sigma_{HD}$, there exists a difference in potential energies between the sigma phase, the quasicrystal and the approximant resulting from a variation in the arrangement of their local particle environments.

At lower densities, the formation of these phases is driven by minimising the number of neighbours per particle. This results in the formation of stripe and honeycomb phases which respectively have two and three neighbours. It is interesting to point out that the next logical structure with four neighbours, i.e. square, is not formed in our system [219, 227]. Instead we find the formation of a six particle-coordinated medium-density hexagonal phase. This is because the square shoulder of the central particle of a square encompasses also the diagonal particles, which results in eight neighbours per particle. Thus, this does not provide any energetic incentive over the hexagonal structure. Further, we deduce that the low-density dodecagonal quasicrystal structure that was previously reported for this system [123] is in fact metastable. It is formed in the two-phase coexistence region of the honeycomb and medium-density hexagonal phase.

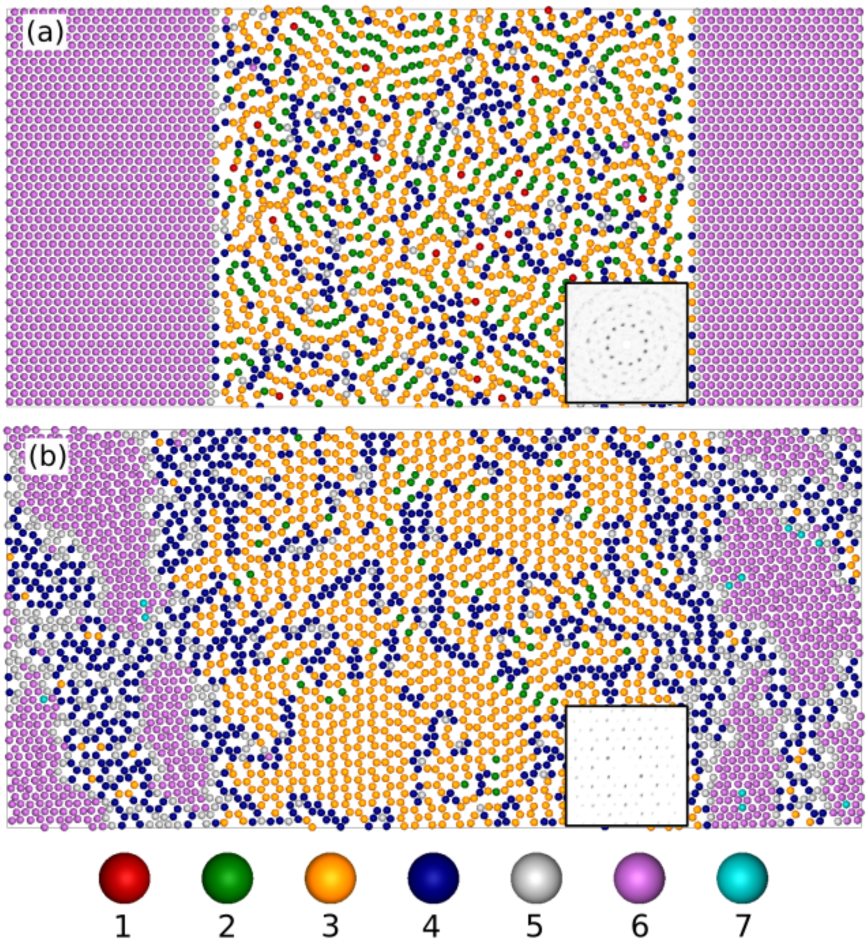

Figure 7.15: Direct coexistence simulations carried out to evaluate the relative stability between the low-density quasicrystal (LQC), honeycomb (HC) and medium-density hexagonal (MDH) phases at a temperature $T^* = k_B T/\varepsilon = 0.15$ and density $\rho^* = N\sigma_{HD}^2/A = 0.65$. **(a)** Initial configuration consisting of MDH and LQC, and **(b)** final configuration consisting of MDH and HC phases. The particles are coloured according to the number of neighbours as shown in the legend at the bottom of the figure. The insets show the diffraction patterns calculated for the non-MDH region of the simulation box.

In addition to the interesting phase behaviour of these phases, the honeycomb [63] and sigma [232] phases are interesting for their applications as photonic crystals. We hope that our results confirming the formation of stripe, honeycomb and sigma phases at different densities in a single system will stimulate experimental investigations on the phase behaviour and self-assembly of such systems containing particles with a core-corona architecture.

Acknowledgements

I thank Vasileios Pyrimidis and Guido Avvisati for critical reading of this chapter and helping me with the cluster identification algorithm. I thank Guido Avvisati also for introducing the anisotropic scaling method to me.

Part III

Photonic properties of quasi-periodic and periodic crystals

8

Photonic properties of a two-dimensional dodecagonal quasicrystal and its approximants

We investigate the photonic properties of a two-dimensional dodecagonal (12-fold symmetric) quasicrystal and four of its periodic approximants. We consider configurations consisting of a material with a high-dielectric constant arranged in the form of rods, walls and connected networks of walls and rods, in a medium with a low-dielectric constant. Our results show that all structures possess transverse magnetic (TM) band gaps in the rod configurations and transverse electric (TE) band gaps in the wall configurations. We find that the local symmetry of the structures has a greater influence on the formation of band gaps in the TE than in the TM polarisation. In addition, we also find that the approximants possess a complete (TM+TE) band gap in the network configuration.

8.1 Introduction

Photonic band gap (PBG) materials are structures composed of two or more materials with different dielectric constants that are arranged in a way that the propagation of specific wavelengths of light through such a structure is forbidden [20, 21]. Although conventional periodic photonic crystals in two- and three-dimensional systems have been studied since long, studies on quasiperiodic photonic crystals have recently gathered interest. The reason is that photonic quasicrystals, which have a long-range orientational order but no translational periodicity, possess higher rotational symmetry than a periodic photonic crystal like simple square or hexagonal lattices in two-dimensional systems which exhibit only four- or six-fold symmetry. Upon increasing the rotational symmetry of the structure, the Brillouin zone becomes more isotropic resulting in the formation of a complete photonic band gap [78]. A photonic band gap in the visible or near-infrared region was reported by Zoorob *et al.* [91] in a dodecagonal (12-fold symmetric) quasicrystal constructed by drilling air holes in a dielectric slab. Even though the validity of this result is debated [92], it is generally well accepted that quasicrystals do form photonic band gaps when the dielectric contrast between the two materials is sufficiently high [86, 92, 245]. Consequently, photonic band gap formation has been investigated in a variety of quasicrystalline structures by both theoretical and experimental studies [90, 246, 247]. Research on photonic quasicrystals is largely limited to two-dimensional systems, but recently three-dimensional icosahedral photonic quasicrystals were fabricated with band gaps in the microwave [93], infrared [94] and visible ranges [95].

Theoretical investigations of PBG materials are often based on periodic dielectric structures, for which the band structure is calculated using the plane wave expansion technique [22] or the Korringa-Kohn-Rostocker (KKR) method [248]. These techniques, however, cannot be employed for quasicrystals, which are by definition aperiodic [245]. Possible ways to solve this is by either studying the photonic properties of periodic approximants of the quasicrystals [88, 249–251] and related Archimedean tilings [68, 232, 252, 253] or by constructing a pseudo-Brillouin zone for the quasicrystals [254]. However, in both cases, the numerical calculations are computationally challenging as the size of the unit cell becomes quite large. Recently, an optimisation scheme was discussed to design two-dimensional quasicrystals with complete photonic bands by a combination of hyperuniformity, uniform local topology and short-range geometric order [67, 255]. In this procedure, vertical rods are placed at the particle positions of a quasicrystal and a trivalent network is formed by employing a Delaunay triangulation of this pattern and by connecting the barycenters of the neighbouring triangles, i.e. the center of mass of the two neighbouring bodies. Such a construction can be made with a small enough system size provided the pattern is sufficiently large to be repeated periodically. However, the downside of this method is that such a structure can only be fabricated by lithography [65, 256]. It is interesting to investigate whether quasicrystals that are self-assembled in soft-matter systems [257, 258] display a complete photonic band gap. In this chapter, we calculate the photonic properties of a random-tiling dodecagonal quasicrystal and its approximants that can be formed in soft-matter systems, as shown in Chapter 3. We construct the network structure by placing dielectric rods at the positions of the particles and connecting these with dielectric walls as has previously been performed for two-dimensional periodic lattices [63]. Although the photonic crystals that we simulate are two-dimensional rods and walls, as opposed to soft-matter systems that consist of a single layer of spherical particles, we believe this study may shed light on the photonic properties of the self-assembled colloidal quasicrystals.

This chapter is organised as follows. We present the structures and the method used to calculate the photonic band structures in Section 8.2. We then individually discuss and compare the photonic behaviour of the quasicrystal and the approximants in Section 8.3. We end with conclusions in Section 8.4.

8.2 Methods

We calculate the photonic band structure diagrams using the open-source 'MIT Photonic-Bands' software package [165]. This software package computes fully-vectorial eigenmodes of Maxwell's equations with periodic boundary conditions by preconditioned conjugate-gradient minimisation of the block Rayleigh quotient in a plane wave basis [165]. We use a super cell approximation in our calculations; where we consider a large cell consisting of a finite sample size as the primitive cell, which is then repeated periodically in a two-dimensional space. The path in the reciprocal space then follows the boundary of the irreducible part of the first Brillouin zone of the square super cell as $\Gamma - X - M - \Gamma$. We use four points to linearly interpolate between each consecutive pair of these $k-$points in reciprocal space. We define a characteristic length scale $a = (\rho)^{-1/2}$, where ρ is the number density of the system defined as $\rho = N/A$ for a system of N particles in a rectangular box of area A. In this work, we use systems with $\rho = 1.07\sigma^{-2}$, where σ is the particle diameter. The photonic properties are calculated in terms of two quantities, (1) the dimensionless (reduced) frequency, $\omega^* = \omega a/2\pi c$ where ω is the frequency of the electro-magnetic field and c is the speed of light in vacuum, and (2) the relative gap width, $\Delta\omega/\omega_m$ where $\Delta\omega$ is the gap width and ω_m is the mid-gap frequency. Finally, the structures we use are composed of particles of a high dielectric constant material, silicon ($\varepsilon = 12$), arranged in a background of air ($\varepsilon = 1$). Given the two-dimensional (planar) nature of the structures studied here, we calculate the photonic properties separately for the case in which either the magnetic field or the electric field is in the structure plane. The earlier is termed as transverse-magnetic (TM) polarisation and the latter as transverse-electric (TE) polarisation.

We compare the photonic properties of a two-dimensional random-tiling dodecagonal quasicrystal with four of its approximants by calculating the photonic band structure diagrams. Approximants are periodic crystals that approximate the structure of a quasicrystal on a local level, i.e. they have an identical local tiling structure as the quasicrystal [175]. For each structure, we calculate the photonic properties using three different configurations corresponding to the arrangement of the high dielectric constant material. This includes the arrangement of the dielectric material in the form of (1) vertical rods (or cylinders), (2) vertical walls, and (3) a network of vertical rods connected by vertical walls in a planar dielectric slab, which respectively are known to promote the formation of band gaps for TM, TE and TM+TE polarisations [60]. This is caused due to the difference in the nature of the electric field in the 2-D plane; the electric field in the plane is a vector in the TE polarisation and a scalar in the TM polarisation [86]. An overview of the different configurations of the quasicrystal and the four approximant structures is given in Figure 8.1. Each panel in the figure contains the real space positions of the particles (top-left) and the variation of the dielectric constant in the rod (top-right), wall (bottom-left), and network (bottom-right) configurations. The inset shows the respective calculated diffraction

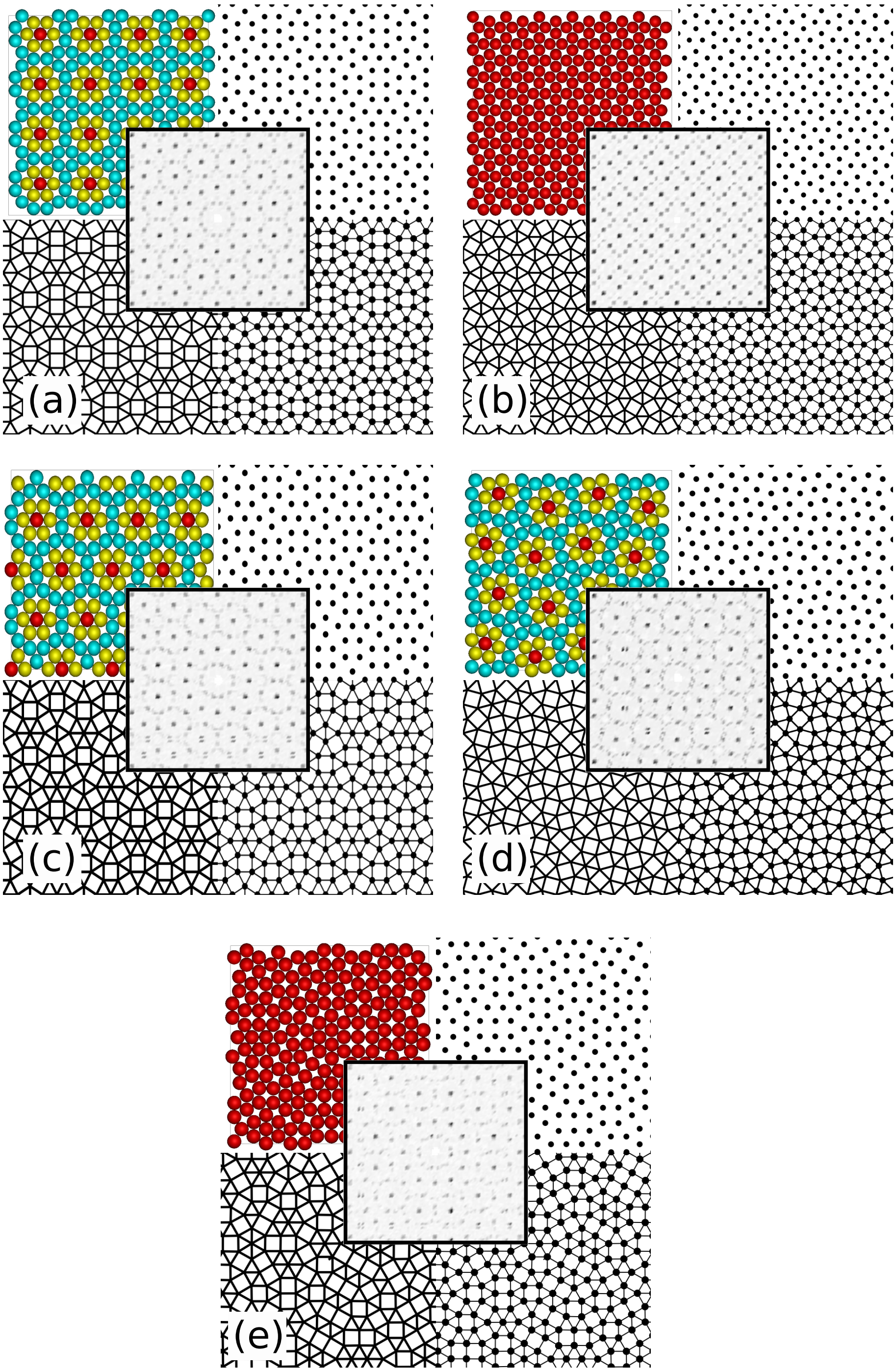

Figure 8.1: Dodecagonal quasicrystal and approximants used in this study **(a)** dodecagons in a square tiling (SQ), **(b)** sigma tiling (SI), **(c)** dodecagons in a triangle tiling (TR), **(d)** dodecagons in a square-triangle tiling (ST), and **(e)** a random-tiling quasicrystal (QC). Each panel contains **(top-left)** the positions of the particles as disks, where the dodecagons are distinctly marked in (a, c, d), and the real space permittivity (dielectric constant) function in **(top-right)** the vertical rod configuration, **(bottom-left)** the vertical wall configuration, and **(bottom-right)** the network configuration. Note that the rods and walls are out of plane of the figure. **Inset** shows the calculated diffraction pattern.

patterns. In Figure 8.1(e), we show the dodecagonal quasicrystal (QC), which is adapted from a non-Stampfli square-triangle approximant [84]. We use a super cell containing 209 particles. The three approximants used here consist of various tilings of dodecagonal arrangement of particles. These tilings include square (SQ), triangle (TR) and square-triangle (ST), and are shown in Figures 8.1(a), 8.1(c), and 8.1(d). The fourth approximant, given in Figure 8.1(b), is a periodic representation of the $\left(3^2.4.3.4\right)$ Archimedean tiling, denoted as σ-phase (SI) based on its analogous three-dimensional Frank-Kasper phase [180, 238]. The unit cell of the SQ, SI, TR and ST approximants, is respectively, composed of 15, 32, 52 and 56 particles. For each of these structures, we calculate and compare the photonic band structure in all configurations as a function of the size of the dielectric, namely the radius of the vertical rod ($r^* = r/a$) and the width of the vertical wall ($w^* = w/a$).

8.3 Results and discussion

In this section, we first compare the photonic properties of the quasicrystal and four of its approximants in the rod and wall configurations. We then present the photonic properties of only the approximants in the network configuration.

8.3.1 Comparison of rod and wall configurations

We compare the photonic properties of the quasicrystal and approximant structures by plotting the band gap map. This involves plotting the locations of the extremities of the photonic band gap in the band structure as a function of a geometrical parameter, i.e. the radius of the rods ($r^* = r/a$) in the rod configuration or the width of the walls ($w^* = w/a$) in the wall configuration. This helps in visualising and comparing the optimal geometrical parameter that maximises the width of the band gap. In Figure 8.2, we plot the TM and TE band gap maps separately for each structure in both the rod and the wall configurations. We make the following observations from this figure: (1) All these structures possess both TM and TE band gaps in both the rod and wall configurations. (2) However, there is no complete (TM+TE) band gap due to misalignments between the TM and TE gaps in each configuration. (3) As expected, the TM band gap is dominant in the rod structures, while the TE band gap is larger in the wall structures. However, we notice that the TE band gap widths in the wall configurations is much smaller than the TM band gap widths in the rod configurations. (4) The position of the band gaps in terms of their mid-gap frequency for all these structures is similar. The first and the last observations agree well with earlier studies [88, 249, 251] that suggest that the photonic behaviour of the rod configurations of the approximants is dominated by their short range environment and thus, the size of the approximant has little influence on the position of the band gap.

To further investigate if there is an effect of the local structure on the photonic behaviour of the quasicrystal and the approximants, we provide a quantitative comparison in Figure 8.3. Figure 8.3(a) shows the comparison for the rod configurations and Figure 8.3(b) for the wall configurations. In both Figure 8.3(a) and Figure 8.3(b), the top panels show the particle dimension (rod radius or wall width) at which the maximum gap width is obtained, the middle panels the maximum gap width (TM in rod and TE in wall configurations) and the bottom panels the mid-gap frequency at maximum gap width. We only plot the TM band gap of the rod

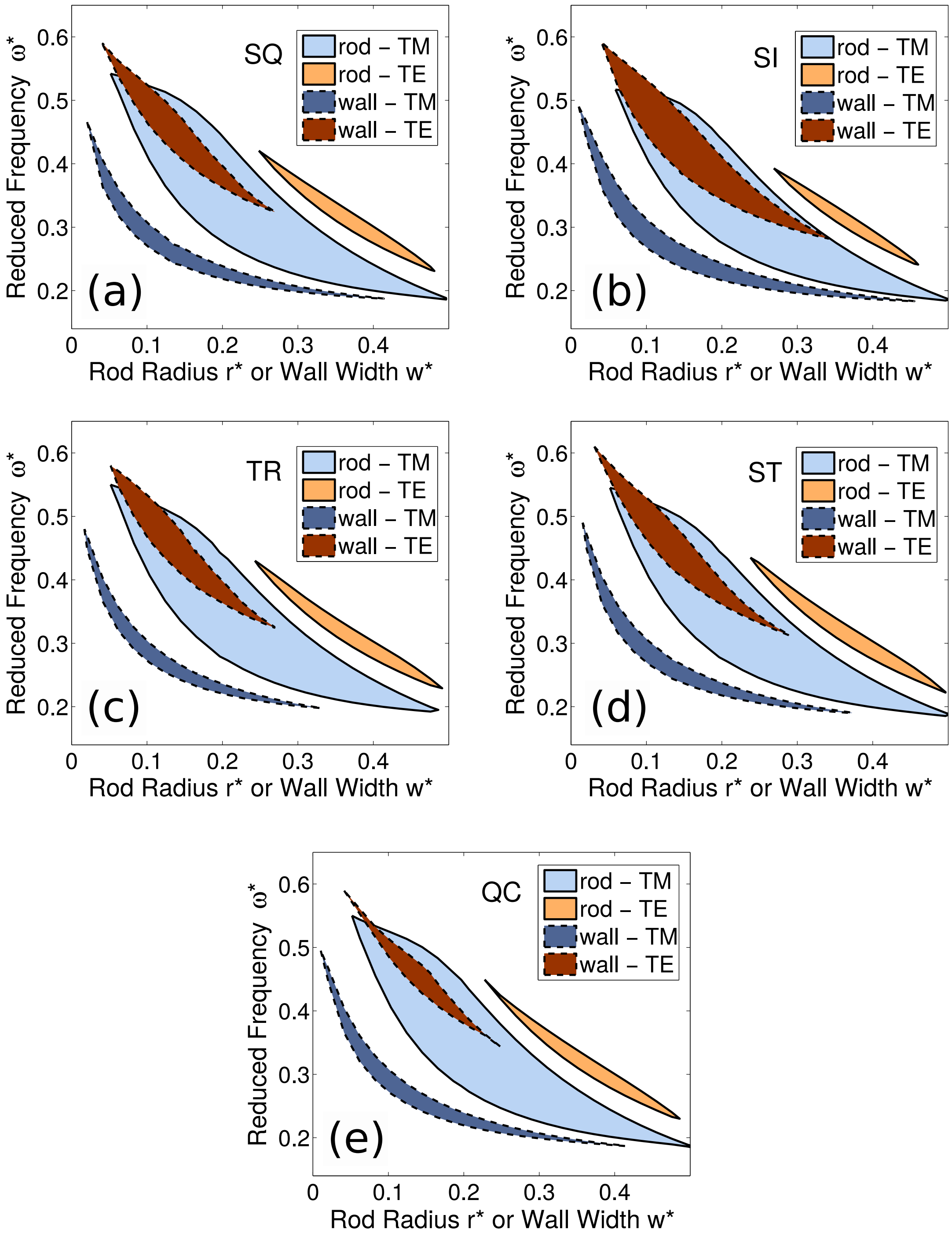

Figure 8.2: TM and TE band gap maps as a function of the radius ($r^* = r/a$) in a rod configuration and the width ($w^* = w/a$) in a wall configuration for the following structures: **(a)** dodecagons in a square tiling (SQ), **(b)** a sigma tiling (SI), **(c)** dodecagons in a triangle tiling (TR), **(d)** dodecagons in a square-triangle tiling (ST), and **(e)** a random-tiling quasicrystal (QC). The blue and brown colours, respectively, denote the TM and TE band gaps. The rod configurations are represented in a lighter shade of the colour and the wall configurations in a darker shade. The reduced frequency is written as $\omega^* = \omega a/2\pi c$.

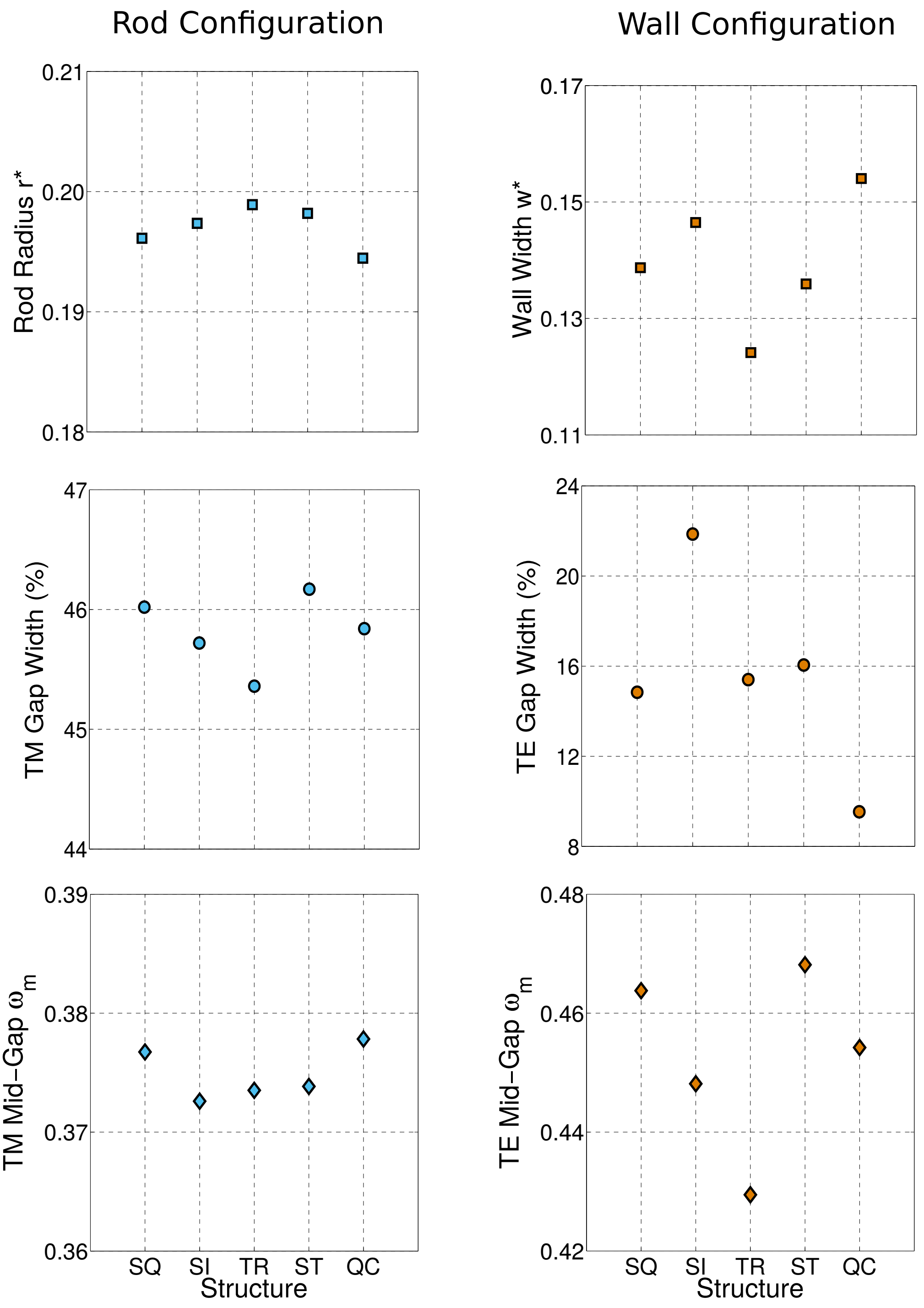

Figure 8.3: Comparison of the maximum band gap width in **(left)** a rod and **(right)** a wall configuration. The **top** panels show the rod radius or wall width at which the maximum gap width is obtained, the **middle** panels show the maximum gap width and the **bottom** panels the mid-gap frequency at the maximum gap width for the following structures: dodecagons in a square tiling (SQ), a sigma tiling (SI), dodecagons in a triangle tiling (TR), dodecagons in a square-triangle tiling (ST), a random-tiling quasicrystal (QC). The reduced quantities are written as $\omega^* = \omega a/2\pi c$, $r^* = r/a$, and $w^* = w/a$.

configurations and the TE band gap of the wall configurations. Let us first pay attention to the rod configurations given in Figure 8.3(a). As in the previous studies [88, 249, 251], we do not find a large variation in the maximum gap width and the mid-gap frequency between the approximants. It is interesting to note that the behaviour exhibited by the quasicrystal and the SI approximant, which do not have local dodecagonal structures, is similar to that of the other approximants constructed using dodecagons. However, such behaviour does not hold in the case of the wall configurations as shown in Figure 8.3(b). We find a large variation in all the three calculated parameters. The only correlation we find in the photonic behaviour of the wall configuration is that the three approximants based on different tilings of the dodecagons, namely SQ, TR and ST, have similar maximum band gap widths. This suggests that the behaviour of the three approximants is governed by their short range environments leading to similar photonic behaviour. However, such a correlation is not observed in case of the mid-gap frequency value, leading to an inconsistency with regard to the previous statement. It is interesting to note that the SI approximant, having a periodic non-dodecagonal particle arrangement, has the largest band gap width and the quasicrystal, having a random non-dodecagonal arrangements, has the smallest band gap width among the structures studied. In addition, we do not find any direct correlations between the size of the approximant and the photonic behaviour in the wall configuration.

8.3.2 Comparison of network configurations

The construction of a network structure for obtaining a complete photonic band gap finds its roots in the different configurations that promote the formation of a TM and a TE band gap. Intuitively, a network consisting of a combination of both these aspects would result in the formation of a complete (TM+TE) band gap. However, identifying and constructing such a structure for a quasicrystal is not straightforward. Recently, there have been optimisation methods provided to design photonic quasicrystals with complete band gaps [67]. In contrast, we follow a simple protocol of a straightforward combination of the above mentioned rod and wall structures to create a network. The advantage of this simplification is that these networks can be experimentally synthesised by sintering and etching colloidal crystal structures [257, 258]. In this study, we wish to evaluate the effect of the local environment of particles in the network configuration on the formation of a complete photonic band gap. However, given the computationally expensive nature of these calculations for the quasicrystal, we have, till now, only obtained the results for the approximants. We will discuss these here in further detail.

In Figure 8.4, we present the surface map of the complete band gap width for the four approximants, namely SQ, SI, TR and ST. Here, the largest complete band gap obtained is plotted as a function of the wall width ($w^* = w/a$) and the rod radius ($r^* = r/a$). We make the following three observations from these plots. Firstly, the maximum band gap width obtained in these structures is about 10 %, which is much smaller than the TM and TE band gaps found in the individual rod and wall configurations. Secondly, it is interesting to note that the maximum band gap in all these structures is obtained in a configuration consisting of large rods connected by thin walls. In other words, it requires only a small connecting material between the rods to open up a complete band gap. Additionally, this also means that these configurations exhibit a dominant TM behaviour. Lastly, the point of difference between these four structures occurs in the regions of thicker walls. Here, the SI has a larger band gap width than the other three. This

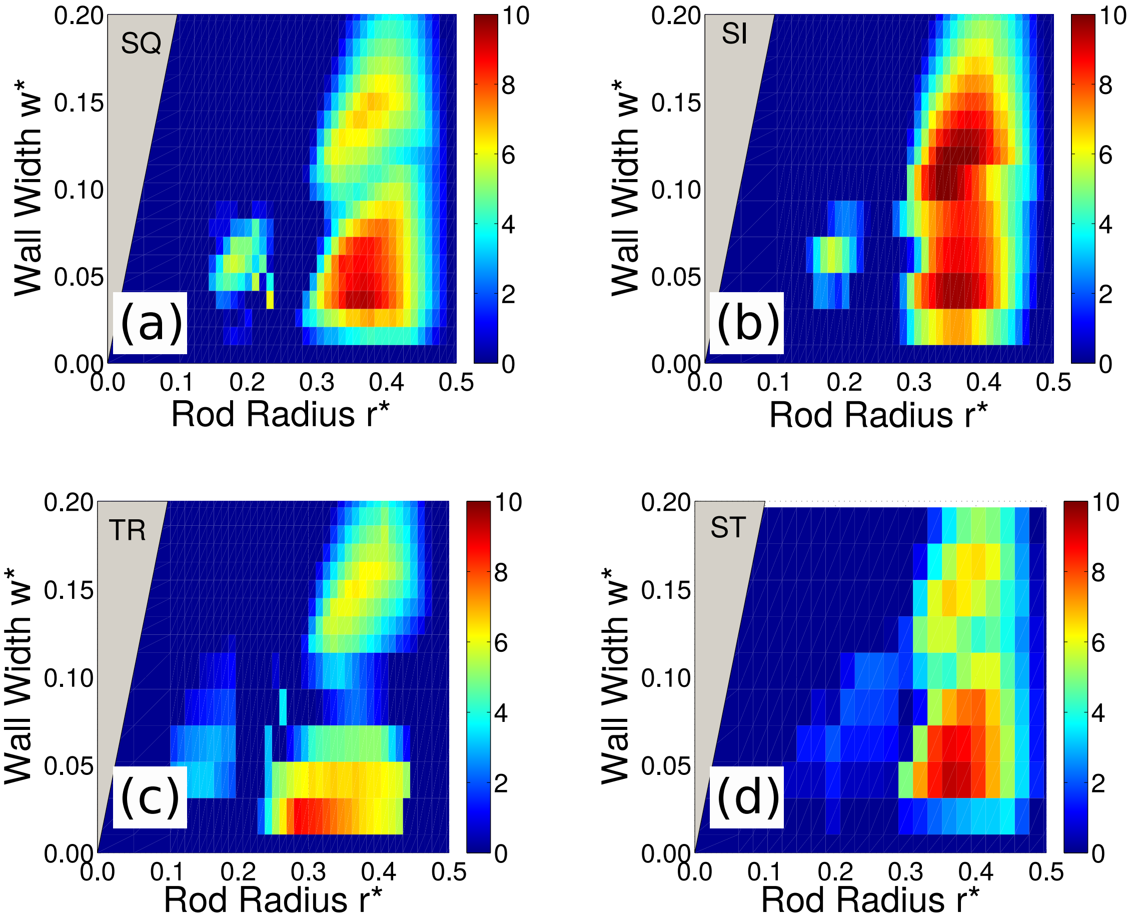

Figure 8.4: Surface map of complete (TM+TE) band gap width as a function of rod radius ($r^* = r/a$) and wall width ($w^* = w/a$) calculated for network configurations of the following structures: **(a)** dodecagons in a square tiling (SQ), **(b)** a sigma tiling (SI), **(c)** dodecagons in a triangle tiling (TR), and **(d)** dodecagons in a square-triangle tiling (ST). The region where $r^* < w^*/2$, i.e. the rods are submerged inside the wall, is shaded in grey.

correlates with the larger TE band gap exhibited by the SI structure in the wall configuration (shown in the previous section). The same behaviour is also exhibited here at thicker wall widths, when the behaviour in the TE polarisation is dominant.

One of the intriguing observations made from the previous figure (Figure 8.4) is regarding the lower band gap width obtained in the network configurations than in the individual rod and wall configurations. To investigate this further, we plot the band gap map as a function of the rod width at a constant wall width ($w^* = 0.03$) for all the approximants in Figure 8.5. The chosen wall width corresponds to the wall width where the maximum band gap is found in these structures. Here, we observe that the overlap between TM and TE bands to create a complete band gap does not occur in the bands at lower frequencies, but at higher frequencies. In contrast, the band gaps reported in the rod and wall configurations pertain to the lowest individual band gap. This mismatch results in the reduction of the gap width in the network configurations. Additionally, it is not surprising to note than the behaviour of the TM bands in the band gap

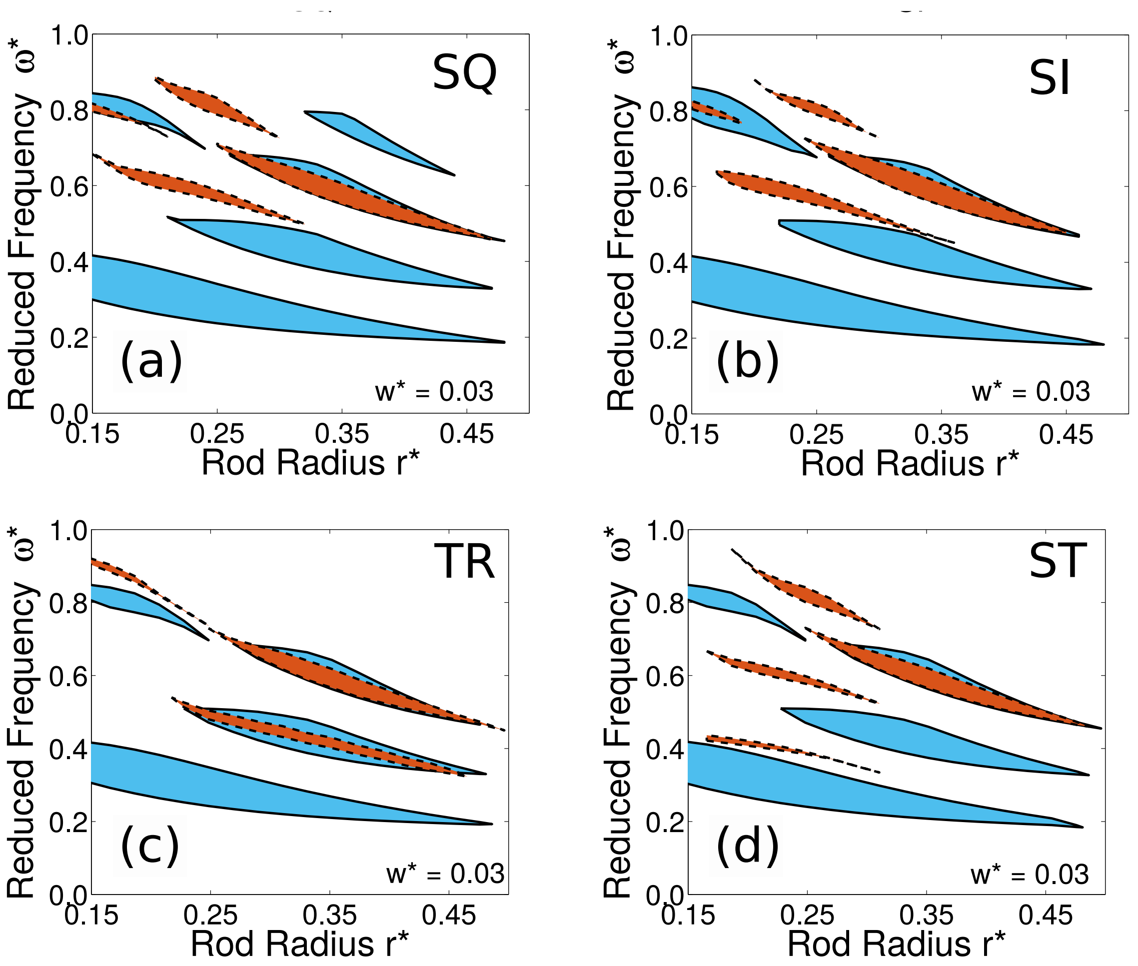

Figure 8.5: Band gap map as a function of rod radius ($r^* = r/a$) at a constant wall width ($w^* = w/a = 0.03$) calculated for network configurations of the following structures: **(a)** dodecagons in a square tiling (SQ), **(b)** a sigma tiling (SI), **(c)** dodecagons in a triangle tiling (TR), and **(d)** dodecagons in a square-triangle tiling (ST). The blue and brown colour, respectively, denote the TM and TE band gaps.

map of all approximants is similar. As previously explained, the configuration explored by this band gap map represents a structure with large rods connected by thin walls, i.e. configurations with dominant TM behaviour. Thus, this behaviour is consistent with Figure 8.2 and Figure 8.3, where all approximants were found to display similar behaviour in the rod configurations under TM polarisation. Also, the difference between the behaviour of the network structure of these aproximants is in the TE band gaps; which is again consistent with the previous observation of different behaviour between the approximants under TE polarisation.

8.4 Conclusions

In summary, we compare the photonic behaviour of a two-dimensional random tiling dodecagonal quasicrystal with four of its approximants in three particle configurations corresponding to the arrangement of the high-dielectric constant material, i.e. a rod configuration, a wall configuration and a network of walls and rods. Firstly, we find that all these structures exhibit the formation of photonic band gaps in both TM and TE polarisations. Further, we find that all these structures exhibit similar photonic behaviour in the rod configuration, but not in the wall configuration. This difference in photonic behaviour seems not to be related to the size of the approximant or the local structure. Surprisingly, we find that all the approximants exhibit similar photonic behaviour in the network configuration that contains a combination of rods and walls. In these structures, the maximum band gap width is obtained at a configuration consisting of large rods connected by thin walls. Comparing the photonic behaviour of the approximants in the network configuration with that in the rod and wall configurations, we extrapolate that the quasicrystal will also exhibit a similar behaviour in the lower wall width regimes.

9

A simple self-assembly route for a photonic crystal with a pyrochlore structure in a three-dimensional core-corona system

---

We report the investigation of a three-dimensional core-corona system using Monte Carlo simulations and its phase diagram determination using free-energy calculations. The core-corona system is modelled as particles with an impenetrable hard core of diameter σ_{HS} surrounded by a purely repulsive soft corona of diameter $\delta = 2.10\sigma_{HS}$. The system exhibits a rich phase behaviour comprising of a fluid, a body-centered cubic, and a face-centered cubic crystal phase in three different density regimes. In addition, two intriguing low-density phases are found in the system, namely a pyrochlore and a hexagonal columnar phase. We find evidences of energetic stabilisation of these structures. The structure of the pyrochlore formed in our simulations has two inherent length scales and displays complete photonic band gaps in both the direct and inverted crystal structure. The hexagonal columnar phase consists of strings, separated by a distance larger than δ, which are arranged on a hexagonal lattice. We also find evidence of slow dynamics in this phase as a result of restricted particle movements between the neighbouring strings.

9.1 Introduction

Photonic band gap (PBG) materials are periodic structures that prevent the propagation of light with a specific wavelength in all directions. Since their initial proposal in 1987 [20, 21], there has been a huge interest in fabricating PBG materials with band gaps in the wavelengths pertaining to the visible and near-infra-red region, because of their wide applicability [42, 188]. For example, three-dimensional PBG materials with the band gap centered around 1.5 μm are interesting for applications not only in the telecommunication sector as lossless wave guides [13], and non-linear optical switches [14], but also in (bio-)sensing, bio-medical engineering, and energy storage and security [3, 15–17]. The current forerunners for these PBG materials are the dielectric diamond and pyrochlore structures created from precursor colloidal particles. They not only display a gap formation at a low refractive-index contrast ratio (around two) and possess a large band gap width-to-frequency ratio, but also exhibit a band gap formation at low lying bands that are more stable against disorder [259]. However, the major obstacle in experimentally realising the PBG materials is the lack of an inexpensive and reliable means of fabrication. Continuous efforts are being made to fabricate the diamond structure. One of the earlier methods included the laborious process of nanorobotic manipulation of colloids [260]. A less laborious alternative is the directed self-assembly of the colloidal analogue of the $MgCu_2$ Laves phase from a binary colloidal dispersion using appropriate wall patterning [42, 43]. One of the components of the Laves phase can then be selectively removed to obtain either the diamond or the pyrochlore lattice. However, formation of this binary crystal for sub-micron sized colloidal particles has not been experimentally realised till now. Other popular methods for fabricating the diamond structure are the use of colloidal particles with selective patches [261–266] or self-assembly of colloids with complex interaction potentials [267, 268]. However, these require complicated potentials that are yet to be experimentally realised. Although there has been a theoretical prediction of a diamond crystal ground state in star polymer solutions in a good solvent [269], we have not come across any reports of their experimental realisation. On the other hand, the only method proposed for manufacturing the pyrochlore lattice is by an arduous layer-by-layer growth procedure [25].

In this work, we study the formation of photonic crystals in experimentally realisable systems. One such system emulates particles with a hard core surrounded by a squishy corona like spherical dendrite micelles consisting of a rigid aromatic core with a deformable shell of alkyl chains [105], or block copolymer micelles consisting of a micellar core of hydrophobic polymer surrounded by a large shell of hydrophilic polymer blocks [106–110]. We model these core-corona systems using an interaction potential with a hard core of diameter σ_{HS} and a purely repulsive square shoulder of diameter δ. The phase behaviour of this core-corona system is greatly influenced by δ. At $\delta \sim \sigma_{HS}$, the system behaves similar to a system of hard spheres; while at $\delta >> \sigma_{HS}$, the hard core becomes effectively irrelevant at low temperatures. However, an interplay between the energetic and entropic considerations promotes the formation of phases with various structures at intermediate shoulder widths.

Under these conditions of intermediate shoulder widths, a rich phase behaviour has been reported in two- [123, 136, 138, 140, 233, 234] and three-dimensional core-corona systems [143–147, 234]. Specifically, a stable diamond cubic phase was reported in a core-corona system with a smoothened potential at $\delta = 1.80\sigma_{HS}$ [144]. Given the similarity between the diamond and pyrochlore lattices in terms of the basic lattice structure (= face-centered cubic) and the coordination number of particles (= 4), we ask ourselves whether a pyrochlore lattice can also form in a core-corona system with certain values of the shoulder width.

To address this question and to map out the entire equilibrium phase diagram of the system, we combine Monte Carlo simulations and free-energy calculations. We fix the shoulder width to be $\delta = 2.10\sigma_{HS}$ and the reasons behind this will be explained in the methods section. We observe a rich phase behaviour which includes the formation of a pyrochlore crystal and a hexagonal columnar phase. Subsequently, we study the photonic properties of the pyrochlore phase and the dynamics of the columnar phase. This chapter is organised as follows. We present our model and the methods that we employ to map out the phase diagram and to calculate the photonic band structure in Section 9.2. The results are presented in Section 9.3, and we draw some conclusions in Section 9.4, where we also outline future research directions.

9.2 Methods

We first explain the simulation model and computational methods used for this study in Section 9.2.1, and then outline the procedure to construct the phase diagram in Section 9.2.2. Following which, we give an account of the analysis methods in Section 9.2.3, and finally, the procedure for photonic band structure calculation is given in Section 9.2.4.

9.2.1 Computational methodology

In this work, we study the phase behaviour of a three-dimensional system of spherical particles with a core-corona architecture. The interaction between the particles is modelled using a radially symmetric hard-core square shoulder (HCSS) pair potential consisting of a hard core of diameter σ_{HS} and a purely repulsive square shoulder of diameter δ. This HCSS potential can be written as a sum of a hard-sphere potential $V_{\mathrm{HS}}(r)$ and a square-shoulder potential $V_{\mathrm{SS}}(r)$, i.e.

$$V_{\mathrm{HCSS}}(r) = V_{\mathrm{HS}}(r) + V_{\mathrm{SS}}(r), \tag{9.1}$$

where

$$V_{\mathrm{HS}}(r) = \begin{cases} \infty, & r \leq \sigma_{HS} \\ 0, & r > \sigma_{HS} \end{cases}, \tag{9.2}$$

and

$$V_{\mathrm{SS}}(r) = \begin{cases} \varepsilon, & r \leq \delta \\ 0, & r > \delta \end{cases}, \tag{9.3}$$

with r the interparticle centre-of-mass distance, and $\varepsilon > 0$ the height of the square shoulder. The HCSS potential introduces two characteristic length scales in the system; namely the hard-core diameter σ_{HS} and the square shoulder diameter δ. We define ε and σ_{HS}, respectively, as the units of energy and length. Our preliminary study on the phase behaviour of the HCSS system with shoulder widths $1.90\sigma_{HS} \leq \delta \leq 2.10\sigma_{HS}$ exhibited the formation of clusters at $\delta \geq 2.00\sigma_{HS}$. This formed the basic motivation for a detailed study on the phase behaviour of a HCSS system with shoulder width of $\delta = 2.10\sigma_{HS}$, and to look for the formation of a pyrochlore lattice, which can be considered to be composed of tetrahedral clusters [24, 43].

We perform Monte Carlo (MC) simulations using a system of N particles in a cubic box of volume V with periodic boundary conditions in the canonical (NVT) and isothermal-isobaric

(NPT) ensembles. We define various reduced (dimensionless) physical quantities to describe the system, namely temperature $T^* = k_B T/\varepsilon$, pressure $P^* = \beta P \sigma_{HS}^3$, and density $\rho^* = N\sigma_{HS}^3/V$, where $\beta = 1/k_B T$ is the inverse temperature with k_B the Boltzmann constant. Depending on the lattice structure, a system size N between 432 and 512 particles is used for the NPT studies.

9.2.2 Phase diagram construction

We employ a three-step process to determine the phase diagram of the system:

(1) We measure the equation of state (EOS) of the phases of interest at a constant temperature T^*. This isothermal EOS is the variation of the bulk pressure P^* as a function of the equilibrium density ρ^*. We perform compression and expansion runs by either increasing or decreasing the pressure P^* in a step-wise manner in the NPT ensemble to obtain the isothermal EOS. The compression runs are started from an isotropic fluid phase, while the expansion runs are started from the concerned crystal phase.

(2) For each of the observed phases, we determine the dimensionless Helmholtz free energy per particle $f = \beta F/N$ as a function of density ρ^* at a fixed temperature T^* by thermodynamic integration of the EOS to a reference density. The free energy at the reference density is calculated for the periodic crystal phases using the Frenkel-Ladd method and for the fluid and columnar phases using the Schilling-Schmid method. Both these methods are explained in Chapter 2.

(3) The thermodynamically stable phases and the corresponding phase boundaries are determined by employing a common tangent construction to the free-energy curves, i.e. the Helmholtz free energy per unit area $\beta F/A$ as a function of the reduced density ρ^*.

9.2.3 Structural analysis

We characterise the different phases formed in our system by calculating the radial distribution function (RDF) of the system $g(r)$. The RDF of a system at density ρ^* gives the probability of finding a pair of particles at a distance $r = |\mathbf{r} - \mathbf{r}'|$, and reads

$$g(r) = \frac{1}{\rho^{*2}} \left\langle \sum_{i=1}^{N} \sum_{j \neq i}^{N} \delta(\mathbf{r} - \mathbf{r}_i)\delta(\mathbf{r}' - \mathbf{r}_j) \right\rangle, \tag{9.4}$$

where $\mathbf{r}_i$ and $\mathbf{r}_j$ are the positions of particles i and j, respectively, and the brackets denote the average over the number of particles.

To assess the dynamic behaviour of the columnar phase, we calculate the self intermediate scattering function (SISF), $F_k(t)$ and the mean squared displacement (MSD) $\Delta r^2(t)$. The SISF at a given wave vector k is the spatial Fourier transform of the van Hove self-correlation function [270, 271] and can be written as

$$F_k(t) = \frac{1}{N} \left\langle \sum_{i=1}^{N} \exp\left(-i\mathbf{k}.(\mathbf{r}_i(t_0 + t) - \mathbf{r}_i(t_0))\right) \right\rangle, \tag{9.5}$$

where the brackets denote the averaging over different configurations. The SISF is measured for a wave vector k that corresponds to the first peak in the static structure factor $S(k)$. The

MSD is calculated as

$$\Delta r^2(t) = \frac{1}{N}\left\langle \sum_{i=1}^{N} (\mathbf{r}_i(t_0+t) - \mathbf{r}_i(t_0))^2 \right\rangle, \tag{9.6}$$

where the brackets denote the averaging over different configurations.

We study the dynamic behaviour as a function of Monte Carlo steps (MCS). While MC simulations are not strictly concerned with time dependent properties, they can be used for this purpose if the proposed particle moves are physically realisable, i.e. diffusive in nature, and if the focus is on the intermediate and long time behaviour [272, 273]. Since this is the case in our simulations, we calculate the SISF and MSD from the MC trajectories.

9.2.4 Photonic band structure calculation

We numerically calculate the photonic properties of the dielectric pyrochlore structure using the open-source 'MIT Photonic-Bands' software package [165]. The software computes fully-vectorial eigenmodes of Maxwell's equations with periodic boundary conditions by preconditioned conjugate-gradient minimisation of the block Rayleigh quotient in a plane wave basis [165]. We consider both the direct structure consisting of silicon spheres in air and the inverse structure made of air spheres in silicon. The dielectric constant of silicon is taken to be twelve and that of air is unity. We discretise the unit cell using a grid consisting of 32 grid points in each direction. We compare the photonic properties of the pyrochlore lattice obtained in our simulations with that of an ideal pyrochlore lattice. We refer to the works by Garcia-Adeva [25, 274] for the description of the crystal structure of the ideal pyrochlore lattice in terms of the basis vectors and the particle positions.

9.3 Results and discussion

In this section, we first present the overall phase behaviour of the system along with the equilibrium phase diagram, then we turn our attention to the two interesting open structures found in the system, namely the pyrochlore and the hexagonal columnar phase.

9.3.1 General phase behaviour

The phase behaviour at this shoulder length is interesting because the size of the shell of the soft corona is comparable to that of the hard core. As a consequence, the behaviour at larger interparticle distances ($r \geq \delta$) is predominantly determined by energy minimisation, while that at lower distances ($r < \delta$) is dominated by entropy maximisation. This, in turn, leads to the formation of clusters that are separated from each other by distances $r \geq \delta$. We plot the phase diagram in the pressure-temperature and temperature-density planes in Figure 9.1. The first observation we make is the rich phase behaviour displayed by the system. We identify and mark the following phases: Fluid (FL), body-centered cubic (BCC), high- (HFCC), medium- (MFCC) and low-density (LFCC) face-centered cubic, pyrochlore (PYR) and hexagonal columnar phase (COL). The driving force for the formation of FCC phases in three different density regimes is the presence of the two length scales in the system. FCC phases with first nearest neighbours at distances equal to that of the shoulder and the hard core are, respectively, formed at low- and high-densities. In the MFCC phase, the second nearest neighbours are at a distance equal to the square shoulder diameter δ.

Let us now consider the high- and low-temperature behaviour separately. At high temperatures, the observed crystal phases include a BCC phase sandwiched between two FCC phases. This behaviour is similar to that reported for the smoother potential system at shoulder widths $1.15\sigma_{HS} \leq \delta \leq 1.55\sigma_{HS}$ by Gribova *et al.* [144]. It is interesting to note that the MFCC phase, which was reported to form at $1.15\sigma_{HS} \leq \delta \leq 1.55\sigma_{HS}$ and was absent at $\delta = 1.80\sigma_{HS}$ [144], is formed again at the larger shoulder width $\delta = 2.10\sigma_{HS}$. At temperatures higher than those reported here, we expect the system to display a behaviour similar to that of the hard-sphere system with FL at low densities and HFCC at high densities, with a two-phase coexistence region in between (not shown here). The MFCC and BCC phases will not be stable at these temperatures. At the low temperatures reported in the phase diagram, we note a re-entrant phase behaviour of the fluid which encompasses various open structures like LFCC, PYR, and COL. It is worth mentioning here that the emergence of interesting crystals at such low densities is purely driven by repulsive interactions, whereas a gas-liquid condensation is absent due to the lack of attractive interactions.

We next compare the phase behaviour at this shoulder width ($\delta = 2.10\sigma_{HS}$) with the reported ones at lower shoulder widths $1.15\sigma_{HS} \leq \delta \leq 1.80\sigma_{HS}$ [143, 144]. Firstly, the reported phase behaviour at lower shoulder widths show a decrease in the stability region of the fluid phase at intermediate densities with increase in shoulder width [144]. Keeping up with this trend, we find that the stability region of the re-entrant fluid here is indeed very small. Secondly, a number of amorphous low-temperature phases have been reported to form in this density region at smaller shoulder widths, which were explained by considering the one-component system as a quasi-binary mixture [143]. We do indeed find the formation of such amorphous structures in our system in this density range, but, all these amorphous phases are metastable with respect to the fluid phase as seen from our free-energy calculations. Further, the diamond cubic phase reported to be stable at $\delta = 1.80\sigma_{HS}$ [144] is found to be metastable here at $\delta = 2.10\sigma_{HS}$ with respect to the FL-COL phase coexistence.

9.3.2 Pyrochlore - structure and photonic properties

The ideal pyrochlore lattice (iPYR) is composed of tetrahedral clusters stacked in such a way that the nearest neighbours are connected according to an FCC lattice. In other words, the centres of the tetrahedra lie on the filled tetrahedral interstitials of a diamond lattice [24]. For this lattice, at its maximum density ($\rho^* = 0.71$), each particle has six equidistant nearest neighbours. In other words, the distance between the neighbouring particles within a tetrahedron and between those in neighbouring tetrahedra is the same. However, we find that not all the four neighbours of a particle are equidistant in our pyrochlore structure (PYR), which is formed by expanding a BCC lattice to a lower pressure at a constant temperature for a range of shoulder widths $1.95\sigma_{HS} \leq \delta \leq 2.25\sigma_{HS}$. In fact, the distance between the inter- and intra-tetrahedral neighbours are different, which results in a substantially lower maximum density for this structure ($\rho^* = 0.39$). We present a comparison between the PYR and iPYR structures in Figure 9.2. In Figures 9.2(a) and 9.2(b), we show different orientations of a sample configuration of our PYR, where the various clusters are marked by different colours. This clearly shows a layered arrangement of tetrahedral clusters. The difference between our PYR and the ideal iPYR struc-

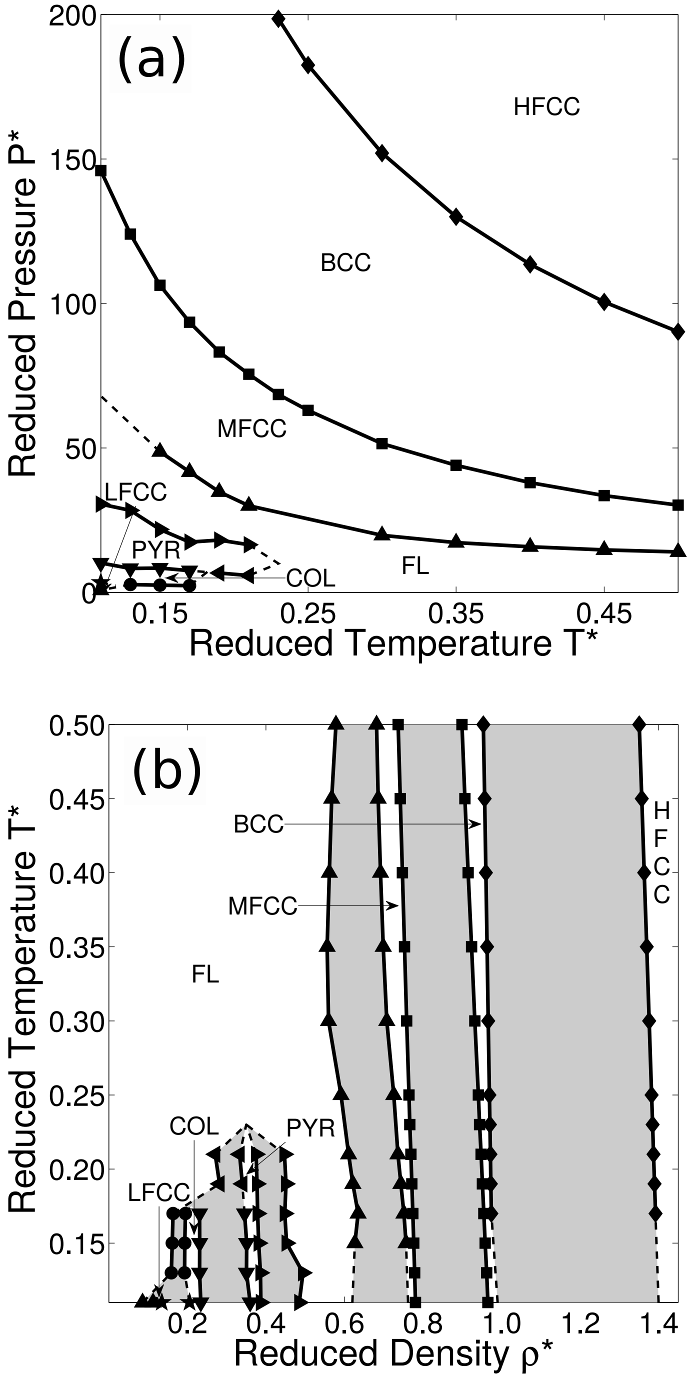

Figure 9.1: Phase diagram in the (reduced) **(a)** pressure-temperature and **(b)** temperature-density representations obtained for the three-dimensional HCSS system with a shoulder width $\delta = 2.10\sigma_{HS}$. The reduced quantities are defined as $T^* = k_B T/\varepsilon$, $P^* = \beta P \sigma_{HS}^3$ and $\rho^* = N\sigma_{HS}^3/V$. The phases shown are fluid (FL), body-centered cubic (BCC), high- (HFCC), medium- (MFCC) and low-density (LFCC) face-centered cubic, pyrochlore (PYR) and hexagonal columnar phase (COL). The grey regions denote the two-phase coexistence regions.

tures is analysed by comparing the RDF as shown in Figures 9.2(c) and 9.2(d). In both Figures 9.2(c) and 9.2(d), the RDF of the PYR phase is calculated at the density corresponding to the close-packing of intra-tetrahedral neighbours, $\rho^* = 0.39$. For the iPYR phase, the RDF in Figure 9.2(c) is calculated at its maximum density $\rho^* = 0.71$, while the density for the calculation in Figure 9.2(d) ($\rho^* = 0.57$) is chosen in order to match the positions of the second peak of the iPYR with the third one of the PYR structure. Though the RDFs in Figure 9.2(c) give an impression that the two structures are different, we can infer from Figure 9.2(d) that this is caused because of the splitting of the first peak in iPYR to two peaks in PYR. This confirms that the PYR structure has two inherent length scales: One between the particles in the tetrahedron and another between the neighbouring tetrahedra. This is done in order to minimise the overlap of the repulsive corona with the neighbouring particles, thereby hinting towards an energetic stabilisation of this structure aided by the range of the interaction potential. We have not found any previous reports of an energetically stabilised pyrochlore phase in systems of isotropic particles. However, there has been one theoretical report of entropic stabilisation of the iPYR structure in a system of triblock Janus particles [266]. The resulting phase diagram consists of a mixture of iPYR and hexagonal tetra-stack lattices [266].

Having characterised the PYR structure, we next investigate whether or not it displays a complete photonic band gap, and how this is affected by the presence of the two length scales. We also calculate the band structure of the iPYR for comparison. It is well established that the iPYR structure possesses a complete photonic band gap [24, 25, 42, 274]. The direct dielectric structure of iPYR consisting of silicon spheres in air has a maximum gap width $\Delta\omega/\omega_m = 13$ % between bands 2 and 3 for a dielectric density of $\rho^* = 0.88$, while the inverse structure of air spheres in silicon has a maximum gap width of $\Delta\omega/\omega_m = 26$ % at an air density $\rho^* = 2.52$. Given that the maximum density of the iPYR is $\rho^* = 0.71$, the particles overlap with the neighbouring particles in both these cases. This represents a sintered structure [188].

A comparison between the photonic properties of the PYR and iPYR in terms of the relative band gap width and the corresponding band gap map is given in Figure 9.3. The relative gap width, $\Delta\omega/\omega_m$, is the ratio of the gap width to the mid-gap frequency, and the frequency is expressed in reduced units as $\omega^* = \omega a/2\pi c$ where ω is the frequency of the electro-magnetic field and c is the speed of light in vacuum. The band gap map involves plotting the locations of the extremities of the photonic band gap in the band structure as a function of a geometrical parameter, i.e. the hard-core diameter σ_{HS}. For convenience, we represent this in terms of the density of the structure ρ^*. In Figures 9.3(a) and 9.3(b), we investigate the direct structures consisting of silicon spheres in air, while in Figures 9.3(c) and 9.3(d), we investigate the inverse structure consisting of air spheres in silicon. Please note that the density given in the direct structures represents that of silicon spheres and that in the inverse structures represents that of air spheres.

First, let us look at the direct structures. In Figure 9.3(a), we plot the band gap width as a function of (reduced) density ρ^*, and in Figure 9.3(b), we show the band gap map. In addition, we draw vertical dashed lines to denote the close-packed density of the iPYR ρ^*_{iPYR} and the two relevant densities in PYR, i.e. ρ^*_{PYR-1} where the spheres in a tetrahedron are in contact and ρ^*_{PYR-2} where the tetrahedra are in contact and the spheres within the tetrahedra overlap with each other. From these figures, we see that both structures possess a complete band gap. However, the band gap width obtained in iPYR is much larger than in our PYR structure. This implies that the presence of two different length scales in PYR, which can be viewed as a

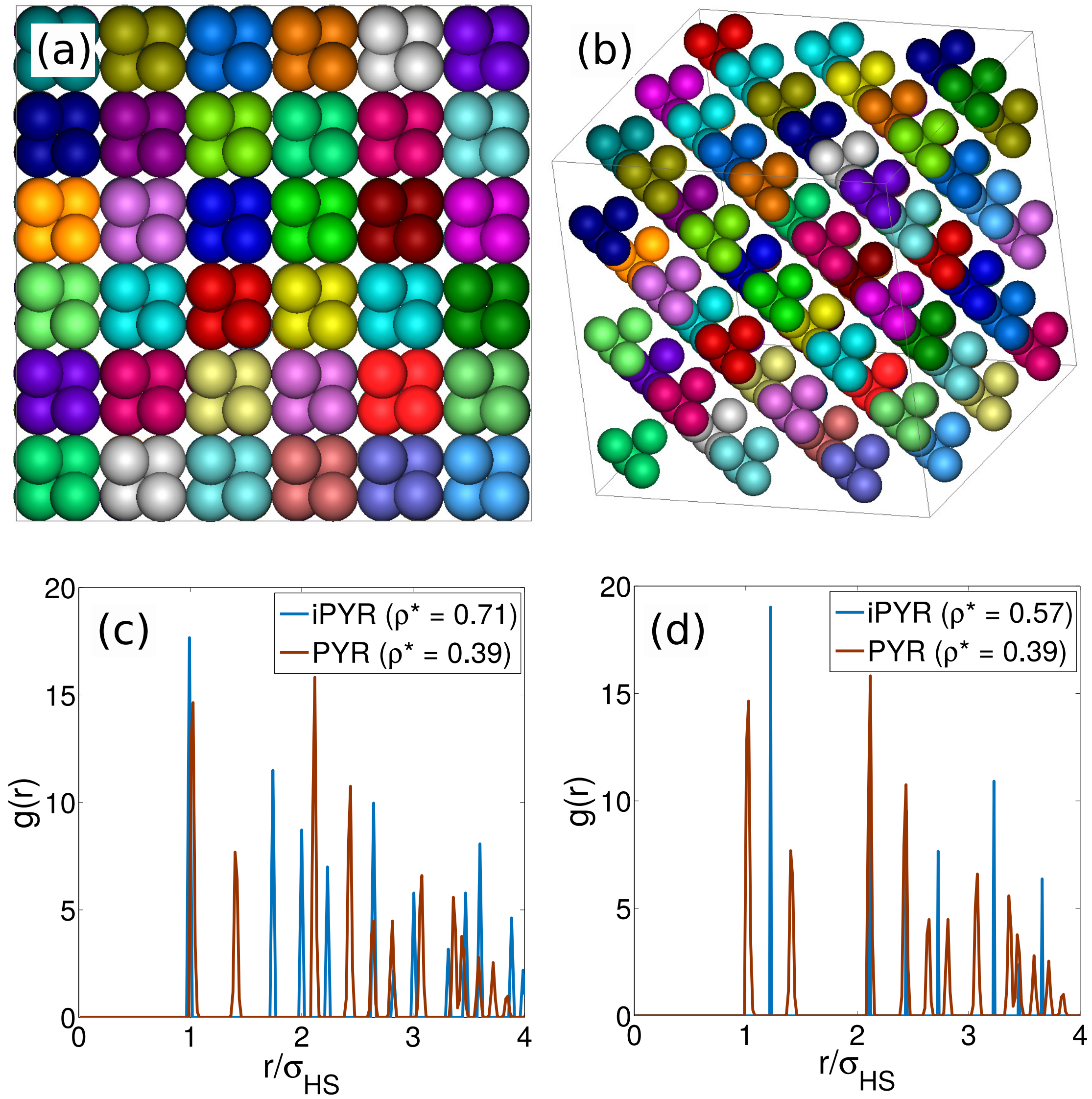

Figure 9.2: Pyrochlore structure: **(a, b)** Different orientations of the sample configuration of the pyrochlore (PYR) lattice obtained in our simulations. Only the hard-cores of the particles are drawn here and the colours represent different clusters. Radial distribution function $g(r)$ for the ideal pyrochlore (iPYR) and the pyrochlore (PYR) obtained in our simulations at **(c)** their respective maximum packing densities, and **(d)** at densities where the positions of the peaks are matched.

reduction in symmetry when compared to iPYR, results in some distortion of the underlying air network in the photonic structure. This, in turn, results in a huge reduction of the band gap width. We also observe that the maximum gap width for iPYR is obtained at a density larger than the maximum packing density ρ^*_{iPYR}, which refers to a sintered structure with overlapping particles [188]. Even though the PYR does not possess a band gap at its close-packed density ρ^*_{PYR-1}, it does at higher densities. This again refers to a structure with sintered particles. It is interesting to note that the band gap width in case of PYR reaches a local maxima at densities slightly higher than the relevant densities ρ^*_{PYR-1} and ρ^*_{PYR-2}. This, further, confirms that the structure of the PYR indeed consists of two-length scales.

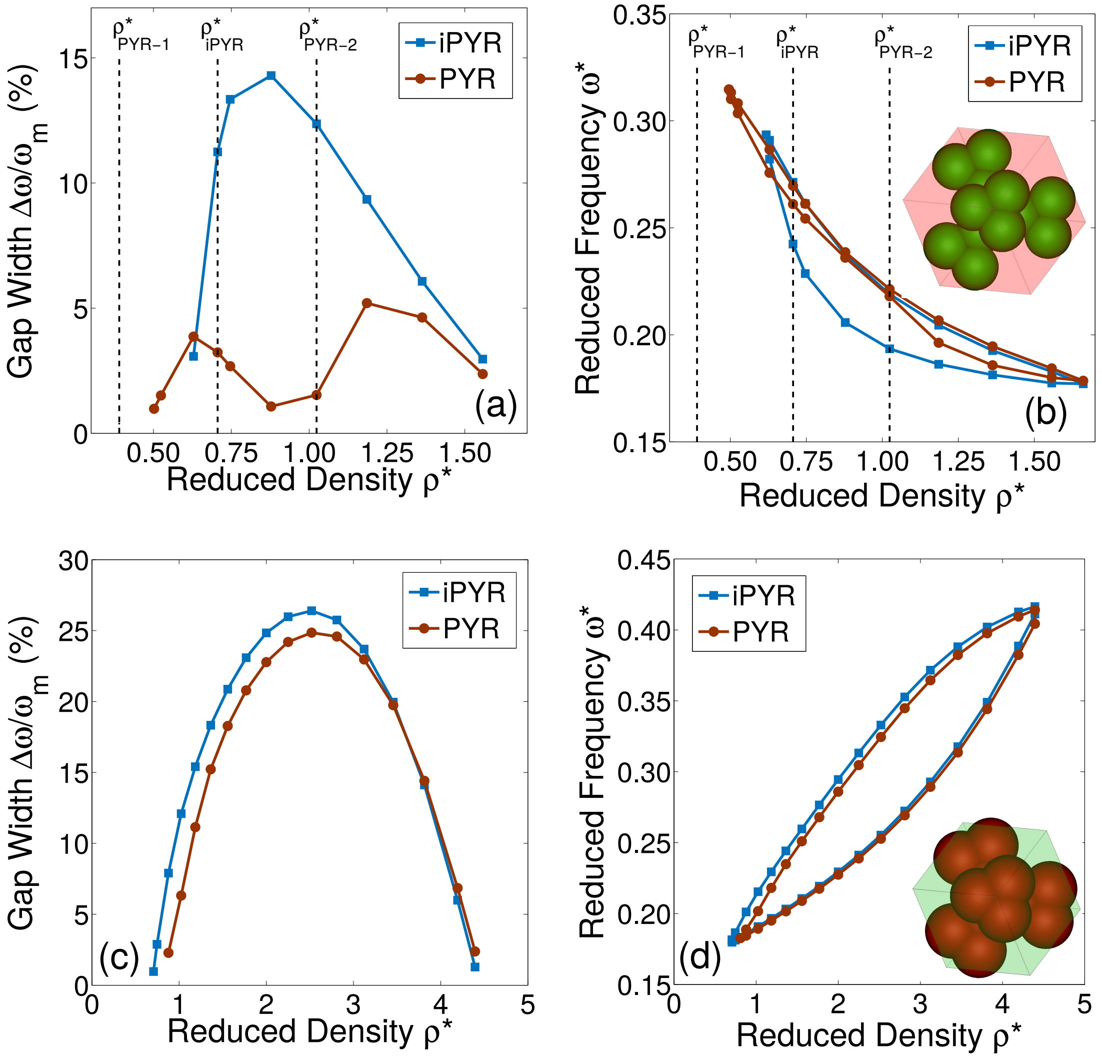

Figure 9.3: Comparison of the photonic properties of pyrochlore structures namely, the ideal pyrochlore lattice (iPYR) and the pyrochlore (PYR) obtained in our simulations: **(a,c)** Relative gap width $\Delta\omega/\omega_m$ as a function of (reduced) density $\rho^* = N\sigma_{HS}^3/V$ and **(b,d)** band gap map calculated for (a,b) direct structure of silicon spheres in air and (c,d) inverse structure of air spheres in silicon. In (a,b) the densities where the particles start to overlap in iPYR (ρ^*_{iPYR}), and where the particles in a tetrahedron $\left(\rho^*_{PYR-1}\right)$ and between neighbouring tetrahedra $\left(\rho^*_{PYR-2}\right)$ start to overlap in a PYR lattice are individually marked. The reduced frequency is written as $\omega^* = \omega a/2\pi c$. A representation of the configuration of PYR pertaining to the density at which the maximum band is obtained is given in (b) for the direct ($\rho^* = 1.18$) structure and in (d) for the inverse ($\rho^* = 2.52$) structure. Here, the green and red colours respectively denote silicon and air.

Now, let us compare the photonic behaviour of the inverse structures of PYR and iPYR as shown in Figures 9.3(c) and 9.3(d). First, we notice that the range of densities plotted here is very different from that for the direct structures. The higher range of densities for the inverse structures refers to structures where the 'air' particles need to sufficiently overlap with each other to create a connected network of air in the dielectric medium. In contrast to the direct

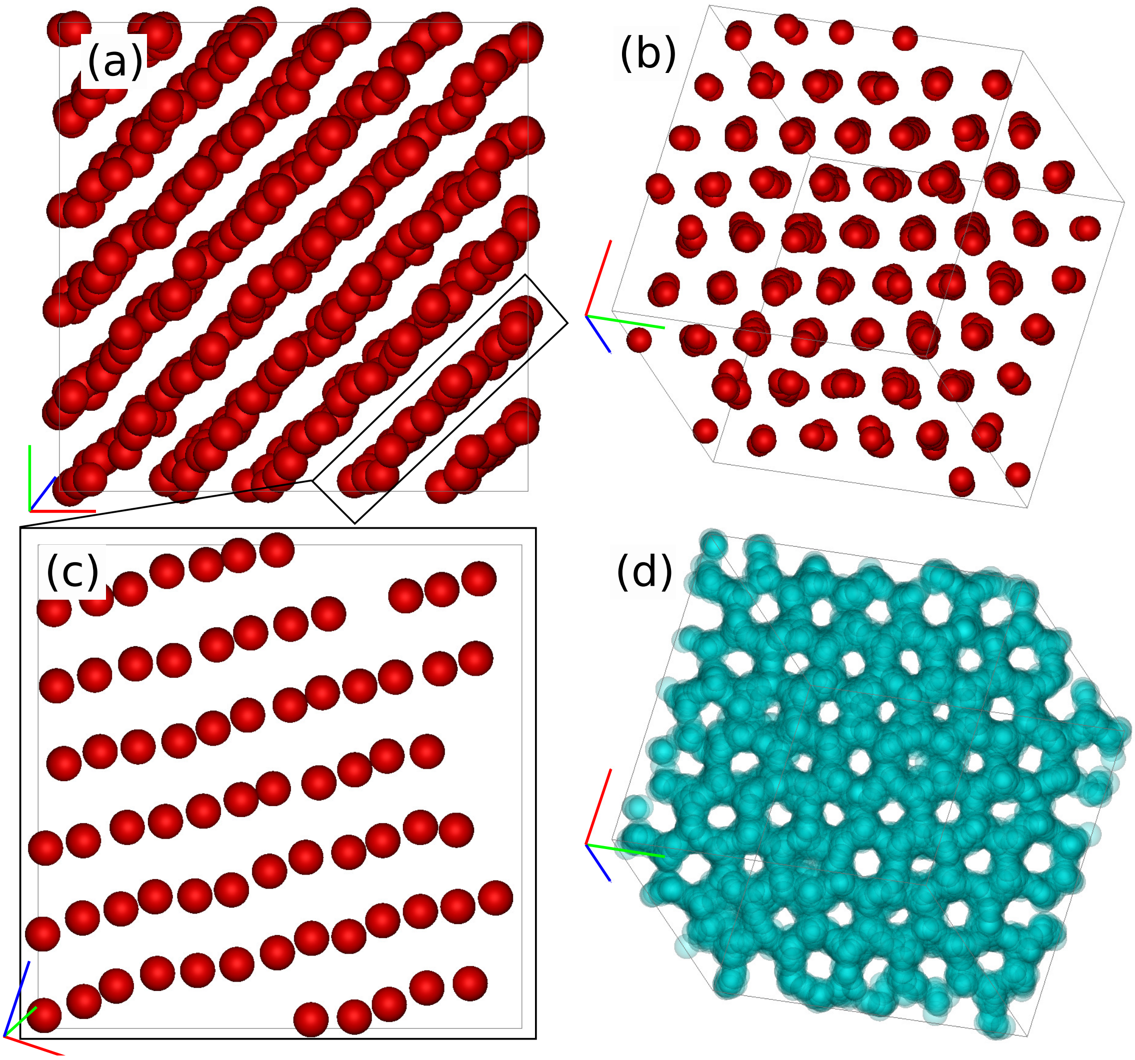

Figure 9.4: Hexagonal columnar phase (COL): **(a,b)** Different orientations of the sample configuration of the COL phase as obtained in our simulations, **(c)** cut-view showing the plane of strings, and **(d)** porous structure obtained by the distribution of voids (in cyan) in the COL phase.

structures, we do not see a huge difference in the photonic behaviour of the inverse structures of PYR and iPYR. This can be explained as follows. In the inverse structures, a connected network of a dielectric material is the primary structure, where air is introduced in the form of particles. As seen in the figure, the photonic band gap starts to form at densities where the particles largely overlap each other. Thus, the presence of two length scales does not have a huge influence in modifying the properties of an already connected air network at these densities. We, thus, do not see a drastic difference between the photonic properties of the inverse structures of PYR and iPYR.

9.3.3 Hexagonal columnar phase - structure and dynamic properties

Columnar phases refer to cylindrical structures with positional order in two dimensions, and are most commonly reported for systems consisting of anisotropic particles [275–277]. The hexagonal columnar phase in our system is spontaneously formed either (1) by compressing an isotropic fluid phase to higher densities at a constant temperature in the NPT ensemble, or (2) by cooling a crystal phase to a lower temperature in the NVT ensemble. An overview of the configurations of this phase as obtained in our simulations is given in Figure 9.4. Figures 9.4(a) and 9.4(b) display the configuration in different orientations. We note the ordering of particles into columns, which are positioned on a hexagonal lattice. In Figure 9.4(c), we present the planar view of particles, which are arranged in strings. We note the ordering of particles in the planes perpendicular to the column axis, while the position of particles along the column axis is irregular. This column axis can be seen as the individual strings in Figure 9.4(c). The incentive for the particles to form these strings is to reduce the number of nearest neighbours, which results in a reduction of the potential energy of the system. The strings are arranged in such a way that each particle has only two neighbours along the strings, and the distance between the neighbouring strings is larger than the shoulder width, thereby resulting in no overlap of coronas between adjacent strings. Similar columnar structures have also been reported for experimental systems of gold nanoparticles functionalised with promesogenic (liquid crystal forming) ligands [278, 279]. We wish to point out that this phase, when spontaneously formed as in the current case, can serve as a template for the fabrication of porous materials, both in its direct or inverse form, as shown in Figures 9.4(b) and 9.4(d). Such a self-assembly of inexpensive porous nanomaterials can be an alternative to molecular caged structures such as zeolites and can be used in applications involving filtration, size-selection, or catalysis [280].

The formation of strings can also be thought of as an energetic caging of particles which essentially restricts the movement of particles in directions perpendicular to the strings. This 'caging' of particles could result in a state of dynamical arrest similar as in gelation [281]. To verify this, we calculate the mean squared displacement (MSD) and self-intermediate scattering

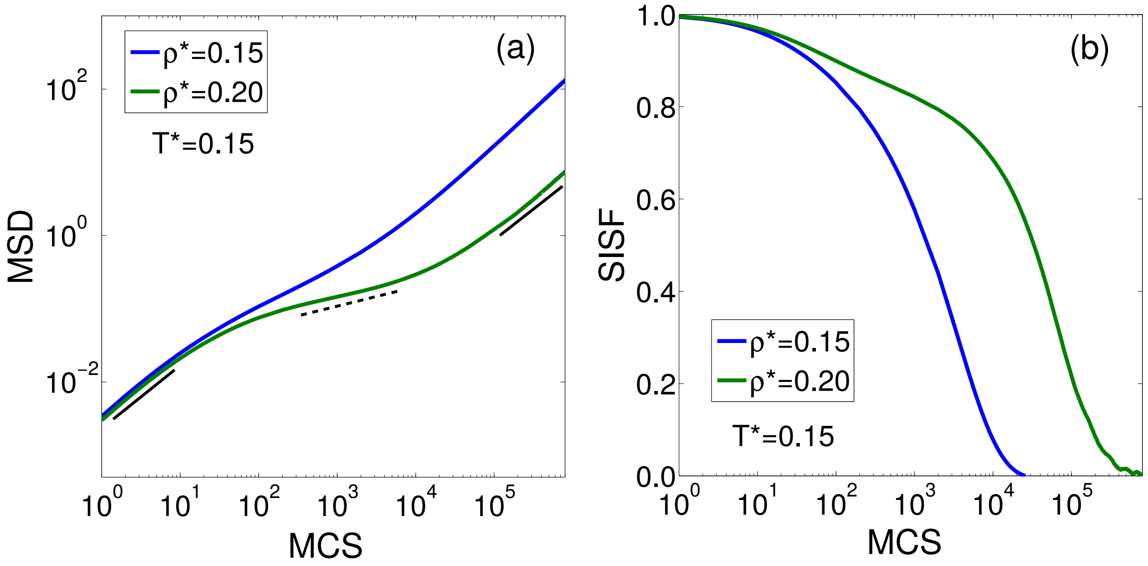

Figure 9.5: Dynamic behaviour of the hexagonal columnar phase (COL): **(a)** Mean squared displacement (MSD) and **(b)** self-part of the intermediate scattering function (SISF) calculated at (reduced) temperature $T^* = k_B T/\varepsilon = 0.15$ and (reduced) densities $\rho^* = N\sigma_{HS}^3/V = 0.15$ and 0.20, respectively, representing the fluid (FL) and columnar (COL) phases.

function (SISF) of the COL phase ($\rho^* = 0.20$) and compare it with those of an isotropic FL phase ($\rho^* = 0.15$). These comparisons calculated at a temperature $T^* = 0.15$ are shown in Figure 9.5. In Figure 9.5(a), we observe an intermediate plateau in the MSD of the COL phase, slope marked by the dashed line in the figure, indicating sub-diffusive behaviour. This is absent in the case of the FL phase. Similar behaviour of the SISF of the COL and the FL phase is noted in Figure 9.5(b); the behaviour of the SISF of the FL phase is exponential in nature, while that of the COL follows a stretched exponential function. The observance of intermediate plateaus in the MSD and SISF imply the presence of a time scale where the dynamics is heterogeneous. This confirms that the formation of strings leads to a heterogeneous dynamics which resembles the relaxation behaviour of liquid crystal phases, which exhibit positional order [282–287].

9.4 Conclusions

In summary, we studied the bulk phase behaviour of a system of colloidal particles interacting with a hard core and a repulsive square-shoulder potential at a shoulder width $\delta = 2.10\sigma_{HS}$, where σ_{HS} is the hard-core diameter. We performed Monte Carlo simulations and free-energy calculations to determine the equilibrium phase diagram. We observe a rich phase behaviour consisting of a fluid, a BCC, three distinct FCC phases, a pyrochlore and a hexagonal columnar phase. We find that the pyrochlore structure formed in our simulations has two characteristic length scales, one corresponding to the distance between particles within a tetrahedron and the other corresponding to the particle distance between neighbouring tetraheda. We calculated the photonic properties of this structure and compared it with the ideal pyrochlore lattice. We found that the presence of two-length scales had a greater influence on the photonic properties of the direct structure than the inverse structure. Contrarily, the photonic properties of the inverse structure for both structures were similar. Finally, we analysed the dynamic behaviour of the hexagonal columnar phase. We infer that the presence of particles in strings leads to slow dynamics in the system.

Acknowledgements

I thank Guido Avvisati for a fruitful collaboration in this project. We jointly performed the cluster identification, RDF, SISF and MSD calculations. We thank Berend van der Meer and Nick Tasios for, respectively, helping us set up the codes for performing the MSD and SISF calculations.

10

The effect of disorder of small spheres on the photonic properties of the inverse binary NaCl structure

---

Inverse opal structures are experimentally realisable photonic band gap materials. They suffer from the drawback of possessing band gaps that are extremely susceptible to structural disorders. A binary colloidal NaCl lattice, which is also experimentally realisable, is a promising alternative to these opals. In this work, we systematically analyse the effect of structural disorder of the small spheres on the photonic properties of a binary NaCl lattice with a size ratio of 0.30 between the small and large spheres. The types of disorders studied include the position of the small spheres in the octahedral void of the large spheres, polydispersity in size of the small spheres, and the fraction of small spheres in the crystal. We find a low susceptibility of the band gap of the inverse NaCl lattice to the disorder of the small spheres. In other words, none of the above disorders completely destroy the photonic band gap of the NaCl lattice, which in most cases result in the reduction of the photonic band gap width.

10.1 Introduction

Photonic band gap (PBG) materials are structures in which the refractive index varies periodically in space on a length scale comparable to the wavelength of light. Similar to the way the motion of electrons is affected by the atomic lattice of a semiconductor, photons can be scattered multiple times by the photonic structure thereby resulting in either propagation or blocking of specific wavelengths of light through this structure. In case that the propagation of bands of wavelengths of light is disallowed for all directions and polarizations, the photonic crystal exhibits a photonic band gap [20, 21]. Three-dimensional photonic crystals with band gaps in the wavelengths pertaining to the visible and near-infra-red regions [42, 188] are believed to be the future of optical devices [13, 14], for which inverse opal structures are promising candidates.

Inverse opal structures consist of spheres made of a low dielectric contrast material embedded at the positions of a face-centered cubic (FCC) lattice inside a material with a high dielectric contrast. Such a structure of air spheres in silicon has a band gap between bands 8 and 9 with a relative gap width of 5 % [26, 27, 288]. Reports of experimental realisations of these structures starting from a precursor colloidal FCC crystal are abundant [17, 35–40]. The inverse crystal can be achieved from the colloidal crystal by infiltrating a high refractive-index dielectric material and then removing the solid spheres by etching or burning to create the air pockets [35]. However, the popularity of these FCC structures is damped by the fact that the photonic band gap formed in such structures is extremely fragile and highly susceptible to the variations in position and size of the spheres [259, 289]. This imposes a strict restriction on the uniformity of these structures. Though there have been efforts to increase the band gap either by connecting the air spheres by cylindrical tunnels [290] or by creating voids by incomplete infiltration of a high dielectric contrast material [188], such increments does not warranty effectiveness against the randomness in the photonic structure. A more attractive solution stems from the reported increase in the photonic band gaps of two-dimensional photonic crystals of dielectric rods in a square, triangular or honeycomb lattice by the addition of smaller interstitial rods [291, 292]. This increase in the gap width is due to the increase in the filling fraction of the dielectric without a disruption in the connectivity of the lattice. Analogously, doping the octahedral interstices of the FCC lattice leads to a binary NaCl lattice, which in its inverse form is reported to possess a band gap with a relative gap width of 9 % [28, 29]. A comparison between the band structures calculated for the close-packed inverse FCC and NaCl structures is given in Figure 10.1. From the figure, we note (1) the larger band gap in NaCl in comparison to the FCC structure and (2) the position of the gap in NaCl is a little higher than in FCC. However, the question regarding susceptibility of this NaCl structure to randomness is, as yet, not investigated.

To answer this question, we first need to understand the construction of the NaCl lattice and consider the different kinds of disorder that results in this structure during its experimental fabrication. The binary NaCl structure consists of spheres of two different sizes, where each species is ordered on a FCC lattice. This inter-penetration of two FCC lattices results in a scenario where the small spheres are positioned in the octahedral voids of the FCC lattice of the large spheres. For a close-packed FCC lattice of large spheres with a radius r_l, the corresponding radius of the small spheres r_s should lie between the radius of the tetrahedral ($r_{te} = 0.22 r_l$) and the octahedral ($r_{oc} = 0.41 r_l$) voids. This ensures that the small spheres do not fit in the tetrahedral voids. Stability of the NaCl structure in binary hard-sphere systems has been predicted

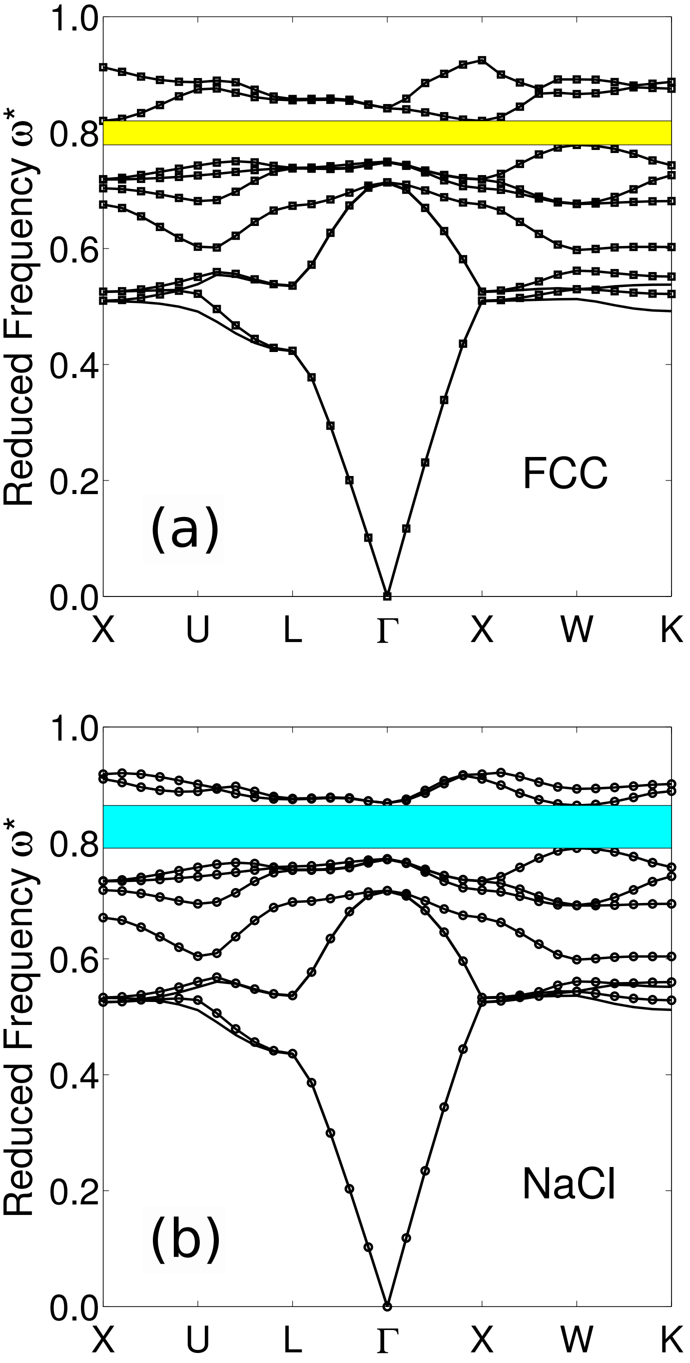

Figure 10.1: Comparison of photonic band structures of **(a)** a face-centered cubic (FCC), and **(b)** a NaCl lattice of air spheres ($\varepsilon = 1$) in silicon ($\varepsilon = 12$). The large spheres in both the structures have a close-packed configuration. In the NaCl structure, the spheres have a size ratio of $q = r_s/r_l = 0.3$, where r_s and r_l are, respectively, the radius of the small and large spheres. The band gap in the FCC and NaCl structures are, respectively, coloured in yellow and cyan. The reduced frequency is written as $\omega^* = \omega a/2\pi c$.

for size ratios ($q = r_s/r_l$) $0.22 < q < 0.41$ by theoretical [293, 294], simulation [295, 296] and experimental [297] studies. Indeed, large binary colloidal crystals with a NaCl structure have been fabricated using hard-sphere-like silica spheres using various external fields such as electric, gravitational, dielectrophoretic fields in combination with colloidal epitaxy [41]. The size ratio of the spheres was $q = 0.30$ with a size polydispersity of about 2 % for the large and 7 % for the small spheres. At this size ratio, the small spheres are not in contact with the large spheres and in principle, can rattle inside the octahedral void. Thus, when the structure is inverted, the position of the small spheres may not be in the centre of the void. Accordingly, the first two parts of this work is concerned with the study of the effect of positional disorder and size polydispersity of the small spheres on the photonic properties of a binary colloidal NaCl lattice.

Furthermore, the phase diagram of a binary mixture of small and large hard spheres with a size ratio $q = 0.30$ was recently reinvestigated using Monte Carlo simulations [296]. It was demonstrated that the so-called interstitial solid solution (ISS) is thermodynamically stable in such a mixture, which consists of a FCC of large spheres but with only a fraction of the octahedral holes filled with small spheres. In addition, it was shown that the fraction of octahedral holes filled with small spheres can be tuned from zero to one, which respectively corresponds to the one-component FCC of only large spheres and the binary NaCl crystal structure. Sedimentation studies of the binary hard-sphere like particles has shown that the fraction of small spheres decreases along the height of the sedimentation column, effectively forming ISSs with varying compositions [29]. Incidentally, ISSs have a huge effect on the photonic properties of the parent material as demonstrated by the change in the structural colour of FCC photonic crystals upon interstitially doping with nanospheres [298]. This leads to the interesting question of how the photonic properties and the photonic band diagrams change for ISSs with varying small sphere compositions in between those of the FCC and the NaCl structures, both of which possess a photonic band gap. Thus, in this work, we also study the effect of small sphere composition on the photonic properties of a binary colloidal ISS with the spheres positioned on an NaCl lattice.

We wish to point out here that although one might expect that the structural disorder of the large spheres has a larger effect on the band gap, we exclusively focus this work on the disorder of the small spheres. This is because of the following reasons: Firstly, we expect the effect of the disorder of the large spheres in the NaCl lattice to be similar to that of the FCC, but less pronounced due to (1) the larger band gap width of the NaCl lattice, and (2) the fact that the small spheres in the NaCl lattice will constrain the movement of the large spheres. We will briefly explain these here. According to (1), for a FCC lattice, a band gap width of about 5 % was nullified with randomness in the position and size of large spheres with a range less than 2 % of the lattice constant [259, 289]. However, as previously mentioned, the band gap width of a NaCl lattice is almost twice as large as that of the FCC lattice consisting of the same dielectric material. Thus, contrary to the situation of increasing the band gap by using a material with higher dielectric constant [259, 289], this could mean that the NaCl lattice can withstand disorders of larger magnitude than the FCC. The situation presented in (2) means that the possible range of positional disorder of the large sphere in a NaCl lattice is limited because of the presence of the small spheres in between them. This, also reduces the effect of the positional disorder of the large spheres. Secondly, during the fabrication of these crystals by sedimentation, the position and composition of the small spheres are more prone to vary in comparison to that of the large spheres and it is thus important to investigate the effect of disorder of the small spheres. However, we have not come across such a study. Our present work is a step in this direction. This chapter is organised as follows. We present the methods used to calculate the photonic band structures in Section 10.2. We then individually discuss our method for studying each of the three types of disorders, and evaluate the effect on the photonic properties of the binary NaCl structure in Section 10.3. We end with some conclusions in Section 10.4.

10.2 Methods

We study the effect of positional disorder, size polydispersity and composition of the small spheres on the photonic properties of a binary colloidal NaCl structure by calculating the photonic band structure diagrams. We focus here on the inverse structures composed of air spheres with dielectric constant $\varepsilon = 1$ in silicon with $\varepsilon = 12$.

We calculate the photonic band structure diagrams using the open-source 'MIT Photonic-Bands' software package [165]. This software package computes fully-vectorial eigenmodes of Maxwell's equations with periodic boundary conditions by preconditioned conjugate-gradient minimisation of the block Rayleigh quotient in a plane wave basis [165]. We describe a primitive cubic NaCl unit cell of lattice constant a by a large sphere with radius $r_l = 0.35350a$, and small sphere with radius $r_s = 0.10605a$. This results in a NaCl structure with a volume fraction $\left(\eta = (4\left(N_l \pi r_l^3 + N_s \pi r_s^3\right)/3V\right)$ of 0.76 and a size ratio of $q = r_s/r_l = 0.30$. For comparison, we mention that the volume fraction of a close-packed FCC lattice is 0.74 and that of a close-packed NaCl lattice with $q = 0.41$ is 0.79. In this primitive representation of the unit cell, the large sphere is positioned at the origin and the small sphere at $(0.50a, 0.50a, 0.50a)$. We normalise each parameter with respect to the lattice constant a. Thus, the band structures can be tuned to any length scale by scaling with a. In order to study the various defects, we make use of a super cell approximation, in which a large crystal with a defect is placed in a super cell and then repeated periodically in a three-dimensional space. We use a super cell containing $3 \times 3 \times 3$ unit cells. Because of memory constraints experienced in running these simulations, different mesh resolutions were used for studying the different aspects of disorder. The resolution cubed equals the number of plane waves included in the calculation, which is equal to the number of grid points used to discretise the unit cell or super cell.

10.3 Results and discussion

In this section, we individually present the results pertaining to each of the three types of disorder.

10.3.1 Effect of positional disorder of the small spheres

First, let us take a look at the effect of the position of the small sphere in the octahedral void. To assess this, we consider lattices in which the position of the small sphere varies from the centre to the periphery of the octahedral void. All three coordinates of the small sphere in a unit cell are collectively changed from $(0.50a, 0.50a, 0.50a)$ to $(0.45a, 0.45a, 0.45a)$ in steps of $0.01a$. We do not change the coordinate of the sphere in a single dimension with respect to the other two. We perform this study using both a unit cell and a super cell. In case of the

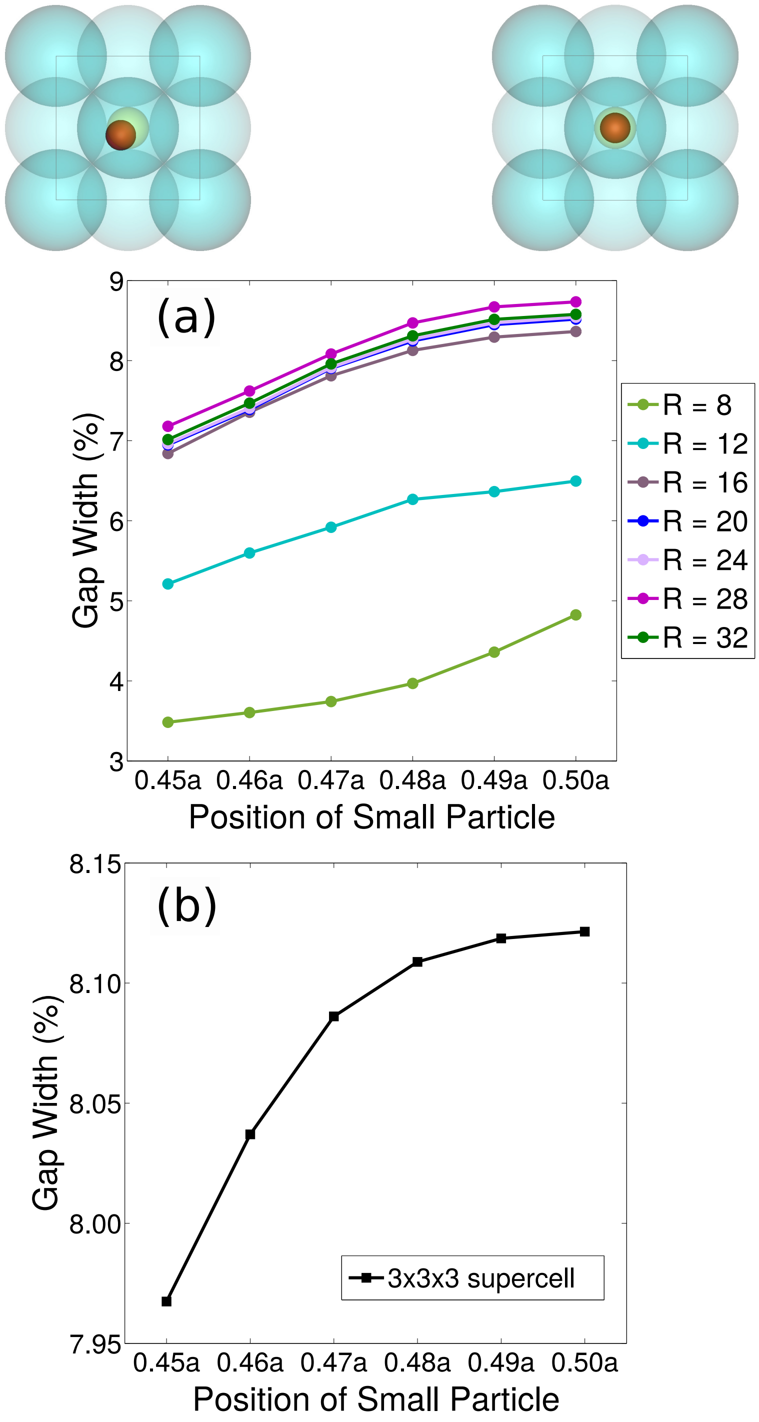

Figure 10.2: Relative gap width of a NaCl lattice of air spheres ($\varepsilon = 1$) in silicon ($\varepsilon = 12$) with a size ratio of $q = r_s/r_l = 0.3$ as a function of the positional coordinate of a small sphere (in units of the lattice constant a) for **(a)** a unit cell calculated at different resolutions R, and **(b)** a super cell of size $3 \times 3 \times 3$ and resolution $R = 24$. The positional extremities are shown in the schematic representations on the **top**. We represent a single small sphere (red) in an octahedral void (green) surrounded by the large spheres (blue).

unit cell, the positional change denotes a collective change in the entire lattice due to periodic boundary conditions. On the other hand, in the case of the super cell, we only vary the position of the central sphere while keeping the position of the others intact. We perform this study at resolutions from 4 to 32 for the unit cell to obtain an indication regarding the resolution to be used in the super cell calculations. On the basis of these results, we decide to use a super cell with a resolution of 24. We compare the various band gaps obtained in each case by calculating the relative gap width, i.e. the ratio of the gap width and the mid-gap frequency.

We plot the relative gap width as a function of the positional coordinate in Figure 10.2. On the top of the figure, we show schematic representations of the extreme positions of the small sphere (red) in the octahedral void (green). The surrounding large spheres (blue) are also shown. Figure 10.2(a) deals with the calculations performed in a unit cell, while Figure 10.2(b) shows that of the super cell. We make four observations from this figure. Firstly, in Figure 10.2(a), we see that the gap width starts to converge at a resolution of 16. This is the lowest resolution that can be used in the super cell calculations. Thus, our resolution value of 24 is justified. Secondly, we observe that the gap width calculated for the ideal NaCl lattice, i.e. at $(0.50a, 0.50a, 0.50a)$, is slightly different in the case of the unit cell (Figure 10.2(a)) and the super cell (Figure 10.2(b)). We attribute this difference to the different mesh resolutions used to discretise the unit cell and super cell. Thirdly, we find that the presence of a photonic band gap is independent of the position of the small sphere, but the relative band gap width decreases with a larger deviation of the small sphere from its ideal position. This is due to the structural disorder that is introduced by the eccentric movement of the small sphere. Lastly, we observe that, at the highest reported resolution for the unit cell, the reduction in the relative gap width is close to two percentage points (around 22 %) when the sphere is moved from the centre to the periphery of the octahedral void. In contrast, the corresponding reduction in case of the super cell is about 0.15 percentage points (about 2 %). This is expected because in the case of the super cell, we calculate the effect of the movement of only a single small sphere; while in the case of the unit cell all small spheres in the system are effectively moved.

10.3.2 Effect of size polydispersity of the small spheres

We study the effect of size polydispersity of the small spheres by changing the radius of a single sphere in a super cell, termed as ‘defect’ particle. We do not, however, change the size of the large spheres, and all particles are kept fixed on their ideal lattice positions. In general, changing the size of the defect sphere results in the addition or removal of dielectric material from the structure and this results in the formation of degenerate states inside the band gap in case of single-component structures [299]. Reducing the size of the dielectric spheres from the ideal radius to zero results in moving the defect state from the lower end to the middle of the band gap. Increasing the size of the dielectric spheres would have an opposite effect, i.e. the defect state moves from the upper end to the lower end of the band gap [299]. However, the behaviour obtained by changing the size of one component with respect to the other in a binary system is not so straightforward. Practically, one would expect polydispersity to be manifested as a random configuration of small particles of different sizes. Our study, where we consider only a single defect per super cell, is a starting point towards this. In our case, we obtain a periodic repetition of the defect.

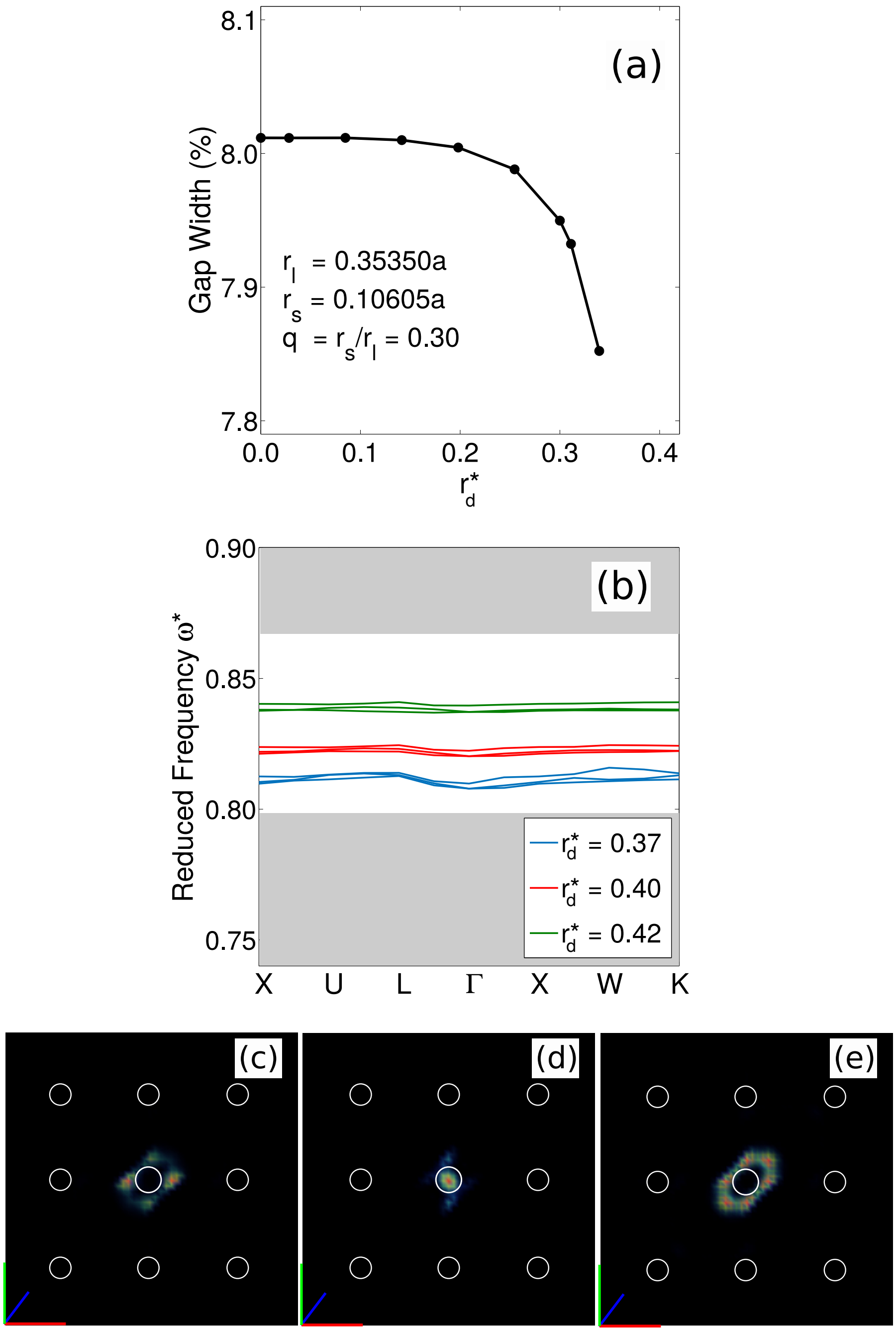

Figure 10.3: Effect of the size of a small sphere on the photonic properties of an NaCl lattice of air spheres ($\varepsilon = 1$) in silicon ($\varepsilon = 12$) with a size ratio of $q = r_s/r_l = 0.3$ calculated by changing the radius $r_d^* = r_d/r_l$ of a single sphere in a super cell of size $3 \times 3 \times 3$: **(a)** Variation in gap width, in %, as a function of radius of the small defect sphere for $r_d^* < 0.37$. **(b)** Frequency of defect states obtained for $0.37 \leq r_d^* \leq 0.42$. The shaded regions indicate the edges of the band gap. The reduced frequency is written as $\omega^* = \omega a/2\pi c$. **(c, d, e)** Electric-field distribution of the resonant modes of the three degenerate defect states at $r_d^* = 0.37$. The open circles represent the position of the small spheres and the defect sphere is at the centre.

Here, we vary the radius of the defect sphere r_d in the calculations from 0.00 to $0.15a$ in steps of $0.01a$. For the analysis, we normalise the defect radius with the ideal radius of the large sphere $r_d^* = r_d/r_l$. The normalised defect radius then varies from 0.00 to 0.42. With this variation, we span the size spectrum from a vacancy to a sphere slightly larger than the radius of the octahedral void, $r_{ov} = 0.41r_l$. This enables us to calculate both the effect of decreasing as well as increasing the radius of the air sphere. For these calculations, we use a super cell of resolution 16. The results are given in Figure 10.3. We find that the resulting behaviour is different for $r_d^* < 0.37$ and $0.37 \leq r_d^* \leq 0.42$. The formation of defect states inside the band gap occurs only at larger defect sizes, i.e. $0.37 \leq r_d^* \leq 0.42$. Let us look at these two situations separately. In Figure 10.3(a), we plot the variation of the gap width as a function of the defect size r_d^*. We find that the gap width decreases upon increasing the defect size. This results in an interesting scenario where the presence of a vacancy in the crystal ($r_d^* = 0.00$) has a larger gap width than the ideal NaCl lattice ($r_d^* = 0.30$). This hints that the presence of an occasional vacancy in the crystal may in fact be beneficial for its photonic properties. A more detailed study of these vacancies (composition) will be presented in the next section (Section 10.3.3). As mentioned, for $0.37 \leq r_d^* \leq 0.42$, we find the formation of defect states in the photonic band gap as shown in Figure 10.3(b). We make the following three observations. Firstly, we notice the presence of three degenerate defect states at each defect size. Such defects can act as a small-sized optical resonator. Secondly, we note that these defect bands are not flat. One would expect a flat defect band for a point defect in an infinite structure. The optical coupling between the different super cells resulting from its finite size results in these non-flat curves. Thirdly, we observe that the frequency of the defect state increases with increasing defect size. This behaviour is similar to that in a single-component system as described above [299]. In Figures 10.3(c), 10.3(d), and 10.3(e), we plot the distribution of the electric field across the sample in the defect states obtained at $r_d^* = 0.37$. The open circles represent the position of the small spheres and the defect sphere is at the centre. We see that the resonant modes of the electric field are localised in the vicinity of the defect, thereby resembling a microcavity. Such a microcavity can be used to enhance the rate of spontaneous emission of a photonic crystal [299]. We note that each defect state is split into three because of the difference in alignment of the defect field with respect to the underlying lattice. Following a previously used naming convention [299], we find that these states are respectively made of two dipole modes (Figures 10.3(c) and 10.3(d)) and a monopole mode (Figure 10.3(e)).

10.3.3 Effect of composition of the small spheres

Finally we study the effect of composition of the binary mixture on the photonic properties. In other words, we study the photonic properties of the interstitial solid solutions with compositions of small spheres intermediate to the FCC and NaCl compositions. At compositions closer to NaCl, this also serves as a study on the effect of vacancies. To this end, we begin with a super cell of FCC and add small spheres in steps of three to it, i.e. from 0 to 27 small spheres in a $3 \times 3 \times 3$ super cell. At each composition, we use three random configurations of small spheres. These calculations were performed at a resolution of 24.

To analyse this, we plot the relative gap width and the gap map as a function of composition in Figure 10.4. We represent the composition as the number ratio of small spheres to all spheres in the system, $x_s = N_s/(N_s + N_l)$, where N_s and N_l are respectively the number of small and

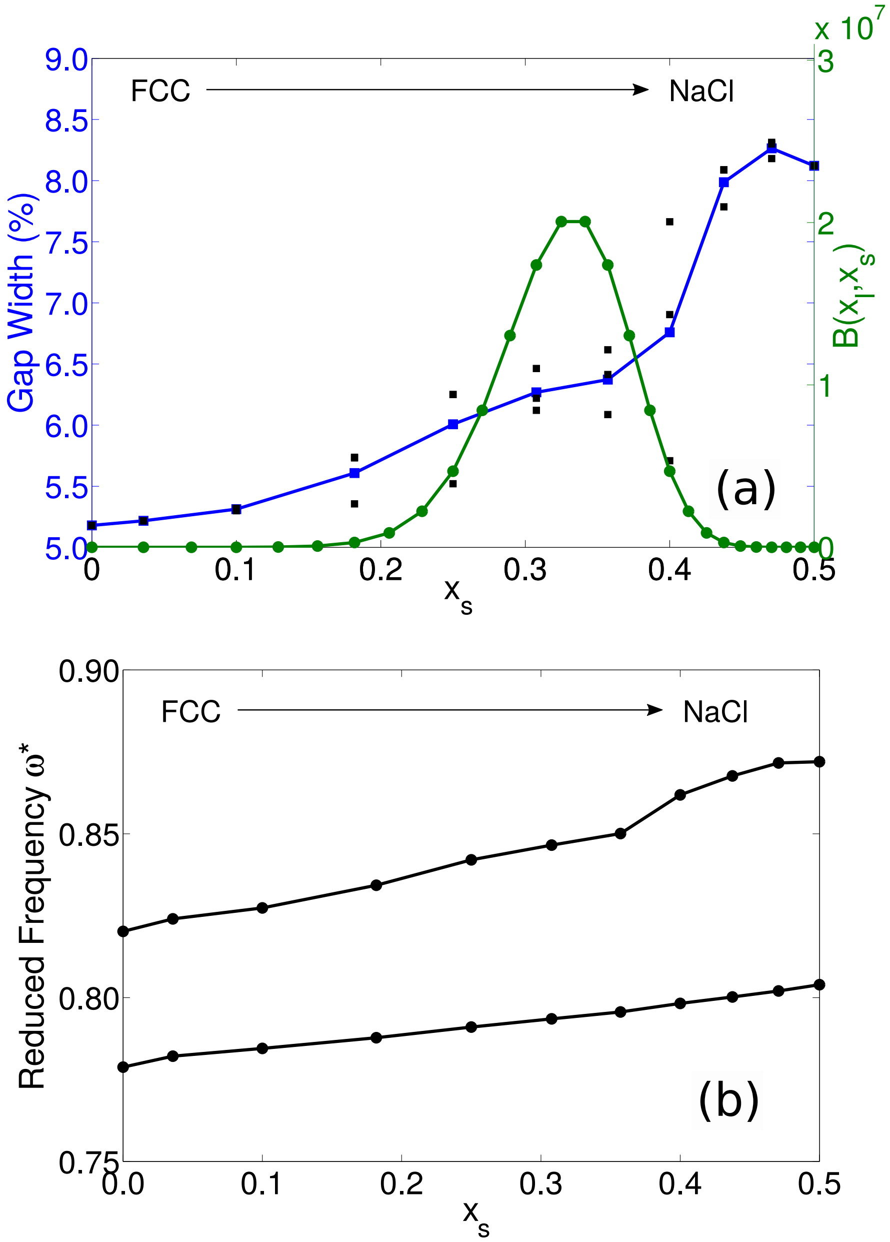

Figure 10.4: Photonic properties of the interstitial solid solution (ISS) with compositions between those of the FCC and NaCl lattices: Variation of **(a)** band gap width, and **(b)** position of the edges of the band gap as a function of composition $(x_s = N_s/(N_s + N_l))$ when going from an inverse FCC to a binary NaCl lattice of air spheres ($\varepsilon = 1$) in silicon ($\varepsilon = 12$) with a size ratio of $q = r_s/r_l = 0.3$ calculated using a super cell of size $3 \times 3 \times 3$. N_s and N_l are, respectively, the number of small and large spheres in the system. In (a), the black dots are the individual values obtained for each of the three configurations used at each composition and the blue curve connects the average of the three values. Here, we also plot a binomial distribution of the number of ways the small spheres can be arranged on the sub-lattice of an NaCl structure in green. In (b), the curve is drawn for the average of the three typical configurations. The reduced frequency is written as $\omega^* = \omega a/2\pi c$.

large spheres in the system. A value of $x_s = 0$ represents a pure FCC lattice, while $x_s = 0.5$ is the NaCl lattice. In Figure 10.4(a), we plot the variation of the gap width as a function of composition. The black dots are the gap width obtained at each of the three configurations used at each composition and the blue curve connects the average of these three values. The behaviour in this plot can be summarised in the following four observations: (1) A continuous curve from $x_s = 0.0$ to 0.5 indicates that the ISS possesses a photonic band gap throughout the entire range of compositions. (2) The band gap increases gradually till $x_s = 0.4$ after which we see a sudden increase in the gap width. This could be due to the filling of most of the octahedral voids and thus, a reduction in the randomness of the structure. (3) The scatter in the gap widths calculated for the various configurations at intermediate compositions is higher than in the extremes. This can be explained by plotting the binomial distribution representing the number of ways the small spheres can be arranged, shown as the green curve in Figure 10.4(a). We notice a direct correlation between the scatter in the gap width and the binomial distribution indicating that the sampling size used at the intermediate compositions may be inadequate. (4) At compositions close to $x_s = 0.50$, we find a small increase in the gap width as reported in the previous section. This reinforces the advantageous effect of the presence of a small concentration of vacancies in the crystal. Correspondingly, we plot the gap map with the position of the band gap as a function of composition in Figure 10.4(b) using the average of the three values. We observe a similar continuous increase from the FCC to the NaCl gap positions, that agrees well with the band structure shown in Figure 10.1.

10.4 Conclusions

In conclusion, we have studied the effect of various disorders pertaining to the small spheres on the photonic properties of a binary NaCl lattice consisting of air spheres in silicon at a size ratio $q = r_s/r_l = 0.30$. Firstly, we confirm that the inverse NaCl structure has a larger band gap than the inverse FCC structure. We then find that the photonic band gap in the inverse NaCl is not very susceptible to disorder in terms of randomness in sphere position, size, and composition of the small particle. We find that the NaCl possess a band gap irrespective of the position of the small sphere inside the octahedral void. However, the relative gap width decreases with larger deviation from its ideal position. Additionally, we find interesting effects of the size polydispersity of the small sphere. We find an increase in the relative band gap width of about 0.15 percentage points (about 19 %) for up to 70 % reduction in the radius of the small particle, i.e. reducing the defect radius r_d from $0.3r_l$ to $0.2r_l$. Furthermore, for a particle radius larger than the ideal size of the small particles, we find the formation of microcavities with resonant states inside the band gap. It is worth pointing out that we find that the presence of up to 10 % vacancies in small spheres does not greatly influence the band gap of the NaCl lattice. Our results, thus, show that the NaCl structure has a low susceptibility to structural defects of the small spheres.

Acknowledgements

I thank Sergei Sokolov (Nanophotonics group) and Guido Avvisati for critical reading of this chapter.

References

[1] International Union of Crystallography, *Report of the Executive Committee for 1991.* Acta Crystallographica, A48:922–946, 1992.

[2] K. M. Ho, C. C. T., and C. M. Soukoulis, *Existence of a photonic band gap in periodic dielectric structures.* Physical Review Letters, 65(25):3152–3155, 1990.

[3] J. Xu and Z. Guo, *Biomimetic photonic materials with tunable structural colors.* Journal of Colloid and Interface Science, 406:1–17, 2013.

[4] S. M. Doucet, M. G. Meadows, and M. Doucet, *Iridescence : A functional perspective.* Interface, 6:S115–S132, 2009.

[5] H. Yin, B. Dong, X. Liu, T. Zhan, L. Shi, J. Zi, and E. Yablonovitch, *Amorphous diamond-structured photonic crystal in the feather barbs of the scarlet macaw.* Proceedings of the National Academy of Sciences, 109(27):10798–10801, 2012.

[6] C. M. Eliason, P.-P. Bitton, and M. D. Shawkey, *How hollow melanosomes affect iridescent colour production in birds.* Proceedings of the Royal Society B, 280(1767):20131505, 2013.

[7] P. Vukusic, B. Hallam, and J. Noyes, *Brilliant whiteness in ultrathin beetle scales.* Science, 315(5810):348, 2007.

[8] M. H. Bartl, J. W. Galusha, L. R. Richey, J. S. Gardner, and J. N. Cha, *Discovery of a diamond-based photonic crystal structure in beetle scales.* Physical Review E, 77(5):050704(R), 2008.

[9] D. G. Stavenga, H. L. Leertouwer, P. Pirih, and M. F. Wehling, *Imaging scatterometry of butterfly wing scales.* Optics Express, 17(1):193–202, 2009.

[10] H. M. Whitney, M. Kolle, P. Andrew, L. Chittka, U. Steiner, and B. J. Glover, *Floral iridescence, produced by diffractive optics, acts as a cue for animal pollinators.* Science, 323(5910):130–133, 2009.

[11] L. Feng, Y. Zhang, M. Li, Y. Zheng, W. Shen, and L. Jiang, *The structural color of red rose petals and their duplicates.* Langmuir, 26(18):14885–14888, 2010.

[12] J.-M. Lourtioz, H. Benistry, V. Berger, J.-M. Gerard, D. Maystre, and A. Tchelnokov. *Photonic crystals: towards nanoscale photonic devices.* Springer, 2005.

[13] S. Noda, K. Tomoda, and N. Yamamoto, *Full three-dimensional photonic bandgap crystals at near-infrared wavelengths.* Science, 289(5479):604–606, 2000.

[14] H. Han, S. Vijayalakshmi, A. Lan, Z. Iqbal, H. Grebel, E. Lalanne, and A. M. Johnson, *Linear and nonlinear optical properties of single-walled carbon nanotubes within an ordered array of nanosized silica spheres.* Applied Physics Letters, 82(9):1458–1460, 2003.

[15] J. Ge and Y. Yin, *Responsive photonic crystals.* Angewandte Chemie International Edition, 50(7):1492–1522, 2011.

[16] G. von Freymann, V. Kitaev, B. V. Lotsch, and G. A. Ozin, *Bottom-up assembly of photonic crystals.* Chemical Society Reviews, 42:2528, 2013.

[17] A. Stein, B. E. Wilson, and S. G. Rudisill, *Design and functionality of colloidal-crystal-templated materials – chemical applications of inverse opals.* Chemical Society Reviews, 42:2763–2803, 2013.

[18] V. P. Bykov, *Spontaneous emission in a periodic structure.* Soviet Journal of Experimental and Theoretical Physics, 35:269, 1972.

[19] K. Ohtaka, *Energy band of photons and low-energy photon diffraction.* Physical Review B, 19(10):5057–5067, 1979.

[20] E. Yablonovitch, *Inhibited spontaneous emission in solid-state physics and electronics.* Physical Review Letters, 58(20):2059–2062, 1987.

[21] S. John, *Strong localization of photons in certain disordered dielectric superlattices.* Physical Review Letters, 58(23):2486–2489, 1987.

[22] J. D. Joannopoulos, S. G. Johnson, J. N. Winn, and R. D. Meade. *Photonic crystals: molding the flow of light*. Princeton university press, second edition, 2011.

[23] M. Maldovan and E. L. Thomas, *Diamond-structured photonic crystals*. Nature Materials, 3(9):593–600, 2004.

[24] T. T. Ngo, C. M. Liddell, M. Ghebrebrhan, and J. D. Joannopoulos, *Tetrastack: Colloidal diamond-inspired structure with omnidirectional photonic band gap for low refractive index contrast*. Applied Physics Letters, 88(24), 2006.

[25] A. J. Garcia-Adeva, *Band gap atlas for photonic crystals having the symmetry of the kagome and pyrochlore lattices*. New Journal of Physics, 8(86), 2006.

[26] H. S. Sözuer, J. W. Haus, and R. Inguva, *Photonic bands: Convergence problems with the plane-wave method*. Physical Review B, 45(24):13962–13972, 1992.

[27] A. Moroz and C. Sommers, *Photonic Band Gaps of Three-Dimensional Face-Centered Cubic Lattices*. Journal of Physics Condensed Matter, 11(4):997, 1999.

[28] J. Thijssen. *Characterization of photonic colloidal crystals in real and reciprocal space*. PhD thesis, Utrecht University, 2007.

[29] E. C. M. Vermolen. *Manipulation of colloidal crystallization*. PhD thesis, Utrecht University, 2008.

[30] E. Yablonovitch, T. J. Gmitter, and K. M. Leung, *Photonic band structure: The face-centered-cubic case employing nonspherical atoms*. Physical Review Letters, 67(17):2295–2298, 1991.

[31] E. Yablonovitch, *Photonic band-gap structures*. Journal of the Optical Society of America B, 10(2):283–295, 1993.

[32] S. Noda, N. Yamamoto, and A. Sasaki, *New realization method for three-dimensional photonic crystal in optical wavelength region*. Jpn. Journal of Applied Physics, 36(Part 1, No. 3B):1907–1911, 1996.

[33] J. Van den Broek, L. Woldering, R. Tjerkstra, F. Segerink, I. Setija, and W. Vos, *Inverse-woodpile photonic band gap crystals with a cubic diamond-like structure made from single-crystalline silicon*. Advanced Functional Materials, 22(1):25–31, 2012.

[34] A. Frölich, J. Fischer, T. Zebrowski, K. Busch, and M. Wegener, *Titania woodpiles with complete three-dimensional photonic bandgaps in the visible*. Advanced Materials, 25(26):3588–3592, 2013.

[35] J. E. G. J. Wijnhoven and W. L. Vos, *Preparation of photonic crystals made of air spheres in titania*. Science, 281(5378):802–804, 1998.

[36] Y. A. Vlasov, X. Z. Bo, J. C. Sturm, and D. J. Norris, *On-chip natural assembly of silicon photonic bandgap crystals*. Nature, 414(6861):289–293, 2001.

[37] R. C. Schroden, M. Al-Daous, C. F. Blanford, and A. Stein, *Optical properties of inverse opal photonic crystals*. Chemistry of Materials, 14(8):3305–3315, 2002.

[38] M. Qi, E. Lidorikis, P. T. Rakich, S. G. Johnson, J. D. Joannopoulos, E. P. Ippen, and H. I. Smith, *A three-dimensional optical photonic crystal with designed point defects*. Nature, 429(6991):538–542, 2004.

[39] Y. Jun, C. A. Leatherdale, and D. J. Norris, *Tailoring air defects in self-assembled photonic bandgap crystals*. Advanced Materials, 17(15):1908–1911, 2005.

[40] Y. Liu, S. Wang, J. W. Lee, and N. A. Kotov, *A floating self-assembly route to colloidal crystal templates for 3D cell scaffolds*. Chemistry of Materials, 17(20):4918–4924, 2005.

[41] E. C. M. Vermolen, A. Kuijk, L. C. Filion, M. Hermes, J. H. J. Thijssen, M. Dijkstra, and B. A. Van, *Fabrication of large binary colloidal crystals with a NaCl structure*. Proceedings of the National Academy of Sciences, 106:16063–16067, 2009.

[42] A.-P. Hynninen, J. H. J. Thijssen, E. C. M. Vermolen, M. Dijkstra, and A. van Blaaderen, *Self-assembly route for photonic crystals with a bandgap in the visible region*. Nature Materials, 6(March):202–205, 2007.

[43] G. Avvisati and M. Dijkstra, *Colloidal Laves phases as precursors of photonic crystals*. Arxiv, pages 1–5, 2016.

[44] T. F. Krauss and R. M. De La Rue, *Photonic crystals in the optical regime - past, present and future*. Progress in Quantum Electronics, 23(2):51–96, 1999.

[45] A. Adreone. *Selected topic in photonic crystals and metamaterials*. World scientific publishing, 2011.

[46] M. Plihal, A. Shambrook, A. Maradudin, and P. Sheng, *Two-dimensional photonic band structures*. Optics Communications, 80(3-4):199–204, 1991.

[47] R. D. Meade, K. D. Brommer, A. M. Rappe, and J. D. Joannopoulos, *Existence of a photonic band gap in two dimensions*. Applied Physics Letters, 61(4):495–497, 1992.

[48] W. M. Robertson, G. Arjavalingam, R. Meade, K. Brommer, A. Rappe, and J. Joannopoulos, *Measurement of photonic band structure in a two-dimensional periodic dielectric array*. Physical Review Letters, 68(13):2023–2026, 1992.

[49] P. R. Villeneuve and M. Piché, *Photonic band gaps in two-dimensional square lattices: Square and circular rods*. Physical Review B, 46(8):4973–4975, 1992.

[50] M. Plihal and A. A. Maradudin, *Photonic band structure of two-dimensional systems: The triangular lattice*. Physical Review B, 44(16):8565–8571, 1991.

[51] D. Cassagne, C. Jouanin, and D. Bertho, *Hexagonal photonic-band-gap structures*. Physical Review B, 53(11):7134–7142, 1996.

[52] R. Padjen, J. Gerard, and J. Marzin, *Analysis of the filling pattern dependence of the photonic bandgap for two-dimensional systems*. Journal of Modern Optics, 41(2):295–310, 1994.

[53] P. Gourley, J. Wendt, G. Vawter, T. Brennan, and B. Hammons, *Optical properties of two-dimensional photonic lattices fabricated as honeycomb nanostructures in compound semiconductors*. Applied Physics Letters, 64(6):687–689, 1994.

[54] T. Krauss, Y. Song, S. Thoms, C. Wilkinson, and R. DelaRue, *Fabrication of 2-d photonic bandgap structures in gaas/algaas*. Electronics Letters, 30(17):1444–1446, 1994.

[55] K. Inoue, M. Wada, K. Sakoda, A. Yamanaka, M. Hayashi, and J. W. Haus, *Fabrication of two-dimensional photonic band structure with near-infrared band gap*. Japanese Journal of Applied Physics, 33(10B):L1463, 1994.

[56] J. Wendt, G. Vawter, P. Gourley, T. Brennan, and B. Hammons, *Nanofabrication of photonic lattice structures in gaas/algaas*. Journal of Vacuum Science & Technology B: Microelectronics and Nanometer Structures Processing, Measurement, and Phenomena, 11(6):2637–2640, 1993.

[57] U. Griining, V. Lehmann, S. Ottow, and K. Busch, *Macroporous silicon with a complete two-dimensional photonic band gap centered at 5pro*. Applied Physics Letters, 68:747, 1996.

[58] V. Pacradouni, W. Mandeville, A. Cowan, P. Paddon, J. F. Young, and S. Johnson, *Photonic band structure of dielectric membranes periodically textured in two dimensions*. Physical Review B, 62(7):4204, 2000.

[59] M. Zelsmann, E. Picard, T. Charvolin, E. Hadji, M. Heitzmann, B. DalZotto, M. Nier, C. Seassal, P. Rojo-Romeo, and X. Letartre, *Seventy-fold enhancement of light extraction from a defectless photonic crystal made on silicon-on-insulator*. Applied Physics Letters, 83(13):2542–2544, 2003.

[60] R. D. Meade, A. M. Rappe, K. D. Brommer, and J. D. Joannopoulos, *Nature of the photonic band gap: some insights from a field analysis*. Journal of the Optical Society of America B, 10(2):328, 1993.

[61] R. Chern, C. C. Chang, C. C. Chang, and R. Hwang, *Large full band gaps for photonic crystals in two dimensions computed by an inverse method with multigrid acceleration*. Physical Review E, 68(2):026704, 2003.

[62] L. Martínez, A. García-Martín, and P. Postigo, *Photonic band gaps in a two-dimensional hybrid triangular-graphite lattice.* Optics Express, 12(23):5684–5689, 2004.

[63] T.-I. Weng and G. Y. Guo, *Band structure of honeycomb photonic crystal slabs*. Journal of Applied Physics, 99(9), 2006.

[64] J. K. Yang, C. Schreck, H. Noh, S. F. Liew, M. I. Guy, C. S. O'Hern, and H. Cao, *Photonic-band-gap effects in two-dimensional polycrystalline and amorphous structures*. Physical Review A, 82(5):1–8, 2010.

[65] W. Man, M. Florescu, K. Matsuyama, P. Yadak, G. Nahal, S. Hashemizad, E. Williamson, P. Steinhardt, S. Torquato, and P. Chaikin, *Photonic band gap in isotropic hyperuniform disordered solids with low dielectric contrast.* Optics Express, 21(17):19972–19981, 2013.

[66] L. S. Froufe-Pérez, M. Engel, P. F. Damasceno, N. Muller, J. Haberko, S. C. Glotzer, and F. Scheffold, *Role of short-range order and hyperuniformity in the formation of band gaps in disordered photonic materials*. Physical Review Letters, 117(5):053902, 2016.

[67] M. Florescu, S. Torquato, and P. J. Steinhardt, *Complete band gaps in two-dimensional photonic quasicrystals*. Physical Review B, 80(15):155112, 2009.

[68] E. Maciá, *Exploiting aperiodic designs in nanophotonic devices.* Reports on Progress in Physics, 75(3):036502, 2012.

[69] M. V. Jaric. *Introduction to quasicrystals*. Academic press, 1988.

[70] C. Janot. *Quasicrystals: A primer*. Oxford university press, 1992.

[71] T. Janssen, G. Chapuis, and M. D. Boissieu. *Aperiodic crystals: from modulated phases to quasicrystals*. Oxford university press, 2007.

[72] J.-M. Dubois. *Useful quasicrystals*. World scientific publishing, 2005.

[73] W. Steurer and S. Deloudi. *Crystallography of quasi-crystals: concepts, methods and structures*. Springer, 2009.

[74] U. Koschella, F. Gähler, J. Roth, and H. R. Trebin, *Phason elastic constants of a binary tiling quasicrystal*. Journal of Alloys and Compounds, 342(1-2):287–290, 2002.

[75] J. de Gier and B. Nienhuis, *The exact solution of an octagonal rectangle-triangle random tiling*. Journal of Statistical Physics, 87:415–437, 1997.

[76] J. B. Suck, M. Schreiber, and P. Häussler. *Quasicrystals: An introduction to structure, physical properties and applications*. Springer, 2002.

[77] M. Engel and H.-R. Trebin, *Self-assembly of monatomic complex crystals and quasicrystals with a double-well interaction potential*. Physical Review Letters, 98(22):225505, 2007.

[78] W. Steurer and D. Sutter-Widmer, *Photonic and phononic quasicrystals*. Journal of Physics D: Applied Physics, 40(13):R229–R247, 2007.

[79] J. I. Urgel, D. Écija, G. Lyu, R. Zhang, C.-A. Palma, W. Auwärter, N. Lin, and J. V. Barth, *Quasicrystallinity expressed in two-dimensional coordination networks*. Nature Chemistry, 8(7):657–662, 2016.

[80] V. Elser, *Indexing problems in quasicrystal diffraction*. Physical Review B, 32(8):4892, 1985.

[81] P. A. Kalugin, *The square-triangle random-tiling model in the thermodynamic limit*. Journal of Physics A: Mathematical and General, 27(11):3599, 1994.

[82] P. Stampfli, *A dodecagonal quasi-periodic lattice in 2 dimensions*. Helvetica Physica Acta, 59(6-7):1260–1263, 1986.

[83] M. Baake, R. Klitzing, and M. Schlottmann, *Fractally shaped acceptance domains of quasiperiodic square-triangle tilings with dedecagonal symmetry*. Physica A: Statistical Mechanics and its Applications, 191(1-4):554–558, 1992.

[84] M. Oxborrow and C. Henley, *Random square-triangle tilings: A model for twelvefold-symmetric quasi-crystals*. Physical Review B, 48(10):6966–6988, 1993.

[85] M. O'Keeffe and M. M. J. Treacy, *Dense quasicrystalline tilings by squares and equilateral triangles.* Acta Crystallographica A, 66:5–9, 2010.

[86] K. Edagawa, *Photonic crystals, amorphous materials, and quasicrystals*. Science and Technology of Advanced Materials, 15(3):034805, 2014.

[87] R. McGrath, U. Grimm, and R. D. Diehl, *The forbidden beauty of quasicrystals*. Physics World, (December 2004), 2004.

[88] Y. Chan, C. Chan, and Z. Liu, *Photonic band gaps in two dimensional photonic quasicrystals*. Physical Review Letters, 80(5):956–959, 1998.

[89] A. Della Villa, S. Enoch, G. Tayeb, V. Pierro, V. Galdi, and F. Capolino, *Band gap formation and multiple scattering in photonic quasicrystals with a Penrose-type lattice*. Physical Review Letters, 94(18):183903, 2005.

[90] S. M. Thon, W. T. M. Irvine, D. Kleckner, and D. Bouwmeester, *Polychromatic photonic quasicrystal cavities*. Physical Review Letters, 104(24):243901, 2010.

[91] M. Zoorob, M. Charlton, G. Parker, J. Baumberg, and M. Netti, *Complete photonic bandgaps in 12-fold symmetric quasicrystals*. Nature, 404(6779):740–3, 2000.

[92] X. Zhang, Z.-Q. Zhang, and C. Chan, *Absolute photonic band gaps in 12-fold symmetric photonic quasicrystals*. Physical Review B, 63(8):081105, 2001.

[93] W. Man, M. Megens, P. J. Steinhardt, and P. M. Chaikin, *Experimental measurement of the photonic properties of icosahedral quasicrystals.* Nature, 436(7053):993–996, 2005.

[94] A. Ledermann, L. Cademartiri, M. Hermatschweiler, C. Toninelli, G. a. Ozin, D. S. Wiersma, M. Wegener, and G. von Freymann, *Three-dimensional silicon inverse photonic quasicrystals for infrared wavelengths.* Nature Materials, 5(12):942–945, 2006.

[95] J. Xu, R. Ma, X. Wang, and W. Y. Tam, *Icosahedral quasicrystals for visible wavelengths by optical interference holography.* Optics Express, 15(7):4287–95, 2007.

[96] D. Shechtman and I. Blech, *Metallic phase with long-range orientational order and no translational symmetry*. Physical Review Letters, 53(20):1951–1954, 1984.

[97] I. Peterson, *Probing deeper into quasicrystals*. Science News, 128(18):278–279, 1985.

[98] L. Pauling, *The nonsense about quasicrystals*. Science News, 129(1):3–3, 1986.

[99] S. Schmid, R. Withers, and R. Lifshitz. *Aperiodic crystals*. Springer, 2013.

[100] D. D. P. and P. J. Steinhardt. *Quasicrystals: The state of art.* World scientific publishing, 1999.

[101] H. Chen, D. Li, and K. Kuo, *New type of two-dimensional quasicrystal with twelvefold rotational symmetry*. Physical Review Letters, 60(16):1645, 1988.

[102] M. Conrad, F. Krumeich, and B. Harbrecht, *A dodecagonal quasicrystalline chalcogenide*. Angewandte Chemie International Edition, 37(10):1383–1386, 1998.

[103] S. Förster, K. Meinel, R. Hammer, M. Trautmann, and W. Widdra, *Quasicrystalline structure formation in a classical crystalline thin-film system*. Nature, 502(7470):215–218, 2013.

[104] N. A. Wasio, R. C. Quardokus, R. P. Forrest, C. S. Lent, S. A. Corcelli, J. A. Christie, K. W. Henderson, and S. A. Kandel, *Self-assembly of hydrogen-bonded two-dimensional quasicrystals*. Nature, 507(7490):86–89, 2014.

[105] X. Zeng, G. Ungar, Y. Liu, V. Percec, A. E. Dulcey, and J. K. Hobbs, *Supramolecular dendritic liquid quasicrystals.* Nature, 428:157–160, 2004.

[106] A. Takano, W. Kawashima, A. Noro, Y. Isono, N. Tanaka, T. Dotera, and Y. Matsushita, *A mesoscopic archimedean tiling having a new complexity in an ABC star polymer*. Journal of Polymer Science Part B Polymer Physics, 43(18):2427–2432, 2005.

[107] T. Dotera and T. Gemma, *Dodecagonal quasicrystal in a polymeric alloy*. Philosophical Magazine, 86(6-8):1085–1091, 2006.

[108] K. Hayashida, T. Dotera, A. Takano, and Y. Matsushita, *Polymeric quasicrystal: Mesoscopic quasicrystalline tiling in ABC star polymers*. Physical Review Letters, 98(19):195502, 2007.

[109] S. Lee, M. J. Bluemle, and F. S. Bates, *Discovery of a Frank-Kasper sigma phase in sphere-forming block copolymer melts.* Science, 330(6002):349–353, 2010.

[110] S. Fischer and A. Exner, *Colloidal quasicrystals with 12-fold and 18-fold diffraction symmetry*. Proceedings of the National Academy of Sciences, pages 1–5, 2011.

[111] D. V. Talapin, E. V. Shevchenko, M. I. Bodnarchuk, X. Ye, J. Chen, and C. B. Murray, *Quasicrystalline order in self-assembled binary nanoparticle superlattices.* Nature, 461(7266):964–7, 2009.

[112] M. I. Bodnarchuk, R. Erni, F. Krumeich, and M. V. Kovalenko, *Binary superlattices from colloidal nanocrystals and giant polyoxometalate clusters.* Nano Letters, 13(4):1699–705, 2013.

[113] X. Ye, J. Chen, M. E. Irrgang, M. Engel, A. Dong, S. C. Glotzer, and C. B. Murray, *Quasicrystalline binary nanocrystal superlattice with partial matching rules*. Nature Materials, 16:214–217, 2016.

[114] Z. Yang, J. Wei, P. Bonville, and M. P. Pileni, *Beyond entropy: Magnetic forces induce formation of quasicrystalline structure in binary nanocrystal superlattices*. Journal of the American Chemical Society, 137(13):4487–4493, 2015.

[115] C. Xiao, N. Fujita, K. Miyasaka, Y. Sakamoto, and O. Terasaki, *Dodecagonal tiling in mesoporous silica.* Nature, 487(7407):349–353, 2012.

[116] Y. Roichman and D. Grier, *Holographic assembly of quasicrystalline photonic heterostructures.* Optics Express, 13(14):5434–5439, 2005.

[117] J. Mikhael, J. Roth, L. Helden, and C. Bechinger, *Archimedean-like tiling on decagonal quasicrystalline surfaces.* Nature, 454(7203):501–504, 2008.

[118] E. A. Jagla, *Phase behavior of a system of particles with core collapse.* Physical Review E, 58(2):11, 1998.

[119] P. W. Leung, C. L. Henley, and G. V. Chester, *Dodecagonal order in a two-dimensional Lennard-Jones system.* Physical Review B, 39(1):446–458, 1989.

[120] K. J. Strandburg, *Random-tiling quasicrystal.* Physical Review B, 40(9):6071–6084, 1989.

[121] A. Skibinsky, S. V. Buldyrev, A. Scala, S. Havlin, and H. E. Stanley, *Quasicrystals in a monodisperse system.* Physical Review E., 60(3):2664–9, 1999.

[122] L. Q. Costa Campos, C. C. de Souza Silva, and S. W. S. Apolinario, *Structural phases of colloids interacting via a flat-well potential.* Physical Review E, 86(5):051402, 2012.

[123] T. Dotera, T. Oshiro, and P. Ziherl, *Mosaic two-lengthscale quasicrystals.* Nature, 506(7487):208–11, 2014.

[124] M. Engel, P. F. Damasceno, C. L. Phillips, and S. C. Glotzer, *Computational self-assembly of a one-component icosahedral quasicrystal.* Nature Materials, 14(1):109–116, 2014.

[125] D. Salgado-blanco and C. I. Mendoza, *Non-additive simple potentials for pre-programmed self-assembly.* Soft Matter, 11:889–897, 2015.

[126] R. P. Dressel and K. J. Strandburg, *Thermodynamic behaviour of a penrose-tiling quasicrystal.* Physical Review B, 41(4):2469–2478, 1990.

[127] J. Dontabhaktuni, M. Ravnik, and S. Zumer, *Quasicrystalline tilings with nematic colloidal platelets.* Proceedings of the National Academy of Sciences, 111(7):2464–2469, 2014.

[128] J. A. Millan, D. Ortiz, G. Van Anders, and S. C. Glotzer, *Self-assembly of archimedean tilings with enthalpically and entropically patchy polygons.* ACS Nano, 8(3):2918–2928, 2014.

[129] A. Haji-Akbari, M. Engel, and S. C. Glotzer, *Degenerate quasicrystal of hard triangular bipyramids.* Physical Review Letters, 107:215702, 2011.

[130] A. Haji-Akbari, M. Engel, A. S. Keys, X. Zheng, R. G. Petschek, P. Palffy-Muhoray, and S. C. Glotzer, *Disordered, quasicrystalline and crystalline phases of densely packed tetrahedra.* Nature, 462(7274):773–777, 2009.

[131] T. Graham, *Liquid diffusion applied to analysis.* Philosophical Transactions of the Royal Society of London, 151:183–224, 1861.

[132] R. Brown, *A brief account of microscopical observations made in the months of june, july and august 1827, on the particles contained in the pollen of plants; and on the general existence of active molecules in organic and inorganic bodies.* Philosophical Magazine Series 2, 4(21):161–173, 1828.

[133] A. Einstein, *Über die von der molekularkinetischen theorie der wärme geforderte bewegung von in ruhenden flüssigkeiten suspendierten teilchen.* Annalen der physik, 322(8):549–560, 1905.

[134] P. C. Hemmer and G. Stell, *Fluids with several phase transitions.* Physical Review Letters, 24(23):1284–1287, 1970.

[135] E. A. Jagla, *Minimum energy configurations of repelling particles in two dimensions.* The Journal of Chemical Physics, 110(1):451–456, 1999.

[136] G. Malescio and G. Pellicane, *Stripe phases from isotropic repulsive interactions.* Nature Materials, 2:97–100, 2003.

[137] P. Camp, *Structure and phase behavior of a two-dimensional system with core-softened and long-range repulsive interactions.* Physical Review E, 68(6):061506, 2003.

[138] G. Malescio and G. Pellicane, *Stripe patterns in two-dimensional systems with core-corona molecular architecture.* Physical Review E, 70(2):021202, 2004.

[139] J. Fornleitner and G. Kahl, *Pattern formation in two-dimensional square-shoulder systems.* Journal of Physics Condensed Matter, 22(10):104118, 2010.

[140] M. Singh, H. Liu, S. K. Kumar, A. Ganguly, and C. Chakravarty, *Excess entropy and structural transitions in a two-dimensional square-shoulder fluid.* The Journal of Chemical Physics, 132(7):074503, 2010.

[141] T. Dotera, *Quasicrystals in soft matter.* Isreal Journal of Chemistry, 51(11-12):1197–1205, 2011.

[142] H. G. Schoberth, H. Emmerich, M. Holzinger, M. Dulle, S. Fö Rster, and T. Gruhn, *Molecular dynamics study of colloidal quasicrystals.* Soft Matter, 12:7644–7654, 2016.

[143] Y. D. Fomin, N. V. Gribova, V. N. Ryzhov, S. M. Stishov, and D. Frenkel, *Quasibinary amorphous phase in a three-dimensional system of particles with repulsive-shoulder interactions.* The Journal of Chemical Physics, 129(6):064512, 2008.

[144] N. Gribova, Y. Fomin, D. Frenkel, and V. Ryzhov, *Waterlike thermodynamic anomalies in a repulsive-shoulder potential system.* Physical Review E, 79(5):51202, 2009.

[145] Y. D. Fomin, E. N. Tsiok, and V. N. Ryzhov, *Complex phase behavior of the system of particles with smooth potential with repulsive shoulder and attractive well.* The Journal of Chemical Physics, 134(4):044523, 2011.

[146] A. Jain, J. R. Errington, and T. M. Truskett, *Inverse design of simple pairwise interactions with low-coordinated 3D lattice ground states.* Soft Matter, 9(14):3866, 2013.

[147] A. Jain, J. R. Errington, and T. M. Truskett, *Dimensionality and design of isotropic interactions that stabilize honeycomb, square, simple cubic, and diamond lattices.* Physical Review X, 4(3):1–8, 2014.

[148] C. I. Mendoza and E. Batta, *Self-assembly of binary nanoparticle dispersions: from square arrays and stripe phases to colloidal corrals.* Europhysics Letters, 13:56004, 2009.

[149] G. Das, N. Gnan, F. Sciortino, and E. Zaccarelli, *Unveiling the complex glassy dynamics of square shoulder systems: simulations and theory.* The Journal of Chemical Physics, 138(13):134501, 2013.

[150] P. Ziherl and R. D. Kamien, *Maximizing entropy by minimizing area: Towards a new principle of self-organization.* The Journal of Physical Chemistry B, 105(42):10147–10158, 2001.

[151] D. Frenkel and B. Smit. *Understanding molecular simulation: From algorithm to applications.* Academic press, 1996.

[152] P. Strating, *Brownian dynamics simulation of a hard-sphere suspension.* Physical Review E, 59:2175–2187, 1999.

[153] A. Scala, T. Voigtmann, and C. D. Michele, *Event-driven brownian dynamics for hard spheres.* The Journal of Chemical Physics, 126(13):134109, 2007.

[154] F. Smallenburg. *Clustering and self-assembly in colloidal systems.* PhD thesis, Utrecht University, 2009.

[155] M. Marechal, M. Hermes, and M. Dijkstra, *Stacking in sediments of colloidal hard spheres.* The Journal of chemical physics, 135(3):034510, 2011.

[156] T. Dasgupta, J. R. Edison, and M. Dijkstra, *Growth of defect-free colloidal hard-sphere crystals using colloidal epitaxy.* The Journal of Chemical Physics, 146(7):074903, 2017.

[157] C. Vega and E. Sanz, *Determination of phase diagrams via computer simulation: methodology and applications to water, electrolytes and proteins.* Journal of Physics Condensed Matter, 153101(15), 2008.

[158] A. Santos, M. Lopez de Haro, and S. Bravo Yuste, *An accurate and simple equation of state for hard disks.* The Journal of Chemical Physics, 103(11):4622, 1995.

[159] J. M. Polson, E. Trizac, S. Pronk, and D. Frenkel, *Finite-size corrections to the free energies of crystalline solids.* The Journal of Chemical Physics, 112(12):5339, 2000.

[160] A. M. Almudallal, S. V. Buldyrev, and I. Saika-Voivod, *Phase diagram of a two-dimensional system with anomalous liquid properties.* The Journal of Chemical Physics, 137(3):034507, 2012.

[161] T. Schilling and F. Schmid, *Computing absolute free energies of disordered structures by molecular simulation.* The Journal of Chemical Physics, 131(23):231102, 2009.

[162] F. Schmid and T. Schilling, *A method to compute absolute free energies or enthalpies of fluids.* Physics Procedia, 4:131–143, 2010.

[163] M. T. Marechal. *Anisotropic colloids: bulk phase behavior and equilibrium sedimentation.* PhD thesis, Utrecht University, 2009.

[164] H. Weber, D. Marx, and K. Binder, *Melting transition in two dimensions: A finite-size scaling analysis of bond-orientational order in hard disks*. Physical Review B, 51(20):14636–14651, 1995.

[165] S. Johnson and J. Joannopoulos, *Block-iterative frequency-domain methods for Maxwell's equations in a planewave basis*. Optics Express, 8(3):173, 2001.

[166] F. Ramos-Mendieta and P. Halevi, *Electromagnetic surface modes of a dielectric superlattice: the supercell method*. Journal of the Optical Society of America B, 14(2):370, 1997.

[167] A. Haji-Akbari, M. Engel, and S. C. Glotzer, *Phase diagram of hard tetrahedra*. The Journal of Chemical Physics, 135:1–12, 2011.

[168] A. Haji-Akbari, E. R. Chen, M. Engel, and S. C. Glotzer, *Packing and self-assembly of truncated triangular bipyramids*. Physical Review E, 88:012127, 2013.

[169] K. Barkan, H. Diamant, and R. Lifshitz, *Stability of quasicrystals composed of soft isotropic particles*. Physical Review B, 83(17):172201, 2011.

[170] R. Lifshitz and H. Diamant, *Soft quasicrystals – why are they stable?* Philosophical Magazine, 87(18-21):3021–3030, 2007.

[171] T. Dotera, *Toward the discovery of new soft quasicrystals: From a numerical study viewpoint*. Journal of Polymer Science Part B Polymer Physics, 50(3):155–167, 2012.

[172] C. V. Achim, M. Schmiedeberg, and H. Löwen, *Growth modes of quasicrystals*. Physical Review Letters, 112(25):255501, 2014.

[173] C. R. Iacovella, A. S. Keys, and S. C. Glotzer, *Self assembly of soft matter quasicrystals and their approximants*. Proceedings of the National Academy of Sciences, 108(52):9, 2011.

[174] M. de Boissieu, *Stability of quasicrystals: energy, entropy and phason modes*. Philosophical Magazine, 86(6-8):1115–1122, 2006.

[175] A. I. Goldman and R. F. Kelton, *Quasicrystals and crystalline approximants*. Reviews of Modern Physics, 65(1), 1993.

[176] A. Kiselev, M. Engel, and H. R. Trebin, *Confirmation of the random tiling hypothesis for a decagonal quasicrystal*. Physical Review Letters, 109(22):225502, 2012.

[177] A. Reinhardt, F. Romano, and J. P. K. Doye, *Computing phase diagrams for a quasicrystal-forming patchy-particle system*. Physical Review Letters, 110(25):255503, 2013.

[178] M. Widom, *Bethe Ansatz solution of the square-triangle random tiling model*. Physical Review Letters, 70(14):2094–2097, 1993.

[179] J. Roth and F. Gähler, *Atomic self-diffusion in dodecagonal quasicrystals*. The European Physical Journal B, 6(4):425–445, 1998.

[180] M. N. van der Linden, J. Doye, and A. Louis, *Formation of dodecagonal quasicrystals in two-dimensional systems of patchy particles*. The Journal of Chemical Physics, 136(5):54904, 2012.

[181] W. Li, H. Park, and M. Widom, *Phase diagram of a random tiling quasicrystal*. Journal of Statistical Physics, 66(1-2):1–69, 1992.

[182] B. Nienhuis, *Exact solution of random tiling models*. Physics Reports, 301(1-3):271–292, 1998.

[183] T. Ishimasa, *Dodecagonal quasicrystals still in progress*. Isreal Journal of Chemistry, 51(11-12):1216–1225, 2011.

[184] E. P. Bernard and W. Krauth, *Two-step melting in two dimensions: First-order liquid-hexatic transition*. Physical Review Letters, 107(15):155704, 2011.

[185] W. Qi, A. P. Gantapara, and M. Dijkstra, *Two-stage melting induced by dislocations and grain boundaries in monolayers of hard spheres*. Soft Matter, 10(30):5449–5457, 2014.

[186] M. Kohmoto, B. Sutherland, and K. Iguchi, *Localization of optics: Quasiperiodic media*. Physical Review Letters, 58(23):2436–2438, 1987.

[187] Z. Vardeny, A. Nahata, and A. Agrawal, *Optics of photonic quasicrystals*. Nature Photonics, 7, 2013.

[188] K. Busch and S. John, *Photonic band gap formation in certain self-organizing systems*. Physical Review E, 58(3):3896–3908, 1998.

[189] B. Y. Xia, G. Byron, Y. Yadong, and L. Yu, *Monodispersed colloidal spheres : Old materials with new applications*. Advanced Materials, 12(10):693–713, 2000.

[190] R. Lifshitz and D. Petrich, *Theoretical model for Faraday waves with multiple-frequency forcing*. Physical Review Letters, 79(7):1261–1264, 1997.

[191] A. M. Rucklidge and M. Silber, *Quasipatterns in parametrically forced systems*. Physical Review E, 75(5):1–4, 2007.

[192] A. J. Archer, A. M. Rucklidge, and E. Knobloch, *Quasicrystalline order and a crystal-liquid state in a soft-core fluid*. Physical Review Letters, 111(16):1–5, 2013.

[193] A. J. Archer, A. M. Rucklidge, and E. Knobloch, *Soft-core particles freezing to form a quasicrystal and a crystal-liquid phase*. Physical Review E, 92(1):012324, 2015.

[194] A. D. Young and B. J. Alder, *Melting-curve extrema from a repulsive "step" potential*. Physical Review Letters, 38(21):1213–1216, 1977.

[195] G. Malescio, F. Saija, and S. Prestipino, *Anomalous melting behavior under extreme conditions: Hard matter turning "soft"*. The Journal of Chemical Physics, 129(24):127–131, 2008.

[196] S. V. Buldyrev, G. Malescio, C. a. Angell, N. Giovambattista, S. Prestipino, F. Saija, H. E. Stanley, and L. Xu, *Unusual phase behavior of one-component systems with two-scale isotropic interactions*. Journal of Physics Condensed Matter, 21(50):504106, 2009.

[197] H. Kawamura, *A simple theory of melting and condensation in two-dimensional system*. Progress of Theoretical Physics, 63(1):24–41, 1980.

[198] K. W. Wojciechowski, *Entropy driven demixing: why?* Physica A: Statistical Mechanics and its Applications, 232:723–736, 1996.

[199] J. G. Kirkwood, E. K. Maun, and B. Alder, *Radial distribution functions and the equation of state of a fluid composed of rigid spherical molecules*. The Journal of Chemical Physics, 18(8):1040–1047, 1950.

[200] R. Piazza, T. Bellini, and V. Degiorgio, *Equilibrium sedimentation profiles of screened charged colloids: A test of the hard-sphere equation of state*. Physical Review Letters, 71(25):4267, 1993.

[201] A.-P. Hynninen, R. van Roij, and M. Dijkstra, *Sedimentation profiles of charged colloids: Entropic lift and charge separation*. Europhysics Letters, 65(5):719, 2004.

[202] T. Biben and J.-P. Hansen, *Localized density profiles in binary colloidal suspensions*. Molecular Physics, 80(4):853–859, 1993.

[203] S. Savenko and M. Dijkstra, *Sedimentation and multiphase equilibria in suspensions of colloidal hard rods*. Physical Review E, 70(5):051401, 2004.

[204] M. Shimoda, T. Sato, A. Tsai, and J. Guo, *Epitaxial crystalline film with psuedo-tenfold symmetry formed by au-deposition on a decagonal al 72 ni 12 co 16 quasicrystal*. Physical Review B, 62(17):11288, 2000.

[205] K. Franke, H. Sharma, W. Theis, P. Gille, P. Ebert, and K. Rieder, *Quasicrystalline epitaxial single element monolayers on icosahedral al-pd-mn and decagonal al-ni-co quasicrystal surfaces*. Physical Review Letters, 89(15):156104, 2002.

[206] V. Fournée, T. Cai, A. Ross, T. A. Lograsso, J. W. Evans, and P. A. Thiel, *Nucleation and growth of ag films on a quasicrystalline alpdmn surface*. Physical Review B, 67(3):033406, 2003.

[207] S. Curtarolo, W. Setyawan, N. Ferralis, R. D. Diehl, and M. W. Cole, *Evolution of topological order in xe films on a quasicrystal surface*. Physical Review Letters, 95(13):136104, 2005.

[208] B. Bilki, M. Erbudak, M. Mungan, and Y. Weisskopf, *Structure formation of a layer of adatoms on a quasicrystalline substrate: Molecular dynamics study*. Physical Review B, 75(4):045437, 2007.

[209] M. Mungan, Y. Weisskopf, and M. Erbudak, *Deposition of atoms on a quasicrystalline substrate: Molecular dynamics study in three dimensions*. Physical Review B, 76(19):195443, 2007.

[210] M. Schmiedeberg and H. Stark, *Colloidal ordering on a 2D quasicrystalline substrate*. Physical Review Letters, 101:218302, 2008.

[211] M. Engel. *Dynamics and defects of complex crystals and quasicrystals : perspectives from simple model systems*. PhD thesis, Universitat Stuttgart, 2008.

[212] M. Engel, M. Umezaki, H. R. Trebin, and T. Odagaki, *Dynamics of particle flips in two-dimensional quasicrystals*. Physical Review B, 82(13):1–9, 2010.

[213] A. Metere, P. Oleynikov, M. Dzugutov, and S. Lidin, *A smectic dodecagonal quasicrystal*. Soft Matter, 12(43):8869–8875, 2016.

[214] R. E. Ryltsev, B. A. Klumov, and N. M. Chtchelkatchev, *Self-assembly of the decagonal quasicrystalline order in simple three-dimensional systems*. Soft Matter, 11:6991–6998, 2015.

[215] P. Ziherl and R. D. Kamien, *Soap froths and crystal structures*. Physical Review Letters, 85(16):3528–3531, 2000.

[216] M. Seul and R. Wolfe, *Evolution of disorder in magnetic stripe domains. I. Transverse instabilities and disclination unbinding in lamellar patterns*. Physical Review A, 46(12):7519–7533, 1992.

[217] A. Yethiraj and A. van Blaaderen, *A colloidal model system with an interaction tunable from hard sphere to soft and dipolar.* Nature, 421(6922):513–517, 2003.

[218] W. D. Ristenpart, I. A. Aksay, and D. A. Saville, *Electrically guided assembly of planar superlattices in binary colloidal suspensions*. Physical Review Letters, 90(12):128303, 2003.

[219] I. Varga, F. Kun, and K. F. Pál, *Structure formation in binary colloids*. Physical Review E, 69(3 1):2–5, 2004.

[220] I. Varga and F. Kun, *Pattern formation in binary colloids*. Philosophical Magazine, 86(13-14):2011–2031, 2005.

[221] A. P. Hynninen and M. Dijkstra, *Phase diagram of dipolar hard and soft spheres: Manipulation of colloidal crystal structures by an external field*. Physical Review Letters, 94(138303), 2005.

[222] N. Osterman, D. Babic, I. Poberaj, J. Dobnikar, and P. Ziherl, *Observation of condensed phases of quasiplanar core-softened colloids*. Physical Review Letters, 99(248301), 2007.

[223] K. S. Khalil, A. Sagastegui, Y. Li, M. a. Tahir, J. E. S. Socolar, B. J. Wiley, and B. B. Yellen, *Binary colloidal structures assembled through Ising interactions*. Nature Communications, 3:794, 2012.

[224] P. Liu, J. W. J. de Folter, A. V. Petukhov, and A. P. Philipse, *Reconfigurable assembly of superparamagnetic colloids confined in thermo-reversible microtubes*. Soft Matter, 11(6201), 2015.

[225] F. Liu, B. Chen, U. Baumeister, X. Zeng, G. Ungar, and C. Tschierske, *The triangular cylinder phase: A new mode of self-assembly in liquid-crystalline soft matter*. Journal of the American Chemical Society, 129(31):9578–9579, 2007.

[226] Q. Chen, S. C. Bae, and S. Granick, *Directed self-assembly of a colloidal kagome lattice*. Nature, 469(7330):381–384, 2011.

[227] C. S. Dias, N. A. M. Araújo, and M. M. T. Gama, *Effect of the number of patches on the growth of networks of patchy colloids on substrates*. Molecular Physics, 113(9-10):1069–1075, 2015.

[228] S. Keller and H. McConnell, *Stripe phases in lipid monolayers near a miscibility critical point*. Physical Review Letters, 82(7):1602–1605, 1999.

[229] J. Maclennan and M. Seul, *Novel stripe textures in nonchiral hexatic liquid-crystal films*. Physical Review Letters, 69(14):2082–2085, 1992.

[230] C. L. Phillips and G. A. Voth, *Discovering crystals using shape matching and machine learning*. Soft Matter, 9(35):8552, 2013.

[231] M. J. Liu, W. H. Li, F. Qiu, and A.-C. Shi, *Stability of the frank-kasper [sigma]-phase in babc linear tetrablock terpolymers*. Soft Matter, 12:6412–6421, 2016.

[232] K. Ueda, T. Dotera, and T. Gemma, *Photonic band structure calculations of two-dimensional Archimedean tiling patterns*. Physical Review B, 75(19):195122, 2007.

[233] Y. Norizoe and T. Kawakatsu, *Monte Carlo simulation of string-like colloidal assembly*. Europhysics Letters, 72(4):583–589, 2005.

[234] Y. Norizoe and T. Kawakatsu, *Particle Monte Carlo simulation of string-like colloidal assembly in two and three dimensions.* The Journal of Chemical Physics, 137(2):024904, 2012.

[235] K. Barkan, M. Engel, and R. Lifshitz, *Controlled self-assembly of periodic and aperiodic cluster crystals*. Physical Review Letters, 113(9):1–5, 2014.

[236] C. Räth, W. Bunk, M. B. Huber, G. E. Morfill, J. Retzlaff, and P. Schuecker, *Analysing large-scale structure - I. Weighted scaling indices and constrained randomization*. Monthly Notices of the Royal Astronomical Society, 337(2):413–421, 2002.

[237] A. V. Ivlev, G. E. Morfill, H. M. Thomas, C. Räth, G. Joyce, P. Huber, R. Kompaneets, V. E. Fortov, A. M. Lipaev, V. I. Molotkov, T. Reiter, M. Turin, and P. Vinogradov, *First observation of electrorheological plasmas*. Physical Review Letters, 100(095003):1–4, 2008.

[238] J. A. Millan and S. C. Glotzer, *Effect of shape on the self-assembly of faceted patchy nanoplates with irregular shape into tiling patterns*. Soft Matter, 11:1386, 2015.

[239] S. B. Rochal, O. V. Konevtsova, I. A. Shevchenko, and V. Lorman, *Soft spherical nanostructures with dodecagonal quasicrystal-like order*. Soft Matter, 12:1238–1247, 2015.

[240] M. Engel, *Entropic stabilization of tunable planar modulated superstructures*. Physical Review Letters, 106(095504):3–6, 2011.

[241] J. Toner and D. R. Nelson, *Smectic, cholesteric, and rayleigh-benard order in two dimensions*. Physical Review B, 23(1):316, 1981.

[242] D. R. Nelson and J. Toner, *Bond-orientational order, dislocation loops, and melting of solids and smectic-a liquid crystals*. Physical Review B, 24(1):363, 1981.

[243] Y. He, Y. Chen, H. Liu, A. E. Ribbe, and C. Mao, *Self-assembly of hexagonal DNA two-dimensional (2D) arrays*. Journal of the American Chemical Society, 127(35):12202–12203, 2005.

[244] Y. He and C. Mao, *Balancing flexibility and stress in DNA nanostructures*. Chemical Communications, pages 968–969, 2006.

[245] M. C. Rechtsman, H. C. Jeong, P. M. Chaikin, S. Torquato, and P. J. Steinhardt, *Optimized structures for photonic quasicrystals*. Physical Review Letters, 101(7):073902, 2008.

[246] A. Micco, V. Galdi, F. Capolino, A. Della Villa, V. Pierro, S. Enoch, and G. Tayeb, *Directive emission from defect-free dodecagonal photonic quasicrystals: A leaky wave characterization*. Physical Review B, 79(7):075110, 2009.

[247] A. Ricciardi, M. Pisco, A. Cutolo, A. Cusano, L. O'Faolain, T. F. Krauss, G. Castaldi, V. Galdi, L. O'Faolain, T. F. Krauss, G. Castaldi, and V. Galdi, *Evidence of guided resonances in photonic quasicrystal slabs*. Physical Review B, 84(8):085135, 2011.

[248] J. Korringa, *On the calculation of the energy of a Bloch wave in a metal*. Physica, 13(6-7):392–400, 1947.

[249] K. Wang, S. David, A. Chelnokov, and J. M. Lourtioz, *Photonic band gaps in quasicrystal-related approximant structures*. Journal of Modern Optics, 50(13):2095–2105, 2003.

[250] P. N. Dyachenko, Y. V. Miklyaev, and V. E. Dmitrienko, *Three-dimensional photonic quasicrystal with a complete band gap*. JETP Letters, 86(4):240–243, 2007.

[251] S.-C. Cheng, X. Zhu, and S. Yang, *Complex 2D photonic crystals with analogue local symmetry as 12-fold quasicrystals*. Optics Express, 17(19):16710–16715, 2009.

[252] R. Gajić, D. Jovanović, K. Hingerl, R. Meisels, and F. Kuchar, *2D photonic crystals on the Archimedean lattices (tribute to Johannes Kepler (1571-1630))*. Optical Materials, 30(7):1065–1069, 2008.

[253] A. C. Stelson, W. A. Britton, and C. M. L. Watson, *Photonic crystal properties of self-assembled archimedean tilings*. Journal of Applied Physics, 121(2):023101, 2017.

[254] A. Rostami and S. Matloub, *Band structure and dispersion properties of photonic quasicrystals*. Progress In Electromagnetics Research, 9:65–78, 2009.

[255] M. Florescu, S. Torquato, and P. J. Steinhardt, *Designer disordered materials with large, complete photonic band gaps*. Proceedings of the National Academy of Sciences, 106(49):20658–20663, 2009.

[256] W. Man, M. Florescu, E. P. Williamson, Y. He, S. R. Hashemizad, B. Y. C. Leung, D. R. Liner, S. Torquato, P. M. Chaikin, and P. J. Steinhardt, *Isotropic band gaps and freeform waveguides observed in hyperuniform disordered photonic solids*. Proceedings of the National Academy of Sciences, 110(40):15886–15891, 2013.

[257] J. Yi, H. S. Jang, J. S. Lee, and W. I. Park, *Bioinspired morphogenesis of highly intricate and symmetric silica nanostructures*. Nano Letters, 12(7):3743–3748, 2012.

[258] R. Fenollosa and F. Meseguer, *Non-close-packed artificial opals*. Advanced Materials, 15(15):1282–1285, 2003.

[259] Z.-Y. Li and Z.-Q. Zhang, *Fragility of photonic band gaps in inverse-opal photonic crystals*. Physical Review B, 62(3):1516–1519, 2000.

[260] F. García-Santamaría, H. T. Miyazaki, A. Urquía, M. Ibisate, M. Belmonte, N. Shinya, F. Meseguer, and C. López, *Nanorobotic manipulation of microspheres for on-chip diamond architectures*. Advanced Materials, 14(16):1144–1147, 2002.

[261] Z. Zhang, A. S. Keys, T. Chen, and S. C. Glotzer, *Self assmebly of patchy particles in to diamond structures through Molecular Mimicry*. Langmuir, 21(25):409–413, 2005.

[262] E. G. Noya, C. Vega, J. P. K. Doye, and A. A. Louis, *The stability of a crystal with diamond structure for patchy particles with tetrahedral symmetry*. The Journal of Chemical Physics, 132(23), 2010.

[263] F. Romano, E. Sanz, and F. Sciortino, *Phase diagram of a tetrahedral patchy particle model for different interaction ranges*. The Journal of Chemical Physics, 132(18), 2010.

[264] X. Mao, *Entropic effects in the self-assembly of open lattices from patchy particles*. Physical Review E, 87(6):1–15, 2013.

[265] X. Mao, Q. Chen, and S. Granick, *Entropy favours open colloidal lattices*. Nature Materials, 12(3):217–222, 2013.

[266] D. Z. Rocklin and X. Mao, *Self-assembly of three-dimensional open structures using patchy colloidal particles*. Soft Matter, 10(38):7569–76, 2014.

[267] A. V. Tkachenko, *Morphological diversity of DNA-colloidal self-assembly*. Physical Review Letters, 89(14):148303, 2002.

[268] É. Marcotte, F. H. Stillinger, and S. Torquato, *Designed diamond ground state via optimized isotropic monotonic pair potentials*. The Journal of Chemical Physics, 138:061101, 2013.

[269] M. Watzlawek, C. N. Likos, and H. Löwen, *Phase diagram of star polymer solutions*. Physical Review Letters, 82(26):5289–5292, 1999.

[270] L. Skarpalezos, N. Tsakiris, P. Argyrakis, and V. S. Vikhrenko, *Memory effects in strongly interacting lattice gases: Self-intermediate scattering function studies*. Physical Review B, 84(7):1–9, 2011.

[271] L. Skarpalezos, P. Argyrakis, and V. S. Vikhrenko, *Self-intermediate scattering function of strongly interacting three-dimensional lattice gases: Time- and wave-vector-dependent tracer diffusion coefficient*. Physical Review E, 89(5):1–7, 2014.

[272] L. Berthier and W. Kob, *The Monte Carlo dynamics of a binary Lennard-Jones glass-forming mixture*. Journal of Physics Condensed Matter, 19(20):205130, 2007.

[273] E. Sanz and D. Marenduzzo, *Dynamic Monte Carlo versus Brownian dynamics: A comparison for self-diffusion and crystallization in colloidal fluids*. The Journal of Chemical Physics, 132(19), 2010.

[274] A. J. Garcia-Adeva, *Band structure of photonic crystals with the symmetry of a pyrochlore lattice*. Physical Review B, 73(7):2–5, 2006.

[275] M. Marechal and M. Dijkstra, *Phase behavior and structure of colloidal bowl-shaped particles: Simulations*. Physical Review E, 82(3):1–11, 2010.

[276] M. Marechal, R. J. Kortschot, A. F. Demiròrs, A. Imhof, and M. Dijkstra, *Phase behavior and structure of a new colloidal model system of bowl-shaped particles*. Nano Letters, 10(5):1907–1911, 2010.

[277] M. Marechal, A. Cuetos, B. Martínez-Haya, and M. Dijkstra, *Phase behavior of hard colloidal platelets using free energy calculations*. The Journal of Chemical Physics, 134:094501, 2011.

[278] X. Zeng, F. Liu, A. G. Fowler, G. Ungar, L. Cseh, G. H. Mehl, and J. E. Macdonald, *3D ordered gold strings by coating nanoparticles with mesogens*. Advanced Materials, 21(17):1746–1750, 2009.

[279] M. M. Wojcik, M. Gora, J. Mieczkowski, J. Romiszewski, E. Gorecka, and D. Pociecha, *Temperature-controlled liquid crystalline polymorphism of gold nanoparticles*. Soft Matter, 7(22):10561, 2011.

[280] B. A. Lindquist, S. Dutta, R. B. Jadrich, D. J. Milliron, and T. M. Truskett, *Interactions and design rules for assembly of porous colloidal mesophases*. Soft Matter, 13(7):1335–1343, 2017.

[281] M. A. Miller, R. Blaak, C. N. Lumb, and J. P. Hansen, *Dynamical arrest in low density dipolar colloidal gels*. The Journal of Chemical Physics, 130:114507, 2009.

[282] M. Bier, R. Van Roij, M. Dijkstra, and P. Van Der Schoot, *Self-diffusion of particles in complex fluids: Temporary cages and permanent barriers*. Physical Review Letters, 101(21):215901, 2008.

[283] A. Patti, D. El Masri, R. Van Roij, and M. Dijkstra, *Stringlike clusters and cooperative interlayer permeation in smectic liquid crystals formed by colloidal rods*. Physical Review Letters, 103(24):248304, 2009.

[284] R. Matena, M. Dijkstra, and A. Patti, *Non-Gaussian dynamics in smectic liquid crystals of parallel hard rods*. Physical Review E, 81(2):021704, 2010.

[285] S. Belli, A. Patti, R. Van Roij, and M. Dijkstra, *Heterogeneous dynamics in columnar liquid crystals of parallel hard rods*. The Journal of Chemical Physics, 133(15):154514, 2010.

[286] A. Patti, D. El Masri, R. Van Roij, and M. Dijkstra, *Collective diffusion of colloidal hard rods in smectic liquid crystals: Effect of particle anisotropy*. The Journal of Chemical Physics, 132(22):224907, 2010.

[287] A. Patti, S. Belli, R. van Roij, and M. Dijkstra, *Relaxation dynamics in the columnar liquid crystal phase of hard platelets*. Soft Matter, 7(7):3533, 2011.

[288] E. Yablonovitch and T. J. Gmitter, *Photonic band structure: The face-centered-cubic case*. Physical Review Letters, 63(18):1950–1953, 1989.

[289] Z.-Y. Li and Z.-Q. Zhang, *Photonic bandgaps in disordered inverse-opal photonic crystals*. Advanced Materials, 13(6):433–436, 2001.

[290] M. Doosje, B. J. Hoenders, and J. Knoester, *Photonic bandgap optimization in inverted fcc photonic crystals*. Journal of the Optical Society of America B, 17(4):600, 2000.

[291] C. M. Anderson and K. P. Giapis, *Larger two-dimensional photonic band gaps*. Physical Review Letters, 77(14):2949, 1996.

[292] J. Broeng, S. E. Barkou, A. Bjarklev, J. C. Knight, T. A. Birks, P. St, and J. Russell, *Highly increased photonic band gaps in silicarair structures*. Optics Communications, 156:240–244, 1998.

[293] A. R. Denton and N. W. Ashcroft, *Weighted-density functional theory of non-uniform fluid mixtures: Application to freezing of binary hard-sphere mixtures*. Physical Review A, 42(12):7312–7329, 1990.

[294] X. Cottin and P. A. Monson, *Substitutionally ordered solid solutions of hard spheres*. The Journal of Chemical Physics, 102(8):3354, 1995.

[295] B. E. Trizac, M. D. E. Madden, and P. A., *Stability of the AB crystal for asymmetric binary hard sphere mixtures*. Molecular Physics, 90(4):675–678, 1997.

[296] L. Filion, M. Hermes, R. Ni, E. C. M. Vermolen, A. Kuijk, C. G. Christova, J. C. P. Stiefelhagen, T. Vissers, A. Van Blaaderen, and M. Dijkstra, *Self-assembly of a colloidal interstitial solid with tunable sublattice doping*. Physical Review Letters, 107(16):168302, 2011.

[297] P. Bartlett, R. H. Ottewill, and P. N. Pusey, *Superlattice formation in binary mixtures of hard-sphere colloids*. Physical Review B, 62(1):900–913, 1992.

[298] O. L. Pursiainen, J. J. Baumberg, H. Winkler, B. Viel, P. Spahn, and T. Ruhl, *Nanoparticle-tuned structural color from polymer opals*. Optics Express, 15(15):9553–9561, 2007.

[299] P. R. Villeneuve, S. Fan, and J. D. Joannopoulos, *Microcavities in photonic crystals: Mode symmetry, tunability, and coupling efficiency*. Physical Review B, 54(11):7837–7842, 1996.

Summary

Have you ever wondered how various natural entities like the feathers of birds, scales of butterflies, petals of flowers, or various gemstones have bright colours? This is a result of manipulation of light by the photonic crystals present in them. So, what exactly are photonic crystals? In general, photonic crystals are defined as structures with alternate regions of high and low dielectric constant materials. They affect the propagation of light in way such that light of certain wavelengths cannot pass through them. In other words, they possess a photonic band gap. Consequently, they allow unprecedented control over the behaviour of light. One way of utilising this property is by trying to replace various components used in the telecommunication sector by photonic crystals to obtain high-speed transmissions. Accordingly, one-dimensional photonic crystals, such as a Bragg grating, have been used for coating lenses or in colour-changing paint. Two-dimensional photonic crystals are the basis for a new class of optical fibre called photonic-crystal fibre. However, the ultimate application is to use three-dimensional photonic crystals as components in optical computers. These optical computers will, then, not be limited by the relatively slow speed of electrons and will be much faster than the present computers. A necessary condition for such applications is that the periodicity of the photonic crystal should be around half the wavelength of the electromagnetic waves that needs to be diffracted. For a photonic crystal to operate in the wavelength between 400 *nm* (blue) and 700 *nm* (red), i.e. in the visible spectrum of light, its lattice periodicity should be between 200 *nm* and 350 *nm*. This brings us to the realm of colloids.

Colloidal dispersions are composed of colloidal particles dispersed in a continuous medium. These colloidal particles, or simply colloids, have at least one dimension in the size range of a few nanometers to micrometers and the particles of the surrounding medium are much smaller. As we can see, the size range of these colloids perfectly fits the above requirement. So, how does one fabricate a photonic crystal from a colloidal dispersion? It is done by simply letting nature take its own course. Colloids experience a kind of random motion, termed as Brownian motion, because of their collisions with the surrounding smaller particles of the medium. This motion allows the colloids to move around the medium and explore various configurations and eventually, settle in a thermodynamically favourable structure. This process is termed as self-assembly. Accordingly, colloids can self-assemble into gas, liquid, and crystal phases. Their phase behaviour, i.e. the stability of the various phases and the transition between different phases, is governed by the properties of the colloids such as its shape and interaction as well as those of the system such as temperature and pressure. If a crystal with a favourable symmetry is self-assembled using colloids with a favourable dielectric constant, we can obtain a photonic crystal operating in the visible region of light. We explore this possibility in this thesis for two- and three-dimensional systems. Specifically, we focus on two-dimensional quasi-periodic crystals and three-dimensional periodic crystals.

Why are we focusing specifically on these two categories? Two-dimensional periodic photonic crystals of hexagonal or square symmetry have been fabricated for a while now. The more exciting research focusses on two-dimensional quasi-periodic crystals exhibiting a photonic band gap. Quasi-periodic crystal, or quasicrystals, are materials that exhibit long range order, but no translational periodicity. What exactly is meant by the lack of periodicity? This means

that the position of each particle in a quasicrystal is known, just as in a periodic crystal; but in contrast to a periodic crystal, if one tries to move a particle in a quasi-crystal and place it on top of its neighbour, it will not re-create the same lattice. This can be further explained using the following example. The simplest example of a one-dimensional quasicrystal is the Fibonacci sequence, where each number is the sum of its preceding two numbers and is written as 1, 1, 2, 3, 5, 8, 13, 21, 34, 55, 89, ... Here, the value of each term is well-defined. However, if the series is started with the number 2 instead of 1, it will give a different series where, again, the terms are well-defined. This refers to the lack of periodicity. The recent discovery of quasicrystals in general and quasi-periodic photonic crystals in particular has opened new avenues of research with regard to answering questions such as how do they form? Are they stable? Do they possess a photonic band gap? etc. We attempt to answers some of these questions in this thesis. Also, as these quasicrystals exhibit complex phase behaviour already in a two-dimensional system, we restrict ourselves to this, i.e. we do not study three-dimensional quasicrystals in this thesis. But then, the lookout for an experimentally realisable three-dimensional periodic photonic crystal is still open and we do address that in this thesis.

In **Chapter 2**, we introduce the simulation model that is predominantly used in this thesis. This model emulates particles with a core-corona architecture, i.e. a hard impenetrable core of diameter σ surrounded by a soft penetrable corona of diameter δ. This corona can be modelled using potentials with a nature that is either purely attractive, purely repulsive, or a combination of the two. In this thesis, we use an interaction potential consisting of a purely repulsive square shoulder to represent the corona. This introduces two length scales in the system, one at the diameter of the core and the other at the corona. We study the phase behaviour of this core-corona system simulated as two-dimensional disks and three-dimensional spheres at various shoulder widths using Monte Carlo simulations. The rest of this thesis is divided into three parts.

In Part I of this thesis, we study various aspects of the phase behaviour of a two-dimensional dodecagonal quasicrystal formed in this core-corona system. Dodecagonal or 12-fold symmetry is the most common symmetry associated with quasicrystals in soft matter systems. To evaluate its phase behaviour, we simulate a system of colloidal hard disks with a diameter σ surrounded by a soft corona of diameter 1.40σ. We exclusively focus on the thermodynamic stability of the dodecagonal quasicrystal in **Chapter 3**. Here, we try to address the question of if this quasicrystal is energetically or entropically stabilised at finite temperatures. This is in fact a pre-question to the question if this quasicrystal is stable at zero temperature. This is because, if the quasicrystal is energetically stabilized at finite temperatures, then it will be the minimum energy configuration at zero temperature and thus, the thermodynamically stable phase. On the other hand, if the configurational entropy of this quasicrystal outweighs its energetic contribution at finite temperatures, then it is said to be entropically stabilized at these temperatures. In this case, this quasicrystal may not be thermodynamically stable at zero temperature where its entropic contribution is nullified. In order to answer this question, we study the relative stability of the dodecagonal quasicrystal and four of its approximants. An approximant is a periodic counterpart which is described by a large unit cell with a structure that resembles a quasicrystal. We compare their stability by calculating their free energies. Here, we used a simplified method to calculate the free energy of the quasicrystal wherein we explicitly account for its configurational entropy using an analytical expression from literature. The configurational entropy accounts for the distinct number of configurations that the quasicrystal can adapt. From these calculations, we find that the dodecagonal quasicrystal is stabilized by its vibrational entropy with respect to the considered approximants at finite temperatures. In other words, this quasicrystal is stable even without its configurational entropy. Further, we find that the potential energies of this quasicrystal and two of its periodic approximants are equal within our statistical accuracy. This lets us to extrapolate its stability region to zero temperature. Additionally, we also map out the equilibrium phase diagram for this system where, in addition to the quasicrystal, we find the presence of stable periodic crystal phases with square and hexagonal symmetries. We also find a re-entrant behaviour of the fluid phase resulting from the two-length scales in the potential.

After realising that the dodecagonal quasicrystal formed in this system is thermodynamically stable, we proceed to critically evaluate its formation in **Chapter 4**. We first examine the formation process in the hard-core square-shoulder system using bond orientational order parameters, correlation functions and tiling distributions. This acts as a summary of various methods that can be utilised to identify the quasicrystal. We then assess the robustness of this formation. We find that the formation of the dodecagonal quasicrystal is robust across changes in temperature, density, range and shape of the interaction potential. For the range of densities and temperatures considered, we observe the formation of the dodecagonal quasicrystal at shoulder widths $1.30\sigma \leq \delta \leq 1.44\sigma$. We then simulate the system using three other interaction potentials with two length scales, namely hard-core plus a linear ramp, modified exponential, and Buckingham (exp-6) potential and observe the presence of the dodecagonal quasicrystal in all three systems. We find that the shape of the interaction potential affects the temperatures at which the quasicrystal is formed.

We then set to explore the formation of this dodecagonal quasicrystal by sedimentation in **Chapter 5**. Sedimentation refers to the inhomogeneous distribution of colloidal particles along the height of a suspension due to the influence of gravity. This allows for the particles at the bottom of the sediment to crystallise when they attain a certain critical density. In other words, sedimentation is one of the most common manifestations of self-assembly of colloidal particles. Our present study, thus, aims to pave the way for the experimental realisation of the colloidal dodecagonal quasicrystal. We evaluate the sedimentation behaviour using Event-Driven Brownian Dynamics simulations. We choose the simulation parameters such that the pressure at the bottom of the sediment corresponds to the stable region of the concerned phases in the phase diagram presented in Chapter 3. We indeed do observe the formation of layers with dodecagonal, square and hexagonal symmetries at the relevant pressures. This two-dimensional layered structure is formed because of energetic constraints. In addition, we also observe a re-entrant behaviour exhibited by the fluid phase, engulfing a hexagonal phase, in the sedimentation column. In other words, a floating crystal with hexagonal symmetry is formed between the fluid regions.

We now proceed to an exploration of formation of phases in the two-dimensional core-corona system at other shoulder widths. We consider systems at shoulder widths $\delta = 1.27\sigma$ and 1.60σ in **Chapter 6** and $\delta = 1.95\sigma$ in **Chapter 7**. We study the phase behaviour and map out the phase diagram at these shoulder widths. The general phase behaviour of the square-shoulder system at $\delta = 1.27\sigma$ and 1.60σ is similar to that at $\delta = 1.40\sigma$, while that at $\delta = 1.95\sigma$ is complicated by the longer interaction range. In the latter case, the square shoulder of a particle almost engulfs its nearest neighbours. We find the formation of a stable octadecagonal (18-fold symmetry) quasicrystal at $\delta = 1.27\sigma$ and a stable decagonal (10-fold symmetry) quasicrystal at $\delta = 1.60\sigma$. Of particular interest is the fact that in a system of particles interacting with a

Lennard-Jones-Gauss potential, this decagonal quasicrystal was reported to be stable at high temperatures which then paves way to an approximant at lower temperatures. We, however, find that for our core-corona system this quasicrystal is stable through the entire range of temperatures considered. This emphasises the necessity of evaluating the stability of quasicrystal in each system separately.

In case of the system at $\delta = 1.95\sigma$, we observe the formation of a plethora of interesting phases including a striped mesophase, a honeycomb lattice, a two-dimensional equivalent of a sigma phase and three distinct hexagonal phases. We notice that the the stripe and the honeycomb phases are formed as a result of energy minimisations, i.e. minimising the number of neighbours of each particle. Each particle in the stripe phase has two neighbours while those in the honeycomb has three. We devote a large portion of this chapter to decipher the formation of the stripe phase. We find that this stripe phase displaying a quasi-long range bond orientational order and a short-range positional order forms from an isotropic FL phase with no bond orientational or positional order upon decreasing the temperature or increasing the density. We initially investigate this transition using several order parameters. Finally, by way of a continuous change in the defect concentration as well as the loss of bond orientational order during these transitions, we conclude this transformation to be a Kosterlitz-Thouless (K-T) transition. Yet another interesting feature of this system is the energetic stabilisation of the sigma phase, which is an approximant to the dodecagonal quasicrystal. This is in stark contrast to Chapter 3, where we found the quasicrystal to be entropically stabilised over the sigma phase and other approximants. This is essentially due to the larger shoulder width in the present case. Here, the position of particles even beyond the second nearest neighbours play an important role in the potential energy of the concerned structure. This further reinforces the fact that the question regarding the stability of a quasicrystal is not unique and needs to be addressed for each system separately.

After establishing the phase behaviour of quasicrystals and other periodic phases, we proceed to study their photonic properties in Part III. In **Chapter 8**, we investigate and compare the photonic properties of the dodecagonal quasicrystal and its approximants considered in Chapter 3. For each of these structures, we consider three configurations consisting of a material with a high-dielectric constant arranged in the form of rods, walls, or connected networks of walls and rods, in a medium with a low-dielectric constant. Given the two-dimensional (planar) nature of these structures, we evaluate photonic properties separately for the case in which either the magnetic field or the electric field is in the structure plane. The earlier is termed as transverse-magnetic (TM) polarisation and the latter as transverse-electric (TE) polarisation. Our results show that all structures possess transverse magnetic (TM) band gaps in the rod configurations and transverse electric (TE) band gaps in the wall configurations. Given the computational restrictions, we have calculated the photonic band structures of only the approximants in the connected network structures. We find that all approximants possess a complete (TM+TE) band gap in their network configurations. In all these three configurations, we find that the local symmetry of the structures has a greater influence on the formation of band gaps in the TE than in the TM polarisation.

We eventually proceed to investigating a three-dimensional system of spheres with a core-corona architecture in **Chapter 9**, where we specifically explore the possibility of formation of photonic crystals. We evaluate the system with a shoulder width $\delta = 2.10\sigma$. In general, either of the following two approaches are followed to self-assemble a three-dimensional photonic crystal from colloidal particles. On the one hand, hard sphere mixtures can be theoretically used to form a binary crystal phase which yields a diamond or pyrochlore lattice by selective dissolution of either component; but such crystals with a photonic band gap in the visible region of light are yet to be experimentally fabricated. On the other hand, one could try to reverse engineer the interparticle potential required to assemble the targeted crystal structures; but this results in quite complex interaction potentials, such as the exemplar 'mermaid' potential, which are difficult to realise experimentally. Quite contrary to these two approaches, we report here that a pyrochlore lattice with a photonic band gap is formed in an experimentally realisable system consisting of particles interacting with a simple isotropic pair-potential. The structure of the pyrochlore formed in our simulations has two inherent length scales and displays complete photonic band gaps in both the direct and inverse dielectric crystal structures. Additionally, we also find the formation of a low-density hexagonal columnar phase in this system. This phase consists of strings, separated by a distance larger than shoulder width, which are arranged on a hexagonal lattice. Such a self-assembly of inexpensive porous nanomaterials can be an alternative to molecular caged structures such as zeolites and can be used in applications involving filtration, size-selection, or catalysis.

Continuing with three-dimensional photonic crystals, we investigate the effect of disorders on the photonic properties of an inverse binary NaCl structure in **Chapter 10**. The binary NaCl structure consists of spheres of two different sizes, where each species is ordered on a FCC lattice. This inter-penetration of two FCC lattices results in a scenario where the small spheres are positioned in the octahedral voids of the FCC lattice of the large spheres. We systematically analyse the effect of structural disorder of the small spheres on the photonic properties of a binary NaCl lattice with a size ratio of 0.30 between the small and large spheres. The types of disorders studied include the position of the small spheres in the octahedral void of the large spheres, polydispersity in size of the small spheres, and the fraction of small spheres in the crystal. We find that none of the above disorders completely destroy the photonic band gap of the NaCl lattice. The last mentioned disorder is especially interesting because the tuning of the fraction of octahedral holes filled with small spheres from zero to one corresponds respectively to the one-component FCC of only large spheres and the binary NaCl crystal structure. And structures with ratios in between these two are termed as interstitial solid solution (ISS). ISSs with varying compositions are formed along the height of a sedimentation column as the fraction of small spheres decreases along the height in binary mixtures of hard-sphere like particles. Incidentally, ISSs have a huge effect on the photonic properties of the parent material. We find that ISSs of all compositions possess a photonic band gap. Alternatively, it is worth pointing out that we find that the presence of up to 10 % vacancies in small spheres does not greatly influence the band gap of the NaCl lattice.

To summarise, this thesis is a step towards the fabrication of quasi-periodic and periodic photonic crystals by self-assembly of colloidal particles with a simple interaction potential. In the first part of the thesis, we find that the dodecagonal quasicrystal is thermodynamically stable, that its formation is robust to changes in the range and shape of the interaction potential and that it can be formed by sedimentation. In the second part, by studying different quasicrystals, we emphasis on the fact that the stability of a quasicrystal is not a unique question and needs to be addressed for each system separately. In the third part of the thesis, using photonic studies, we infer that the core-corona system is a lucrative system to look for photonic crystals.

Samenvatting

Heb je je ooit afgevraagd hoe de veren van vogels, schubben van vlinders, bloemenblaadjes en edelstenen hun kleuren krijgen? Dit is een gevolg van de manipulatie van licht door de fotonische kristallen die in deze dingen aanwezig zijn. Wat zijn eigenlijk fotonische kristallen? Fotonische kristallen bestaan uit afwisselend stukjes van materialen met een hoge en lage diëlektrische constante. Deze kristallen beïnvloeden de voorplanting van licht zodanig dat licht met specifieke golflengten niet door de kristallen kan. Anders gezegd, ze hebben een fotonisch verboden zone. Dit maakt ongekende controle over het gedrag van licht mogelijk. Deze eigenschap kan in telecommunicatie gebruikt worden waarbij verschillende componenten vervangen kunnen worden door fotonische kristallen voor nog snellere communicatie. Eendimensionale fotonische kristallen worden gebruikt als reflectielaag op lenzen en in kleur veranderendeverf. Tweedimensionale fotonische kristallen worden toegepast in een nieuw soort optische vezels: fotonisch kristallen-vezels. Echter, de meeste interessante toepassing is het gebruik van driedimensionale fotonische kristallen als componenten in optische computers. Deze optische computers zijn dan niet beperkt door de snelheid van elektronen en kunnen daaromveel sneller dan de huidige computers worden. Een noodzakelijk voorwaarde voor deze toepassing is dat de periodiciteit van de fotonische kristallen de helft van de golflengte van de afgebogen elektromagnetische golven moet zijn. Om de fotonische kristallen in het zichtbaar spectrum te laten werken, i.e. golflengte tussen 400 en 700 *nm*, moet de roosterperiodiciteit tussen 200 en 350 *nm* liggen. Dit brengt ons tot het rijk van colloïdale deeltjes.

Colloïdale dispersies bestaan uit colloïdale deeltjes die in een oplosmiddel gesuspendeerd zijn. Deze colloïdale deeltjes hebben tenminste een dimensie binnen het groottebereik van een paar nanometer tot micrometer. De grootte van de colloïdale deeltjes voldoet aan de hierboven gestelde voorwaarde. Hoe wordt nu een fotonische kristal vanuit een colloïdale dispersie fabricerenaangemaakt? Dit kan gedaan worden door de natuur haar gang te laten gaan. Colloïdale deeltjes ondervinden Brownse beweging door de botsing met de kleinere deeltjes van het oplosmiddel. Door deze beweging kunnen de colloïdale deeltjes zich bewegen in het oplosmiddel en verschillende configuraties ontdekken. Uiteindelijk kunnen ze zich verzamelen in een thermodynamisch gunstige structuur. Dit proces heet zelforganisatie en colloïdale deeltjes kunnen zich tot een gas, een vloeibare of een kristalfase organiseren. Het fasegedrag van colloïdale deeltjes zoals de stabiliteit van de verschillende fasen en de overgang tussen de fasen wordt bepaald door de eigenschappen van de colloïdale deeltjes, zoals hun vorm en interactie, en die van het systeem, zoals temperatuur en druk. Als wij een kristal met een gunstige symmetrie kunnen opbouwen door zelforganisatie van colloïdale deeltjes met een gunstige diëlektrische constante kunnen wij een fotonische kristal verkrijgen die in het zichtbaar spectrum kunnen werken. In dit proefschrift onderzoeken wij deze mogelijkheid voor twee- en driedimensionale systemen. Specifiek concentreren wij ons op tweedimensionale quasi-periodische kristallen en driedimensionale periodische kristallen.

Waarom onderzoeken wij alleen deze twee categorieën? Tweedimensionale periodische fotonische kristallen met een zeshoek- of vierkantsymmetrie kunnen al een tijdje gemaakt worden. Tweedimensionale quasi-periodische kristallen met een fotonische bandgaping zijn recent ontwikkeld. Quasi-periodische kristallen, of quasikristallen, zijn materialen die over lange afstand orde hebben, maar geen translatie periodiciteit. Net als in een periodisch kristal is de positie van elke deeltje in een quasikristal bekend. Maar in tegenstelling tot het periodische kristal, kan men, als men een deeltje in een quasikristal naar zijn buur verplaatst, niet dezelfde structuur terugkrijgen. Dit kunnen wij aan de hand van een voorbeeld beter begrijpen. Het meest simpele quasikristal is de Fibonacci reeks. Hier is elke term een som van de voorafgaande twee termen. Dit is als 1, 1, 2, 3, 5, 8, 13, 21, 34, 55, 89, ... geschreven. Zoals wij kunnen zien, is elke term in deze reeks bekend. Maar als de reeks met nummer 2 in plaats van 1 begint dan heeft de reeks een andere volgorde. Elke term in deze nieuwe reeks is ook bekend maar is niet hetzelfde als in de oude reeks. Dit verwijst naar het gebrek aan periodiciteit. Door de recente ontdekking van quasikristallen in het algemeen en quasi-periodische fotonische kristallen in het bijzonder is nieuw onderzoek mogelijk. De volgende vragen zijn nu ontstaan. Hoe vormen deze kristallen? Zijn ze stabiel? Hebben ze een fotonische verboden zone? Wij pogen sommige van deze vragen in dit proefschrift te beantwoorden. Omdat deze quasikristallen al een complex fasegedrag vertonen in een tweedimensionaal systeem, beperken wij ons hiertoe en bestuderen wij geen driedimensionale quasikristallen in dit proefschrift. Maar aangezien de mogelijkheid op een experimenteel realiseerbaar driedimensionaal periodiek fotonische kristal in het vooruitzicht ligt, bespreken wij deze in dit proefschrift.

In **Hoofdstuk 2** stellen wij het simulatie model voor dat hoofdzakelijk in dit proefschrift is gebruikt. Dit model bootst deeltjes met een core-corona architectuur na. Dit betekent een harde ondoordringbare core (of kern) met diameter σ die omringd is door een zachte doordringbare corona met diameter δ. De corona kan met verschillende potentialen gemodelleerd worden. Deze potentiaal kan alleen aantrekkend of alleen afstotend, of een combinatie van beide zijn. De potentiaal die in dit proefschrift is gebruikt is zuiver afstotend met een vorm van een vierkante schouder. Door deze vorm krijgen wij twee lengteschalen binnen het system, een op de diameter van de core en de andere op die van de corona. Wij bestuderen het fasegedrag van dit core-corona systeem van tweedimensionale schijven of driedimensionale bollen met hulp van Monte Carlo simulaties bij verschillende lengten van de schouder. De rest van dit proefschrift is in drie delen verdeeld.

In het eerste deel van dit proefschrift onderzoeken wij het fasegedrag van een tweedimensionaal twaalfhoekig quasikristal dat in dit core-corona systeem is gevormd. Twaalfhoekige symmetrie is de meeste algemene symmetrie van quasikristallen in zachte gecondenseerde materie. Wij simuleren een system van colloïdale harde schijven met een diameter van σ en een corona met een diameter van 1.40σ om het fasegedrag te bestuderen. Wij concentreren ons op de thermodynamische stabiliteit van het quasikristal in **Hoofdstuk 3**. Hier proberen wij de vraag te beantwoorden of dit quasikristal door energie of entropie bij eindige temperaturen wordt gestabiliseerd. Dit is eigenlijk een vraag voorafgaand aan de vraag of dit quasikristal stabiel is bij het absolute nulpunt van de temperatuur. Dit is omdat als het quasikristal op hogere temperaturen door energie gestabiliseerd is, dan is het ook de meest stabiele fase bij het absolute nulpunt. Maar als het quasikristal door zijn configurationele entropie is gestabiliseerd, dan het is mogelijk dat dit niet de meest stabiele fase bij het absolute nulpunt is. Dit komt dan doordat bij het absolute nulpunt zijn entropie te verwaarlozen is. Om deze vraag te beantwoorden onderzoeken wij de relatieve stabiliteit van het quasikristal en vier van zijn approximanten. Een approximant is een periodische vorm van een quasikristal met een grote eenheidscel. Wij vergelijken de stabiliteit van het quasikristal en zijn approximanten door de berekening van hun vrije-energieën. Wij gebruiken een vereenvoudigde methode om de vrijeenergie van het quasikristal te berekenen. In deze methode rekenen wij de configurationele entropie van het quasikristal uit door een analytische uitdrukking uit de literatuur. De configurationele entropie staat voor de verschillende configuraties die mogelijk zijn. Uit deze berekeningen volgt dat het quasikristal door zijn vibratie-entropie wordt gestabiliseerd. Met andere woorden, het quasikristal is stabiel zelfs zonder de toevoeging van de configurationele entropie. Wij vinden ook dat de potentiele energie van het quasikristal en twee van zijn approximanten gelijk is, binnen onze statistische zekerheid. Hierdoor kunnen wij het stabiliteitsgebied van het quasikristal extrapoleren tot het absolute nulpunt. Wij hebben ook het fasediagram van dit systeem in kaart gebracht, waarbij wij ook kristalfasen vinden met een zeshoek- en een vierkantsymmetrie.

Nadat wij weten dat het quasikristal thermodynamisch stabiel is, proberen wij zijn zelforganisatie proces goed te analyseren in **Hoofdstuk 4**. Wij onderzoeken dit proces met behulp van verbindingsoriëntatie ordeparameters, correlatiefuncties en tegelverdelingen. Dit is ook gelijk een samenvatting van de verschillende methoden die gebruikt kunnen worden om een quasikristal te identificeren. Wij beoordelen vervolgens de robuustheid van de formatie. Wij vinden dat het proces robuust is voor veranderingen in tempratuur, dichtheid, schouderlengte en vorm van de interactiepotentiaal. Wij vinden dat het quasikristal wordt gevormd op systemen met schouderlengten $1.30\sigma \leq \delta \leq 1.44\sigma$ binnen het bereik van de dichtheden en temperaturen die wij hebben onderzocht. Daarna simuleren wij het system met drie andere potentialen met twee lengteschalen zoals hard-core met een lineaire helling, gemodificeerde exponentieel en Buckingham (exp-6) potentiaal. Wij vinden het quasikristal in alle drie systemen. Maar wij vinden dat de vorm van de potentiaal invloed heeft op de vormingstemperatuur.

Vervolgens onderzoeken wij de vorming van dit twaalfhoekige quasikristal door sedimentatie in **Hoofdstuk 5**. Sedimentatie betekent de inhomogene distributie van colloïdale deeltjes langs de hoogte van de suspensie onder invloed van zwaartekracht. Hierdoor kristalliseren de deeltjes in de bodem van het sediment bij een bepaalde kritische dichtheid. Met andere woorden, sedimentatie is een van de meest voorkomende manifestaties van zelforganisatie van colloïdale deeltjes. Onze huidige studie heeft het uiteindelijke doel om de experimentele realisatie van een colloïdal twaalfhoekig quasikristal mogelijk te maken. Wij evalueren het sedimentatiegedrag door middel van Gebeurtenis-Aangedreven Brownse Dynamica simulaties. Wij hebben de simulatieparameters zo gekozen dat de druk op de bodem van het sediment vergelijkbaar is met de stabiele regio van betreffende fases in het fasediagram zoals in Hoofdstuk 3. Wij zien inderdaad de vorming van lagen met twaalfhoekige, vierkant- en zeshoeksymmetrieën bij relevante drukken. Deze tweedimensionele laagstructuur is gevormd door energetische belemmeringen. Bovendien zien wij ook herintredend gedrag van de vloeibare fase, die de zeshoekige fase overneemt in de sedimentatie kolom. Met andere woorden, een drijvend kristal wordt gevormd tussen de twee vloeibare regio's.

In het tweede deel van dit proefschrift gaan we door met het onderzoeken van de vorming van fasen in het tweedimensionale core-corona systeem bij andere schouderlengtes. Wij hebben systemen op schouderlengtes $\delta = 1.27\sigma$ en 1.60σ in **Hoofdstuk 6** en $\delta = 1.95\sigma$ in **Hoofdstuk 7** gesimuleerd. Wij onderzoeken het fasegedrag en genereren het fasediagram bij deze schouderlengtes. Het algemene fasegedrag van de vierkant-schouder systeem bij $\delta = 1.27\sigma$ en 1.60σ is vergelijkbaar met die bij $\delta = 1.40\sigma$, echter die van $\delta = 1.95\sigma$ is gecompliceerder door het grotere interactie bereik. Hier slokt de vierkant-schouder van een deeltje bijna zijn naaste buren op. Wij vinden de vorming van een stabiel achttienhoekig quasikristal op

$\delta = 1.27\sigma$ en een stabiel tienhoekig quasikristal bij $\delta = 1.60\sigma$. Het is vooral interessant dat in een Lennard-Jones-Gauss potentiaal systeem deze tienhoekige quasikristal stabiel bevonden is bij hogere temperaturen, terwijl bij lagere temperaturen een approximant stabiel werd bevonden. Wij vinden, echter, dat voor ons core-corona potentiaal systeem het quasikristal stabiel is over het hele bereik van bestudeerde temperaturen. Dit benadrukt het belang van het evalueren van de stabiliteit van het quasikristal voor elk systeem afzonderlijk.

In het geval van het systeem met $\delta = 1.95\sigma$ vinden wij de vorming van meerdere interessante fasen, waaronder een gestreepte mesofase, een honingraatrooster, een tweedimensionaal equivalent van een sigmafase en drie aparte hexagonale fasen. Wij vinden dat de gestreepte fase en de honingraatfase zijn gevormd door de vermindering van energie, i.e. het minimaliseren van het aantal buren van elk deeltje. Elk deeltje in de gestreepte fase heeft twee buren, terwijl die in de honingraatfase er drie heeft. In dit hoofdstuk is er veel aandacht besteed aan de vorming van de gestreepte fase. Wij vinden dat de gestreepte fase, die een quasi-lange afstand verbindingsoriëntatie orde en een korte afstand positionele orde heeft, wordt gevormd vanuit een isotropische vloeibare fase met geen verbindingsoriëntatie of positionele orde wanneer de temperatuur verlaagd of de dichtheid verhoogd wordt. Wij onderzoeken deze transitie door middel van een aantal order parameters. Tenslotte concluderen wij dat deze transformatie een Kosterlits-Thouless (K-T) transitie is. Een ander interessant kenmerk van dit systeem is de energetische stabilisatie van de sigmafase, die een approximant van het twaalfhoekige quasikristal is. Dit is in tegenstelling tot Hoofdstuk 3, waarin het quasikristal stabieler was dan zijn approximant door zijn entropie. Dit is vanwege de langere schouder lengte in dit specifieke geval. Hier speelt de positie van de deeltjes ook verder dan de tweede buren een belangrijk rol in de potentiële energie van de betreffende structuur. Dit benadrukt verder het feit dat de stabiliteit van het quasikristal niet uniek is en voor elke systeem afzonderlijk bekeken moet worden.

In het derde deel bestuderen wij de fotonische eigenschappen van de deeltjes. In **Hoofdstuk 8** onderzoeken en vergelijken wij de fotonische eigenschappen van het twaalfhoekige quasikristal en zijn approximanten van Hoofdstuk 3. Voor elke structuur beschouwen wij drie configuraties die bestaan uit een materiaal met hoge diëlektrische constante in de vorm van staven, muren, of aaneengesloten netwerken van muren en staven, in een medium met een lage diëlektrische constante. Aangezien het gaat om tweedimensionale (planar) structuren, bestuderen wij de fotonische eigenschappen apart voor het geval waarin het magnetische veld of het elektrische veld in het vlak van de structuur ligt. Het eerste geval noemen wij transversalemagnetische (TM) polarisatie en de tweede transversaleelektrische (TE) polarisatie. Onze resultaten laat zien dat alle structuren TM verboden zones in de staf-configuratie en TE verboden zones in de muur-configuratie hebben. In verband met computationele beperkingen, hebben wij de fotonische bandstructuur van alleen de approximanten in de aaneengeslotennetwerkstructuur berekend. Wij vinden dat alle approximanten een complete (TM+TE) verboden zone in hun netwerkconfiguratie hebben. In al deze drie configuraties vinden wij dat de lokale symmetrie van de structuren een grotere invloed heeft op de vorming van de verboden zones in de TE dan in de TM polarisatie.

In **Hoofdstuk 9** onderzoeken wij het driedimensionale systeem van bollen met een core-corona architectuur, waarin wij specifiek kijken naar de mogelijkheden tot vorming van fotonische kristallen. Wij bestuderen het systeem met een schouderlengte $\delta = 2.10\sigma$. In het algemeen wordt één van de volgende twee methodes gevolgd om de driedimensionale fotonische kristallen vanuit de colloïdale deeltjes aan zelforgnisatie te laten doen. Aan de ene kant blijkt uit theoretisch onderzoek dat hardebollen-mengsels gebruikt kunnen worden om een binaire kristalfase te vormen. Daarna kunnen deze binaire kristallen gebruikt worden om een diamant- of pyrochloorstructuur te krijgen door selectieve oplossing van een van de twee componenten. Maar zulke kristallen met een fotonisch verboden zone in het zichtbare spectrum van licht zijn nog niet gemaakt. Aan de andere kant proberen wij de juiste interactiepotentialen te vinden door middel van 'reverse engineering'. Maar dit resulteert in complexe interactiepotentialen zoals de 'mermaid'-potentiaal, die experimenteel moeilijk zijn te realiseren. In tegenstelling tot de eerdere twee aanpakken hebben wij een pyrochloor rooster met een fotonisch verboden zonegevonden in een system die door experimenten gemaakt kan worden. De structuur van de pyrochloor die in ons systeem wordt gevormd heeft twee lengteschalen en heeft een volledige verboden zone in zowel het directe als hetgeïnverteerde diëlektrische kristal. Daarnaast vinden wij ook een zeshoekige kolomvormige fase met een lage dichtheid in dit system. Deze fase bestaat uit draden van deeltjes, die een tussenafstand groter dan de schouderlengte hebben, die een hexagonaal geordend zijn. Zulke zelforganisatie kan een alternatief worden voor geordende moleculaire structuren zoals zeolieten. Deze kunnen in verschillende toepassingen zoals filtratie, grootteselectie of katalyse gebuikt worden.

In **Hoofdstuk 10** gaan wij verder met driedimensionale fotonische kristallen. Wij onderzoeken het effect van wanorde op de fotonische eigenschappen van een inverse binaire NaCl structuur. De binaire NaCl structuur bestaat uit bollen van twee verschillende maten waarin elke soort in een FCC-structuur zit. Deze vervlechting van de twee FCC structuren resulteert in een scenario waarin de kleinere bollen in de octahedrale gaten van de FCC structuur van de grotere bollen zitten. Wij analyseren het effect van wanorde in de structuur van de kleine bollen op de fotonische eigenschappen van de NaCl structuur met een grootte-ratio van 0.30 tussen de klein en grote bollen. Het type wanorde dat onderzocht wordt zijn de posities van de kleine bollen binnen de octahedrale gaten, de polydispersiteit van de kleine bollen en het aantal kleine bollen. Wij vinden dat geen van deze drie wanordes de fotonische verboden zones vernietigd. De laatste soort wanorde is erg interessant omdat door de verandering in de verhouding kleine tot grote bollen een NaCl structuur (kleine en grote bollen) vanuit een FCC-structuur (alleen grote bollen) kan verkregen worden. Structuren die tussen deze twee structuren in zitten worden interstitiële vaste oplossingen (IVO) genoemd. IVO's met verschillende composities worden gevormd langs de hoogte van de sedimentatie kolom omdat het aantal kleine deeltjes verminderd met de hoogte in een binair mengste van harde-bollen. Wij vinden dat de IVO's van alle composities een fotonische verboden zone hebben. Het is ook interessant om te vermelden dat tot bijna 10 % lege ruimtes weinig invloed heeft op de verboden zone van de NaCl structuur.

Samenvattend is dit proefschrift een stap in de richting naar de fabricatie van periodische en quasi-periodische fotonische kristallen door zelforganisatie van colloïdale deeltjes met een simpele interactie potentiaal. In het eerste deel hebben wij gevonden dat het twaalfhoekige quasikristal stabiel is, dat het vormingsproces robuust is voor veranderingen in de lengte en de vorm van de interactiepotentiaal en dat het door sedimentatie gevormd kan worden. In het tweede deel benadrukken wij, na verschillende quasikristallen te hebben bestudeerd, dat de stabiliteit van een quasikristal niet is uniek en voor elk systeem afzonderlijk bekeken moet worden. In het derde deel hebben wij geconcludeerd, door fotonisch onderzoek, dat het core-corona systeem een lucratief systeem is om naar fotonische kristallen te kijken.

Thanks to Santosh Gurunath, Ernest van der Wee, Dieter Aerts and Kristein Bortels for helping with the Dutch translation.

Thank you | Dank u | Dhanyawad | Nandri

It is finally the time to simultaneously look back at the fine print as well as the helicopter view of the PhD journey. For me, this journey started the day my brother, Sriram (Annu), started his Bachelor studies in engineering and then proceeded to a doctorate. I knew then that this is what I was going to be; just the field was yet to be decided. Annu, with your guidance, I became a materials engineer and here I am, on my way to completing my PhD. I have wondered countless times during these past four years about why did you not warn me how hard this journey is going to be and how do I get out of it. But, on other times, I was happy that you didn't do that as it gave me the opportunity to find my own way through this complicated maze. Thank you for that. Of course, I could not have navigated this maze all on my own. I take this opportunity to thank the people who were part of my effective and efficient support system and made this possible.

The first person to thank is my supervisor Marjolein Dijkstra. They say that first impressions last forever. Mine certainly does. It started on a Friday evening in October 2013. I had received the results of the previous round of interviews and the project proposals from Shell late in the evening. And I woke up the Saturday morning to find an email from you, Marjolein, with an invitation to visit your group and instructions on what you need and how to proceed. This was even before I had gone through the proposals myself! Then and during our first meeting, I was impressed by your sincerity, knowledge, and straight-forwardness. That has not changed over the four years that I have spent in your group. It was encouraging to find that your office doors were always open for us and that you were always eager for short/long discussions. Through the years, you have ensured a strict schedule of my work and I am extremely thankful for that. You have motivated me to work harder during the times when I was not, and that has helped me strive for better. You maintained a perfect balance of giving me the freedom on what I want to do and letting me know if and when something is going wrong or not working. In short, I am glad that we opted for each other during the matching process and I could not have asked for a better supervisor.

The next goes to the staff of the Soft Condensed Matter group, Alfons van Blaaderen, Arnout Imhof, René van Roij, Laura Filion, Marijn van Huis, Krassimir Velikov, and Patrick Baesjou for creating and maintaining a multi-disciplinary environment. In particular, I would like to thank Alfons for pointing out different simple and obvious yet overlooked points during the work discussions and in this thesis, and René for the valuable comments that helped me broaden. Arnout, it was a pleasure working as a teaching assistant in your course. You have organised it so well that it did not leave a lot for us to do. Patrick, it was enjoyable working with you during the course as well. It was an enriching experience with all of us trying to figure out things together. Laura, thank you for the talks about life at various instances and for explaining the various free-energy calculations. Finally a big thanks to Marion, Thea, Peter, Chris, Judith, and Relinde for ensuring a smooth flow of the technical and administrative jobs.

Being a part of an Industrial Partnership Program has its own advantage. Especially the Computational Sciences for Energy Research (CSER) programme provided me an opportunity to get to learn a lot of new things over a broad range of research topics. I thank Maria Teuwissen, Martijn de Jager, Maria Sovago and Joost Weber from FOM and Kumar Ramachandran, Pratibha Priyadharshini, Xena Thomas, Shubha Jayappa, Sanjay Suri, Nilanjana Bhattacharya, and Paul Mak from Shell for organising various events and arranging the administrative activities over the years. I am thankful to my coach Joost Smits for his encouragement and interest in my work. Thank you for your quick replies to my emails which ensured a smooth functioning. I also thank the other coaches Sipke Wadman, Sander van Bavel, and Hans Geerling for working together and organising our yearly meetings. It provided an unique advantage for us to be guided by more than one coach.

I would then like to thank the people who helped me get through my initial days of settling-in in the SCM group, Anjan and John. Anjan, thank you for patiently teaching me the basics and for helping me get through the simulation course material. I enjoyed our walks through the garden trying to figure out various problems. John, I still remember our first meeting when I had come for my interview. You were the only simulator around and no one else had come to work yet. You took it up on you to give me a comprehensive view about everything. And the same continued even after I joined the group. A special thanks to you for pulling me out of the abyss at the end of my first year. Thank you also for the numerous times when you hosted us at your place and cooked delicious food (esp. the amazing rasam and eggplant that doesn't taste like eggplant ;)), and for the times when we stayed over because we had to catch an early train.

I am lucky and grateful to have the same set of office mates throughout this journey and I could not have asked for better ones. Guido, thank you for helping me settle down in the office. I still do not understand how you smoothly transferred your role of watering the plants to me, without me realising it. Although I am not sure if I enjoyed all your pranks, I am happy they happened because they took the seriousness out of any normal day. I applaud your patience for answering my numerous 'do you have a minute' calls through the years, which never ever lasted just a minute, sometimes going in to days. I enjoyed collaborating with you and learnt a lot. Thank you for being there when I needed the most. I am not sure if I will ever get over the fact that you always mess up my invitations; perhaps not messing up on my defense would help ;) Nick, it is funny to think back now about how we did not talk anything more than a few words of pleasantries in our first few months. I am glad that we did not stay there and have matured through the years. It was nice to see your transformation from never turning up at work to beating Guido and myself in the work discussion counter. I am also glad that the pleasant and tasty smoking flavours stopped. I still can not forget the gummy bear one you got. I am sure that I did not trouble you with questions as much as I did Guido, and it was hugely because I could not follow your geeky explanations most of the time. Thank you both for maintaining a joyful atmosphere through out and (patiently ;)) putting up with my heater cribbing.

I am grateful for the presence of my personal 'jesters' who could always pull me out any bad mood: Somil and Vatsan. Somil, I know you are going to hear this a lot. But I still laugh thinking about your message asking me what should you do as you have burnt down the microwave! I am sorry that I did not initially live up to your expectations of a 'senior', but hopefully I have made up for it thereafter. A huge kudos to you for getting me interested in table tennis and the gym, albeit for a short time. Vatsan, seeing you consciously try to obey your 'house-rules' in my office and each time end up failing miserably was fun. Your road-trips are a perfect guide of how-not-to-be and I will remember them.

I have not extensively interacted with the group members. I attribute that to an introvert living outside Utrecht. However, I have, in a way, had a focussed patchy interaction! Thank you Jissy, Wessel and Vatsan, who at various times have been my bus buddies. I enjoyed these talks very much, even though it cut into my reading time ;) Wessel, I commend your efforts for trying to get me out of the office for the coffee breaks and for the numerous times you brought delicious cakes and cookies. Thank you Ernest, Fabian, and Judith for being my Dutch buddies. Ernest, a special thanks to you for reading through so many of my documents and emails and helping me to continuously improve my Dutch skills. You definitely deserve a special mention for reading through the long and tedious Dutch summary well under an almost impossible deadline. Frankje, thank you for dropping by my office for unannounced breaks; I enjoyed talking about engineers versus physicists with you. Toni, it has been pleasure to share a room with you at various instances. Thanks for putting up with my early waking up schedule. I am grateful for your efforts in trying to get me out of the locked bathroom, even though you were more concerned about your talk-time balance than my faster rescue. Sid, thank you for being a patient listener every time I come to your office with stories. Vassilis (the elder brother), thanks to you the name Harini-chan is going to remain with me for long. Da, I will think of you every time I have a laddu. Simone, I have enjoyed the historic and fun facts in your presentations and the don't-care attitude with which you deliver them. I also appreciate your well thought about comments on my articles. Last on the list, I really enjoyed the various trips to the Dutch Soft Matter meetings, Veldhoven, Lisbon and Berlin. In totality, the time spent at the SCM group has been pleasant. For this, I thank all current and past members. In addition, I also thank Chris Everts and Lourens van Dijk for respective collaborations on the core-corona particles and plasmonic calculations. It was a learning experience to work with you even though it did not result in a productive conclusion.

Finally, I would thank the CSER community in Utrecht who have courageously acted as scapegoats for the various dishes I made for different festivals. Sandeep, I enjoyed our conversations at Minnaert trying to get our head around the whole program and to find out way through it. I am truly in awe of how you have progressed in your PhD. Somil and Toni, it was a pleasure to welcome you here and help you with numerous things over the time. Sid, it was an experience to be your 'buddy', which I think was namesake as you did not need one at all. Ajinkya and Priyanka, although we have not spent a lot of time together, it was nevertheless nice to get to know you. If there is going to be an opportunity of us being colleagues in the future, I look forward to it.

Lastly, it is time to thank the people who are the reason I am where I am today - my parents, Usha and Pattabhiraman. Thanks a lot for your constant support throughout, for encouraging me to try new things and letting me follow my dreams. Thank you for putting our interests before your needs. I could not have achieved this without you. Annu, you have been my guide and go-to person since the beginning. I am really glad for that. Thank you for being the best brother and guide ever and for creating difficult footsteps for me to follow ;). Further, I am lucky to have found an equally supportive extended family in my parents-in-law, Jyoti and Gurunath, sister-in-law Abhinaya and brother-in-law Sanjay. Thank you for your support and encouragement.

Finally it boils down to the person who has stood by me through the ups and downs of the last four years, my husband Santosh. You knew exactly what I needed and when I needed even when I did not realise it. Thank you for believing in me even when I did not and for encouraging me during my bad days and subduing me during the good days. You knew somehow how to put me into ease with regard to the work anxieties. You helped me challenge and question myself and motivated me do better everyday. I cannot not thank the chauffeur service during the years and especially during thesis writing ;) I do not think I could have survived with out that. I really cannot believe that you read through my entire thesis numerous times and came up with tons of corrections and suggestions, every. single. time. Finally, a huge thank you for writing the ‘about the author’ section; I could have never done justice to that.

This list is incomplete if not for a final thanks to HTM, NS, and U-OV for ensuring that I reach work on most of the days, and for giving me something to complain about on the days when they did not work! It is because of you that I rediscovered my love for books. Thank you!

List of publications

This thesis is partly based on the following publications:

- H. Pattabhiraman, A. P. Gantapara, M. Dijkstra, *On the stability of a quasicrystal and its crystalline approximant in a system of hard disks with a soft corona*, The Journal of Chemical Physics, 143, 164905 (2015) (Chapter 3).
- H. Pattabhiraman, M. Dijkstra, *The effect of temperature, interaction range, and pair potential on the formation of dodecagonal quasicrystals in core-corona systems*, Journal of Physics: Condensed Matter, 29, 094003 (2017) (Chapter 4).
- H. Pattabhiraman, M. Dijkstra, *Phase behaviour of quasicrystal forming systems of core-corona particles*, The Journal of Chemical Physics, 146, 1114901 (2017) (Chapters 3 & 6).
- H. Pattabhiraman, M. Dijkstra, *On the formation of stripe, sigma, and honeycomb phases in a core-corona system*, Soft Matter, manuscript accepted (2017) (Chapter 7).
- H. Pattabhiraman, G. Avvisati, M. Dijkstra, *A novel two-length scale pyrochlore crystal with a photonic band gap self-assembled using colloids with a simple interaction potential*, manuscript submitted (Chapter 9).
- H. Pattabhiraman, M. Dijkstra, *The effect of disorder of small spheres on the photonic properties of the inverse binary NaCl structure*, manuscript submitted (Chapter 10).
- H. Pattabhiraman, M. Dijkstra, *The curious case of periodic layers of dodecagonal quasicrystal and floating crystals*, manuscript in preparation (Chapter 5).

Other publications by the author:

- G.V. Prasad Reddy, P. Harini, R. Sandhya, K. Bhanu Sankara Rao, R. K. Paretkar, *On dual-slope linear cyclic hardening of Hastelloy X*, Material Science and Engineering A, 527:16, 3848-3851 (2010).

Oral and poster presentations

A part of the contents of this thesis was presented at the following meetings/conferences:

- 22nd Dutch Soft Matter Meeting, Delft, The Netherlands, May 2017 (oral)
- Physics@Veldhoven, Veldhoven, The Netherlands, January 2017 (oral)
- Computational Sciences for Future Energy Conference 2016, Utrecht, The Netherlands, October 2016 (poster)
- Annual Bangalore CSER Days, Bengaluru, India, May 2016 (poster)
- Physics@FOM, Veldhoven, The Netherlands, January 2016 (poster)
- 8th Conference on Aperiodic Crystals - Aperiodic 2015, Prague, Czech Republic, September 2015 (oral)
- Physics@FOM, Veldhoven, The Netherlands, January 2015 (poster)

About the author

Harini Pattabhiraman was born on 13 September 1988 in Chennai, India. She spent her childhood in various schools (six to be precise) across South and West of India, not only excelling in studies, but also honing her skills in Bharatanatyam, an Indian classical dance form. In 2006 she moved to Nagpur, India to start her Bachelor studies in Metallurgical and Materials Engineering at Visvervarya National Institute of Technology. In 2009, she was selected as one of the 15 students from across India for an INAE (Indian National Academy of Engineering) fellowship; where she conducted research on the low-cycle fatigue behaviour of Hastelloy X at Indira Gandhi Center of Atomic Research at Kalpakkam. Her bachelor thesis titled 'Synthesis and characterisation of nano-structured silica from rice husk' received the maximum possible grade. In 2010, Harini completed her Bachelor studies with distinction and stood third in her batch. During her bachelor studies, Harini was quite passionate about social causes; she was one of the initial members of a social foundation, Prayaas, providing education to children in villages near Nagpur.

After completing her bachelor studies, Harini followed a short stint at Viraj Profiles Limited, a steel plant in Mumbai, India. As a technical assistant in the quality control department, she developed several tools to monitor and improve the billet quality at the plant. In 2011, she moved to The Netherlands to start her Master studies at Technische Universiteit Delft in Material Science and Engineering, with a specialisation in Metal Science and Technology. During her masters, Harini completed an internship and master thesis at TATA Steel, IJmuiden, The Netherlands. Here, she studied the microstructural properties and transformational kinetics in a dual phase steel using computer simulations. Harini was also part of the departmental education committee at TU Delft, where she played a pivotal role in feedback between the faculty and students.

In 2013 Harini was selected for the Computational Sciences for Energy Research (CSER) PhD programme, a joint research initiative of Shell Global Solutions and Nederlandse Organisatie voor Wetenschappelijk Onderzoek (NWO). As part of this programme, she started her PhD under the supervision of Prof. dr. ir. Marjolein Dijkstra at the Soft Condensed Matter group in Universiteit Utrecht, The Netherlands. During her PhD, she worked on simulating the phase behaviour of two-dimensional colloidal quasicrystals and other photonic crystals and later extended to studying their photonic properties. The main results of this work are presented in this thesis.

Apart from her love for material science, Harini enjoys activities like reading and roller-coaster hopping during her spare time. She also enjoys travelling and collecting currency and puzzles during them. Solving large jigsaw puzzles is her favourite hobby, with walls dedicated to her puzzles at her home.